An integrated approach to plasma generation and heterogeneous reactions on microbubble gas-liquid interfaces

Thomas David Holmes

This thesis is submitted for the degree of Doctor of Philosophy

Department of Chemical and Biological Engineering, University of Sheffield

December 2014

Acknowledgements 5
Abstract 6
1 Introductory review – ozone, AOP's and RONS for water treatment 7
1.1 Summary 7
1.2 The need for alternatives to chlorination 7
1.3 Ozone 9
1.3.1 Conventional ozone generation 10
1.3.2 Chemistry of ozone generation in plasma 12
1.3.3 Thermodynamic and stoichiometric limits of ozone generation 13
1.3.4 Utilisation of ozone - transfer from gas to liquid 14
1.4 Indirect ozonation reactions and Advanced Oxidation Processes 15
1.4.1 Fenton based processes and other chemical methods 16
1.4.2 UV and other radiation based processes 17
1.4.3 Electric/electrochemical methods 18
1.4.4 Ultrasound/cavitation/microbubble collapse 18
1.4.5 Other bubble effects 19
1.4.6 Catalysed ozone decomposition 20
1.4.7 Comparison of AOP's 21
1.5 Reactive Oxygen and Nitrogen Species (RONS) 26
1.5.1 Plasma Microreactors/Microplasmas 26
1.6 Investigation into the combination of plasma microreactor and microbubble technologies – the scope of this work 27
1.6.1 Discussion 27
1.6.2 University of Sheffield technologies 29
1.6.3 Outline and objectives of subsequent chapters 31
2 A pilot scale trial of a plasma micro-reactor device with microbubble diffuser 33
2.1 Summary 33
2.2 Chapter introduction - The "ozone dosing lance" 34
2.3 Field trials of the ozone dosing lance 37
2.3.1 The pilot plant 37
2.4 Practical constrains in the field 39
2.4.1 The final effluent quality 39
2.4.2 Observations of lance performance 40
2.5 Results of field trials 41

2.5.1 UVt 41
2.5.2 DOC, TOC, BOD & COD 42
2.5.3 Salicylic acid 46
2.5.4 Nitrogen & phosphorus species 47
2.5.5 Pathogenic microorganisms 49
2.5.6 Organic priority substances 50
2.5.7 Heavy Metals 50
2.6 Laboratory measurement of dosing lance ozone output 51
2.6.1 Ozone output dry test 51
2.6.2 Ozone output wet test - KI titration 53
2.7 Discussion 53
2.7.1 Fluidic oscillator effects 54
2.8 Further work required 54
2.9 Conclusions 55
3 Kinetic modelling of air feed plasma and air/water interface 56
3.1 Summary 56
3.2 Rationale for the model 56
3.3 Basic model framework 59
3.4 Plasma 63
3.4.1 Plasmas – Basics 63
3.4.2 Stepwise ionisation by electron impact 65
3.4.3 Background free electrons 65
3.4.4 Basic plasma equations and parameters 65
3.4.5 Rate equation 66
3.4.6 Electron energies 67
3.4.7 Emission of light from excited species 68
3.4.8 Dielectric barrier discharge (DBD) 69
3.4.9 Complete scheme of O2/N2 mixture, plasma and afterglow simulation 69
3.4.10 Addition of water, discussion 71
3.4.11 Exclusion of argon 71
3.5 Air/water interface 73
3.5.1 Air water interface – basics 74
3.5.2 The water dimer 75
3.5.3 OH radicals at the interface 76

3.5.4 Air/water interface electrochemical characteristics 77
3.6 Proposed interfacial kinetic simulations 79
3.6.1 Simplified surface model 80
3.6.2 Nihonyanagi/Vacha model 81
3.6.3 Shen and Ostroverkhov model 85
3.6.4 Gas species interaction with the surface – droplet skin chemistry – accommodation coefficients 86
3.7 Bulk liquid reactions 87
3.8 Full integrated model 87
3.9 Discussion 90
3.10 Conclusions 92
4 On the design aspects of a microplasma/microbubble reactor 93
4.1 Summary 93
4.2 Electrical aspects 93
4.2.1 Power supply signal requirements 95
4.2.2 Gap size and tolerances 96
4.2.3 Conductivity of the cables and electrodes 101
4.2.4 Radiative resistance of the cables 101
4.2.5 Dielectric barrier electrical behaviour 101
4.2.6 Plasma conductivity 103
4.3 Materials aspects 104
4.3.1 Mechanical properties of materials 105
4.3.2 Maintenance of temperature 105
4.3.3 Adhesive methods of dielectrics to electrodes 108
4.4 Diffuser aspects 108
4.4.1 Effect of water vapour re-entrainment into the reactor on ozone formation alone 108
4.4.2 Effect of water re-entrainment into the reactor 109
4.4.3 Diffuser materials 111
4.4.4 A note on the effect of the diffuser geometry 113
4.4.5 Microbubble Formation pressure 113
4.4.6 Reactions of plasma with diffuser material surfaces 114
4.4.7 Effect of fluidic oscillator on plasma conditions 115
4.5 Discussion 116
4.5.1 Possible explanations of the dosing lance performance 117

4.5.2 Conclusions 118
5 Development and characterisation of a single bubble pore plasma capillary reactor 119
5.1 Summary 119
5.2 Introduction 119
5.2.1 Implications from the kinetic simulation chapter 119
5.2.2 Implications from the field trials 120
5.2.3 Implications from the design principles 121
5.3 Aims 122
5.4 Development of design 122
5.5 Characterisation of a single glass capillary tube reactor 125
5.5.1 Emission spectrum measurements analysis and relation with kinetic model predictions 130
5.5.2 Oscillatory flow versus non-oscillatory flow 133
5.5.3 Voltage and current characteristics 136
5.5.4 Glass capillary reactor – bubble formation versus plasma formation 140
5.6 Solution to water re-entrainment from increasing proximity 142
5.7 Discussion and conclusions 148
5.7.1 Future work 150
References 151
Appendix 1 165
Appendix 2 167
Appendix 3 194
Appendix 4 278

Acknowledgements

I would like to give my most sincere gratitude to Professor William Zimmerman for his support, encouragement and inspirational positivity throughout the course of this work. To Andrew Patrick, Stuart Richards, Keith Penny and Steve Blackburn for the practical knowledge and experience which they were so generous in sharing. To Fahad Rehman, Dr Wameath Abdul-Majeed and Yining Liu for their suggestions, helpful comments, and much needed kind words. To Adam Samuel, Donald Willey and Anggun Siswanto for their friendship, and for understanding when literally no one else could. Last but most certainly not least, I wish to offer my warmest thanks to my family for their continued and unyielding support throughout the most difficult periods of this work. Without them it could never have happened and I am, as always, forever in their debt.

Abstract

Oxidizing agents have many uses, and the need for oxidizing agents which can be sustainably generated and biodegradable, such as ozone, is growing daily. From studies of available literature it was found that there are many short lived reactive oxidant species generated in plasmas which have similar and in some cases greater oxidation potential than ozone. It was hypothesised that closer proximity of the plasma to the point of use could make use of these, and that the air/water interface could have properties which can catalyse ozone breakdown and possibly catalyse other chemical processes.

A 0D chemical kinetic model with conditions varying to successively simulate the plasma, afterglow, air/water interface, and bulk liquid, consisting of over 700 reactions was compiled. Subsequent simulations suggested that increasing the proximity of the plasma to the air/water interface allows the short lived O atom (which during the time the plasma is active is present in much higher quantities than ozone) to form hydroxyl radicals directly at the air/water interface, and that increasing the interfacial surface area to volume ratio increased the rate of base catalysed ozone decomposition, both of which would lead to increases in efficiency of oxidation simply by decreasing the bubble size and increasing the proximity of the plasma to the bubble.

A pilot scale field trial of a plasma/microbubble device for oxidation of a number of chemicals in wastewater was conducted and the results analysed. The results of the field trials were reviewed in combination with relevant literature and laboratory tests to suggest design principles for plasma/microbubble reactors. Drawing from the suggested design principles, and the results of the kinetic simulations, a single channel plasma microbubble reactor design was fabricated and tested with a view to maximising the proximity of the plasma to the air water interface whist still allowing for continuous bubble formation. Results suggested that the fluidic oscillator has a stabilising effect on this plasma and that increasing the proximity of the plasma to the air water interface increased the extent to which the contents of the water were oxidised.

1 Introductory review – ozone, AOP's and RONS for water treatment

1.1 Summary

In a world where resource energy sustainability and environmental issues are of increasing importance, technologies which move away from fossilised coal and crude oil and other such raw materials, and the energy costs associated with their extraction, refinement and transportation, are gaining increasing attention. In the same way, chemicals and chemical processes which do not persist in the environment or cause other damage to natural resources due to their use, are increasingly favourable.

Oxidising agents are one group of chemicals that are extremely useful in many areas, and the aim of this chapter was to gain an overview of the different water treatment techniques that can be used in such a way, namely ozonation and Advanced Oxidation Processes (AOP's), by reviewing the relevant literature. A closer look at these techniques revealed that, chemically speaking, they are very similar, and that the active species involved in ozonation and AOP's all come under the category of Reactive Oxygen and Nitrogen Species (RONS) some of which are formed intermittently in plasmas in the processes of ozone formation, and could be used alongside it, theoretically increasing those plasmas oxidation capabilities. There are two processes that have been recently developed at the University of Sheffield that could be used to realise this efficiency increase, a microbubble generation process and a plasma microreactor based process for ozone generation. The chapter concludes with the possibility of making an advance by combining these two, and the need for an investigation into this.

1.2 The need for alternatives to chlorination

In the 1970s the use of chlorination as a sterilisation method for drinking water was found to give rise to carcinogenic properties within the water (Marx, 1974). The presence of chlorinated organic compounds in drinking waters where chlorine was applied was then discovered (Bellar, Lichtenberg, & Kroner, 1974), providing an explanation for the carcinogenic properties. Mechanisms by which these natural chemicals might become chlorinated were subsequently proposed by Rook (1975).

Chlorine is a strong electron acceptor, and as such is reacted strongly with electron dense regions such as carbon double bonds (Figure 1). This high oxidation potential makes it a good disinfectant, as it reacts with the organic chemicals of the microbiota bodies, impairing their functions.

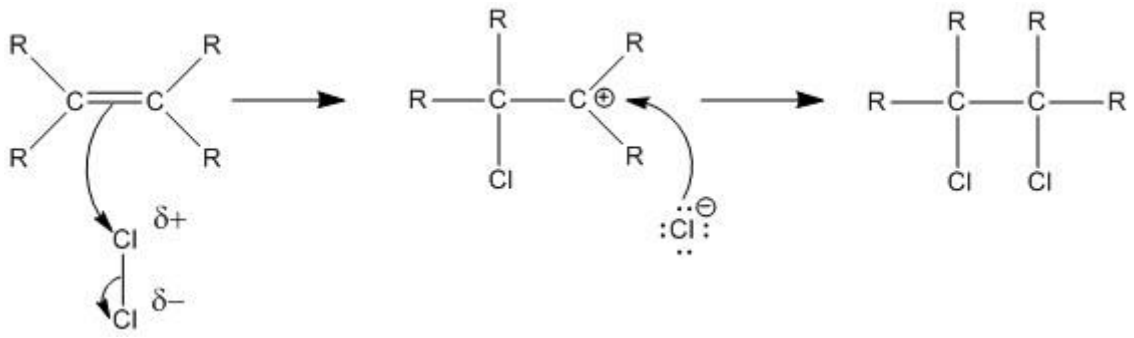

Figure 1: The mechanisms of the electrophilic addition reaction of chlorine with a carbon double bond. The negative charge of the double bond causes a temporary dipole in the chlorine molecule, the Cl-Cl bond electrons go to the far chlorine atom, breaking the bond, and two electrons from the C=C double bond are donated to the near chlorine atom, resulting in the formation of a bond between the chlorine atom and one of the carbon atoms. The remaining chlorine ion is attracted to the positive charge of the carbocation opposite the chlorinated carbon, and donates two electrons, resulting in another C-Cl bond.

Chlorines reactivity means it will also react with many other constituents of natural waters. Humic acids, for example, have electron dense regions in the benzene rings in their molecules. Figure 2 shows a proposed molecular structure of a humic acid. The important features to note are the carboxylic acid groups which account for much of the humic acids' solubility, the benzene rings and other double bonds, which are electron dense regions and as such are potential targets for oxidising agents such as chlorine. As humic acids are formed from the decomposition of large organic molecules of which there are an enormous variety, there are many different possible humic acid molecules. Carbon double bonds are almost universal across organic life however, and will inevitably be a constituent of most humic acid molecules. Benzene rings are also very common structures in natural organic molecules, and the electron dense region at their centre is another site with an affinity for reaction with oxidising agents.

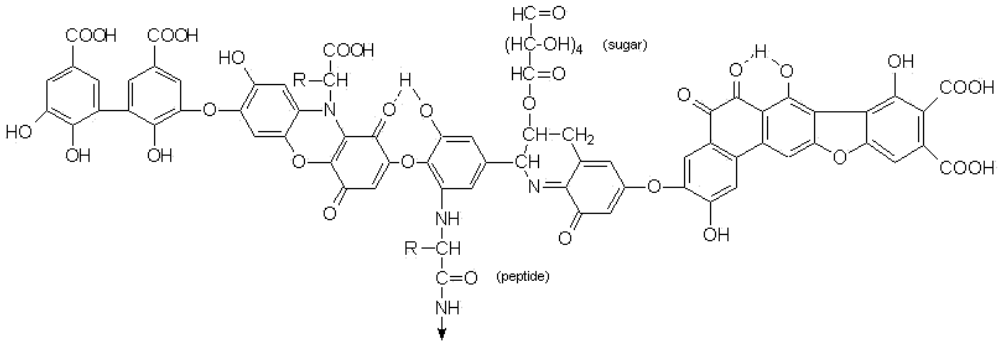

Figure 2: Molecular structure of a humic acid (Stevenson, 1994).

Reactions of humic acids with chlorine lead to the formation of chlorinated by-products, many of which are harmful carcinogens (Figure 3) (Richardson, Plewa, Wagner, Schoeny, & Demarini, 2007). Many similar anthropogenic chlorinated organic structures (such as dioxins and PCB's) exhibit high toxicity, and are undesirable especially where human consumption and environmental protection are concerned. The chlorination in these molecules also makes them resistant to natural degradation, and thus they can persist in the environment and can bioaccumulate in living organisms.

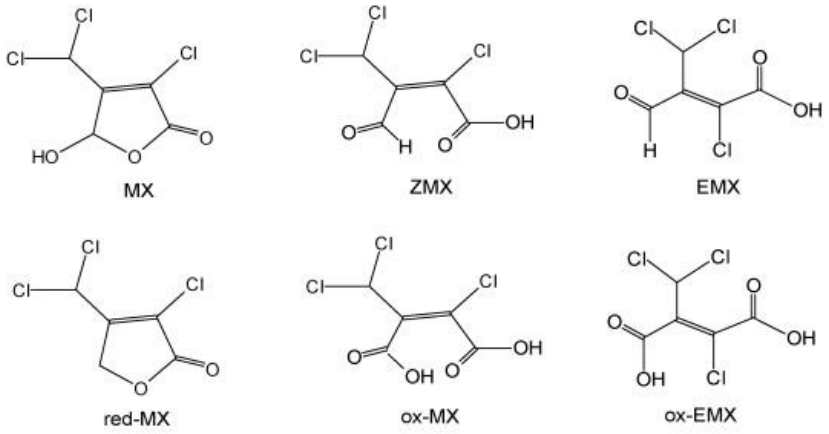

Figure 3: Examples of carcinogenic chlorinated by-products of the chlorination of drinking water: [3Chloro-4-(dichloromethyl)-5-hydroxy-2(5H)-furanone (MX), (Z)-2-chloro-3-(dichloromethyl)-4-oxobutenoic acid (ZMX), (E)-2-chloro-3-(dichloromethyl)-4-oxobutenoic acid (EMX), and their reduced (red-) and oxidised (ox-) forms (Richardson et al., 2007).

Clearly, treatment methods which can prevent the formation of harmful by-products, or can eliminate them, are required.

1.3 Ozone

Ozone reacts with electron dense regions such as carbon double bonds in a similar way to chlorine, and results in the breaking of C=C double bonds (Figure 4) (Criegee, 1975). Due to this, as well as its disinfection capabilities, it has the advantage of being able to break down persistent, harmful organic compounds (such as those mentioned in the previous section) into simpler, less harmful ones (Beltrán, 2003). These direct ozonation reactions are highly selective and specific (Hoigné & Bader, 1976). In almost all applications oxidation-reduction reactions and electrophilic substitution reactions can occur as well as the addition reactions shown in Figure 4. Each of these processes

contributes to breakdown of organic molecules or to disinfection (Beltrán, 2003) and the by-products produced during ozonation, tend to be less persistent and less harmful than the initial substrates (Glaze, 1986).

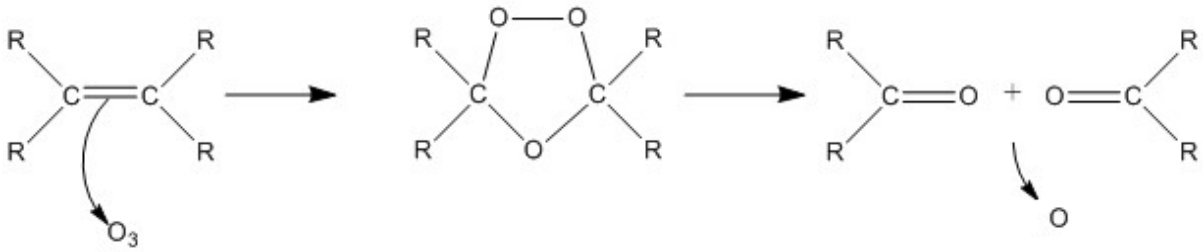

Figure 4: Mechanism of electrophilic addition reaction of ozone with carbon double bonds (Criegee, 1975).

Ozone is an unstable gas and therefore cannot be stored or transported far, and must be generated close to the point of use. With this in mind, any consideration to use ozone must take into account its generation method.

1.3.1 Conventional ozone generation

As of 1999, large ozone generators are capable of producing up to 5% by weight of ozone in an air feed and up to 18% by weight of ozone from a pure oxygen feed and typically consume power in the order of megawatts to give ozone outputs in the order of hundreds of kg per hour (Kogelschatz, Eliasson, & Egli, 1999).

Large scale generation of ozone for drinking water treatment has been around for over 100 years (Kogelschatz et al., 1999). Its existence, means of generation, and use as a water treatment method have been known about for even longer. Conventional ozone generation is most commonly done by discharging electric currents at high voltages across either air or oxygen, which when sufficient to overcome the first ionization energies of some or all of the constituent atoms and molecules, will result in a mixture of free electrons, ions and neutral particles from the original gas, which is known as a plasma. Within this new state of matter particles can undergo very high energy collusions, which lead to the formation of ozone when oxygen is present, and resulting ozone enriched gas can then be dosed into water. Two main gas discharge types are used for ozone formation; corona discharge (CD)and dielectric barrier discharge (DBD) (Fridman, 2008), the latter being the predominant method used in industry.

The main difference between the two reactors is their electrode configuration. A corona discharge typically consists of a thin central electrode in a cylindrical outer electrode, powered by DC. Dielectric barrier discharges tend to have much smaller distances between the electrodes and are powered by AC (Figure 5), however the most essential feature of the dielectric barrier discharge is, as the name suggests, the presence of a dielectric barrier which prevents the flow of direct current. This feature need not be present in order to maintain a corona discharge.

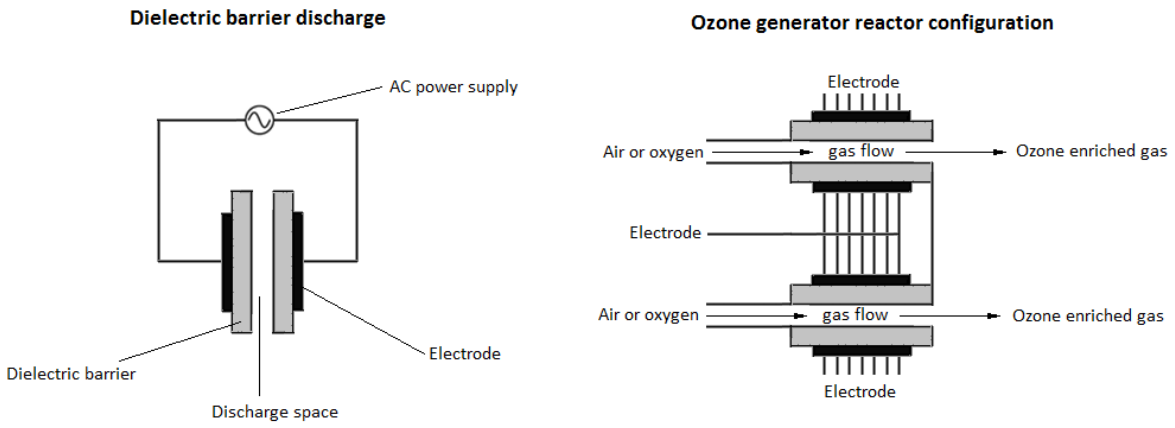

Figure 5: (left) Diagram of dielectric barrier electrode configuration for plasma discharge formation, some configurations omit one of the dielectric barriers over the electrodes. (right) Reactor configuration for ozone generation by dielectric barrier discharge, the two gap spaces are often between two concentric cylinders.

Dielectric barrier discharge plasmas have been used to generate ozone for over 150 years, the first DBD being suggested for ozone production by W. Siemens in 1857 (Kogelschatz et al., 1999). Many other technologies for the generation of ozone from plasmas have been developed since, but the principle means of ozone generation is still via DBD. A common reactor configuration for ozone generation consists of two concentric cylinders, the outer of stainless steel, the inner of glass or ceramic with an electrode on its inner side, the discharge forming in the radial gap between the glass and the steel tube. Conventional DBD ozone generators are composed of arrays of these discharge tubes (Kogelschatz et al., 1999).

The two methods differ in the power supplies used, and in the configuration of electrodes, but the basic principle of energising the air using electric fields to allow high energy reactions such as ozone formation to proceed, is essentially the same for both methods.

1.3.2 Chemistry of ozone generation in plasma

The process of ozone formation in the plasma begins with the electronic excitation of O_2 by electron impact, subsequent dissociation occurs due to one or more further electron impact reactions (B Eliasson & Kogelschatz, 1999):

$$e + O_2 \rightarrow O_2^*(A^3\Sigma_u^+) + e \rightarrow O(^3P) + O(^3P) + e$$

$$e + O_2 \rightarrow O_2^*(B^3\Sigma_u^-) + e \rightarrow O(^3P) + O(^1D) + e$$

O_2 dissociation can also happen as the result of vibrational excitation, dissociative attachment, and ion related processes. However, the above reactions are considered to be the most important. The O atom reacts with O_2 molecules with the contribution of a third body (M, normally O_2 if the gas is oxygen) in a three-body recombination reaction:

$$O + O_2 + O_2 \rightarrow O_3 + O_2$$

Unfortunately, the O atom that is so essential for ozone formation is also the key agent in its destruction:

$$O + O_3 \rightarrow O_2 + O_2$$

The O atom will also recombine with itself in another 3 body recombination process, thus eliminating itself from the plasma:

$$O + O + O_2 \rightarrow O_2 + O_2$$

In air, the formation of the O atom can occur by other pathways involving reactions with nitrogen species (B Eliasson & Kogelschatz, 1991):

$$N + O_2 \rightarrow NO + O$$

$$N + NO \rightarrow N_2 + O$$

$$N_2(A^3\Sigma_u^+) + O_2 \rightarrow N_2O + O$$

$$N_2(A^3\Sigma_u^+, B^3\Pi_g) + O_2 \rightarrow N_2 + O + O$$

However, there are also discharge poisoning effects when the NO concentration becomes too high, that remove not just the O atom that is necessary for ozone formation, but also the O_3 itself. The NO and NO_2 regenerate themselves in 2 step processes of O destruction, and can thus be regarded as having a catalytic effect on the removal of O from the plasma.

$$O + NO + M \rightarrow NO_2 + M$$

$$O + NO_2 \rightarrow NO + O_2$$

$$O_3 + NO \rightarrow NO_2 + O_2$$

It is thus essential in air plasma, to ensure that conditions where NO_x poisoning of the ozone generation does not occur. Higher temperatures in ozone generators favour NO generation (B Eliasson & Kogelschatz, 1991), and thus ozone generators often require cooling systems to prevent temperature build-up.

Increasing the power input into the reactor increases the amount of excited N and O species formed, but due to the effects of the O atom in oxygen gas, and NO_x in air, increasing the power input does not produce a proportional increase in ozone output.

1.3.3 Thermodynamic and stoichiometric limits of ozone generation

Ozone formation from oxygen is an endothermic process, and the energy required per mole of ozone formed is equal to the enthalpy of the following reaction:

$$3O_2 \rightarrow 2O_3$$

$$\Delta_r H^\circ (298\ K) = 143\ kJ/mol$$

Ozone is formed from oxygen in the molar ratio 3:2 (oxygen:ozone) and so the amount of ozone formed from oxygen cannot exceed 2/3 of the oxygen supplied. The values of 0.67 moles of O_3 per mole of O_2, and 0.14 moles of O_3 per mole of air are thus the maximum theoretical values of ozone yield for any process. As mentioned in section 1.3.2, there are kinetic constraints to achieving this thermodynamic limit.

A perfect ozone generator would produce ozone at 0.8275 kWh per kg, with 0.67 moles of ozone produced for every mole of oxygen in the feed gas. The electrical power consumption of large scale commercial ozone generators typically varies from 7.5 to 10 kWh per kg of ozone in a pure oxygen feed, and can be up to 20 kWh per kg of ozone in an air feed (Vezzu, Lopez, Freilich, & Becker, 2009). Furthermore, the efficiency of ozone production in conventional reactors tends to decrease as larger ozone quantities are produced. The relationship between ozone concentration and reactor efficiency is shown in Figure 6.

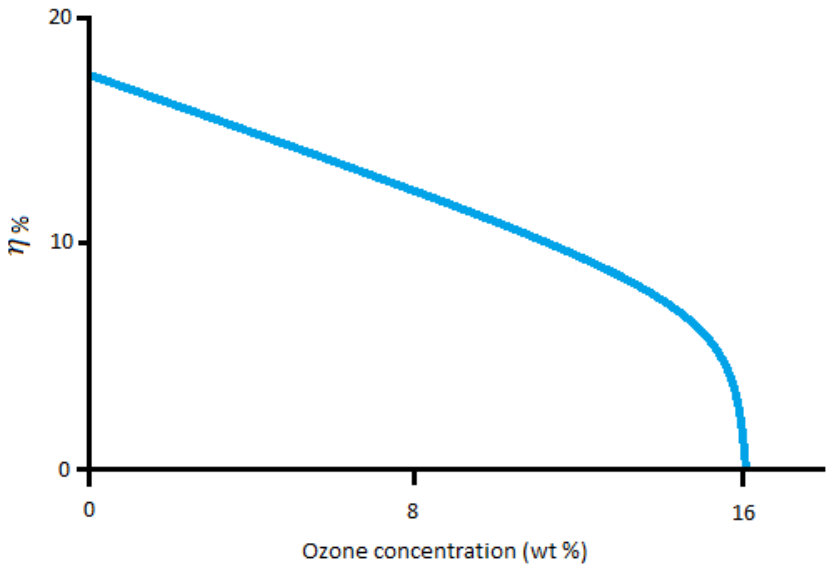

Figure 6: Graphical representation of the trade-off between ozone yield and energy efficiency (Vezzu et al., 2009) **the efficiency is given as** $\eta = 0.82/E_s \times 100[\%]$ **where** η **is the power efficiency (%) and** E_s **is the specific energy consumption (kWh kg^{-1}).**

1.3.4 Utilisation of ozone - transfer from gas to liquid

Generation of ozone is only one aspect of its use. Ozone obviously does not instantly and uniformly dissolve in water (Beltrán, 2003), it must somehow be transferred from the gas phase into the dissolved state. As ozone is sparingly soluble in water, mass transfer is an important factor in ozonation systems. One of the reasons ozone is not used in many applications is its low utilization efficiency - only a fraction of what is generated is actually used (Li, Tsuge, & Itoh, 2009). Mass transfer is normally done by bubbling of the gas through the water that needs to be treated. One of the simplest statements of mass transfer of ozone is:

$$m = E \cdot k_L a \left(C_L^* - C_L\right),$$

where m is the specific mass transfer rate, a is the volumetric interfacial area, k_L is the mass transfer coefficient, C_L is the concentration in the bulk liquid phase, C_L^* is the concentration in equilibrium with the gas phase and E is the enhancement factor which is used to adjust the calculation of the mass transfer rate to account for the chemical conditions in the water which can affect it (Gottschalk, Libra, & Saupe, 2000). The enhancement factor is dependent on the reactivity of ozone with the constituents of the liquid phase, and ranges from 1 in pure water, to 5 in waters with many potential reagents for ozone to react with.

The mass transfer rate increases proportionally with a decrease in bubble diameter in systems where mass transfer is the limiting factor (Bredwell & Worden, 1998), as this increases the amount

of surface area available for mass transfer for the same volume (increasing the value of α). Microbubbles have a higher mass transfer rate than larger bubbles due to the higher interfacial area, and are therefore beneficial to ozonation processes. The rate of ozonolysis has been shown to be enhanced with the use of microbubbles as a distribution system for the ozone (Li, Tsuge, et al., 2009).

As well as their large surface area to volume ratio, another reason that the microbubbles have a higher mass transfer rate is due to the microbubbles having a higher internal pressure, as suggested by the Young-Laplace equation (where ΔP is the pressure difference, γ is the surface tension and r is the bubble radius):

$$\Delta P = \frac{2\gamma}{r}$$

which due to Henrys Law increases the equilibrium quantity of gas transferred into the liquid phase (Li, Tsuge, et al., 2009).

1.4 Indirect ozonation reactions and Advanced Oxidation Processes

Whilst ozone is a strong oxidising agent, it often cannot oxidise all the organic chemicals in the water and indirect ozonation reactions are responsible for the degradation of chemicals that are not vulnerable to direct ozonation. Indirect reactions of ozone occur once the initial direct reactions of ozone begin to die down, and the rate of ozone decomposition begins to compete with the rate of ozone's reaction with the remaining substrates. Indirect reactions of ozone generally involve radical intermediates, such as the superoxide radical and hydroxyl radical, which are formed from the breakdown of ozone molecules (Beltrán, 2003).

The hydroxyl radical (·OH) is one of the most notable of the reactive intermediates of indirect ozonation reactions. It is more reactive than any other oxidising species employed in the treatment of water and wastewater (Von Sonntag, 2008) and has 1.35 times the oxidising power of ozone (see Table 1). It is therefore often desirable to maximise the production of hydroxyl radicals for treatment methods. The hydroxyl radical is extremely short lived due to its high reactivity, with a lifetime on the order of ms as the vast majority of its reactions in aqueous solutions have rate constants on the order of 10^7 to 10^{10} L mol^{-1} s^{-1} (Buxton, Greenstock, Helman, & Ross, 1988; Kwon, Ryu, & Yoon, 2009). Even in pure water the hydroxyl radical can be consumed in a number of rapid reactions with water molecules, and the various products of radical-water reactions. Hydroxyl radicals (and other radical "intermediates") therefore have even less capacity to be stored than ozone, and must be

formed in situ. Some methods focus primarily on generating this reactive intermediate and these processes are collectively known as Advanced Oxidation Processes (AOP's). AOP's do not exclusively generate the hydroxyl radical, but most studies focus specifically on this radical when explaining the chemistry of the processes (Andreozzi, Caprio, Insola, & Marotta, 1999; Ribeiro, Nunes, Pereira, & Silva, 2015; Rosenfeldt, Linden, Canonica, & von Gunten, 2006; Von Sonntag, 2008). There are a wide variety of different AOP's and the main processes are introduced in the following sections.

Table 1: Redox potentials of some oxidant species (Beltrán, 2003).

Oxidant	**E^O (V)**	**Relative potential of ozone**
Fluorine	3.06	1.48
Hydroxyl radical	2.80	1.35
Atomic oxygen	2.42	1.17
Ozone	2.07	1.00
Hydrogen peroxide	1.77	0.85
Hydroperoxide radical	1.70	0.82
Permanganate	1.67	0.81
Chlorine dioxide	1.50	0.72
Hypochlorous acid	1.49	0.72
Chlorine	1.36	0.66
Bromine	1.09	0.53
Iodine	0.54	0.26
Oxygen	0.40	0.19

1.4.1 Fenton based processes and other chemical methods

As can be seen from Table 1, H_2O_2 is a good oxidising agent, and it can itself be applied as a chemical agent. H_2O_2 alone is not always effective for high concentrations of reactions due to low rates of reaction even at reasonably high levels of H_2O_2. Improvements on the H_2O_2 method can be made by the addition of (for example) transition metal salts, ozone or uv-light to break down the H_2O_2 into hydroxyl radicals.

The use of specifically iron salts to catalyse H_2O_2 breakdown, is known as a Fenton process, named after Henry John Horstman Fenton, who initially developed it as an analytical reagent (Fenton,

1894). The hydroxyl radical is the direct reactant generated by Fenton processes (Sedlak & Andren, 1991; Yoon, Lee, & Kim, 2001) in the reaction

$$Fe^{2+} + H_2O_2 \rightarrow Fe^{3+} + \cdot OH + OH^-.$$

The use of Fentons reagents requires control of the pH, and naturally the handling and storage of H_2O_2 as well as its production (at some point). The iron must also be recovered at some stage after the process (Neyens & Baeyens, 2003).

Other chemical methods include other catalysts for hydrogen peroxide decomposition both homogeneous (Bokare & Choi, 2014; Mackul'ak, Prousek, & Švorc, 2011) and heterogeneous such as zeolites (Grčić, Mužic, Vujević, & Koprivanac, 2009; Kusić, Koprivanac, & Selanec, 2006) or ozone (Catalkaya & Kargi, 2009; W. R. Chen, Wu, Elovitz, Linden, & Mel Suffet, 2008; Qiang, Liu, Dong, & Zhang, 2010), the use of other chemical oxidising agents such as persulfates and other peroxides (Fang, Dionysiou, Wang, Al-Abed, & Zhou, 2012; Rastogi, Al-Abed, & Dionysiou, 2009; Yang, Cheng, Sun, Hu, & Liang, 2013), and processes which combine Fenton reagents with additional non-chemical methods (Babuponnusami & Muthukumar, 2014). These processes can also be combined with electric discharge (electro-Fenton processes) and UV light (photoelectron-Fenton processes).

1.4.2 UV and other radiation based processes

The hydroxyl radical can be formed in nature as a result of the photolysis of water by UV light (Barrett & Baxendale, 1960; Dhar, 1934), and application of artificial UV light to water is an established water treatment technique. The physics of the photodissociation of water has been dealt with extensively in a 1984 review (Andresen, Ondrey, & Titze, 1984). The basic principle behind the use of ultraviolet (UV) light is to break the water molecule bond using light with a wavelength corresponding to the energy required to break the bond, as in

$$H_2O + hv \rightarrow H\cdot + \cdot OH.$$

Different UV techniques revolve around using different UV sources and different geometries of tanks and water flow regimes in order to optimise the light penetration (Heering, 2004; Matafonova & Batoev, 2012; Morimoto, Sumitomo, Yoshioka, & Takemura, 2004; Pirnie, Linden, & Malley, 2006). Although the desired wavelength of light is predominantly 254nm, different wavelengths of light can also be used such as in the case of vacuum UV treatment (Gonzalez, Oliveros, Worner, & Braun, 2004; Zoschke, Börnick, & Worch, 2014) where wavelengths in the range of 100-200nm (in which water absorbs strongly) are used to hydrolyse the water.

Although UV is the most prevalent, radiation methods besides UV include the use of microwave radiation (Zhihui, Peng, & Xiaohua, 2005), electron beam irradiation (Petrovic, Gehringer, Eschweiler, & Barceló, 2007) and even the use of gamma radiation (Ismail, Khan, Sayed, & Cooper, 2013) all to achieve the aim, either directly or indirectly, of lysing water molecules. The range of radiation based methods can also be expanded to include photocatalytic processes, where wavelengths of light (including UV) excite either homogenous or heterogenous chemicals (TiO_2 being the predominantly used photocatalyst) making them catalytically active for the production of hydroxyl radicals from water or the breakdown of other chemicals such as hydrogen peroxide (Chong, Jin, Chow, & Saint, 2010; Fujishima, Zhang, & Tryk, 2007; Rizzo, 2009; Tachikawa & Majima, 2007; Thiruvenkatachari, Vigneswaran, & Moon, 2008).

1.4.3 Electric/electrochemical methods

Electrochemical processes provide the energy for the lysis of water molecules from a potential difference across two electrodes. Hydroxyl radicals are formed from the oxidation of water on the anode surface in the following reaction

$$H_2O \rightarrow \cdot OH + H^+ + e^-$$

Variations in electrochemical methods consist of doping the electrodes with different materials to favour different chemical pathways, and with different added chemicals in the water to get different conductivities and interactions (Chaplin, 2014). Other electrochemical processes also include electrofenton processes which generate hydrogen peroxide in situ and subsequently break it down using the fenton process (Cavalcanti, Garcia-Segura, Centellas, & Brillas, 2013; Pipi, Sirés, De Andrade, & Brillas, 2014). The hydroxyl radical can also be formed by the direct discharge of electrical current into water, either with electrodes directly in contact with the water (Da Silva, Franco, Forti, Jardim, & Boodts, 2006) or with a stream of oxygen bubbling through it (Sahni & Locke, 2006).

1.4.4 Ultrasound/cavitation/microbubble collapse

Akin to the previous methods, the ultrasound supplies the energy necessary to lyse the water molecules in the form of pressure waves. The pressure waves actually form microscopic gas pockets in the liquid known as cavities, these cavities are then oscillated by the pressure waves (Ashokkumar, 2011; Beckett & Hua, 2001). The rapid expanding and contracting of these cavities results in their gaseous interiors in the contraction phase heating up to temperatures in excess of

4000K (Rae et al., 2005; Tauber, Mark, Schuchmann, & von Sonntag, 1999). It is therefore in fact thermolysis, and not sonolysis, which is the direct method at work

$$H_2O \xrightarrow{\Delta} H\cdot + \cdot OH.$$

The products of this reaction can undergo further reactions, and so the process will have efficiency losses due to the reactions

$$\cdot OH + H\cdot \rightarrow H_2 + O$$

$$2\cdot OH \rightarrow H_2O + O$$

$$O + \cdot OH \rightarrow O_2 + H\cdot$$

(Adewuyi, 2005). Ultrasound as a technique can be combined with others to good effect, such as in sonocatalysis (Joseph, Li Puma, Bono, & Krishnaiah, 2009), but alone it is dependent very much on fluid properties and tank geometry in a similar way to UV techniques (Mahamuni & Adewuyi, 2010).

The ultrasound provides a pressure change which is responsible for the cavitation effect, but this pressure change can be achieved by other means. One study combined the use of ozone with acoustic and hydrodynamic cavitation techniques for the use of treating water. The ultrasound technique was shown to greatly enhance the effect of the applied dose of ozone. However the hydrodynamic cavitation showed comparatively little effect, having only slight increases in the efficiency (5-10%) of low doses (0.5 mg L^{-1}) of ozone (Jyoti & Pandit, 2004).

Similar to the effects by natural cavitation, the high temperatures and pressures created by enforced microbubble collapse result in the formation of radical chemical species, such as the hydroxyl radical. Adding a copper catalyst can enhance this process (Li, Takahashi, & Chiba, 2009). It has also been found that hydroxyl radicals are formed in greater quantities from the natural collapse of microbubbles if strong acids (nitric, hydrochloric and sulphuric acids) are added to the water. The precise mechanism of this is currently not well understood.

1.4.5 Other bubble effects

As well as the thermolysis of water which occurs inside the oscillating bubble, there are interfacial properties of bubbles which are also of interest as they may present new opportunities when the

surface area of the bubbles relative to the volume of gas they contain increases (i.e. in the case of microbubbles.

For example, there is scope for microbubbles (10-50µm diameter bubbles) and nanobubbles (<200nm diameter bubbles) themselves to be used as water cleaning techniques from the natural chemical effects of their surfaces (Agarwal, Ng, & Liu, 2011). Although currently this is not as effective as using an agent such as ozone in the bubbles, it presents an interesting phenomena that certainly warrants further investigation, as in the absence of any cavitation phenomena, the fact that the bubbles exhibit chemistry must be attributed to their interfacial properties.

1.4.6 Catalysed ozone decomposition

The ozone decomposition rate in the dissolved phase is highly dependent on the pH and temperature of the water (Sotelo, Beltran, Benitez, & Beltran-Heredia, 1987). When the conditions are basic (a high OH^- concentration) the ozone decomposition reaction rates increase significantly (Tomiyasu, Fukutomi, & Gordon, 1985). Adding alkali to water as it is dosed with ozone is a method of hydroxyl radical formation known as base-catalysed ozone decomposition. The rate of ozone decomposition can also be affected by the presence of metal ions in the water, the presence of iron and manganese in particular (as well as others) has been shown to increase the rate of ozone decomposition (Ni, Chen, & Yang, 2003). Ozone decomposition can also be catalysed by activated carbon (Alvarez et al., 2006). All these techniques serve to facilitate OH radical formation as a result of the decomposition of ozone.

Also, as well as transferring the ozone into the water more effectively, ozone distribution by microbubbles has been shown to increase the rate of oxidation by increasing the rate of ozone breakdown resulting in the formation of hydroxyl radicals. In a microbubble system used in a study of dye decomposition by Chu et al. (2007), which used a recycling pump, gyratory accelerator and an injector with 45 µm diameter pores, the concentration of dissolved ozone rose rapidly and then reached saturation more rapidly compared to a conventional bubble diffuser. The rate of dye decomposition in the microbubble system was 3.2-3.6 times higher than the non-microbubble system, which was not entirely accounted for by the increase in mass transfer, as the mass transfer coefficient is only 1.8 times higher in the microbubble system. It was found from an experiment using terephthalic acid (Chu et al., 2007) that an increase in the formation of hydroxyl radicals could be associated with the use of microbubbles (Figure 7). This would suggest that, as well as increasing the mass transfer rates, the use of microbubbles has an additional effect on the rate at which ozonation can be used as an AOP.

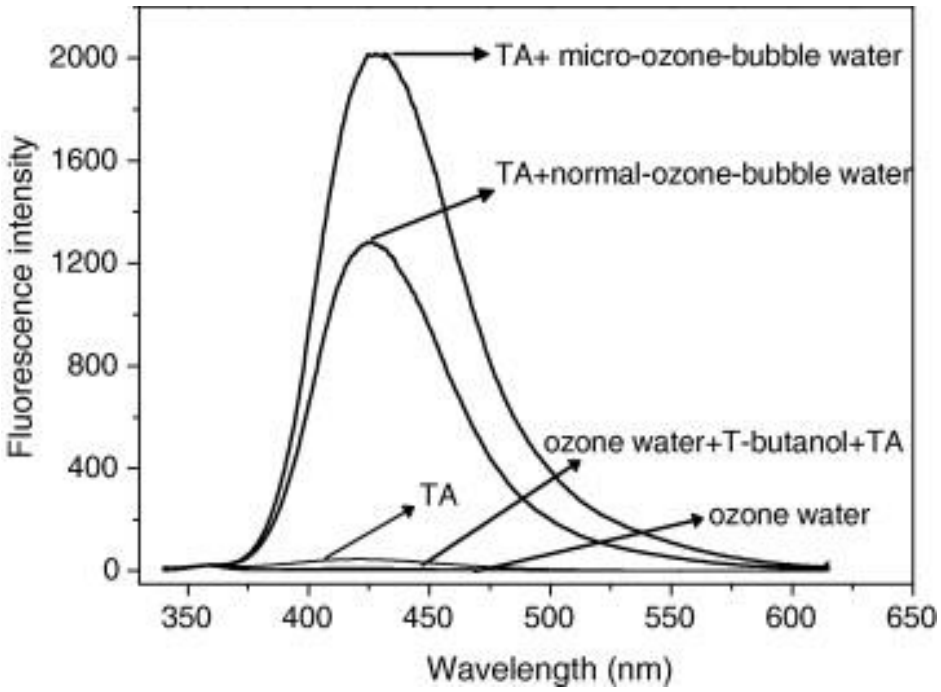

Figure 7: Fluorescence spectra of samples of terephthalic acid treated with ozone and ozone microbubbles. The fluorescence is due to the formation of hydroxyterephthalic acid via the hydroxyl radical reacting wth terephthalic acid, the higher the fluorescence intensity, the more hydroxyl radicals were generated. It can be seen that the microbubbled ozone generated more hydroxyl radicals. Taken from Chu et al. (2007).

The use of microbubbles was also found to increase the mineralisation efficiency, measured as the Total Organic Carbon (TOC) removal efficiency. 80% of the TOC was removed after 80 min, compared to 34% after 130 min using the normal bubble contractor (Chu et al., 2007). Chu et al (2007) attributed this effect to the higher pressures in microbubbles, but it could also (at least in part) be due to the interfacial effects mentioned above.

1.4.7 Comparison of AOP's

Advanced oxidation processes are difficult to compare. They can be compared for a given application, such as chlorophenols in the case of Pera-Titus et al. (2004), but then for a different application they must all be compared again for the new specific application.

Comparison could be by measuring ·OH radical production (Rosenfeldt et al., 2006), but this assumes that ·OH radicals are the most appropriate for every case and given the non-selective way that OH radicals react they can be consumed in some processes by scavengers before they can react with the target chemicals (Wols & Hofman-Caris, 2012). Another important point is that there are also other radicals that can contribute significantly in advanced oxidation processes besides the hydroxyl radical (Fernández-Castro, Vallejo, San Román, & Ortiz, 2015).

Again, the methods could be compared using their oxidation potential, but again, the mere ability to oxidise doesn't give any indication of what the results of such oxidation will be.

Some extensive reviews of AOP's exist but due to the difficulty of direct comparison most of these are predominantly qualitative, a brief list of pros and cons for each process is presented in Table 2 (Andreozzi et al., 1999; Antonopoulou, Evgenidou, Lambropoulou, & Konstantinou, 2014; Comninellis et al., 2008; Klavarioti, Mantzavinos, & Kassinos, 2009; Oller, Malato, & Sánchez-Pérez, 2011; Ribeiro et al., 2015; Suty, Traversay, & Cost, 2004).

Given that this is the case, the most logical way to compare the different AOP's is to compare the effectiveness of different AOP's for one application, with those of the effectiveness with similar studies for other applications, in order to get a "feel" for which AOP's work best for which applications (see Table 3).

Table 2: A comparisson of pros and cons of the main AOP processes.

	Pros	Cons
Fenton/chemical	• Simple, requires only the addition of certain chemicals and some monitoring of water parameters • Cheap • Robust, does not require the installation of large amounts of expensive and delicate electrical equipment • Reliable, has been used successfully for many decades	• Requires handling of chemicals • Iron must be recovered or continually supplied • Requires pH control
UV	• Does not require any addition to the water • Non-intrusive • Can be very beneficial when combined with other methods, e.g. via photocatalysis •	• High starting costs • Requires specific water conditions/flow regimes
Electric/electrochemical	• Requires very little addition of other chemicals • Can be combined with catalysts on the surface of the electrodes. • As well as forming the OH radicals, the	• Corrosion of electrodes over time • Applications are limited to where current can be safely introduced into the water

	electrode currents can have effects on other water constituents	
Ultrasound	• Requires very little chemical addition or alteration to the water • A very simple technique, the sound horns simply need to be submerged and activated • Can be used alongside other processes, e.g. to supress algal growth and biofilm formation which can interfere with other equipment	• Not particularly efficient when used in isolation • Ultrasound can interfere with other processes if not shielded
O3 decomposition	• The addition of O3 to other processes can improve their efficiency • O3 is a tried and tested technology • O3 can be generated from the air, thus reducing the need for chemical additives	• Processes will necessarily become more complex depending on which method is used for ozone decomposition • Whichever technique is used to accelerate ozone decomposition, the ozone decomposition will have the necessary drawbacks of that technique, such as the use of alkaline chemicals in base catalysed ozone decomposition • Still limited by the efficiency of ozone generation

Table 3: Measured values of the effectiveness of various AOP's on different applications.

Reference	Parameter	H2O2	Fenton process	O3	O3/Fe2+	O3/UV/Fe2+	O3/H2O2	O3/UV	H2O2/UV	O3/H2O2/UV	UV	Photocatalysis	UV/H2O2/Fe3+	UV/H2O2/Fe2+	O3/UV/Fe2+/H2O2
(Azbar et al 2004)	COD removal (%)		96	92				94	90	99					
(Azbar et al 2004)	Colour removal (%)		94	90				93	85	96					
(Azbar et al 2004)	Cost ($m-3)		0.23	5.28				6.38	1.26	6.54	1.1				
(Esplugas et al 2002)	Half life of phenol degradation, t 1/2 (h)		0.0312	0.157			0.325	0.221	0.111	0.166	1.31	1.19			
(Esplugas et al 2002)	Cost evaluation (costs/kg) ($)		3.92	0.81			2.71	9.28	13.1	7.12	172.2				
(Badawy et al 2006)	TOC conversion after 30 minutes of reaction time (φ30)		23.2				48.5				13.7		81.1	94	
(Badawy et al 2006)	Estimated specific energy required (kWh/kg TOC removed)								1700				500	250	
(Lamsal 2011)	UV254 after treatment (cm-1)			0.053				0.081			0.012				
(Lamsal 2011)	TOC after treatment (mg/L)			0.18				0.98			0.11				

(Lamsal 2011)	DOC after treatment (mg/L)			0.06				0.85			0.12				
(Lamsal 2011)	SUVA after treatment (m-1/(mg/L))			1.73				2.61			0.23				
(Catalkaya & Kargi 2007)	Colour removal (%)	24	84.6	91			81.2		41		6.6			82.5	
(Catalkaya & Kargi 2007)	TOC removal (%)	5.1	88	29			30.9		11.1		4.1			82.8	
(Catalkaya & Kargi 2007)	AOX removal (%)	34	89	62.4			95		18.5		17			94	
(Asaithambi et al 2014)	Colour removal (%)		55.97	39.62	53.95	57.71		50.92	73.72	81.72				100	100
(Asaithambi et al 2014)	COD removal (%)		53.85	29.17	48	59		41.67	66.67	92				99.99	100
(Asaithambi et al 2014)	Electrical energy determination (kWh/m3 order1)			0.64	0.64	0.76		1.19	0.27	1.04				0.097	0.01

1.5 Reactive Oxygen and Nitrogen Species (RONS)

Aside from the hydroxyl radical and ozone, there are many other non-chlorinated species which can contribute to disinfection and breakdown of organic compounds in water. Those consisting of oxygen, nitrogen and hydrogen are collectively termed Reactive Oxygen and Nitrogen Species (RONS, see Table 4) and are of particular interest in biochemistry as many are agents in cellular radical processes (Graves, 2012).

Table 4: List of various reactive oxygen and nitrogen species (Graves, 2012).

Reactive oxygen and nitrogen species (RONS)			
Radical	***Non-radical***	***Radical***	***Non-radical***
Superoxide, O_2^-	Hydrogen peroxide, H_2O_2	Nitric oxide, NO	Nitrous acid, HNO_2
Hydroxyl, OH	Ozone, O_3	Nitrogen dioxide, NO_2	Nitrosyl cation, NO^+
Hydroperoxyl, HO_2	Peroxynitrite, $ONOO^-$	Nitrate radical, NO_3	Nitroxyl anion, NO^-
Singlet oxygen, ($^1O_2$)	Peroxynitrate, $O2NOO^-$		Dinitrogen trioxide, N_2O_3
	Peroxynitrous acid, ONOOH		Dinitrogen tetroxide, N_2O_4
			Dinitrogen pentoxide, N_2O_5

Like ozone and OH, other RONS are unstable species and need to be generated close to their point of use (some are more stable than others, e.g. hydrogen peroxide). Many of these chemical species are continuously created as by-products in the bulk of the plasma during ozone generation (as can be seen from section 1.3.2). The plasma conditions are such that these species are also continuously destroyed and so they cannot be considered as products unless the volume of the plasma reactor is small enough, or the geometry is such, that the species can exit before they are destroyed further along in the body of the plasma reactor. Plasma reactors with small volumes thus have the potential to take advantage of these species.

1.5.1 Plasma Microreactors/Microplasmas

Microplasmas are simply plasmas occupying small volumes, and can be formed by any method which can result in the ionisation of the gas to form plasma. Microdischarges on the other hand are specifically microplasmas which are formed via electric discharge methods. The terms "Microplasmas" and "microdischarges" are not always used with clear definition. DBD discharges, for example, are not always referred to as microdischarges, but although the applied systems are large, the gaps between DBD electrodes are often smaller than 1mm (Fridman 2008). Microdischarges should therefore be considered independent entities (as opposed to extensions of

their general discharge type) if the process of scaling down brings about some new properties. The scaling down of plasma discharges to sub-millimetre sizes is known to have the following effects:

- Scaling down of plasma discharges increases the pressure at which plasma can be formed with the same voltage.
- Due to the small size of the microdischarges, they experience intensive heat losses which allow their power density to be increased.
- The plasma composition can be different for microdischarges as the relative speed between diffusion losses and volumetric recombination changes in favour of the volumetric recombination (especially in three body processes) at high pressures. A significant amount of molecular ions are found in noble gas microdischarges at high pressures for example (Kushner 2004).

Plasma microreactors, by contrast, are simply microreactors which contain plasmas, and since clearly the plasmas contained in the microreactors must be correspondingly small, the terms microplasma and microdischarge can be used to refer to the plasma present within such reactors.

1.6 Investigation into the combination of plasma microreactor and microbubble technologies – the scope of this work

1.6.1 Discussion

From the contents of this chapter it can be seen that there are many viable alternatives to traditionally used chemical methods involving chlorine, many of which do not require the input of any chemicals at all. Ozone, as well as having disinfection capabilities has the added benefit of being able to break down organic chemical contaminants in water.

From the above it is clear that there are also many other techniques collectively known as advanced oxidation processes, most of them using some form of electrical device.

Cavitation methods such as ultrasound are dependent on the energy consumption of the ultrasound horns, and are limited by the occurrence of natural cavities in the water. Treatment of water by UV light is already an established AOP but is limited by the turbidity of the water and the efficiency of the UV lamps. Electrolytic methods are also limited by the composition of the water. The chemical methods such as the Fenton reagents require the synthesis and transport of the chemical reagents, so whilst there application may require little energy, the overall process including the synthesis of the chemicals may be no more energy efficient than the electrical processes. Each of the advanced

oxidation processes has its advantages and disadvantages depending on the water type as well as other factors, but they nearly all revolve around the formation of the hydroxyl radical. Ozone can also be used indirectly to generate hydroxyl as a water treatment technique.

Ozone and OH radicals both come under the category of RONS, and other RONS apart from these are formed in the plasma discharges required for ozone formation. All these processes can be conveniently summarised in Figure 8.

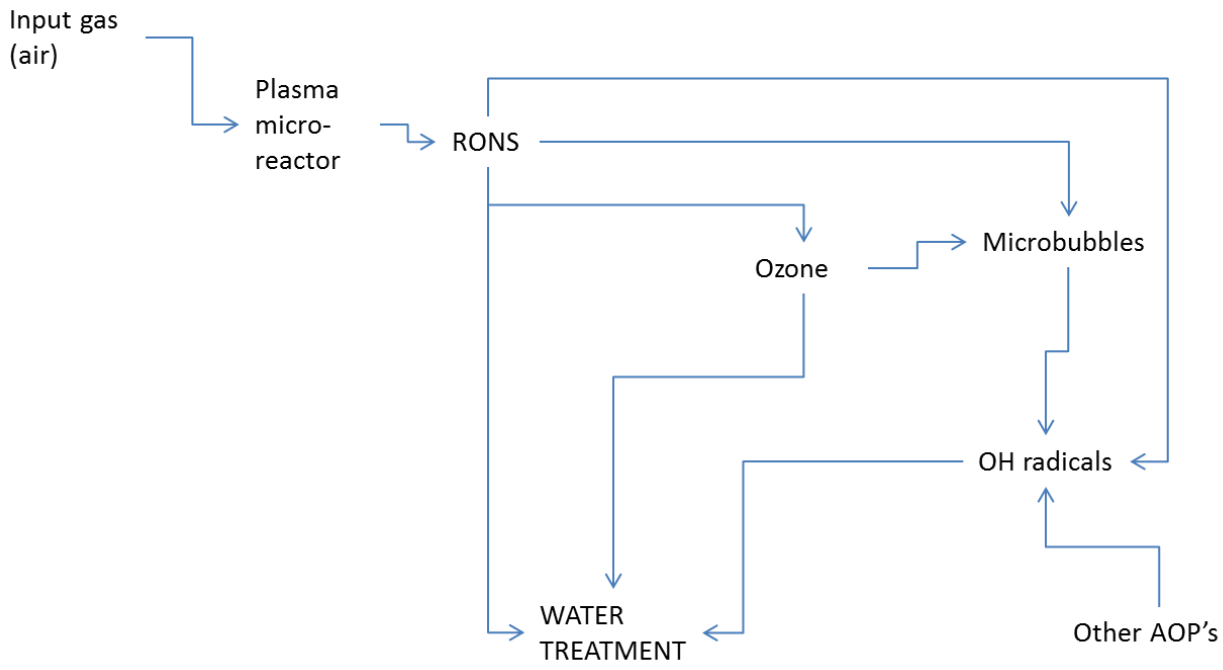

Figure 8: Delineation of the general processes involved in water treatment using "non-chemical" reactive oxidants. The diagram is there to illustrate the chemical similarities between the processes.

The use of plasmas to generate RONS has the potential to be more efficient than ozone generation, as efficiency losses in the formation of ozone in the plasma and the transport and utilisation of ozone in the dissolved phase can theoretically be bypassed. Due to their small volumes, microplasmas are ideally placed for high efficiency generation of RONS. Once generated however, the instability of some of these species is a problem as some are so reactive (such as the OH radical and O atom, Table 1) that they will even be destroyed during transit from the reactor to the source. The use of microplasmas for this application therefore requires the plasmas be very close to the point of use.

A method of combining microplasma generation and microbubble generation has the potential to be used for the generation and utilisation of RONS as a non-chemical method of water treatment, and

may have other potential uses in green chemistry as the chemicals generated in such a method all have the following properties:

- They can be made in situ, thus do not consume energy in the transport of chemicals
- The proximity to their point of use means they can be made in quantities that match the requirements of the point of use, thus can theoretically keep waste and harmful excesses to a minimum
- Use of non-chemical methods leave much less harmful residual non-biodegradable by-products than do chemical methods

1.6.2 University of Sheffield technologies

The University of Sheffield has a means of generating microbubbles from a diffuser using the fluidic oscillator described in Zimmerman et al (2011). Its principle of operation is as follows: In an ideal situation, the formation of bubbles from a diffuser would be uniform across the surface of the whole diffuser. However in reality this is not the case. The tendency is for one bubble to reach the 'hemispherical limit shape' before the rest. Once the bubble has passed this point, the pressure required for the air to exit the aperture is less in this single aperture than in the other apertures, and the air will preferentially take this route. This will in turn lead to large bubble formation through this aperture, and also will prevent bubble formation in the other apertures (W. B. Zimmerman, Hewakandamby, Tesař, Bandulasena, & Omotowa, 2009). A diagram of the apparatus for the process is shown in Figure 9.

The use of a fluidic oscillator in this process has the effect of terminating the growth of the bubbles halfway through the oscillation period. Once the growth of the bubbles has been terminated, they detach from the aperture, and new bubble formation takes place at the start of the next oscillation period (W. B. Zimmerman et al., 2009). The Zimmerman microbubble generation technique is such that it allows plasma microreactors to be situated within the diffuser, which allows the transit time between the plasma and the point of use to be reduced significantly if the microbubbles are generated in the water that is required to be treated. This has already been applied for hydrogen and ozone generation (W. B. J. Zimmerman & Lozano-Parada, 2010).

A single channel plasma microreactor, as a novel means of plasma generation for ozone production, has also been developed at the University of Sheffield (Lozano-Parada, 2007). A special feature of the device is the importance it places on the reaction kinetics in controlling the chemistry inside the

plasma (Lozano-Parada & Zimmerman, 2010) and a kinetic model consisting of over 100 reactions was compiled in Lozano-Parada (2007). As the kinetics of the individual steps of ozone reactions have been studied at length in investigations of stratospheric ozone depletion mechanisms by the scientific community, the conversion of oxygen into ozone using the plasmas was the best logical starting point since so much kinetic data was already available.

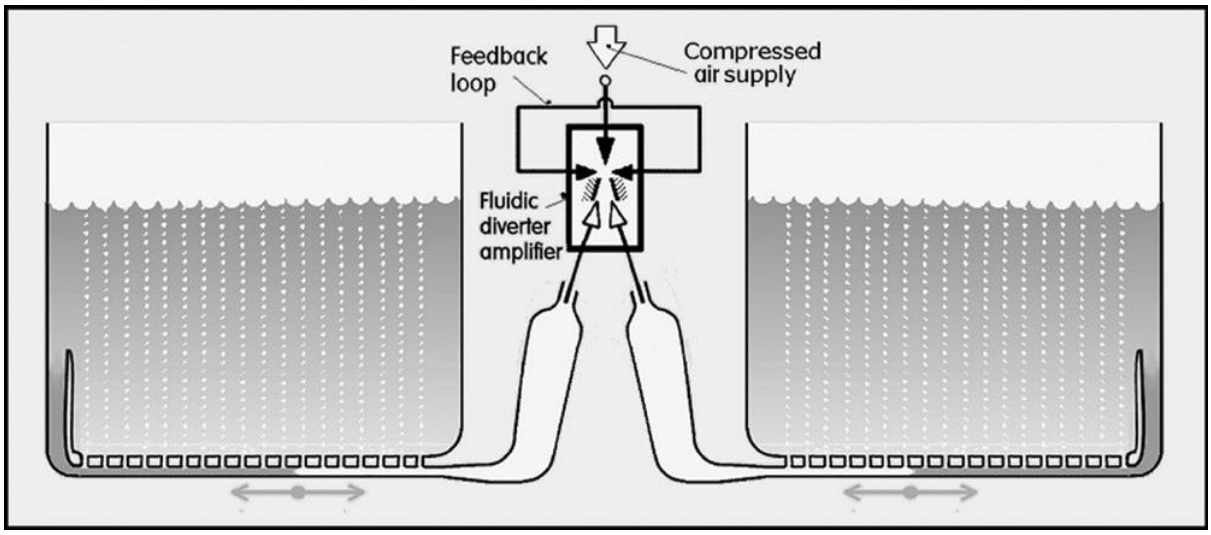

Figure 9: A diagram of the fluidic oscillator microbubble formation method (W. B. Zimmerman et al., 2009).

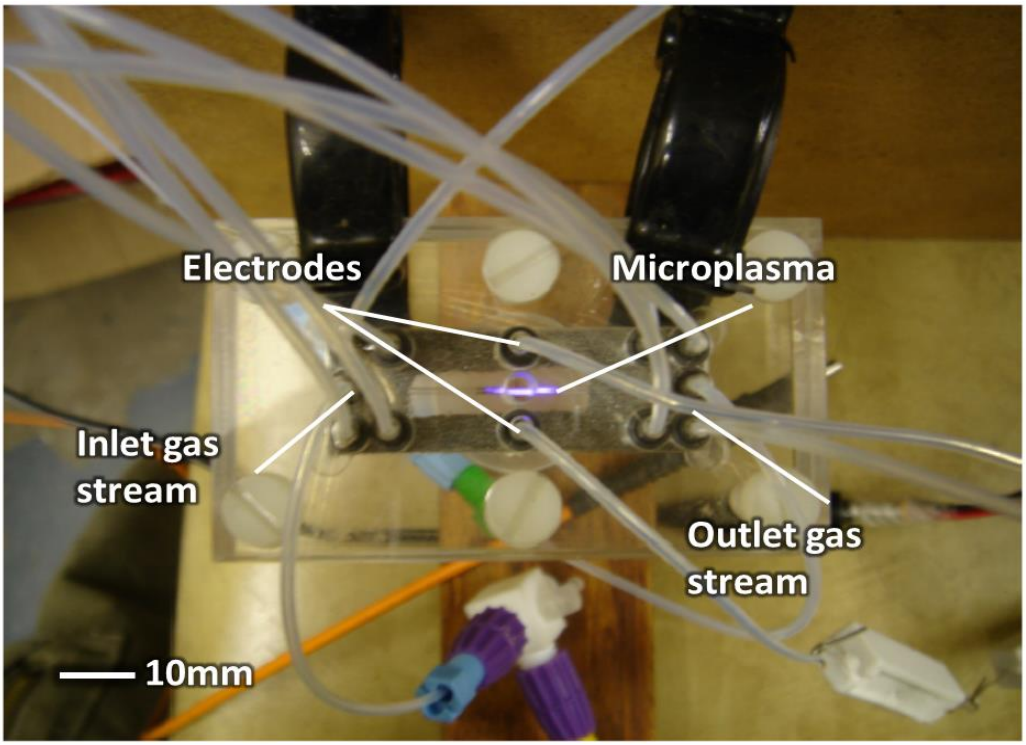

Figure 10: Image of the operational single channel plasma microreactor and its glow discharge (Lozano-Parada & Zimmerman, 2010).

These two technologies have the potential to fulfil both the short residence time requirements for the use of RONS in the case of the microplasmas, and the requirements for short distance from the plasma to the interface in the case of microbubble formation from a pore. As there is potential for the RONS formed in the plasma to be utilised as oxidizing agents, and there are two technologies available at the University of Sheffield which could take advantage of this, it is worth investigating the potential for integrating those two technologies into the design of a reactor that can take advantage of the short lived RON species inherent in air plasma through the combination of microplasma reactors and microbubble formation. Doing so will require investigating the chemistry that might arise from a combination of air plasma and air/water interfaces in microbubbles, and to investigate the practical engineering aspects of fabrication of a reactor for utilising this chemistry.

1.6.3 Outline and objectives of subsequent chapters

The subsequent chapters begin by detailing the results and methods of an industrial pilot scale trial of a technology approaching a direct combination of microbubbles and microplasmas as a starting point, sufficing almost as a feasibility study.

Then follows a chapter on the chemical kinetics of a combination of plasma and bubbles which is investigated for the purpose of making a kinetic model to predict likely chemical products of combinations of plasma and bubbles.

The work then attempts to assess and define the necessary design criteria for the fabrication of a microplasma/microbubble reactor, drawing on the relevant design data.

Finally, the work describes the building and testing of a single microbubble/microplasma reactor in order to practically assess the feasibility of such a device.

The thesis in its entirety will be an investigation into the potential of an integrated approach to combining microplasmas and microbubbles as an advanced oxidation technique.

It is hoped that the knowledge gained from this work will also be applicable to other chemistry as understanding these processes for air and water will also lead to knowledge which can be transferred to processes using different gases and liquids, as long as they all conform to the same basic scheme (Figure 11).

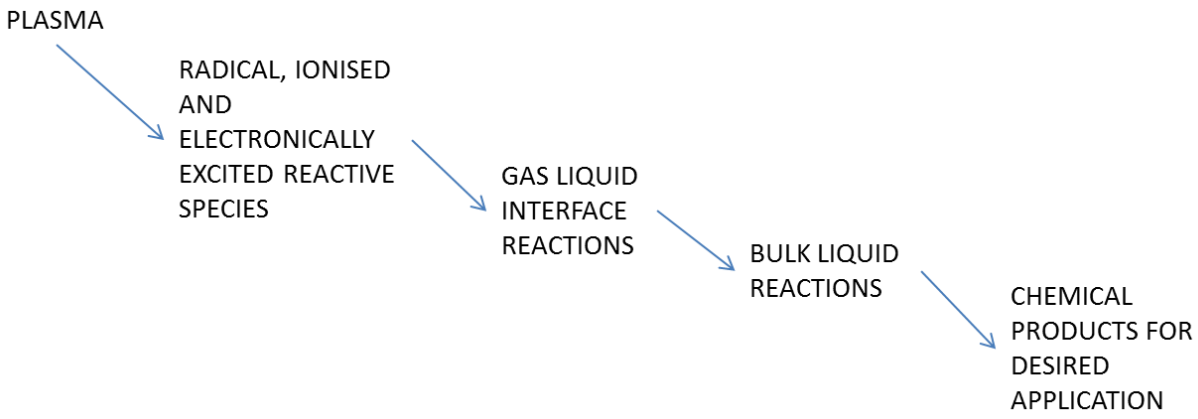

Figure 11: Basic scheme of plasma bubble processes.

2 A pilot scale trial of a plasma micro-reactor device with microbubble diffuser

2.1 Summary

The aim of this chapter is to analyse the performance of a device combining the plasma micro-reactor and microbubble processes recently developed by Zimmerman and Lozano-Parada. A pilot plant was designed and constructed to collect data on the performance of the device outside of laboratory conditions, in industrial wastewater. Batch trials of the operation of the device in wastewater were then conducted, taking samples of the water to analyse the effect on the Biochemical Oxygen Demand (BOD), Chemical Oxygen Demand (COD), Total Organic Carbon (TOC), Dissolved Organic Carbon (DOC), total suspended solids, transmission of UV light at 254nm (a wavelength strongly absorbed by compounds which ozone selectively reacts with), a range of organic and inorganic species, and Enterococci, Escherichia coli (E.coli) and total coliforms. Operational parameters of the device such as pressure, flow rate, and power consumption were also measured during the trials, and the ozone output of the device was measured in laboratory conditions.

The observations made at the industrial field trials can be used to inform work on development of this technology into something which further integrates the microplasma and microbubbles. A discussion of the field trials at the end of the chapter outlines the necessary work required to bring this about.

2.2 Chapter introduction - The "ozone dosing lance"

The generation of ozone using a microplasma method has previously been demonstrated on a single channel microreactor (Lozano-Parada & Zimmerman, 2010; Lozano-Parada, 2007). This single channel device was also subsequently scaled up to consist of 26 individual plasma microreactors, each of which is over 20 times wider than the original single channel device, theoretically allowing greater throughput whilst maintaining the characteristics of the original single channel. This reactor was designed to be tested in a custom built industrial wastewater treatment pilot plant.

The reactor designed for the industrial pilot trial was designed to mimic the action of a conventional injection lance and be inserted via a corporation cock into a mains water pipe wherever an injection of chemical agents is required (Figure 12). It would then generate ozone using the plasma micro-reactors and simultaneously dose it through a diffuser into the water. The device was referred to as the "ozone dosing lance".

The basic principle of the device was to generate the ozone as close to the water as possible, to minimise losses of ozone during transit by collisions with any pipe walls. As the corporation cock flanges had only a limited fixed diameter, the plasma micro-reactors had to be packed rather tightly together to maximise the number of them that could be inserted into the water. The dosing lance consisted of a one dimensional array of electrode pairs packed tightly together. Each electrode pair had a gap distance of 0.8mm, each electrode was also covered by a thin sheet of glass which was bonded to it using a kind of silicone sealant (RS silicone rubber compound flowable fluid 692-542). This inadvertently reduced the gap size further to around 0.4mm. These individual reactors were housed in a 30 cm long, 3 cm wide "ladder" built from Perspex, with slots into which individual reactors were inserted. Perspex was used for its transparency, to allow observation of the processes inside the reactor. This "ladder" was in turn housed in a semi cylinder made from quartz glass, to allow UV light from the plasma to reach the water and contribute to the treatment process. Another semi-cylinder made of porous ceramic media was fitted to the Perspex module for bubble formation, much like a ceramic tube diffuser.

Air was fed into the dosing lance from a pipe through an inlet at one end, it was then channelled underneath the electrodes and then through the inter-electrode gaps (Figure 13). Power was supplied to these electrodes through high voltage cables alongside the air-inlet pipe. When the correct power signal was supplied, the air between the electrodes became plasma, and ozone formation reactions took place within it. After leaving the inter-electrode gap space, the ozonated air was then channelled through a ceramic diffuser directly above the electrode array, where it then entered the water in the form of bubbles (Figure 14 & Figure 15).

Figure 12: A photograph of the ozone dosing lance fitted into the corporation cock ready for insertion into the column.

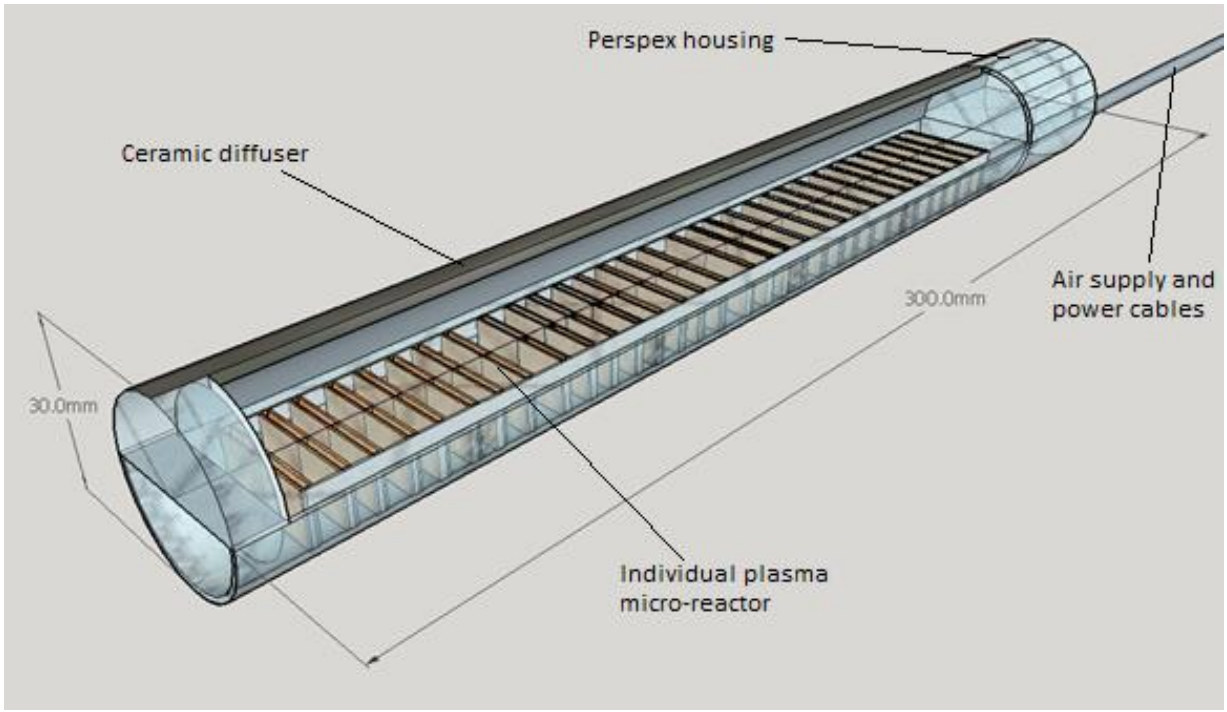

Figure 13: A CAD drawing of the ozone dosing lance. A cross section is cut into the diffuser to show the arrangement of the individual plasma microreactors inside.

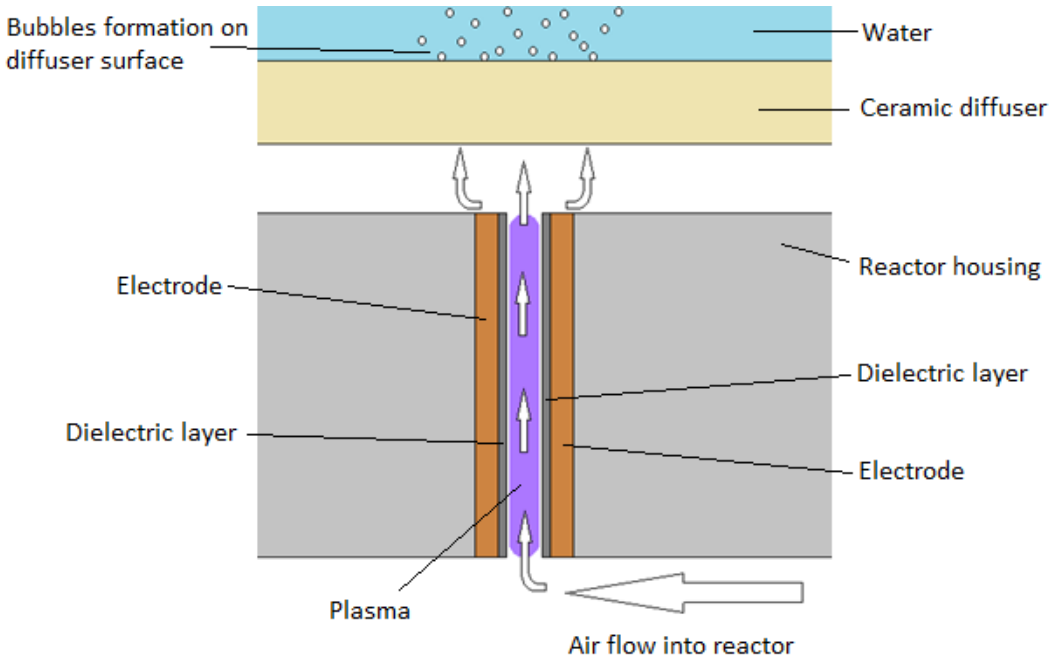

Figure 14: A diagram to show the configuration of the ozone dosing lance plasma microreactor microbubble technology.

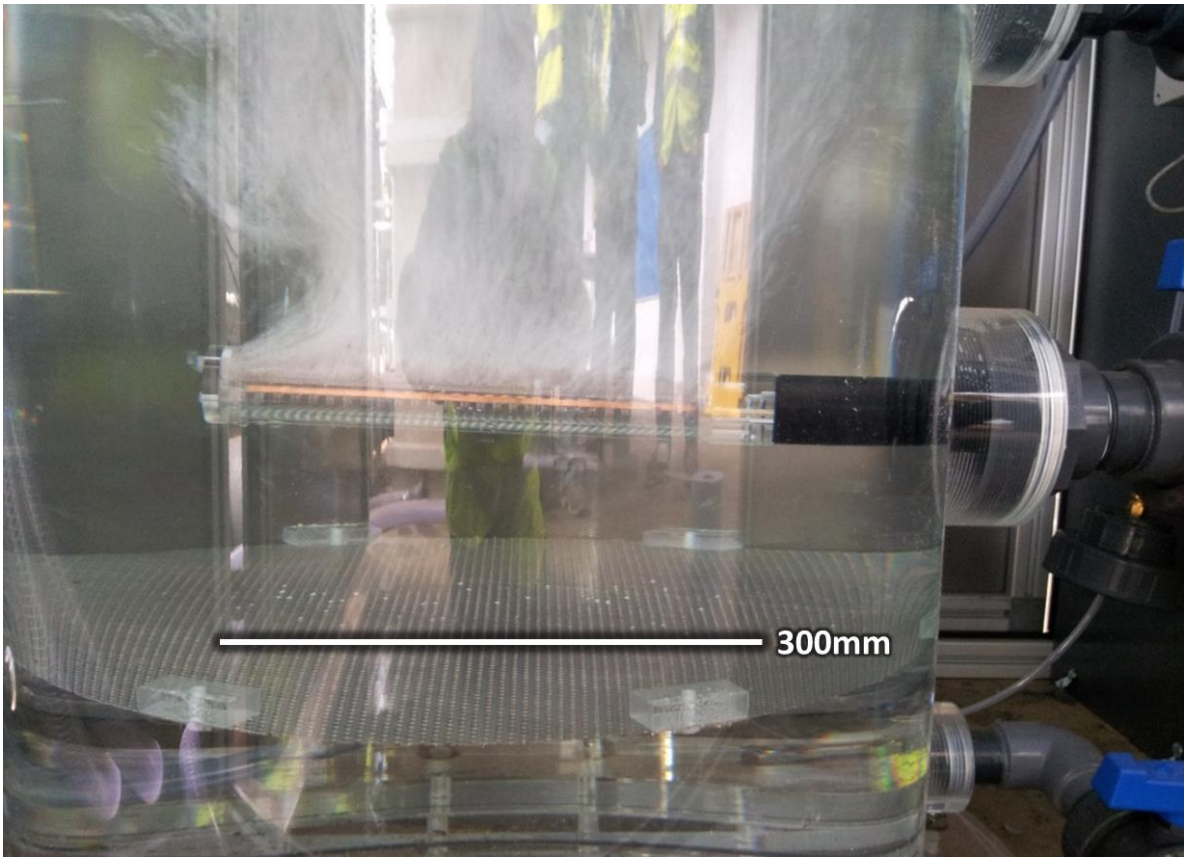

Figure 15: A photograph of the dosing lance in operation, inserted through the bottom flange of the column.

The ozone dosing lance was designed at the University of Sheffield prior to the author's involvement. The task of the author was the pilot scale testing of this dosing lance device, and the author played a central role in the design and construction of the pilot plant, in association with the University of Sheffield and AECOM. A brief explanation of the pilot plant follows.

2.3 Field trials of the ozone dosing lance

The experiments were carried out at the United Utilities facility: Blackburn Wastewater Treatment Works. The site was located between Blackburn and Preston and was selected by United Utilities due to the relatively high quantity of priority substances found in its final effluent compared to other United Utilities sites.

2.3.1 The pilot plant

The pilot plant consisted of an acrylic column designed for the continuous flow of final effluent from the wastewater treatment works to flow through it (Figure 16). The effluent flow could also be stopped to enable batch processes to be tested. The effluent entered the column from the small 1 inch bsp inlet pipe in the bottom of the column and exited from an outlet pipe with identical diameter at the top.

Along the height of the column there were 6 flanges identically sized, to which were attached 6 corporation cocks (Figure 16) through which devices could be inserted into the column as required. A liquid sampling point was fixed on to one of the corporation cocks to allow samples to be taken from inside the column during operation. The ozone dosing lance could be removed and re-inserted into any one of the flanges whilst the column was still full of water using the corporation cocks. For the duration of the trial the lance was inserted into the lowermost corporation cock.

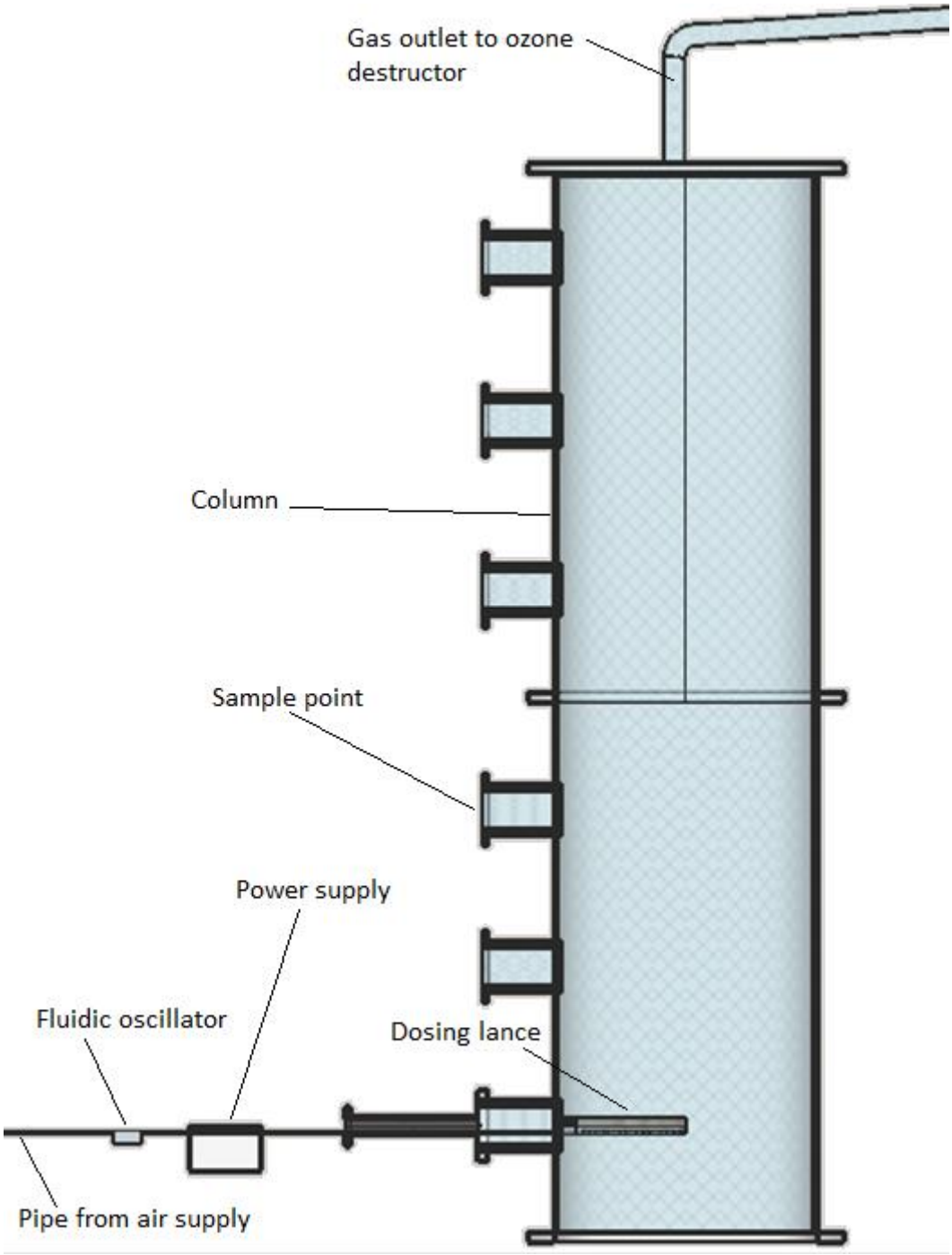

Figure 16: A diagram of the experimental pilot plant for testing of the dosing lance.

As the dosing lance required a constant flow of air through it, a 1 inch bsp outlet pipe was fitted on the top of the column to allow air or other gasses to escape, preventing pressure build up. An ATI in-line ozone gas monitor (0-100ppm range) was fitted along this pipe to monitor any excess ozone not absorbed by the water. This pipe was then fed through a simple diffuser into a quench tank

consisting of activated carbon submerged in potassium iodide solution to destroy any excess ozone before the ozonated air was allowed to re-enter the atmosphere.

Any oil could react with the ozone as well as interfere with the chemical tests that United Utilities intended to make, thus ensuring there was no oil in the air supply was a priority. An oil-free, water-free, and particulate-free compressor was selected to supply a continuous air feed to the dosing lance. The compressor power drawn was monitored by taking readings from the distribution board.

The influent final effluent into the tank had an ABB flow meter positioned along it. This could measure to an accuracy of ±0.01 L s^{-1}.

The power consumption of the compressor and the dosing lance power supply was measured by a monitored distribution board, SQUARE D Quickline II Universal (read "Monitored Distribution Board, FED FROM BBB-TT-LV 103-5L3). Measuring the voltage and current entering the lance directly was not possible during the field trials, as due to the nature of the high voltage probes too much conductive material would have had to be exposed, which was not desirable due to safety concerns onsite.

2.4 Practical constrains in the field

2.4.1 The final effluent quality

The final effluent supplied to the column was much more dirty than anticipated. The lance was not even visible inside the column when it was submerged due to the colouration of the water (Figure 17).

It was intended that the ozone concentration in the liquid could be quantified using the indigo method (Bader & Hoigné, 1981), and the concentration of hydroxyl radicals could be determined using the terephthalic acid method (Mason, Lorimer, Bates, & Zhao, 1994). As the indigo and terephthalic acid methods required the water to be very clear, it was considered that these tests would be too inaccurate for the water in question. It was also not possible to use submerged ozone probes as these also required the water to be at least of drinking water quality (Toledo, n.d.). The effects of the ozone on the wastewater were measured on site using the transmittance at 254 nm, which is a wavelength common to many compounds with which ozone selectively reacts (Beltran, Garcia-Araya, & Alvarez, 1999; Beltrán, 2003; Croue, Beltran, Legube, & Dore, 1989).

Figure 17: A photograph of the column half filled with the final effluent. The photograph clearly shows the high turbidity of the effluent.

2.4.2 Observations of lance performance

Several problems were encountered with the dosing lance in the final effluent, mainly due to the materials from which the lance was made. In early attempts at trial runs, arcing occurred frequently inside the dosing lance, and every time this happened the lance could no longer generate plasma, and had to be returned to the university to be repaired and cleaned up. This took a lot of time and delayed the trials somewhat.

Due to the mechanical stresses on the lance, cracks would appear in the acrylic material of the lance, especially near the end where the lance was attached to the corporation cock, and would gradually propagate over time if they were not repaired. In some cases these cracks resulted in slight leaks of ozone which caused the experiments to be halted. These leaks also had to be repaired, which again delayed the trials.

The plasma discharges were also visually observed to grow duller over time from the point at which the electrodes were newly installed into the lance. The ozone output consequently decreased gradually over time, meaning that a direct comparison between the lance operating on two different days was difficult. This was also made even more difficult by the fact that the effluent would be different each day.

Electromagnetic interference was also caused by the dosing lance and affected some extremely sensitive equipment, such as the in-line ozone monitor if it was placed too close to the lance, and any other sensitive electrode techniques. This had implications for the characterisation of the dosing lance back at the university, as the tanks used to characterise the lance were much smaller, and required the in-line monitors to be much closer to the lance.

2.5 Results of field trials

Due to persistent practical difficulties onsite, and contractual constraints, only a limited number of complete experimental runs could eventually be performed and repeats were not possible. Thus the reader should be aware of this when viewing the following sets of results.

2.5.1 UVt

UVt is the the Ultraviolet Radiation transmittance, or in other words the extent to which the water allows light at the 254 nm wavelength to pass through it. The aromatic components, such as the benzene rings, of many organic compounds (including pollutants, see Appendix) in water absorb at this wavelength, which makes it a good indication of the extent to which the aromatic rings in compounds have been broken. The transmittance of water at 254 nm was measured by analysing samples of the water on site with a Jenway 6305 UV-Visible Spectrophotometer. The dosing lance clearly has an effect on the wastewater, as the UVt of the water samples increased during dosing with the lance. The use of microbubbles clearly improved the performance of the dosing lance in treating the final effluent, as shown by the steeper slope of the UVt increase (see Figure 18).

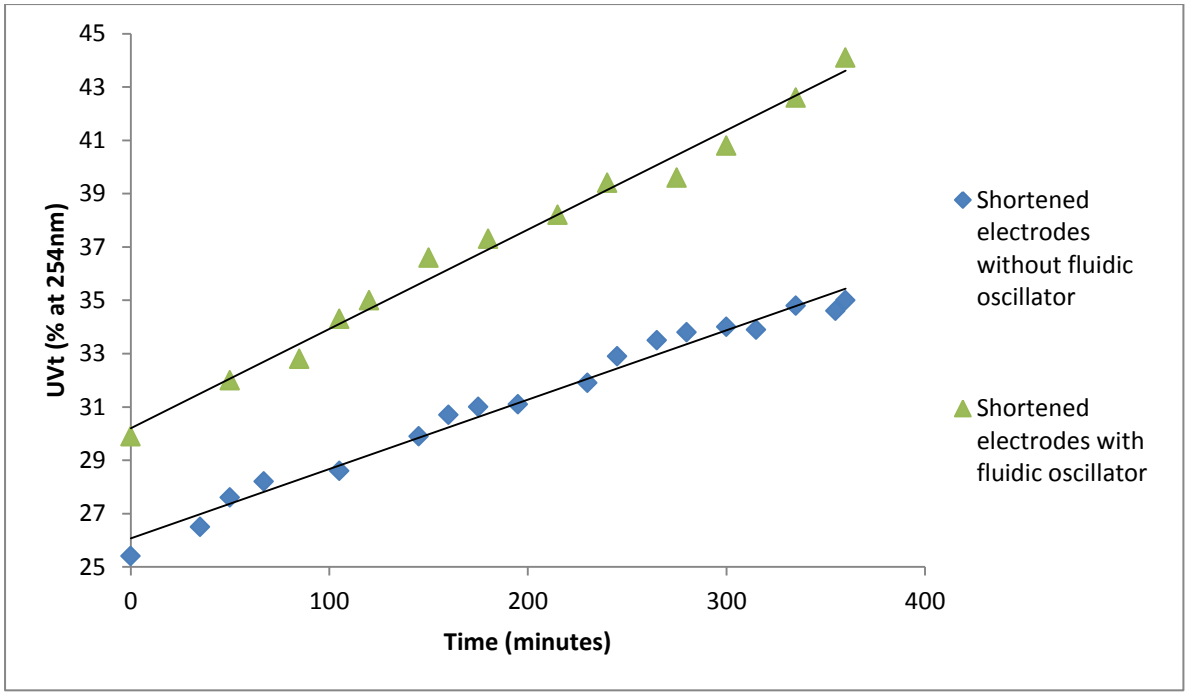

Figure 18: A plot of the change in UV transmittance at 254 nm over time for the batch processes with and without the fluidic oscillator. The "shortened electrodes" in the legend refers to the refined electrode configuration required to prevent arcing.

The variation in the rate of increase in UVt (Figure 18) is most likely due to the removal of water for sampling purposes and the consequent reduction in volume of the water body, causing a slight increase in the quantity of ozone per unit volume of water to be oxidised. The sampling time coincides with the change in rate of UVt increase.

2.5.2 DOC, TOC, BOD & COD

Marked increases in the removal of Dissolved Organic Carbon (DOC) as well as the Total Organic Carbon (TOC), Biochemical Oxygen Demand (BOD) and Chemical Oxygen Demand (COD) were observed with the fluidic oscillator when compared with the trials run without (Figure 19-Figure 22). The BOD was determined using the 5 Day BOD test (Standard Method 5210 B), COD was measured by the dichromate test (Standard ASTM D1252), TOC by the High Temperature Oxidation method (Standard ASTM D4129) and the DOC measured by the same method, but with samples filtered of particulates.

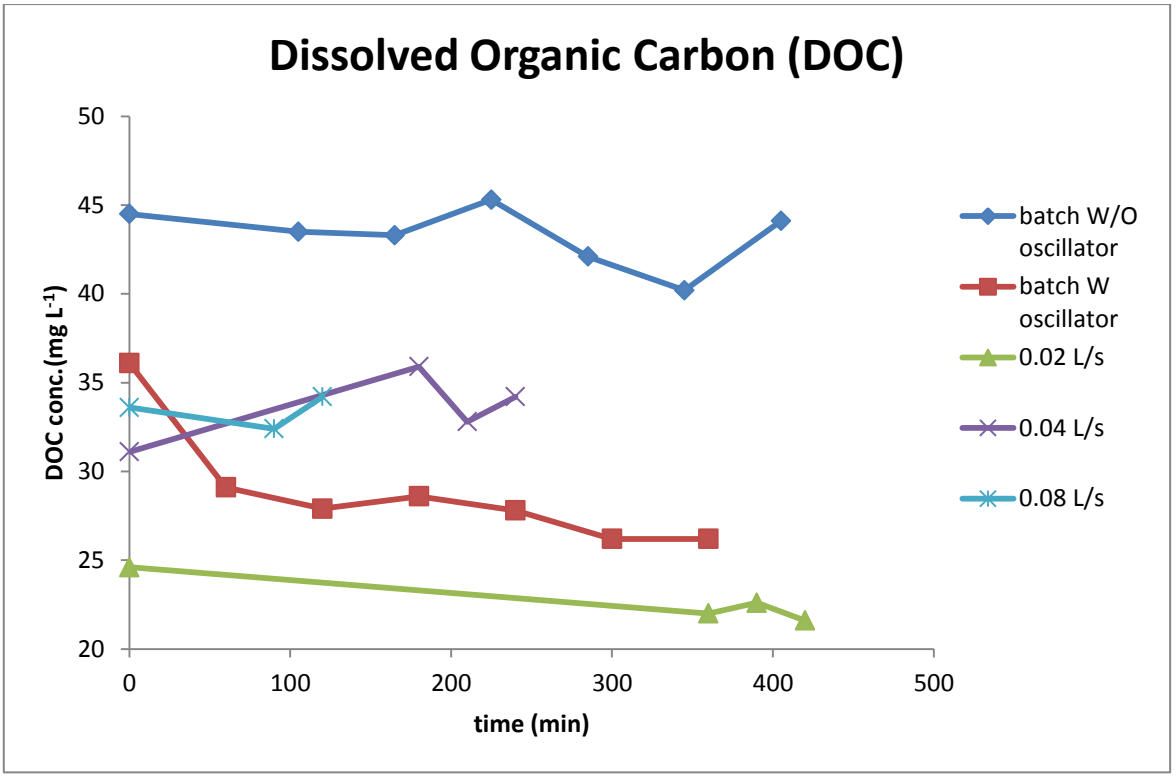

Figure 19: A plot of dissolved organic carbon concentration against time for each of the trail conditions, with the fluidic oscillator (W oscillator) without the oscillator (W/O oscillator) and for continuous effluent flow conditions with the flow rates shown.

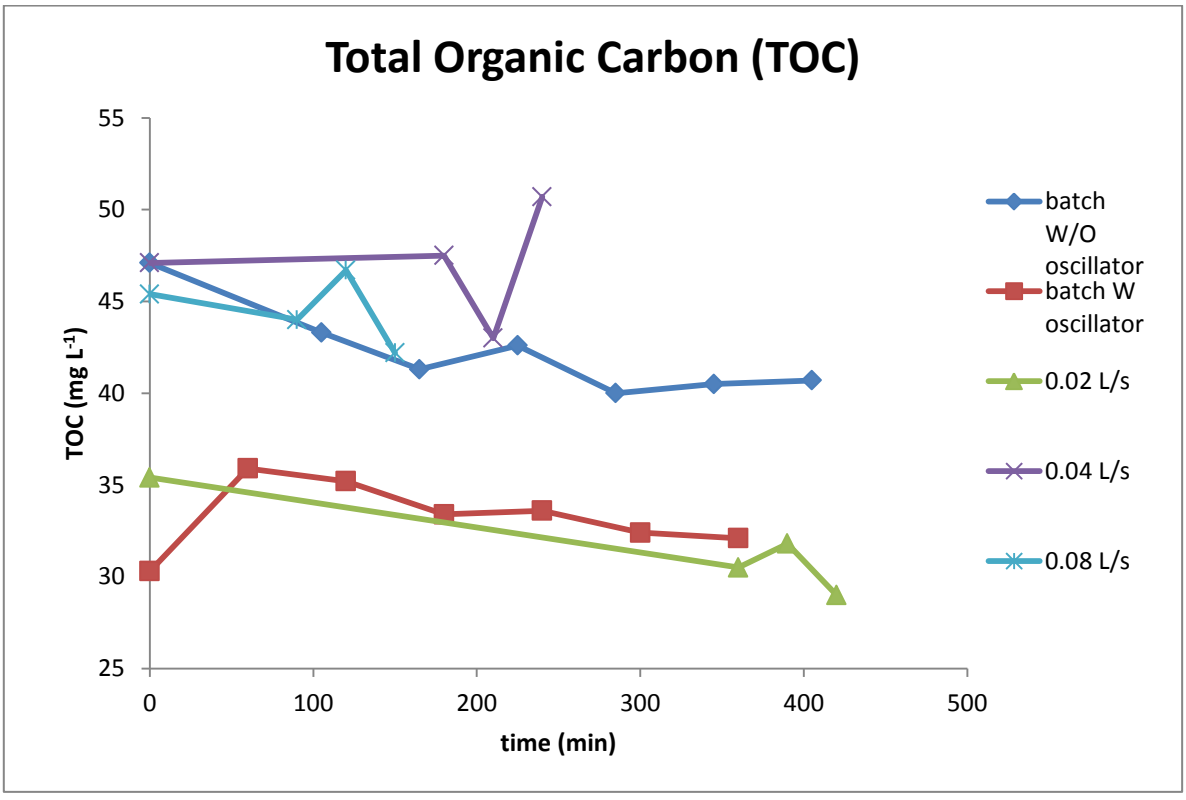

Figure 20: A plot of total organic carbon concentration against time for each of the trail conditions, with the fluidic oscillator (W oscillator) without the oscillator (W/O oscillator) and for continuous effluent flow conditions with the flow rates shown.

The most encouraging explanation of this is that the ozonation reactions are causing mineralisation of the organic carbon molecules into inorganic CO_2 and carbonates, as simply breaking down larger complex molecules into smaller ones would not reduce the total amount of carbon, as the same mass of carbon present in the large organic molecules would now be shared between a larger number of smaller organic molecules, but would still be present in the water. Assuming the reaction with ozone did not result in precipitation of the constituents, this argument could at least be true for the observed reduction in dissolved organic carbon.

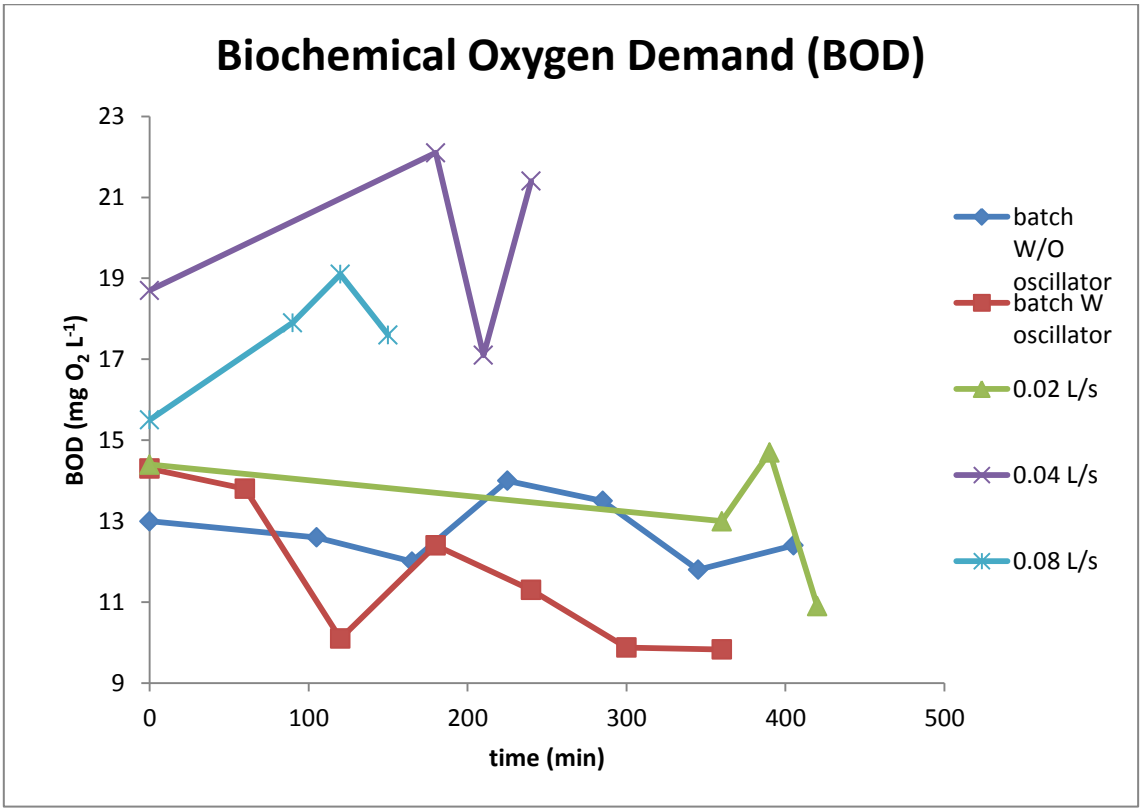

Figure 21: A plot of biochemical oxygen demand against time for each of the trail conditions, with the fluidic oscillator (W oscillator) without the oscillator (W/O oscillator) and for continuous effluent flow conditions with the flow rates shown.

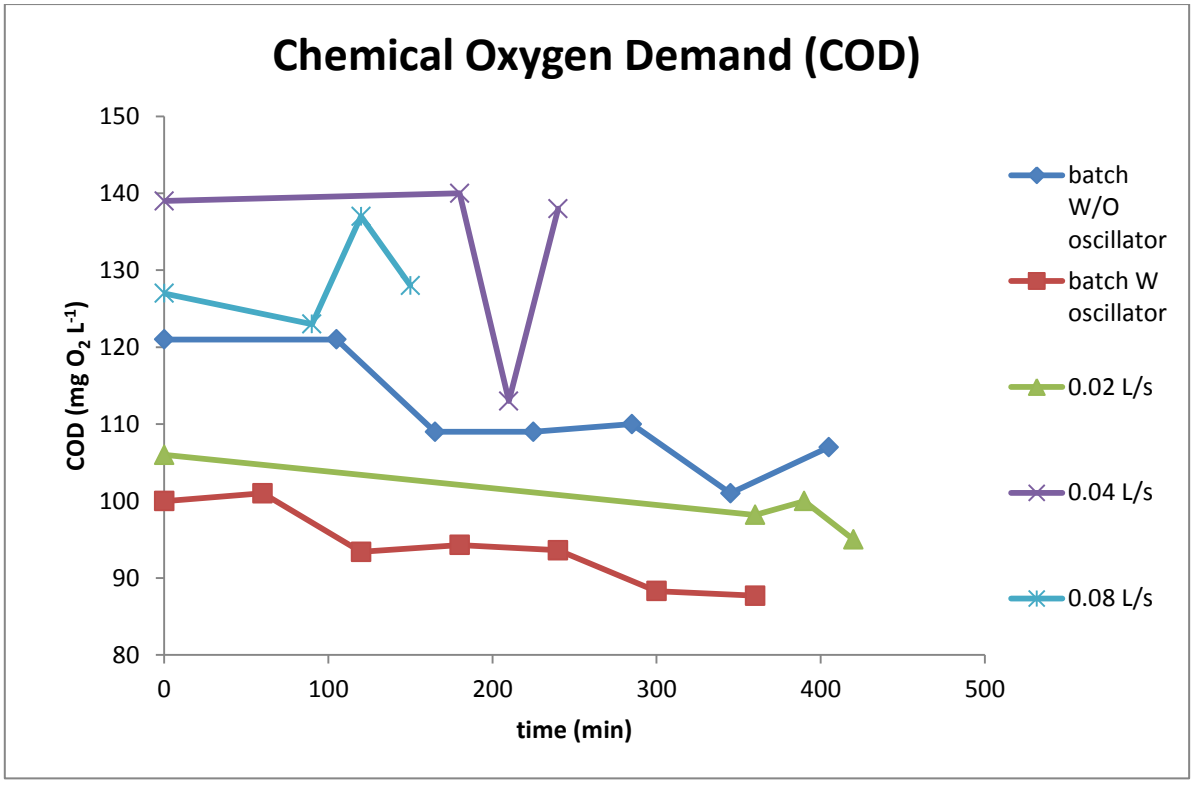

Figure 22: A plot of chemical oxygen demand against time for each of the trail conditions, with the fluidic oscillator (W oscillator) without the oscillator (W/O oscillator) and for continuous effluent flow conditions with the flow rates shown.

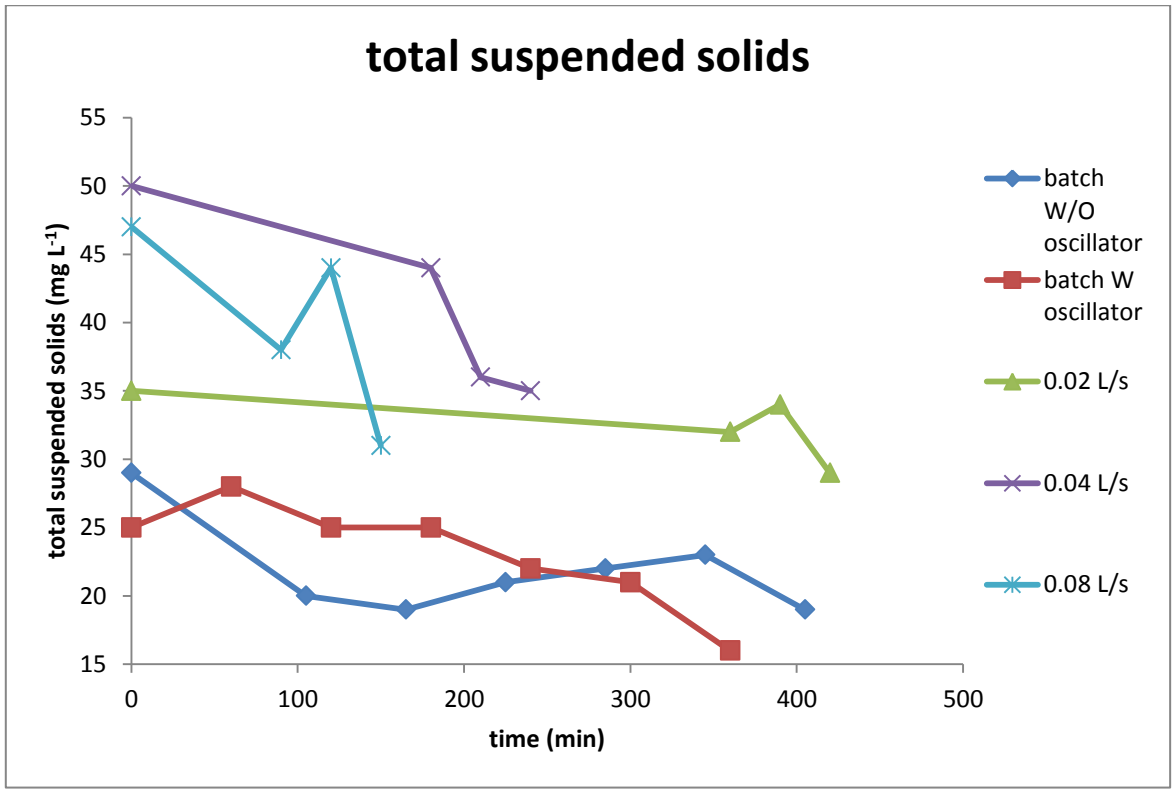

Figure 23: A plot of total suspended solids against time for each of the trail conditions, with the fluidic oscillator (W oscillator) without the oscillator (W/O oscillator) and for continuous effluent flow conditions with the flow rates shown.

It is likely that the removed TOC is due partly to the action of ozone mentioned above, but also partly to the action of suspended solids removal by the bubble diffusion. Over the course of each batch trial run, a head of foam forming on the top of the water body was observed, and clearly contained solid material. It is unlikely that the ozone reactions alone could be responsible for the removal of solid material. The solids removal was more effective with the fluidic oscillator (Figure 23).

2.5.3 Salicylic acid

Most notably, salicylic acid appeared to increase and then decrease again after the initial 2-3 hours (Figure 24). This is likely to be due to either the breakdown of aspirin (a substance which was not tested for) into salicylic acid by ozone or one of its by-products, or due to some release of salicylic acid from suspended particulate matter from which it could have previously been adsorbed onto. Once all the aspirin has been used up, the remaining salicylic acid can be broken down. The decrease in the concentration of salicylic acid is much more pronounced with the fluidic oscillator. Thus the data would suggest that the fluidic oscillator enhances the hydroxyl radical production somehow, perhaps due to the effects of reduced bubble size observed by Chu *et al*. (2007).

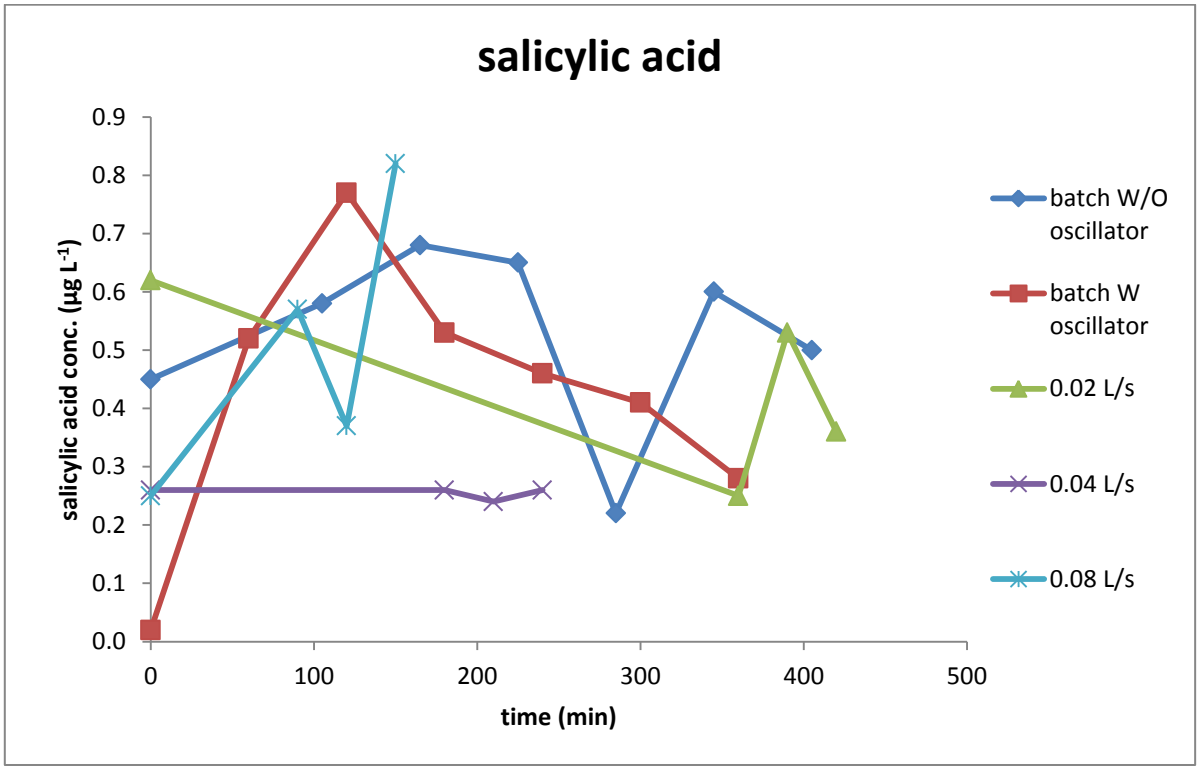

Figure 24: A plot of salicylic acid concentration against time for each of the trail conditions, with the fluidic oscillator (W oscillator) without the oscillator (W/O oscillator) and for continuous effluent flow conditions with the flow rates shown.

2.5.4 Nitrogen & phosphorus species

The nitrogen and phosphorus species remained relatively constant throughout the trials (Figure 25-Figure 28). Any variations were extremely minor, and this was most likely due to the relatively low quantities of ozone produced by the lance.

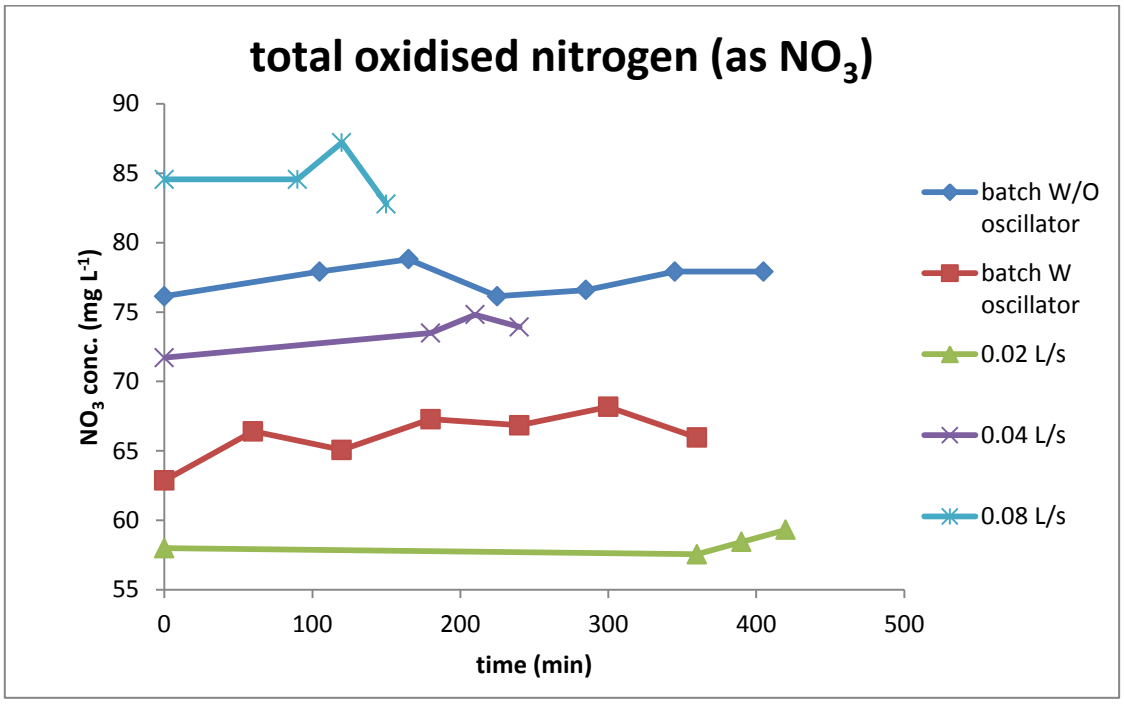

Figure 25: A plot of NO_3 concentration against time for each of the trail conditions, with the fluidic oscillator (W oscillator) without the oscillator (W/O oscillator) and for continuous effluent flow conditions with the flow rates shown.

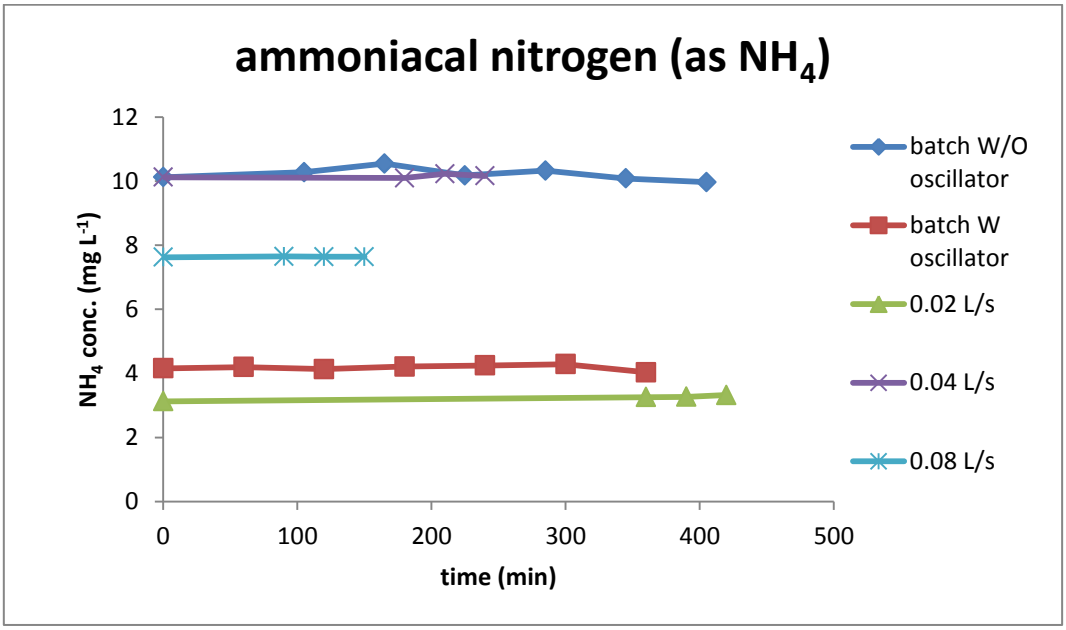

Figure 26: A plot of NH_4 concentration against time for each of the trail conditions, with the fluidic oscillator (W oscillator) without the oscillator (W/O oscillator) and for continuous effluent flow conditions with the flow rates shown.

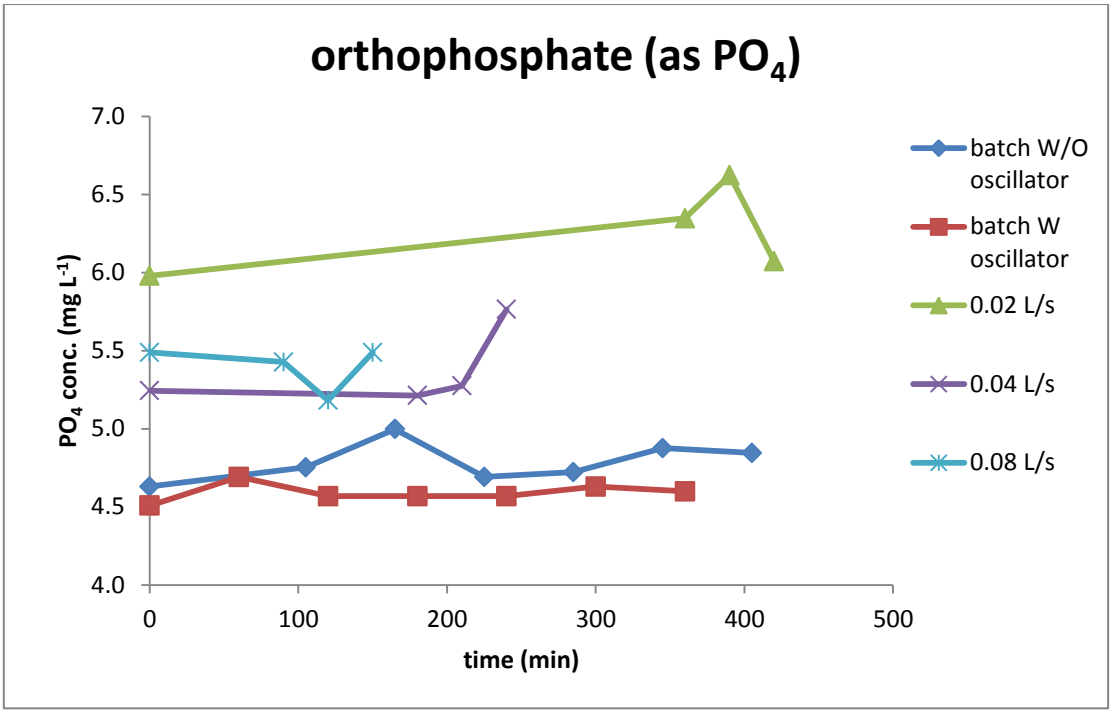

Figure 27: A plot of PO_4 concentration against time for each of the trail conditions, with the fluidic oscillator (W oscillator) without the oscillator (W/O oscillator) and for continuous effluent flow conditions with the flow rates shown.

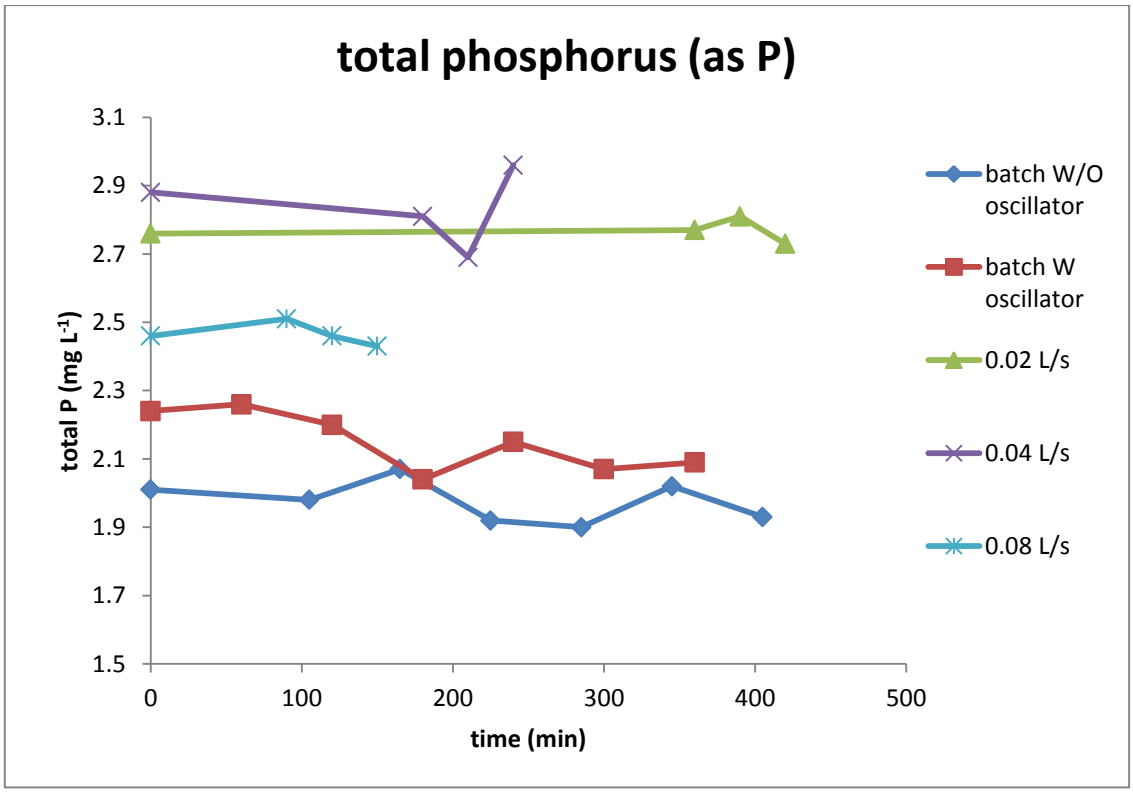

Figure 28: A plot of total phosphorus concentration against time for each of the trail conditions, with the fluidic oscillator (W oscillator) without the oscillator (W/O oscillator) and for continuous effluent flow conditions with the flow rates shown.

A sufficiently large quantity of ozone would be expected to oxidise a significant amount of the ammonia to nitrates, especially as ozone has an apparent affinity for electron dense regions such as the lone electron pairs on the nitrogen atom of an ammonia molecule.

2.5.5 Pathogenic microorganisms

The microbe count fell significantly during a batch test with the fluidic oscillator (Figure 29). The graph was plotted again with a logarithmic scale to see if this trend would continue even with much lower numbers of bacteria (Figure 30) and it was apparent that the logarithmic trend was linear, meaning that the effect of the dosing lance on bacteria destruction as a percentage of the bacterial population would be the same regardless of how small the bacteria population was.

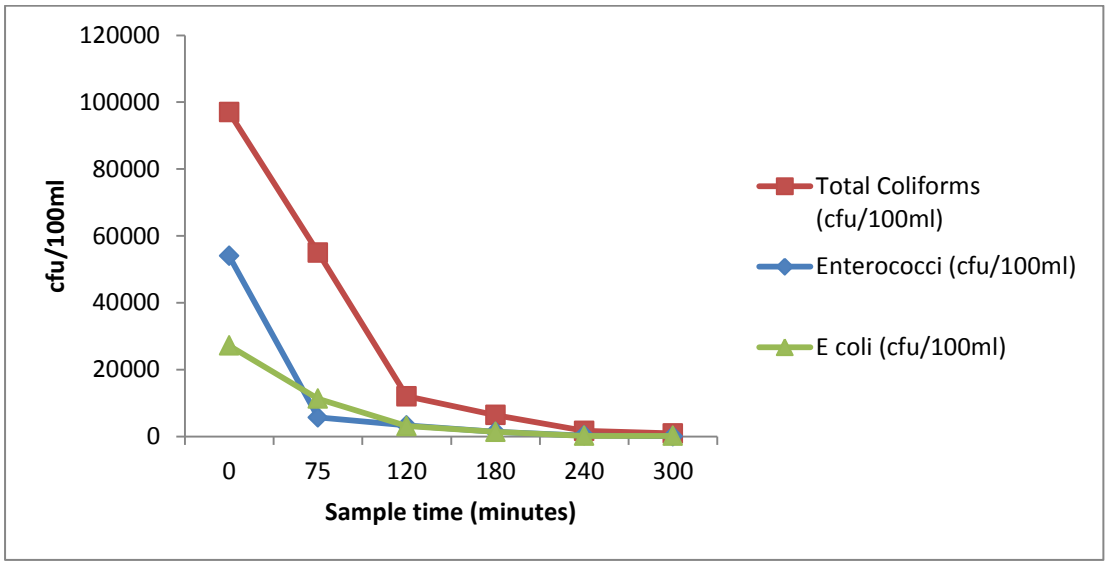

Figure 29: A plot of the effect of the dosing lance with the fluidic oscillator on the bacteria in final effluent in the second batch trial of the dosing lance on final effluent.

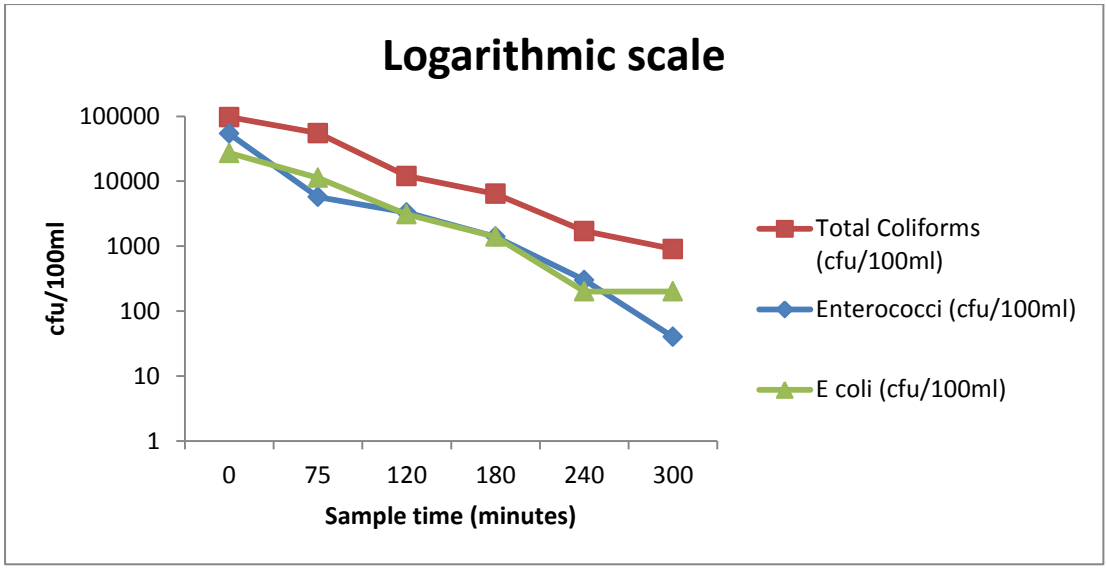

Figure 30: A logarithmic plot of the effect of the dosing lance with the fluidic oscillator on the bacteria in final effluent in the second batch trial of the dosing lance on final effluent.

2.5.6 Organic priority substances

The results of the priority substance tests are included in Appendix , as there was too much data to be included in the main body of the text without cluttering it up.

Generally speaking, the overall effect on the priority substances was that, when they were present, their concentrations decreased significantly, and in many cases they were removed completely, or at least to below the limit of detection in the batch processes.

The exceptions to this were ofloxacin, diethylhexylphthalate, 2,2',4,4',5,6'-hexabromodiphenyl ether (PBDE 154) and nonylphenol 4-nonylphenol, which did not show patterns of either net increase or decrease, and bisphenol A, which was actually observed to increase in the batch reaction with the fluidic oscillator. The increase in bisphenol A can be explained as it is a known constituent of epoxy resin, which was one of the adhesives and sealants used in the fabrication of the lance. From these results it can be concluded that epoxy resins should not be used in any commercial versions of the lance.

2.5.7 Heavy Metals

The effect of the dosing lance on heavy metal concentrations was difficult to assess, as heavy metals were not tested for during the batch processes due to constraints at the site. The results from the

continuous flow trials did not reveal anything significant, but have been included in Appendix nonetheless.

2.6 Laboratory measurement of dosing lance ozone output

As the measurement of the ozone output of the device onsite was impractical, measurements of the ozonation capacity of the dosing lance were made in the laboratory after the field trials.

2.6.1 Ozone output dry test

An experiment was carried out to test the output of the ozone plasma microreactor in a dry test over time, as it was observed in the field that the ozone output and brightness of plasmas tended to decrease over time. The lance was activated at a power of 150 W, and an air flow rate of 70 L min^{-1}.

The experimental setup in the lab is shown in Figure 31 and Figure 32. The tank had the internal dimensions: Height 60 cm, Width 30 cm, Length 60 cm.

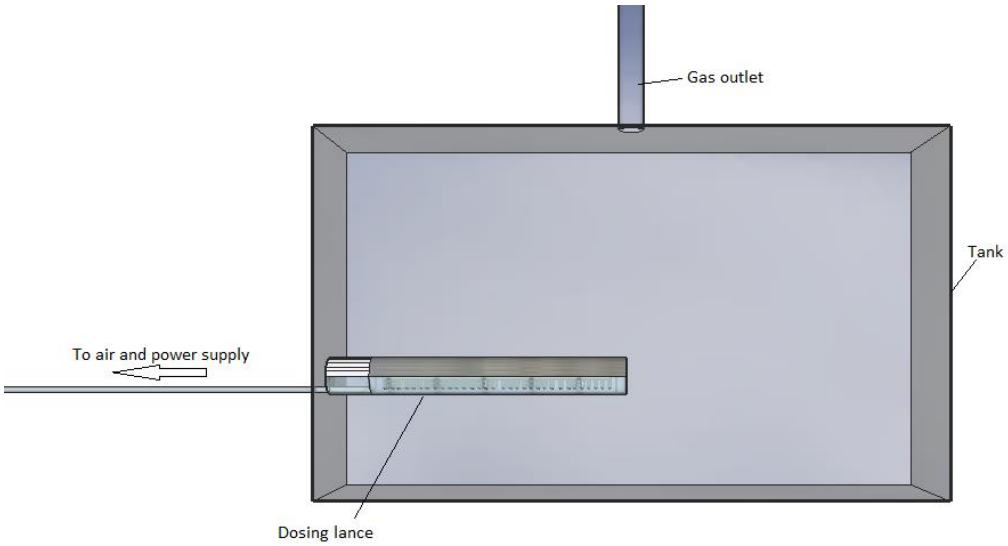

Figure 31: A diagram of the experimental dosing lance tank in the laboratory.

The fluidic oscillator will only work if the two air flow rates coming out of the two exit points are equal. This is normally achieved by fixing identical diffusers to each pipe, in this case, only one dosing lance is available, and the balancing air flow must be bled out into the atmosphere. A bleed valve must also be attached between the fluidic oscillator and the dosing lance to allow the air flow

to be balanced (see Figure 32). It was observed that the ozone output decreased quite rapidly over a period of 10 min and then seemed to level out (Figure 33), it was observed that whilst the ozone rate was decreasing, the brightness of the plasmas also decreased.

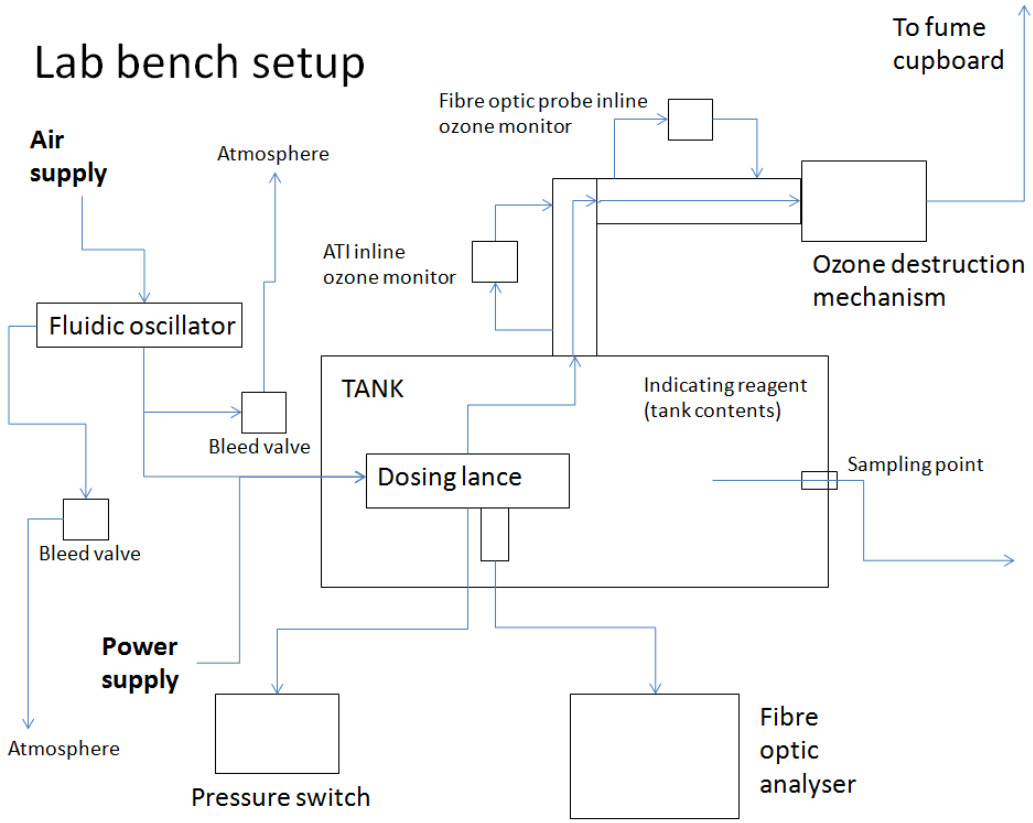

Figure 32: Diagram of the laboratory testing system.

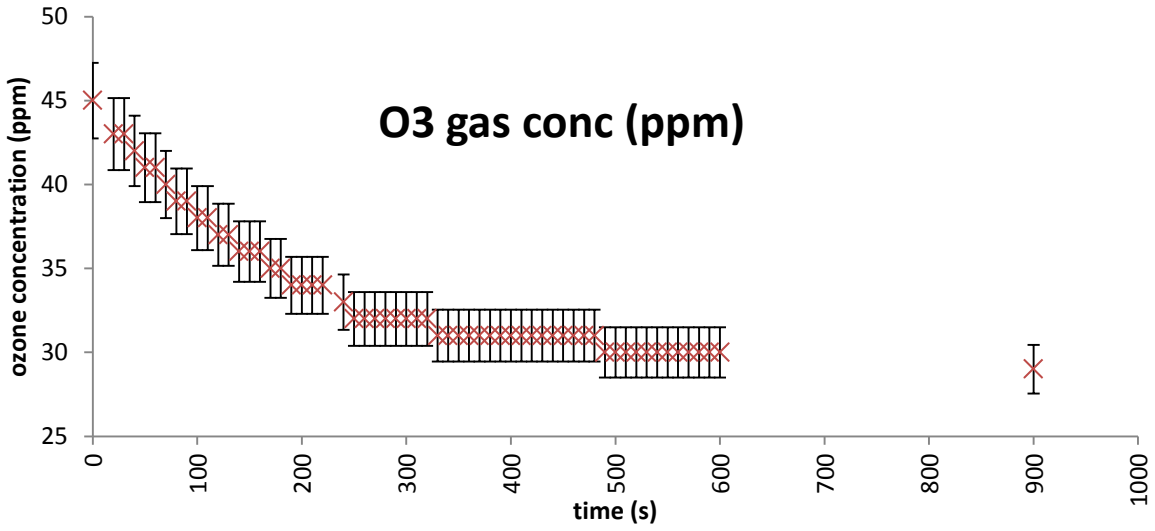

Figure 33: A plot of the ozone output of the dosing lance with time in a dry test in the laboratory. The air flow rate was 70Lmin^{-1} and the power setting was the same as that used onsite (approximately 150 watts). Ozone concentration (y axis) is in parts per million in the output gas, the unit of time on the x axis is seconds.

2.6.2 Ozone output wet test - KI titration

After the field trials were completed, and the performance of the lance had improved due to improvements of the electrode configuration and air flow path through the lance, the ozone generated by the dosing lance in conditions similar to those of the field trials was measured to be 150 ppm using a standard potassium iodide titration. This indicated that the limited effect of the lance on the water was due to the fact that the ozone production was extremely low.

A potassium iodide titration had to be used instead of indigo or other chemical methods due to the flow rates involved with the dosing lance. An air flow rate of 50 $Lmin^{-1}$ was too large to be blown through a standard gas washing flask, and larger gas washing flasks would have been difficult to get hold of. This problem was solved by filling the whole lab tank with an ozone detecting solution. As the costs involved in using indigo trisulfonate for this were simply too large, KI powder was used to fill the tank instead. An in-line ozone gas monitor (ATI B12-69-6-0100-1 Ozone Wet Gas Detector with flow cell accessory) was also used in this experiment to measure any excess ozone escaping from the “KI bath”.

2.7 Discussion

The lance had a clear effect on many water constituents. The combination of the plasma ozone generation with the ceramic diffuser and fluidic oscillator directly into the water makes the lance a novel technique for water treatment, and it was found that the lance could be inserted directly into the water under a head of up to 2m and still function, producing ozone continuously for up to 12 hours.

The motion of the bubbling had a mixing effect on the liquid, and the build-up of froth on the top of the water clearly showed that there was an added flotation effect, which could be seen in the gradual decrease of the total suspended solids (Figure 23). Solids removal is an important process in water and wastewater treatment and the fact that the lance could contribute to this as well as removing chemical constituents from the water means it could be an alternative, or complimentary method, to other solid removal techniques such as air flotation.

The concentrations of some of the constituents, especially the total concentrations of elements, appeared from the data to rise and fall. Since elements clearly cannot be destroyed or created by reaction with ozone, this would suggest that the composition of water in the tank is not homogeneous. A recirculation system should be used for similar field trials in future.

It was thought at first that the increase in concentration of salicylic acid might be due to re-circulation problems in the column, but as the increase and subsequent decrease in salicylic acid was observed in the both oscillatory and non-oscillatory batch runs, it is unlikely that this is the case. A more likely explanation is that the salicylic acid is being produced from the breakdown of something else, probably aspirin. The subsequent decrease in concentration of salicylic acid is suggestive of hydroxyl radical activity, as salicylic acid is slow to react with ozone but its reaction with the hydroxyl radical is rapid. Whether or not the salicylic acid removal can be attributed to the hydroxyl radical is not possible to know due to the complexity and number of unknowns of the wastewater. However, the bubbles formed did not appear to be sub-millimetre bubbles even with the fluidic oscillator, and it is not likely that there would be a particularly significant increase in the hydroxyl radical formation with only slightly smaller bubbles, since the effects observed by Chu et al. (2007) were with bubbles on the order of 50µm. The faster salicylic acid destruction rate might otherwise be explained by the higher mass transfer rate of ozone as a result a smaller bubble size.

2.7.1 Fluidic oscillator effects

During one operation test of the lance in the laboratory, after it had been repaired following a problem at the pilot plant, it was observed that the ozone output of the lance in a dry test was the same with and without the fluidic oscillator, suggesting that the chemistry of the plasmas in the dosing lance was not affected by the oscillating flow to a great extent. The fluidic oscillator, however, was observed to decrease the amount of ozone detected above the water by the in-line ozone monitor when it was connected upstream of the lance. This suggested, as was expected, an increase in the mass transfer rate of the ozone due to the reduction in bubble size resulting from the effect of the fluidic oscillator on the air flow patterns through the diffuser. It is likely that the flow rate through the dosing lance was too high for the oscillatory and non-oscillatory flow to have any noticeable effect on the plasma.

2.8 Further work required

Whilst the dosing lance affected many of the constituents of the water, it took 6 hours of continuous operation to make a significant difference, in most cases to a volumes under 200L of water. This would not be practical for application to the flow rates encountered in the full scale municipal wastewater treatment works.

An investigation into how the oxidative output could be improved is a complex task, requiring understanding of all the relevant disciplines involved, but is necessary if the potential of the technology is to be explored. It is not clear from the field trials how big a part, if any, was played by

RONS in the oxidation of the water constituents, but finding this out was beyond the scope of the field trials.

If it is possible to generate sufficient quantities of oxidant using plasma microreactors without the need to separate the water vapour and the nitrogen from the input gas stream to give a pure oxygen feed then this is preferable, hence another need for an air feed model for the plasma microreactor. This will require kinetic modelling of the reactor processes, for which the author will begin collecting data, and then compile.

Optimising the production of hydroxyl radicals in the plasmas themselves is likely to require a radical change in the design of the dosing lance. Either water or steam will need to be introduced into the reactors in order to form •OH or the reactors will need to be brought as close as possible to the water, even closer than they are in the current design of the lance. There will also have to be some circulation of the water to and from the surface of any such reactor, as the •OH radical is so short lived that it will only be active within a very short distance from where it was generated. Refining the design of the dosing lance for such •OH production will be one of the further research aims of the author.

The other means of optimising •OH radical production is via the reduction in bubble size as discussed earlier in the text. Thus the optimisation of OH radical and the optimisation of microbubble formation go hand in hand, and another of the author's further research aims will be in this area.

2.9 Conclusions

- The concept of a plasma micro-reactor/microbubble device to be inserted into water has been proven on a pilot scale
- The process removed many of the water constituents as well as disinfecting the water
- The total suspended solids were reduced, indicating the device could simultaneously be used for floatation
- The ozone output was very low, the reasons for this need to be investigated.
- More needs to be known about the chemical kinetics in the plasma and the water for the microplasma/microbubble combination to be investigated

3 Kinetic modelling of air feed plasma and air/water interface

3.1 Summary

The aim of this chapter is to provide a kinetic model of the chemistry involved in the air plasma, air/water interface and bulk liquid water, in a microplasma/microbubble reactor such as the dosing lance. The hope is that this model could be used to enhance and optimise the performance of plasma bubble reactors.

There are many possible reactions that can occur, and many metastable and short lived species that play very important roles in plasma chemistry. There are also often a large number of reactions happening simultaneously in the plasma. Thus due to the complex nature of plasma chemistry, even in simple plasmas, without a kinetic model real time analysis of the plasma reactions is quite limited. It is important that these reactions are understood as well as possible in order to optimise plasma conditions for plasma chemical engineering purposes.

A combined kinetic model of the plasma, afterglow, gas/liquid interface and bulk liquid is a novel undertaking, but essential to allow the possibility of optimisation of plasma bubble processes. More importantly new potential processes could be identified with this tool. Some potential reaction mechanisms have been inferred from literature studies of the nature of the air water interface, but it must be stressed that there are many interfacial processes that are still unknown, thus kinetic modelling of the interface must be pursued with an acceptance of this limitation. Nevertheless, a first attempt is presented here using COMSOL MULTIPHYSICS.

The reaction schemes are extensive and the large number of reactions would make the elements of a fluid dynamic mesh extremely complicated, thus the kinetic scheme here is done in time dependent zero dimensional conditions, which can still be used with some level of accuracy when the conditions in the plasma are relatively symmetrical.

3.2 Rationale for the model

In any chemical reactor the most important processes are the chemical processes. The chemistry is the foundation on which everything else is built, and the design of a reactor can be thought of simply as the design of the means to allow the chemistry to work at its optimum. The performance of the dosing lance cannot be analysed, nor improvements made, until the chemistry which takes place during its operation can be better understood.

From Figure 14 it can be seen that there are a number of distinct regions in the dosing lance, where the chemistry will differ, namely the plasma, post plasma region (afterglow), diffuser region, bubble interior region, and bulk liquid region. The interface between the gas and the liquid may also be treated as a region itself, about which relatively little is understood in comparison to the others. Gas molecules will move successively through the regions from the plasma to the bubble, undergoing reactions along the way, until they enter the dissolved phase in the bulk liquid region and then undergo reactions in solution. The reactions which occur will depend on the conditions prevalent, the species present, and the residence times in each of the successive regions.

Ultimately the purpose of the reactor is to affect the chemistry in solution in the bulk liquid region. The chemicals which enter the bulk liquid region are affected by conditions in the gas/liquid interface, which in turn is affected by conditions in the bubble, which is affected by conditions and dimensions in the diffuser. Which chemicals enter the bulk liquid phase is also dependent on which chemicals are produced in the plasma, which reactions occur in the post plasma region, and interactions with the plasma and the walls of the diffuser, and also any reactions which may occur on the gas/liquid interfaces of the bubbles. Given that the regions are all interconnected, they cannot be considered in isolation, and any simulation must in some way integrate each of these regions in order to be representative of the chemistry in a reactor where they are present.

Many bulk liquid simulations exist for ozone in water (Beltrán, 2003), but there are so far none that deal with the full range of chemicals that can be produced from an air plasma. There are studies for some of the individual species (Buxton et al., 1988; Neta, Huie, & Ross, 1988) but as of yet not a full suite.

Very little is known about the interface, and there are to date no chemical kinetic simulations of an air/water interface in pure water. Any attempt at building a chemical kinetic model would be a novel undertaking, and a useful contribution to the current body of knowledge in the area.

Many people have simulated plasma kinetic schemes in the literature for non-equilibrium low temperature plasmas in air, for different plasma discharge types such as plasma jets (Bibinov, Dudek, Awakowicz, & Engemann, 2007; Tsai & Hsu, 2010), corona discharges (Šimek, Člupek, Babický, & Šunka, 2006), microwave plasmas (Ferreira, Gordiets, Tatarova, Henriques, & Dias, 2012; Guerra & Loureiro, 1999), dielectric barrier discharges (Popov, 2011; Trushkin & Kochetov, 2012), hollow cathode discharges(Castillo, Herrero, & Tanarro, 2002) and even spark discharges (Aleksandrov, Bazyelan, Kochetov, & Dyatko, 1997) as well as glow discharges (Gatilova et al., 2007; Gordiets et al., 1995) and other discharge types (Sato, Ito, & Nishiyama, 2004). Some of the simulations focus more

on the vibrationally excited states (Smirnov, Rybkin, & Kholodkov, 2002) or the electronically excited states (Zhao, Garikipati, Hu, Argyle, & Radosz, 2005). There are also a number of 1D (Barni, Esena, & Riccardi, 2005; Pintassilgo, Kutasi, & Loureiro, 2007; Poggie, Adamovich, Bisek, & Nishihara, 2013) and 2D (Kulikovsky, 1997, 1998; Naidis, 1997) simulations in which the chemistry, if it is considered at all, must necessarily be kept simple.

The afterglow is simply the post plasma region, where there are remaining chemicals from the plasma still undergoing reactions. Most plasma simulations by default include an afterglow region, however some studies have dealt explicitly with the afterglow (Mrázková et al., 2009; Oinuma et al., 2008; Pintassilgo, Guerra, Guaitella, & Rousseau, 2010; Pintassilgo, Loureiro, & Guerra, 2005; Popov, 2010; Ricard, Oh, & Guerra, 2013; Vasina et al., 2004).

In air at atmospheric pressure, plasma jets, corona discharge, dielectric barrier discharge and glow discharge regimes are all relatively similar in terms of their chemistry (Barni et al., 2005; Bibinov et al., 2007) and the different plasma kinetic models generally use the same rate constants. The models differ primarily in which reactions they allow to occur, which species they include, and in which conditions they simulate with regards to the expected spatial variations in the systems they are trying to simulate.

In almost all cases, however, the kinetic rate constants are functions of the gas temperature, electron energy and gas density. The models will vary these conditions in accordance with what is known about the systems they are trying to simulate, e.g. Gordiets et al. (1995) modelled a low pressure glow discharge where the conditions are mostly homogeneous. Kossyi et al. (1992) used a similar situation in which the plasma being modelled can be treated as homogeneous. At higher pressures where streamers are involved, either the chemistry or the geometry considerations must necessarily be simplified in accordance with the available computing power.

In the case of non-homogeneous plasmas, a number of publications deal with the streamers and the knowledge gained from them can be used to inform the 0D chemical kinetic modelling in other simulations. This approach has been used in Sakiyama et al. (2012) where the knowledge of the EEDF of pulses was used to inform a steady value of the mean electron energies and electron temperatures used in the rate constant functions. The Sakiyama approach has been adopted in this study, along with its extensive range of reactions, for the reason that a greater number of reactions holds the promise of revealing useful chemistry which could potentially be the subject of future investigations. Whilst Sakiyama et al. (2012) has an extensive scheme of reactions, the kinetic scheme does not include many reactions of excited species which give rise to the emission of

photons, which are measurable in experiments. Reactions of this type can be found in Kossyi et al. (1992) and Capitelli et al. (2000) and have been combined with those of Sakiyama et al. (2012), to form the kinetic scheme of plasma reactions which are used in this study.

In summary, there are currently no models in the literature which combine all the chemical regions encountered in the dosing lance. The simulation of each individual region will be considered independently and then the resulting individual simulations combined to form a model which, once given some essential conditions for the reactor design, can be used to make predictions of the effect of a reactor design on the chemistry in the bulk liquid.

3.3 Basic model framework

The conditions in one of the reactors for the dosing lance are too complex to simulate precisely. In order to focus on the chemical reactions, the conditions must be simplified for the sake of the model. The assumptions that are made for the sake of this simulation are outlined in Figure 34, and the modelling is divided into four distinct zones. For an element to be simulated as if it is moving through these zones, the conditions will be changed accordingly using the rate constants of the reactions simulated. For the reaction A + B → C, the rate equation is

$$\frac{[C_c]}{t} = \mathrm{r} = \mathrm{k}\, C_A C_B$$

Where C_A, C_B and C_C are the concentrations of A, B and C respectively, and k is the reaction rate constant. The concentration of any individual chemical species (e.g. x) for each time step in the model is calculated from the sum of its production reaction rates over the sum of its destruction reaction rates

$$\frac{[C_x]}{t} = \frac{\sum k\, C_{x\,production}}{\sum k\, C_{x\,consumption}}$$

k , the rate constant is a function of one or more variables which can be representative of the conditions

$$k = f(g, i, j, etc.)$$

where g, i, j, are variables which can be changed to affect the reaction rates in accordance with the simulated conditions, as is outlined in Figure 35 and Figure 36.

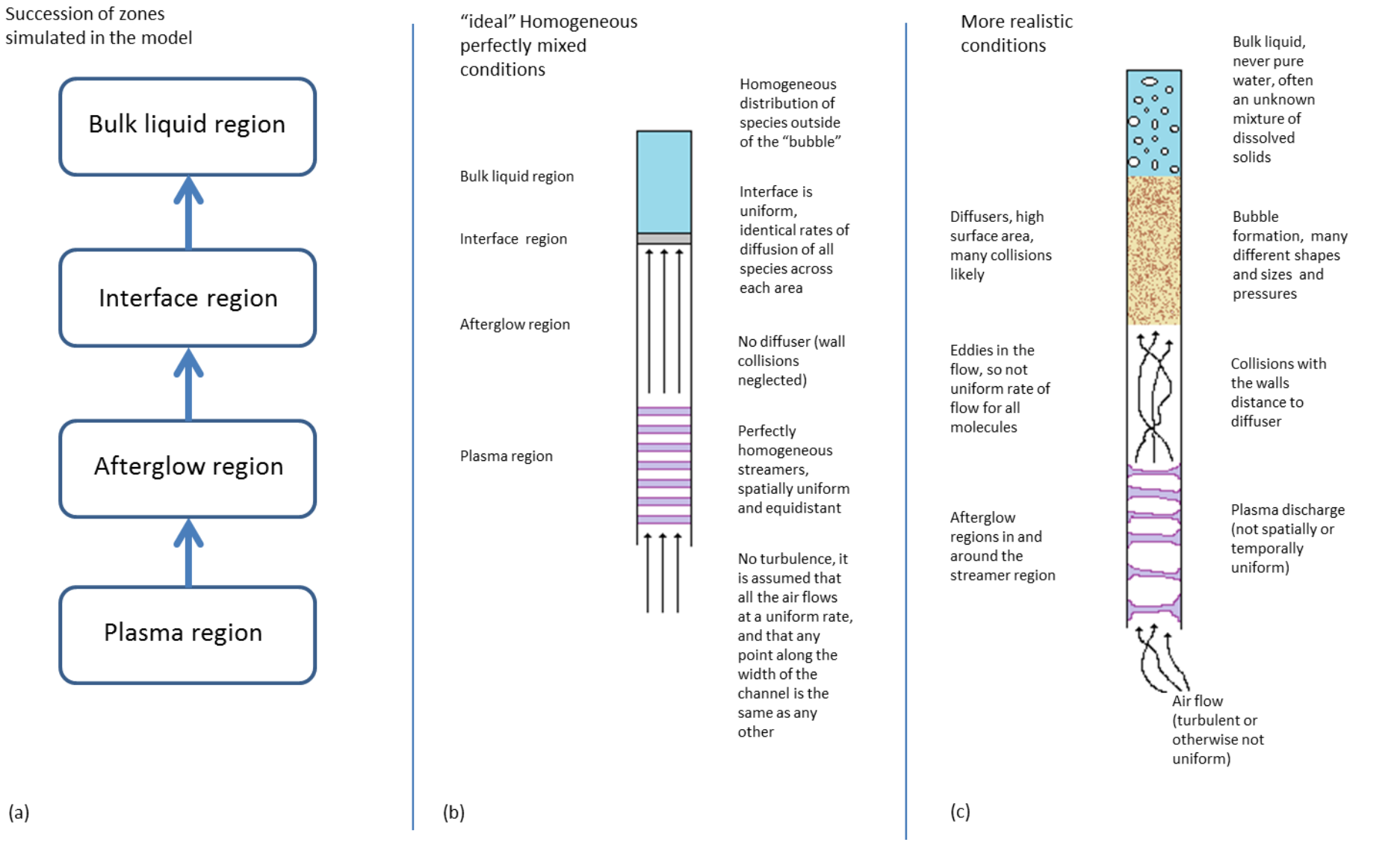

Figure 34: (a) Delineation of the successive model regions to be used in the simulation (b) simplified conditions for the model simulation (c) conditions likely to occur in reality.

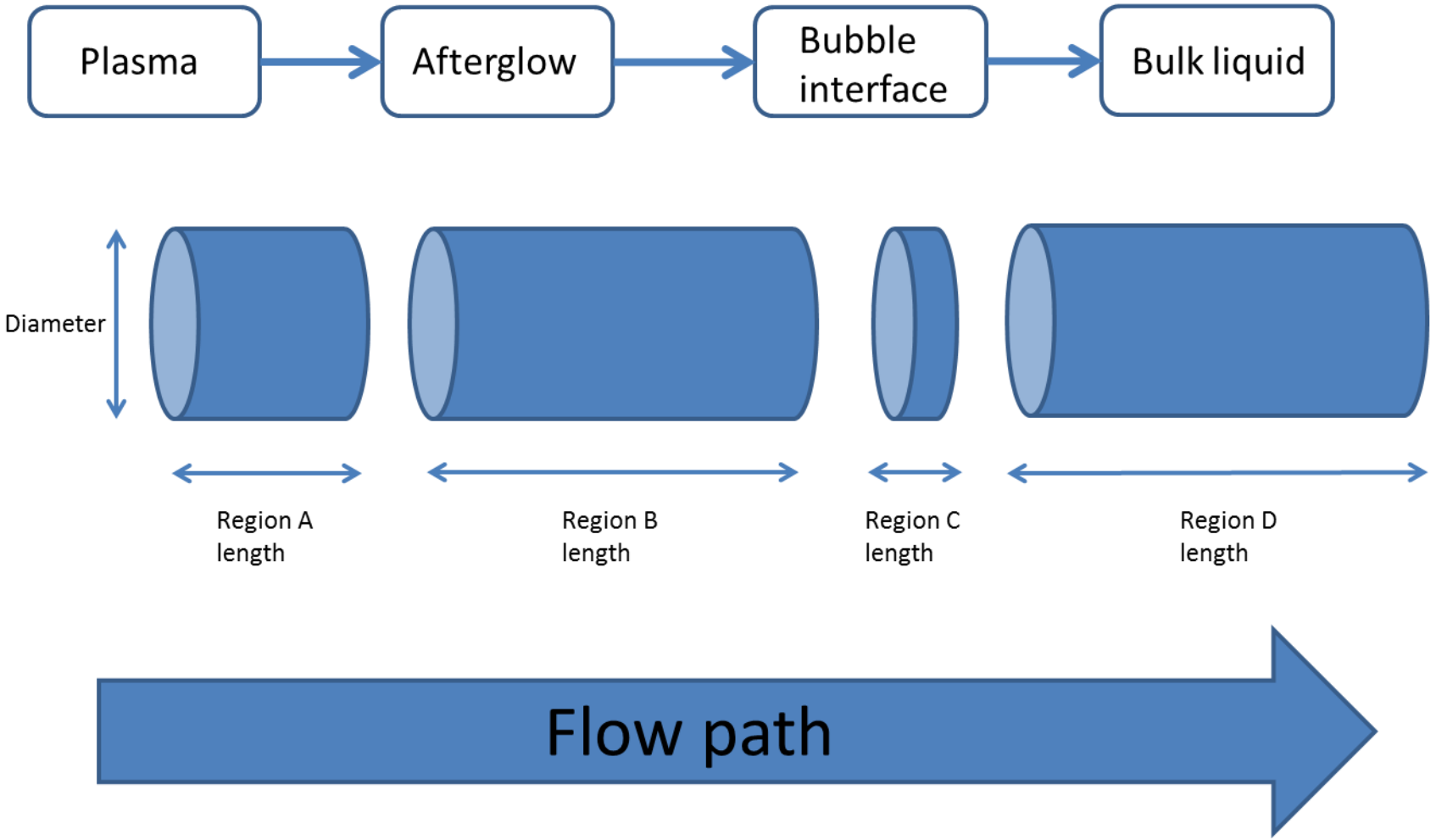

Figure 35: Diagram of reaction dimensions used in the model.

Using the COMSOL stepwise function, the variables can be set at certain values for certain time intervals that would be representative of the residence times of the elements in the zones where those conditions prevail according to

$$Residence\ time\ in\ region = \frac{Region\ length}{Flow\ velocity}$$

$$Flow\ velocity = \frac{Volumetric\ flow\ rate}{Reactor\ cross\ sectional\ area}$$

$$Cross\ sectional\ area = \pi(reactor\ diameter/2)^2$$

Therefore, setting k= f(x_{A1}, x_{A2}, x_{A3}) for t_A time iterations would give chemical kinetics that are representative of Region A. Zones are not so discrete in reality. The transition of the conditions of two zones can be gradual, smooth and continuous if all the zones are in the same model. This is more reflective of a situation that would occur in reality, for example, the transition between interface and bulk liquid is not discrete but gradual (see section 3.5).

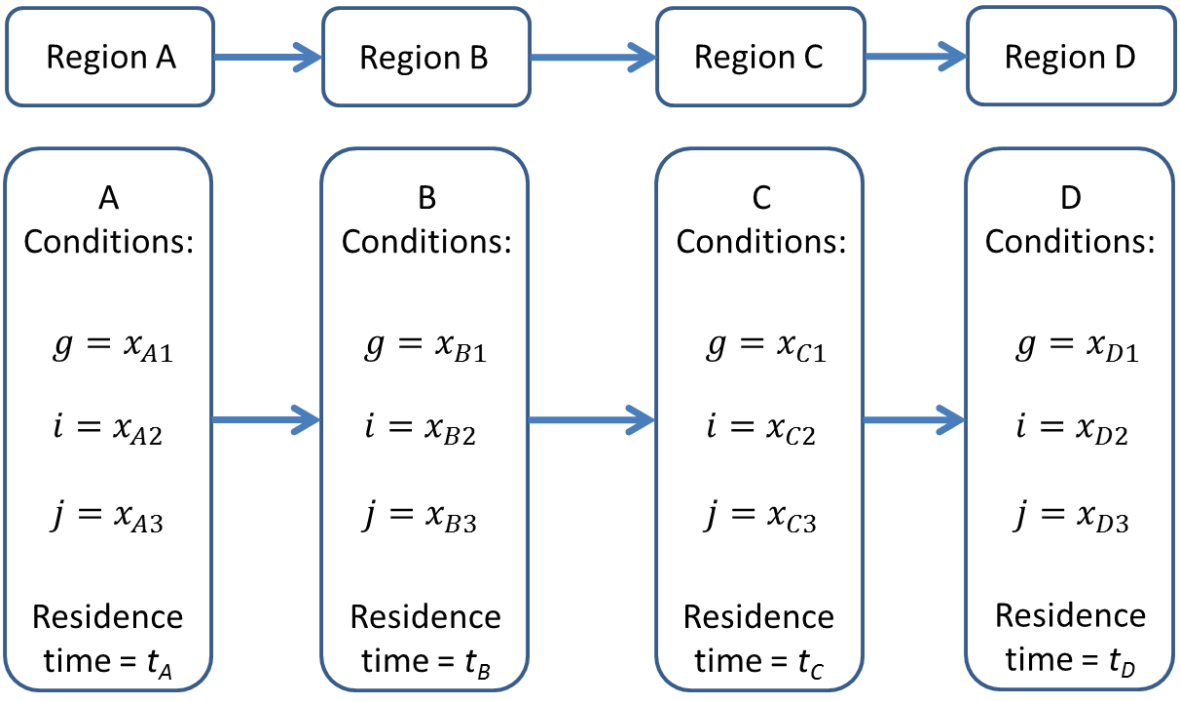

Figure 36: Generalised example of how conditions chemical conditions can be varied to simulate different conditions by changing the values of the variables used in the function of the rate constant (k).

The concentration of certain reactants in particular zones can also be altered to simulate changing conditions. For example, as the gas enters the bubble conditions the concentration of water vapour will increase, which will have an effect on the rates of any reactions which involve water vapour. The output of the simulation is the variation of the concentration of each individual chemical species with time, as shown in Figure 37.

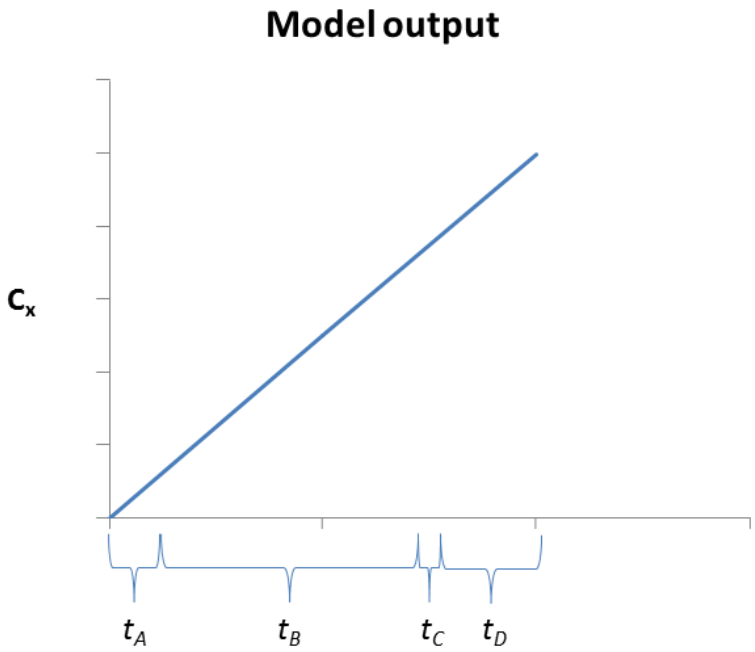

Figure 37: Hypothetical simulation output over a total number of time steps made up of the residence times of the distinct zones. The variable on the y axis is the concentration of the hypothetical chemical species (x).

The simulation of the four regions of the model will be addressed in the following sections.

3.4 Plasma

3.4.1 Plasmas – Basics

Most people imagine either a glowing gas or the colourless blood medium when thinking of plasma. The former was in fact named in reminiscence of the latter by Irvin Langmuir (Langmuir, 1928) due to the tenuous and fluid like appearance of early experimental glow discharges, the word “plasma” coming from an ancient Greek word meaning “To mold”.

The glowing is due to excited atoms and ions, and the excitation is a result of the high energy conditions, especially of the electrons, in the plasma. These high energy electrons are one of the

main benefits of using plasmas. High energy reactions that would not normally take place, not even at temperatures of 1000K, can take place at near room temperature in a “cold” plasma due to the extremely high energy of the electrons (Fridman, 2008). Once liberated from their parent atoms (by either direct ionization from the electric field, by radiation, or by ionization by collisions with other particles) the electrons receive their energy from the electric field, and due to their low mass, the electrons can move much more rapidly under the influence of the potential than can the ions. As a result of the higher mobility of the electrons than the ions (Figure 38), areas of the plasma can have localised positive charges, but the net charge of the plasma will still be zero, prompting the Chen (1984) definition of a plasma as “a quasineutral gas of charged and neutral particles which exhibit a collective behaviour”.

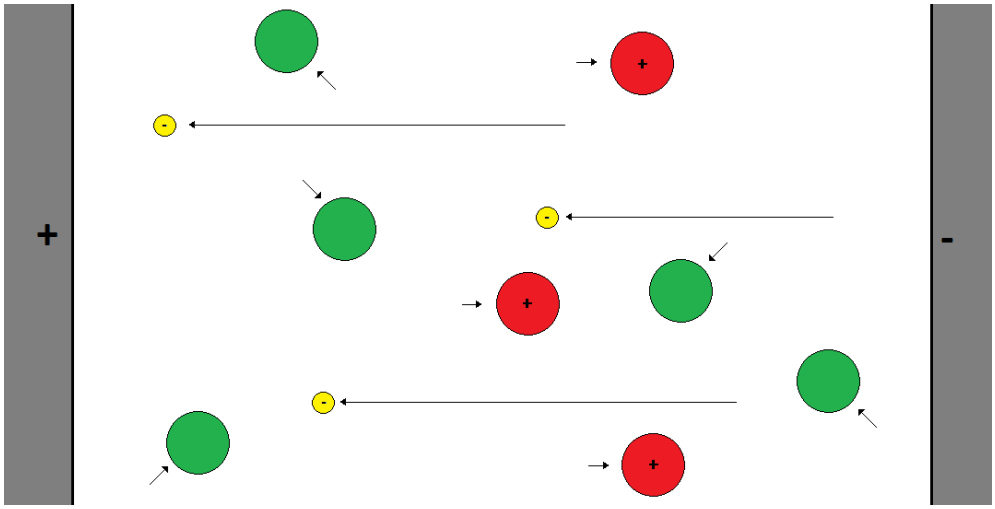

Figure 38: A representation of the movement of particles in a non-thermal plasma, not to scale. The electrons motioned by the electric field move with a relatively high velocity towards the positive electrode. The relatively more massive ions (red) move towards the negative electrode with a velocity on the same order as that of the random movement of the neutral particles (green)

If the electrons were moving in a vacuum they would move directly to the positive electrode. If a few molecules were added to this vacuum most of the electrons would still probably make it to the electrode unimpeded but there would be the occasional collision. Keep increasing the pressure and it becomes more likely that the electrons will collide with other particles on their way to the positive electrodes (Figure 38). When these collisions occur, the electrons impart some of their energy to the particles with which they collide, if the energy of the electron is high enough then a reaction with the electron and the other particle (most likely a molecule or ion) is likely to occur. Once the electron has interacted, or reacted with the molecule, the products of this reaction will then undergo other reactions.

3.4.2 Stepwise ionisation by electron impact

Before the electric field is even activated, there exists a small number of free electrons present in the gas. Once the field is activated, these electrons move, and collide with atoms. Successive collisions with electrons cause atoms to first be excited, and then eventually be ionised, or if the electron velocity is high enough the atoms will be ionised directly. The liberated electrons then move and collide with more atoms and the process repeats itself. This is called an electron avalanche (Fridman 2008).

3.4.3 Background free electrons

The small number of free electrons in the ambient air occur due to ionisation occurring as a result of natural radioactivity or cosmic radiation (Fleagle & Businger 1980). Such electrons are very short lived however, and after several literature searches experimental measurements of typical concentrations of free electrons in ground level air were found not to be readily available. Previous simulations have assumed the background concentration of free electrons to be 1 per cm^3, but the theoretical basis for this is not obvious.

3.4.4 Basic plasma equations and parameters

The electrons in the plasma do not all have the same energy, a range of electrons moving at different velocities will exist in the plasma, and the range is described mathematically by the electron energy distribution function (EEDF). Where the electron temperature (T_e) mostly determines the EEDF, can be used to describe the electron energy

$$f(\varepsilon) = 2\sqrt{\frac{\varepsilon}{\pi(kT_e)^3}}\exp\left(-\frac{\varepsilon}{kT_e}\right),$$

where T_e is the electron temperature, k is a Boltzmann constant, and ε is the electron energy. It is worth noting that most DBD discharges have electron temperatures in the range of 1-5eV (Fridman, 2008). The electron energy distribution function gives a normalised relative probability of an electron having a specific energy ε. The mean electron energy $\langle\varepsilon\rangle$, which can be derived from integrating the EEDF, is also useful to know for plasmas

$$\langle\varepsilon\rangle = \int_0^\infty \varepsilon f(\varepsilon) d\varepsilon$$

The rate constants for reactions involving collisions with electrons are often functions of the mean electron energy (see Appendix 3). In the case of a Maxwellian EEDF, the mean electron energy is given by $3/2T_e$ (Fridman, 2008). Two other distributions, the Druyvesteyn and Margenau distributions (Fridman, 2008)100-104pp, can also be used for the EEDF's of non-thermal plasmas, the equations are included here for interest.

Druyvesteyn (for constant λ and $\nu_{en}=\nu/\lambda$)

$$f(\varepsilon) = Bexp\left[-\frac{3m}{M}\frac{\varepsilon^2}{(eE\lambda)^2}\right]$$

Margenau

$$f(\varepsilon) = Bexp\left[-\frac{3m}{M}\frac{\varepsilon^2}{(eE\lambda)^2}(\varepsilon^2 + \varepsilon M\omega^2\lambda^2)\right],$$

where B is the pre exponential normalization factor, m is the mass of an electron, M is the mass of a neutral particle, e is the charge on an electron, ε is the electron energy, E is the electric field strength, λ is the electron mean free path, and ω is the electric field frequency. The Margenau is essentially the same as the Druyvesteyn distribution, but takes into account alternating electric fields (Fridman, 2008)100-104pp.

For the purposes of the kinetics studied here, a Maxwellian EEDF is assumed as it is common in many studies of DBD plasmas.

3.4.5 Rate equation

The general rate equation for reaction

$$xA + yB = products$$

is given as

$$Rate = k\,[A]^x[B]^y,$$

where [A] and [B] are the concentrations of reactants per unit volume, x and y are the orders of reaction (found in this study from the stoichiometry of the reaction) with respect to A and B respectively, and k is the rate constant.

Rate constants for electron impact reactions can be predicted from experimentally determined cross sections of collisions of electrons with other particles. The cross sectional functions from (Lieberman & Lichtenberg, 2005) were used in the following equation:

$$k_{A+B} = \int \sigma(\upsilon)\upsilon f(\upsilon)d\upsilon = \langle\sigma\upsilon\rangle .$$

Where (υ) is the cross section of the interaction between A and B for a given velocity, and (υ) is the probability of the particles having that velocity. Using the mean electron energy as the integral of the electron energy distribution function, the cross section can simply be taken at that energy

$$k_{A+B} = \int \sigma(\upsilon)\upsilon\langle\upsilon\rangle d\upsilon = \int \sigma(\varepsilon)\varepsilon\frac{3}{2}T_e = \langle\sigma\upsilon\rangle .$$

The units of the energy distribution function must first be converted into units of velocity for the velocity distribution function (Lieberman & Lichtenberg, 2005). The mean electron energy should be converted into a function of one of the variables already existing in the model for convenience.

The rate constants of the dissociation by electron impact reactions were found from (Guerra, Pinheiro, Gordiets, Loureiro, & Ferreira, 1997), assuming an oxygen/ (oxygen +nitrogen) ratio (δO_2) of 1 / 4.76.

3.4.6 Electron energies

The rates of electron impact reactions are a function of the electron energy, expressed as either electron temperature, reduced electric field, or the mean electron energy. These can be related to each other.

Assuming a Maxwell-Boltzmann distribution of electron energy, the mean electron energy is related to the electron temperature as

$$\langle\varepsilon\rangle = \frac{3}{2}T_e .$$

As a rough approximation, the relationship between the electron temperature T_e and the reduced electric field (E/n_0) can be described as

$$T_e = \left(\frac{E}{n_0}\right)\frac{e}{\langle\sigma_{en}\rangle}\sqrt{\frac{\pi}{12\delta}},$$

where δ is the average fraction of an electron energy lost in a collision with a neutral particle, $\langle\sigma_{en}\rangle$ is the mean cross section of electron-neutral collisions, e is the charge on an electron, E is the

electric field strength and n_0 is the number density of gas (Fridman, 2008, p. 104). The above is a rough approximation, and the electron temperature variation as a function of reduced electric field is different for each gas. It is better to use empirical data when it is available. Where required, the mean electron energy was found from the reduced electric field from Pekárek (2003), within the ranges of 1-6eV and 50-250×10^{-17} Vcm^2 for mean electron energies and reduced electric fields respectively.

3.4.7 Emission of light from excited species

Photon emission reactions are useful to include in the plasma model, as they allow relation of the model with experimental observations of the emission spectrum of the plasma. From the electronic excitation reactions found in Kossyi et al. (1992), rate coefficients of electronic relaxation by photon emission for these excited states could be included. Rate coefficients for emission relaxations were found in (Capitelli et al., 2000).

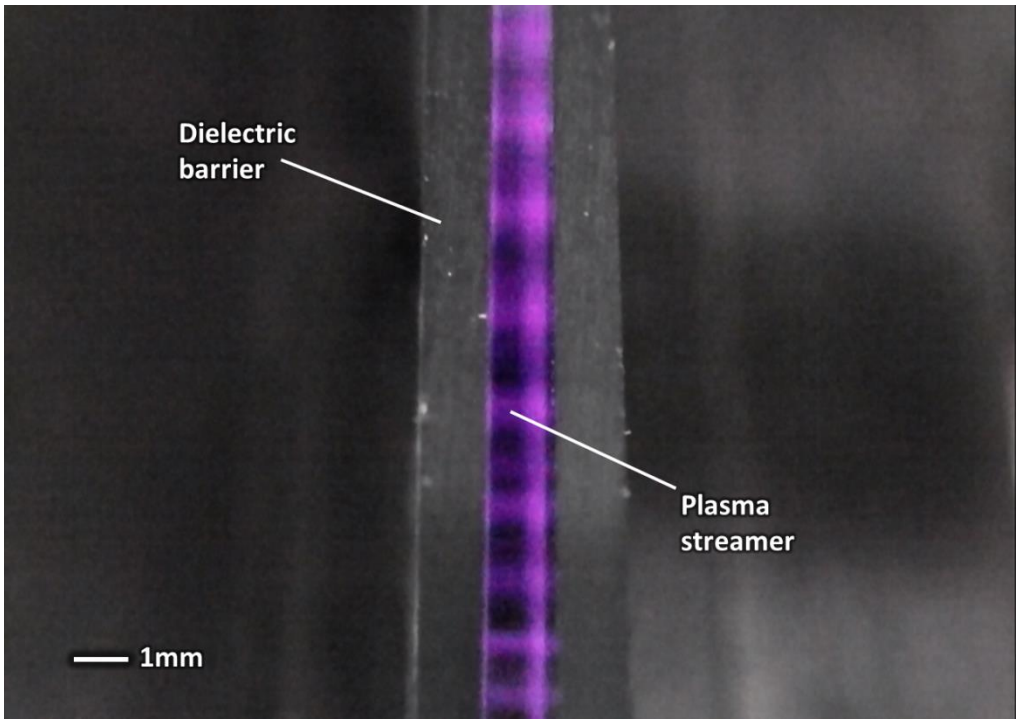

Figure 39: A photograph of a dielectric barrier discharge in air at atmospheric pressure. The individual purple microdischarges can be clearly seen between the two dielectric plates.

3.4.8 Dielectric barrier discharge (DBD)

To protect the electrodes and prevent glow to spark transition (transition of plasma from non-thermal to thermal regime) of streamers, dielectric layers can be placed over each electrode to stop the flow of direct current, preventing build-up of single high energy direct current channels and thus allowing plasma discharges to be evenly distributed. This arrangement is known as Dielectric Barrier Discharge (DBD) (Kogelschatz, Eliasson, & Egli, 1997).

At atmospheric pressure, the plasma is often not perfectly homogeneous but forms into small filaments called microdischarges (see Figure 39). These microdischarges are the result of localised streamers that repeatedly form in the same spatial location in each rise and peak of the alternating current due to the DBD memory effect (Fridman, 2008).

The microdischarges are randomly distributed in space and time, but are effectively identical (Baldur Eliasson & Kogelschatz, 1991; Fridman, 2008). Increasing the power increases the number of microdischarges per unit time.

The local electric field in the microdischarges must also be borne in mind when modelling them. Microdischarge formation is such that the local electric field within a microdischarge at the point of its formation and growth will differ from the overall electric field between the electrodes due to the motion of charged particles.

3.4.9 Complete scheme of O2/N2 mixture, plasma and afterglow simulation

Several publications have compiled kinetic schemes of O2/N2 mixtures. Rate constants and reactions vary slightly but most kinetic simulations of air plasmas are very similar. Rate constants for the nitrogen oxygen mixture were selected mainly from Kossyi et al. (1992) and Sakiyama et al. (2012) and are given in Appendix 3.

A simulation was run on COMSOL Multiphysics® and the resulting concentrations with time of the species are shown in Figure 40. As the duration of a single DBD streamer is on the order of a few nanoseconds (B Eliasson & Kogelschatz, 1991; Fridman, 2008), the model was run for this time (10^{-8}s) and then the mean electron energy, electron temperature, and reduced electric field (related to each other in section 3.4.6) were all lowered to 0.01 of their original values. Dropping the values to zero would mean some parameters of the rate constant functions would divide by zero which would cause problems in the computation. The kinetics have then entered the afterglow stage. In this region the concentration of excited species decreases rapidly, and the rate of reactions involving electrons decrease significantly.

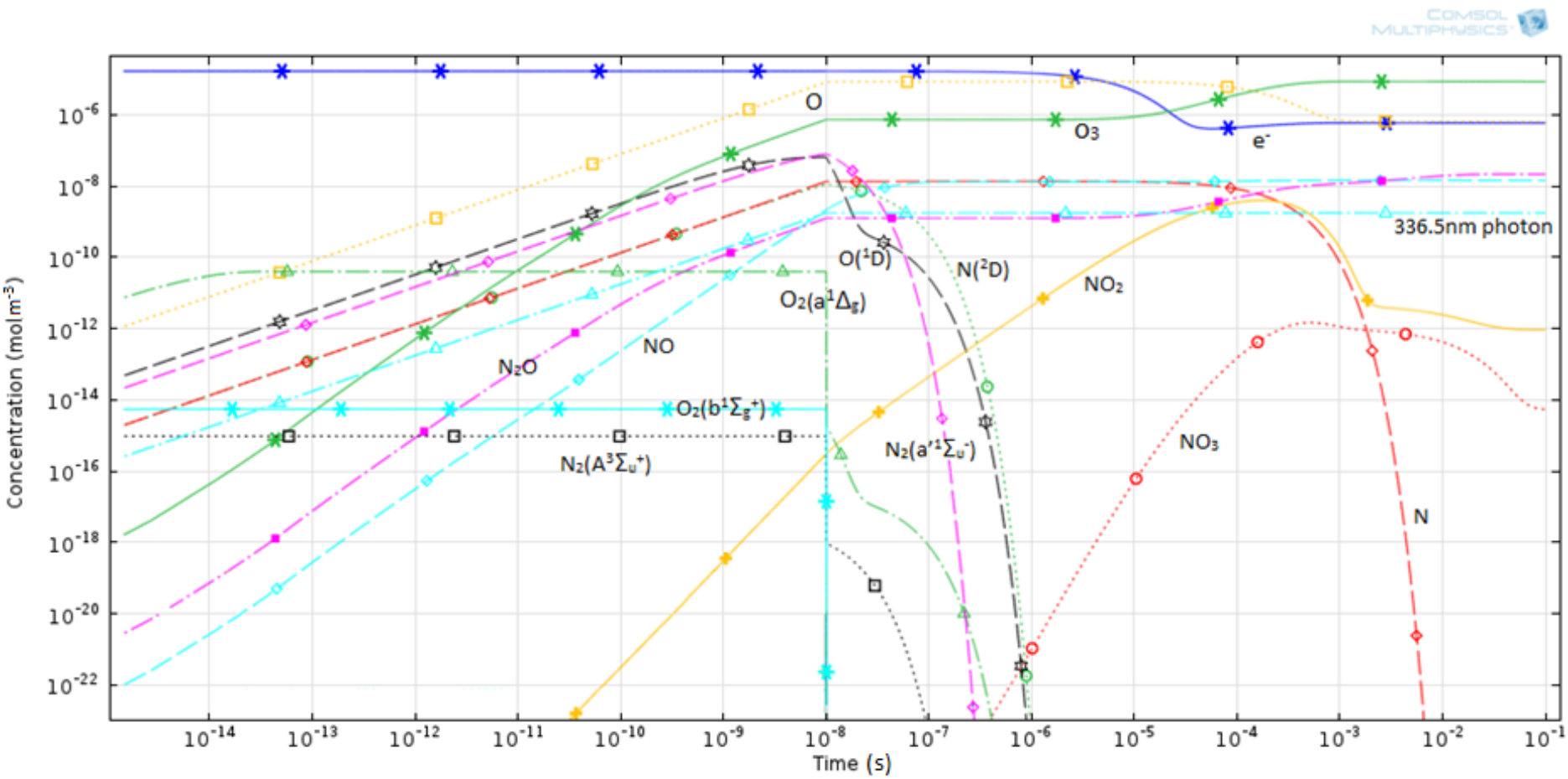

Figure 40: Evolution of selected species concentration in a single microdischarge streamer in dry air lasting of 10ns duration, beginning at time 0 and using reactions involving only nitrogen and oxygen in plasma conditions. Note that the photon of 336.5nm wavelength (the wavelength of light typically produced in the highest intensity) is also included, the concentration levels off after 10ns as no more photons are being emitted, the level is thus an estimate of the number of moles of photons produced in 10ns.

If the air entering the plasma reactor has a very low dew point (-60°C or less) then the contributions of water molecules can be ignored, and a scheme consisting only of oxygen and nitrogen can be used to make predictions of the chemistry. However, even small amounts of water vapour can interfere with the plasma kinetics, and the air supplied to ozone generators is required to be kept dry for this reason (Razumovsky & Zaikov, 1974, p. 322).

In the situation where the plasma is extremely close to the air/water interface, however, even if the ozone entering the reactor is thoroughly dried the close proximity of the reactor to the water will almost certainly lead to the water content of the air increasing considerably. Due to this, the contribution of water reactions cannot be ignored and will be considered in the next section.

3.4.10 Addition of water, discussion

The addition of water into the kinetic scheme complicates it even further, requiring a much greater number of reactions. The addition of water to the kinetic regime also alters the chemistry of the plasma. The reactions involving water are included in the kinetic model. Saturated air at room temperature has around 1mol m^{-3} the initial H_2O concentration was set to this. The resulting species concentrations over time are shown in Figure 41. The ozone formation behaviour of the model agreed with other kinetic studies in the literature (B Eliasson & Kogelschatz, 1991; Kossyi et al., 1992), which confirms to some degree the functionality of the plasma region of the model. It is interesting to note that the model predicted the formation of hydrogen peroxide, albeit in very low concentrations (10^{-10} mol m^{-3}), which could be useful in ozone decomposition processes.

3.4.11 Exclusion of argon

Although argon constitutes almost 1% of atmospheric air, reactions involving argon are not included in this model. Argon does interact with the chemicals in the plasma, but is too inert to form any chemical compounds. To include the individual interactions of each plasma constituent with argon would complicate the model and is not absolutely necessary for the scope of this work. Reactions for argon will therefore not be included in this model, but it is recommended that argon be included in future versions.

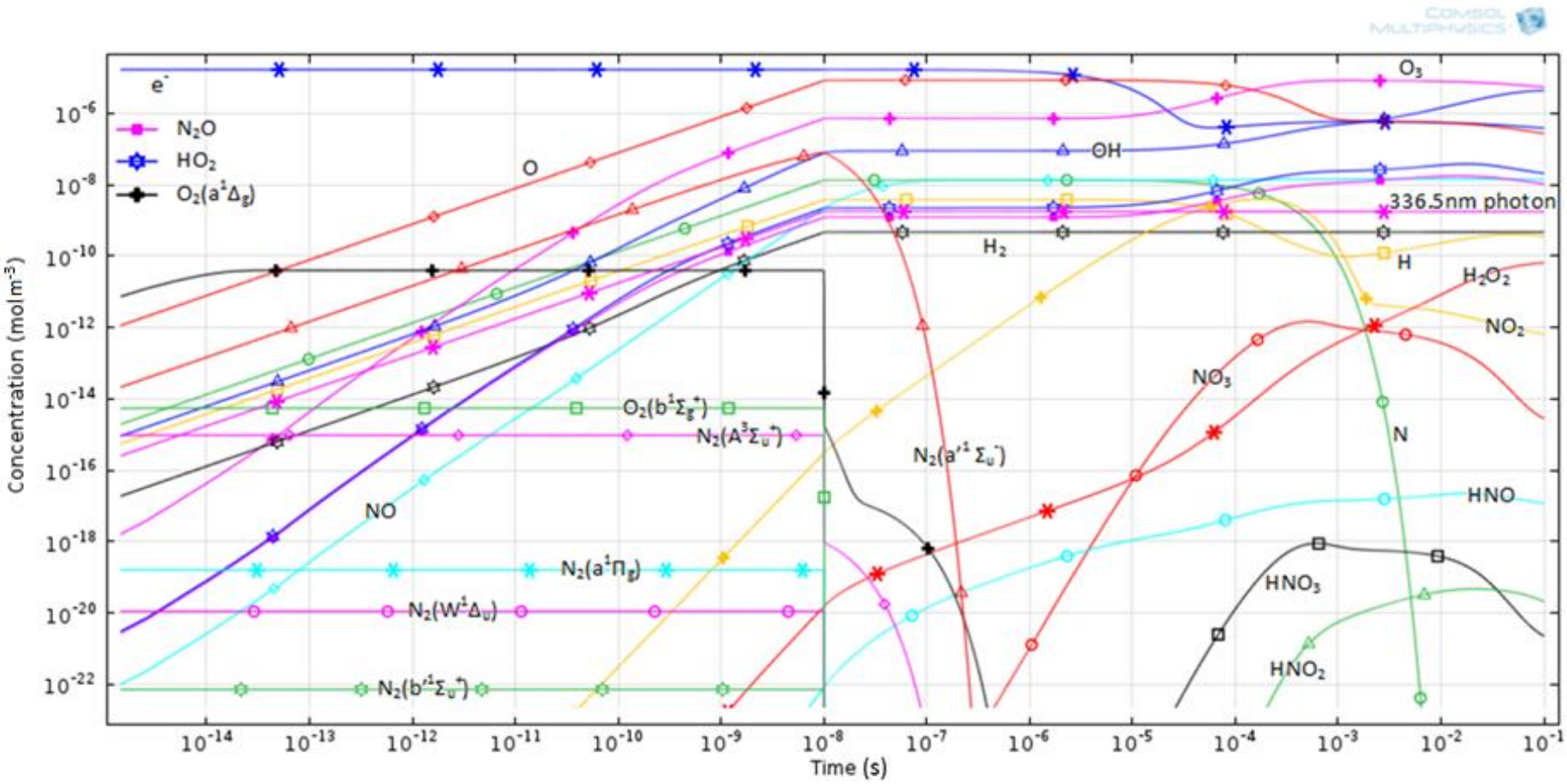

Figure 41: Evolution of selected species concentration in a single microdischarge streamer in moist air lasting of 10ns duration, beginning at time 0 and using reactions involving nitrogen, oxygen and water in plasma conditions.

3.5 Air/water interface

For any transfer of a gas into a liquid, microbubbles are an attractive prospect, as decreasing the bubble size increases the gas transfer rate into the liquid by increasing the surface area to volume ratio. It has also been observed in the literature that using microbubbles to deliver ozone increases the ozone breakdown beyond what would be expected by decreasing the bubble size (Chu et al., 2007). This suggests there are processes going on in microbubbles that would be of great interest from a chemical engineering perspective. The air/water interface (or skin) of the bubble is likely to play an essential part in this, and in order to take full advantage of microbubbles it is necessary to understand the processes at the surfaces. The chemistry of these processes, once understood, can be used to identify other chemical processes which could potentially take place on the microbubble skin.

The chemistry of the air/water interface is something that is still not very well understood, but recent advances in molecular dynamic simulations have been made in this field to the point where explanations of the mechanisms at work can be evaluated and applied. To understand which kinetics might be most significant at the air/water interface, it is essential first to review what is known about its nature.

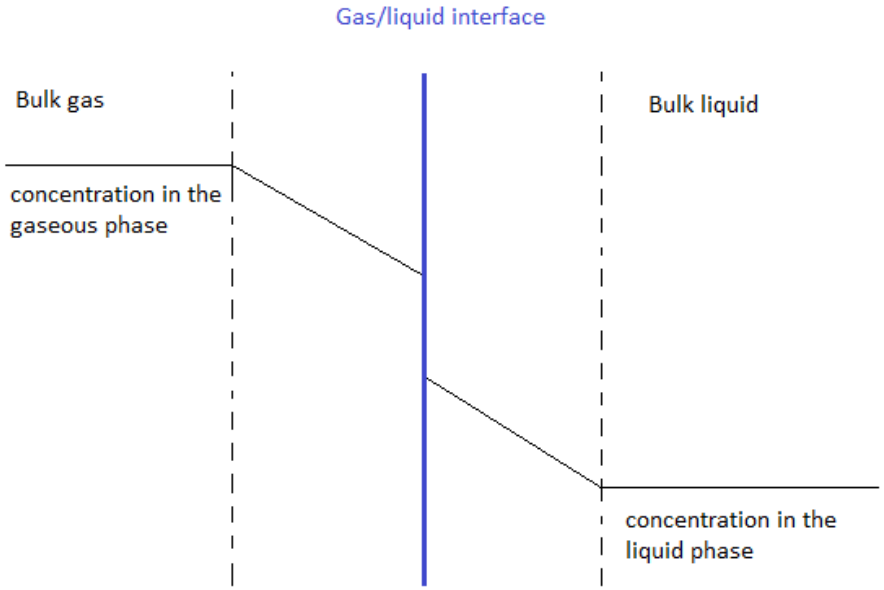

Figure 42: Diagram of the two film theory of mass transfer of a gas into a liquid (Beltrán, 2003).

3.5.1 Air water interface – basics

The two film theory (or two resistance theory) is a classical mass transfer model of a gas liquid interface and treats it as an intermediary zone consisting of two intermediary regions between the bulk liquid and bulk gas (Beltrán, 2003; Gottschalk et al., 2000; Lewis & Whitman, 1924) (Figure 42). These regions are much thinner than the bulk phases, and can be thought of as films. This view of the air/water interface is useful in mass transfer calculations but tells us little about the chemistry at the interface except for what the distribution of phases ought to be.

A closer view of the interface involves surface tension. The generally accepted view is that as the molecules at the surface of a liquid have nothing to bond to on the gaseous side, they therefore bond more strongly with neighbouring molecules and thus the liquid surface is a relatively strong film (Israelachvili, 2011). This laterally attractive force can be observed in the tendency of water droplets to revert to spherical geometries to minimise their surface area.

The increased lateral hydrogen bonding is a generalised view of the structure of the air/water interface, and the rearrangement of bonds in this phenomenon is likely to result in other chemical properties that differ from the bulk liquid, as the structure of the individual molecules at the surface must differ from those in the bulk.

Ishiyama and Morita (2009) ran computerized predictions of the most likely orientations of water molecules at the air/water interface, and also covered interactions between a pair of water molecules.

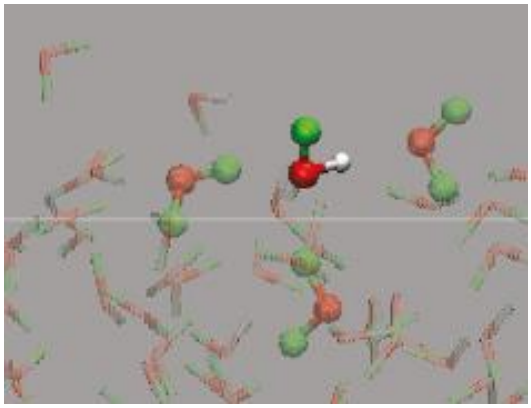

Figure 43: Predicted most common orientation of water molecules at the air/water interface, the grey line marks the interfacial line (Nihonyanagi et al., 2011).

The exact molecular structure of the air/water interface is still the subject of debate. Nihonyanagi *et al* (2011) suggested according to their spectral data, that there are strong “in-plane” H-bonds

between the water molecules at the outermost surface of the water (Figure 43). The evidence for this suggestion is the presence of the OH(x) band in the VSFG (Vibrational Sum Frequency Generation) spectrum. Their paper gives the view that the air/water interface is an orientationally correlated but somewhat dynamic system where resonance between adjacent water molecules is responsible for the observed spectrum. The findings of their work agree with those of Ishiyama and Morita (2009) who also proposed a similar model of the air/water interface.

A seemingly conflicting point of view is the slightly earlier suggestion that "the water surface has a partially disordered icelike structure" (Shen and Ostroverkhov 2006) (Figure 44). Shen & Ostroverkhov (2006) detected both "ice like" and "liquid like" bands in the VSFG spectrum of the air water interface. Their work also proposes that there is a quarter monolayer of "dangling OH bonds" as suggested by experiments conducted by adding a surface concentration of methanol of 25% to the water's surface and testing for OH peak signals (Shen & Ostroverkhov, 2006).

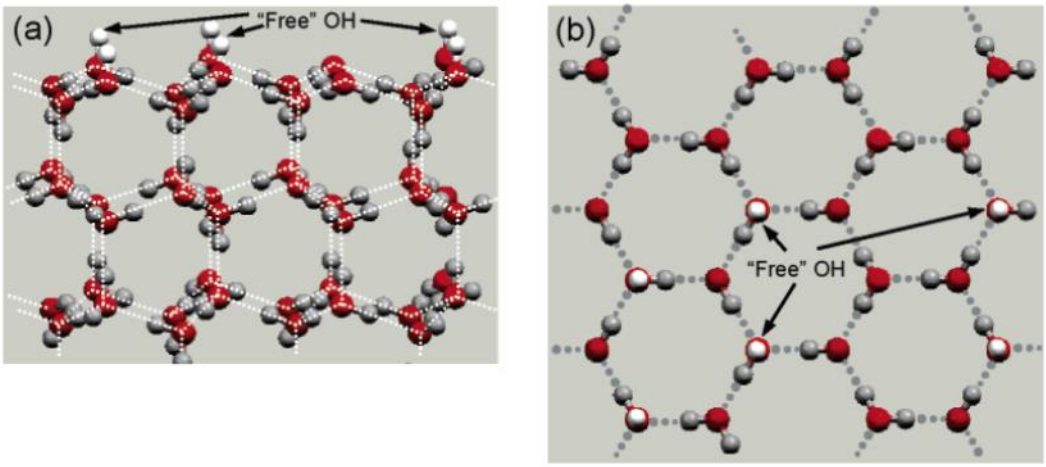

Figure 44: Model of the molecular structure of ice. (a) The bulk structure (b) A single ice layer, such as may be present of the surface of the air/water interface (Shen & Ostroverkhov 2006)

3.5.2 The water dimer

"Bulk water is believed to consist mainly of (distorted) tetrahedrally coordinated water structures, either as part of a continuum or as a distinct state" (Nihonyanagi et al., 2011). In contrast to this, the air/water interface is composed of a much larger number of hydrogen bonds between two water molecules, which suggests the presence of a larger number of dimers than would be present in the bulk water. The data in (Ishiyama & Morita, 2009) and (Nihonyanagi et al., 2011) suggests the most common repeating structure is a H-bonded dimer. (Nihonyanagi et al., 2011) have also shown that the interfacial region has a larger number of H-bonds, which would effectively point to an increase in the concentration of the water dimer $(H_2O)_2$. They also disagree with the idea that the surface of the

water has an increased tetrahedral structure that is “ice like” as is proposed in (Shen & Ostroverkhov, 2006).

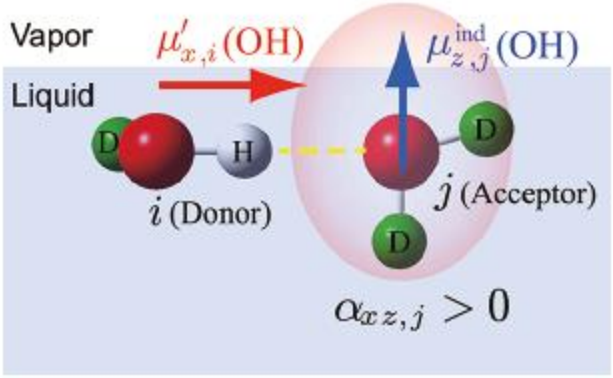

Figure 45: Theoretical most common repeating structure in a deauterated air/water interface, the water dimer (Nihonyanagi et al., 2011).

Rate constants governing the formation and destruction of this dimer have been suggested by (Yao, He, Mebel, & Lin, 2009). How these dimers would respond to ozone and to other radicals, however, is not known. No kinetic data has yet been found on the reactions of the water dimer with ozone or any of the other reactive oxygen and nitrogen species, thus until such rate constants are either measured or derived, assumptions must be made about the air water interface which allow it to be simulated in a 0 dimensional kinetic simulation.

3.5.3 OH radicals at the interface

A paper by Roeselová et al. (2004) suggested that the OH radical has a tendency for migration to the air water interface, and that due to this, and also due to the energy difference between surface sorbed and fully hydrated OH, there may be a one order of magnitude enhancement of the OH concentration at the interface compared to the bulk water.

This may, in part, explain why there is such an enhanced effect of ozone decomposition at the interface, since the OH radical is migrating to the surface once it is formed, where it can react (and thus initiate further ozone breakdown) with fresh ozone molecules at the surface.

3.5.4 Air/water interface electrochemical characteristics

Aside from the molecular structural aspects, there are electrostatic aspects of the air/water interface which can shed more light on the arrangement of molecules at the surface.

Electrochemical probe investigations have concluded that the air/water interface has a slightly negative potential of -25±10 mV relative to the standard hydrogen electrode potential (Farrell & McTigue, 1982), many studies since have produced similar results, which suggests that more negatively charged components of the water molecules are present around the air/water in the interface than in the bulk liquid.

The slight negative potential of the air/water interface can also be observed from the behaviour of bubbles in response to an electric field, as they move towards a cathode. Early observations of the electrophoretic mobility of bubbles include the work done by Quincke (1861), McTaggart (1914a); McTaggart (1914b), and Alty (1924). Some notable later studies have employed more refined techniques (Collins, Motarjemi, & Jameson, 1978; Graciaa, Morel, Saulner, Lachaise, & Schechter, 1995; Okada & Akagi, 1987; Usui, Sasaki, & Matsukawa, 1981). All these techniques clearly show that air bubbles in water move in response to an electric field.

From the bubble mobility the potential of the bubble skin, or zeta potential, can be calculated (Takahashi, 2005a):

$$\zeta = \eta\mu/\epsilon$$

Where ζ is the zeta potential (V), η is the viscosity of water (kg m^{-1} s^{-1}), ϵ is the permittivity of water (kg^{-1} m^{-3} s^2 C^2), and μ is the particle or bubble mobility (m^2 s^{-1} V^{-1})

The surface of shear (also known as the slip surface) can be conceptualised as a “sheath” surrounding the particle that consists of stationary fluid and moves along with the particle when the particle is in motion. The zeta potential is a measure of the average potential in the surface of shear (Figure 46).

The observable zeta potential is thought to be a consequence of an increase in the concentration of charged particles (or effective charged particle concentration made from the sum of a greater number of dipoles), and this concentration can be measured from the concentration of oppositely charged particles in solution required to cancel out the effect.

From kinetic model predictions involving changes in the concentration of charged particles, one could also predict the zeta potential. Conversely, from the particle velocity in a known electric field, one can make inferences on the concentration of charged particles in the interfacial region at the

time of measurement. Since the interfacial region is believed to be relatively simple, at least in the sense of chemical speciation, the concentration of charged particles (or effective concentration) can give us a great deal of information to characterise the interfacial chemistry.

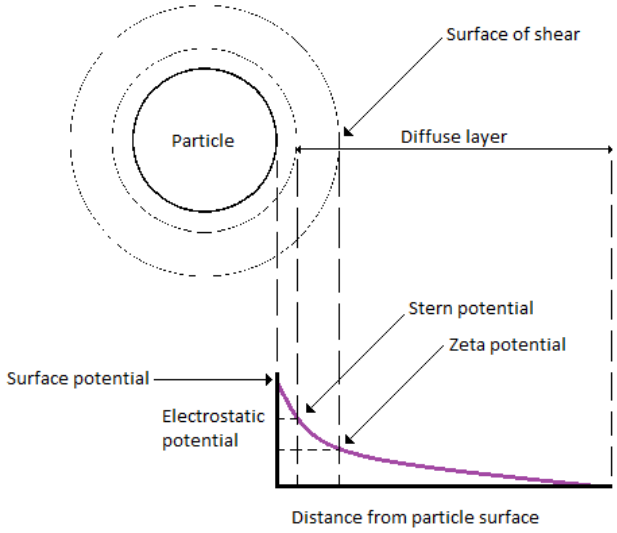

Figure 46: Diagramatic representation of the theoretical distribution of electrostatic potential on the surface of a particle or bubble.

In pure water, the negatively charged particles responsible for the charge are currently thought to be hydroxide ions (Gray-Weale & Beattie, 2009). Creux et al (2009) postulated that this was due to the fact that OH- ions have a high affinity to the interface and that the surface charge is due to migration of OH- ions from the bulk liquid to the interface. In contrast to this, Winter et al. (2009) say that there is not enough evidence to support the migration of the OH- ions to the interface, and Liu et al. (2012) presented the argument that the presence of OH- ions is due to a combination of autolysis of water and a much less significant contribution from migration of OH- ions from the bulk liquid, suggesting that autolysis is the major process, as the surface relaxation time is on the same order as the autolysis time. Whatever the discrepancies on how the OH- ions reach the interface, all agree that the OH- ions are the main agent at work. Thus for the purposes of simulation, the surface charge can be related almost exclusively to the concentration of hydroxide ions.

Assuming the inner charge is shielded by the outer charge, the sum of free anions (or equivalent summed negative dipoles) can be said to be equal to the particle charge:

$$\sum Charged\ particles = Q_e$$

The electrophoretic charge can then be related to the zeta potential as follows:

$$Q_e = N_{OH-} = \left([OH^-] * (volume\ of\ interfacial\ region)\right) * N_A$$

$$Volume\ of\ interfacial\ region \approx surface\ area\ of\ sphere\ of\ diameter\ \mathrm{d} * interfacial\ layer\ thickness$$

In the case of a bubble in pure water, the only negatively charged particle would be OH^- in the case of other solutions, N_{OH-} would be replaced by the total number of all negatively charged particles.

Takahashi (2005) measured the zeta potential of microbubbles with diameters from 60µm down to 15 µm in distilled water at pH5.8 to be 35±10mV, agreeable with Farrell & McTigue (1982), and found that there was no appreciable variation in zeta potential with bubble size in this range. This may suggest that the curvature of the bubble does not affect the chemical structure of the interface significantly. This is reasonable as the diameter should not affect the surface structure unless the curvature is significant on a molecular level. This conveniently allows information on large air/water interfaces (such as those in Langmuir troughs) to be extrapolated to microbubble skins. However it should be noted that Takahashi's measurements may not have taken into account the effect that the bubbles have on the movement of each other, e.g. a single bubble may rise more quickly than an array of bubbles.

Usui, Sasaki, & Matsukawa (1981), did observe an increase in zeta potential with a decrease in mean bubble size. Their observations, however, were of the potentials of whole bubble plumes and not of single bubbles, and extrapolating their data would give bubbles of below 100 µm a zeta potential of around -70 to -110 mV and bubbles of >1500 µm a positive potential.

According to molecular dynamic simulations by (Vacha et al., 2012) the water interfacial area in contact with the air is actually slightly positively charged and the negative region occurs at roughly 0.5 nm away from the interface into the water. This is in contrast to Shen & Ostroverkhovs (2006) more rigid ice-like structure where charge could be attributed to a discrete layer of "dangling" OH groups on the surface.

3.6 Proposed interfacial kinetic simulations

Some models suggest that the water surface is very thin indeed (only one molecule thick (0.1-0.2 nm)) (Shen & Ostroverkhov, 2006), whereas others suggest that there is a more gradual transition

from the surface to the bulk water, in other words the interface is spread over a much larger (in relative terms) length (about 2.5 nm)(Liu et al., 2012).

3.6.1 Simplified surface model

A simple model of a microbubble surface treats it as a flat surface with an area equal to the microbubble surface area, and adapts the equations according to various assumptions.

The bubble volume is given by

$$V_b = \frac{4}{3}\pi(0.5d)^3 ,$$

where d is the bubble diameter in metres. From the bubble diameter, the volume of the interface can also be calculated as

$$V_i = z_i 4\pi(0.5d)^2 ,$$

where z_i is the interfacial thickness, also measured in metres. From the relative volumes of the interface and bubble volumes, and if the concentration of ozone in the gas phase is known, and the concentration of OH^- ions at the interface estimated from the zeta potential or some other means, the molar ratio of ozone to hydroxide ion in the bulk liquid is given as:

$$Molar\ ratio = \frac{([O_3][V_b])}{([OH^-][V_i])} = \frac{\left([O_3]\left[\frac{4}{3}\pi(d/2)^3\right]\right)}{([OH^-][(4\pi(d/2)^2)z_i])} .$$

As the isoelectric point of the air/water interface occurs at around pH 4 (Takahashi, 2005b), it can be inferred that the concentration of OH^- at the surface of the microbubbles generally must have a concentration of $[OH^-] = 10^{-4}$ mol dm^{-3} in order to balance out this charge.

So to give just one example of how the air water interface can have effects on the chemistry of a system, the hydroxide ion catalyses ozone decomposition (Sotelo *et al*, 1987), which leads to the formation of hydroxyl radicals (Merenyi, 2010). The smaller the bubbles are, the more surface area to gas volume there is, the more OH^- per gas volume there is, thus the more OH radicals one should expect to form. Thus as the bubble size goes down, the ratio of the absolute number of moles of O_3 to moles of OH^- goes down (Figure 47).

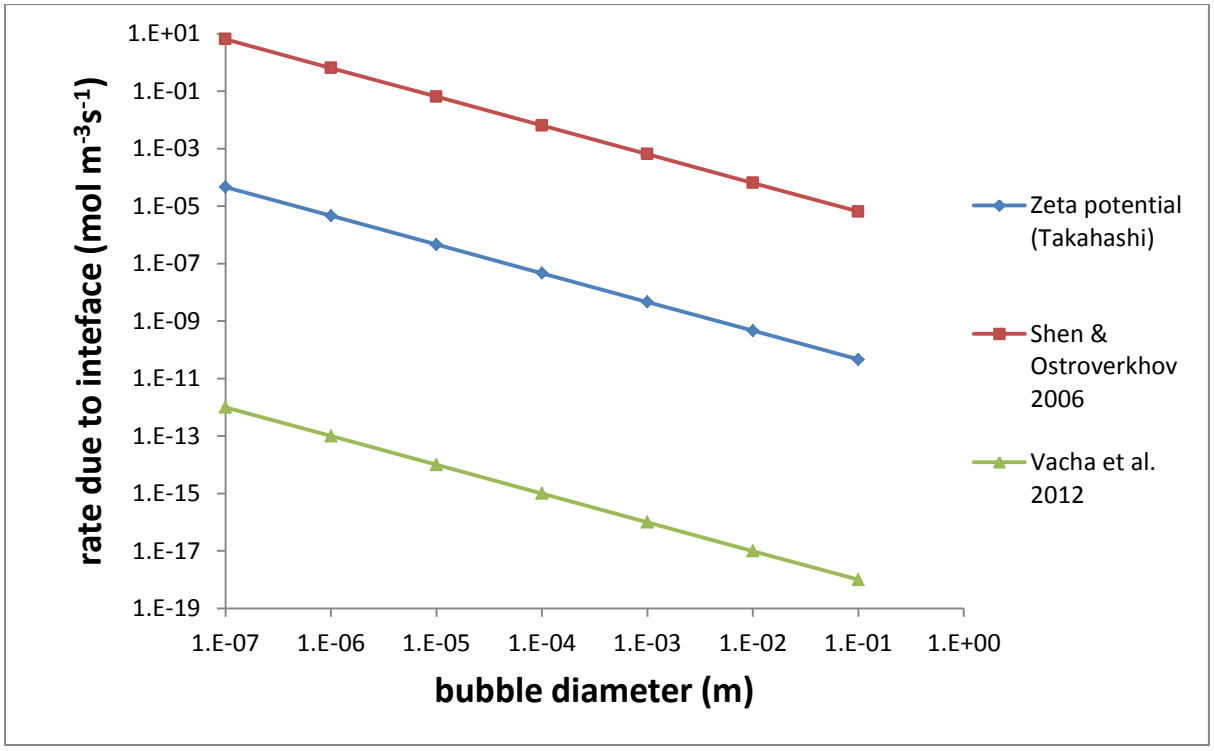

Figure 47: Theoretical effect of bubble diameter on base catalysed ozone decomposition, assuming an OH- ion interfacial concentration of 10^{-4}mol dm^{-3} and a gaseous ozone concentration of 1000ppm.

3.6.2 Nihonyanagi/Vacha model

The two papers (Nihonyanagi et al., 2011; Vacha et al., 2012) are not in disagreement with each other, as one explains only the bonds, and the other explains the charge. As mentioned above, however, the increase in bonding is difficult to simulate due to the lack of kinetic data on the water dimer. Due to this, until more data is available, only the charge will be considered for this model.

If we were follow this charge theory for our own kinetic simulation, we would find a surplus of hydrogen bond acceptors on the surface, which would have a more positive dipole, and then a concentration of more negative charge which ozone (as an electronegative molecule) would be more attracted to. To simulate this, it is necessary to make assumptions about the nature of hydroxide and hydroxonium ion ends of the water dimers described in (Vacha et al., 2012), e.g. the charge could be accounted for by a smaller number of "free" OH^- and H^+ ions instead of a larger number of less "discrete" dipoles of hydrogen bonds (if we assume a medium of pure water, it is reasonable to only consider OH^- and H^+ as significant charge carriers). For example, the number of hydrogen bond donors could be equated to a proportional number of H^+ ions whose total charge would equal the total charge of all the hydrogen bond donors, and the number of hydrogen bond acceptors to a proportional number of OH^- ions. This can be modelled in a kinetic scheme by varying

the concentrations of H+ and OH- temporally, and assuming that the diffusion is constant and only in one direction, outward from the centre of the bubble, which (along with the rate of diffusion of the particles) would allow a spatial variation with distance from the interface to be represented temporally in a 0 dimensional reaction engineering simulation. As the mass transfer through the interface is not in equilibrium, the liquid concentration of many of the plasma species will be close to zero, and the net direction of movement will be radially outward from the bubble to the liquid, thus this is not an unreasonable assumption

Another assumption could be, for example, that whilst the "dipoles" in the hydrogen bonds are not equivalent to "free" OH- and H+ ions, that their charge is proportional to their probability of reaction with ozone and thus that the extent of a charge could be represented by an equivalent concentration OH- or H+ ions that would consume an equivalent number of moles of O_3 as an equally sized charge would. This assumes that the products of such O_3 reactions would also be representative as what the products of the equivalent reactions with water-water dipoles would be, which is not an unreasonable assumption if you bear in mind that nearly all ions in water are bonded to another water molecule to some extent.

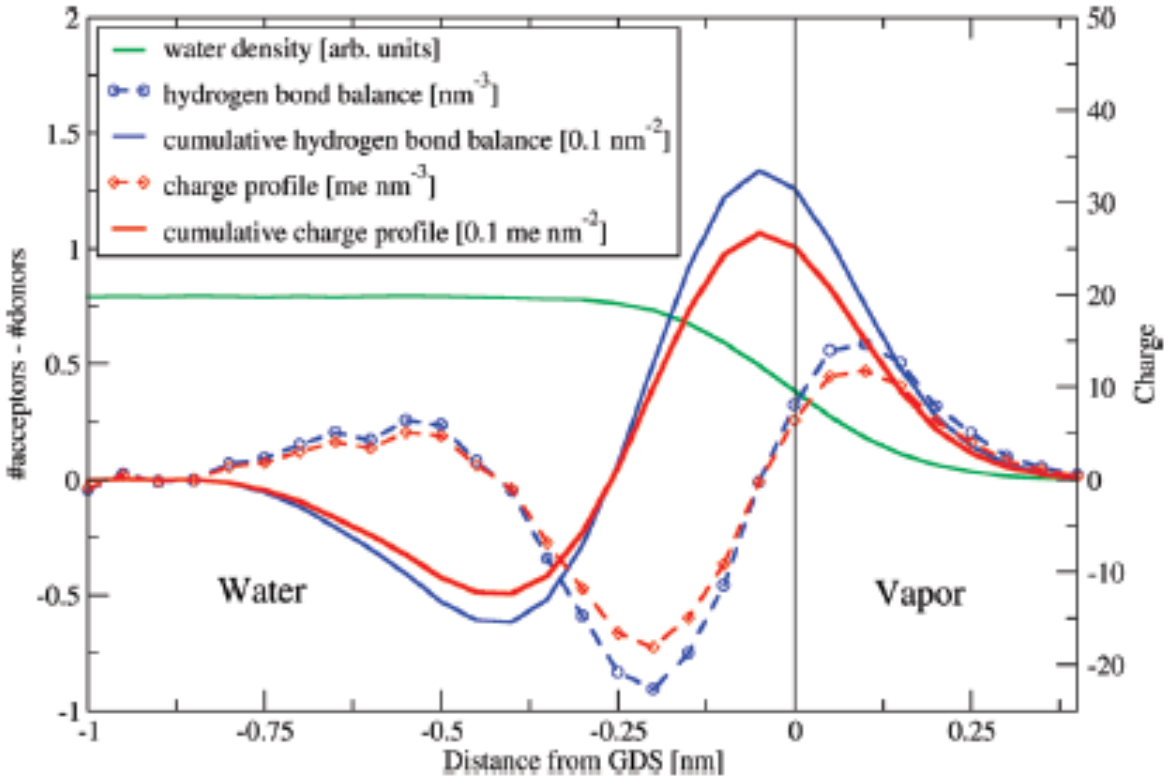

Figure 48: Balance between hydrogen bond acceptors and donors and charge distribution at the air water interface region, the GDS stands for Gibbs Dividing Surface and is the hypothetical line that divides the gas region from the liquid region (Vacha et al., 2012).

From Figure 48 it can be seen that the negative charge has a peak of -1.3 me (milli electron charge units) per nm^2 of surface area at a point roughly 0.4 nm away from the interfacial dividing line. If each charge unit were accounted for by a hydroxide ion, this would translate to approximately 0.0013 hydroxide ions per nm^{-2} at this point. Taking into account the rate of diffusion of each of the chemical species as they travel through the air water interface (and assuming that this is constant, and in one direction only) the extra ion concentration can be added to that already present in water in a +SIN(t) function or +PI()*t type function. Density will be neglected for the present but for future simulations using this model one must bear in mind that the density also changing.

A model for the surface was drawn by creating two stepwise functions and setting the rate constants for the creation of OH- and H+ ions from an "imaginary" species as the derivative of the effective expected "concentration profiles" of OH- and H+ (which in turn were taken from the charge profiles).

The following function should begin when the particles are expected to enter the charge zone, and end when they expect to leave it. The function should simulate one half of a sine wave, peaking at a charge of -1.3 me. The charge difference from one time step to the next is then given as

$$Q_{Max}\left[\sin\left(\left\{\pi\left[{}^{1}/_{t_{zone}}\right]\right\}t_i\right)\right],$$

where Q_{Max} is the peak charge, t_{zone} is the time taken for a particle to pass from one end of the charge zone to the other and t_i is the time step number.

The time taken to pass through the charge zone at the interface is a function of the length of the charge zone, and the length travelled for the average particle per unit time (i.e. its velocity) which is again a function of the diffusion coefficients of the particles.

Oxygen has a molecular diffusivity of approximately 2×10^{-5} $cm^2\ s^{-1}$ (20 $nm^2\ s^{-1}$) in water (Han & Bartels, 1996) meaning that the diffusion through the interface would be on the order of milliseconds and microseconds. The peak of negative charge begins in the interface at about -0.25 nm from the GDS and ends at about -0.75 nm from the GDS. Thus an oxygen molecule travelling through the interface at around 20 nm s^{-1} would travel through this in 0.5/20 = 0.025 seconds. From its frame of reference, the oxygen molecule would experience a change in concentration of OH- ions with time of:

$$[OH^-] + \left\{[OH^-]_{Max}\left[\sin\left(\left\{\pi\left[{}^{1}/_{0.025}\right]\right\}t_i\right)\right]\right\},$$

where $[OH^-]_{Max}$ is the peak concentration of OH^- ions. It would then experience an equal variation in the H+ ion concentration with time, as the charges must balance, which is given as:

$$[H^+] + \left\{[H^+]_{Max}\left[\sin\left(\left\{\pi\left[{}^{1}/_{0.025}\right]\right\}t_i\right)\right]\right\},$$

where $[H^+]_{Max}$ is the peak concentration of hydrogen ions. With only two reactions enabled, the concentration profiles of the OH^- (c_OH_1m) and H^+ (c_H_1p) ions that a particle travelling at constant diffusion rate in one direction through the interface from the vapour phase to the liquid phase would experience, can be simulated.

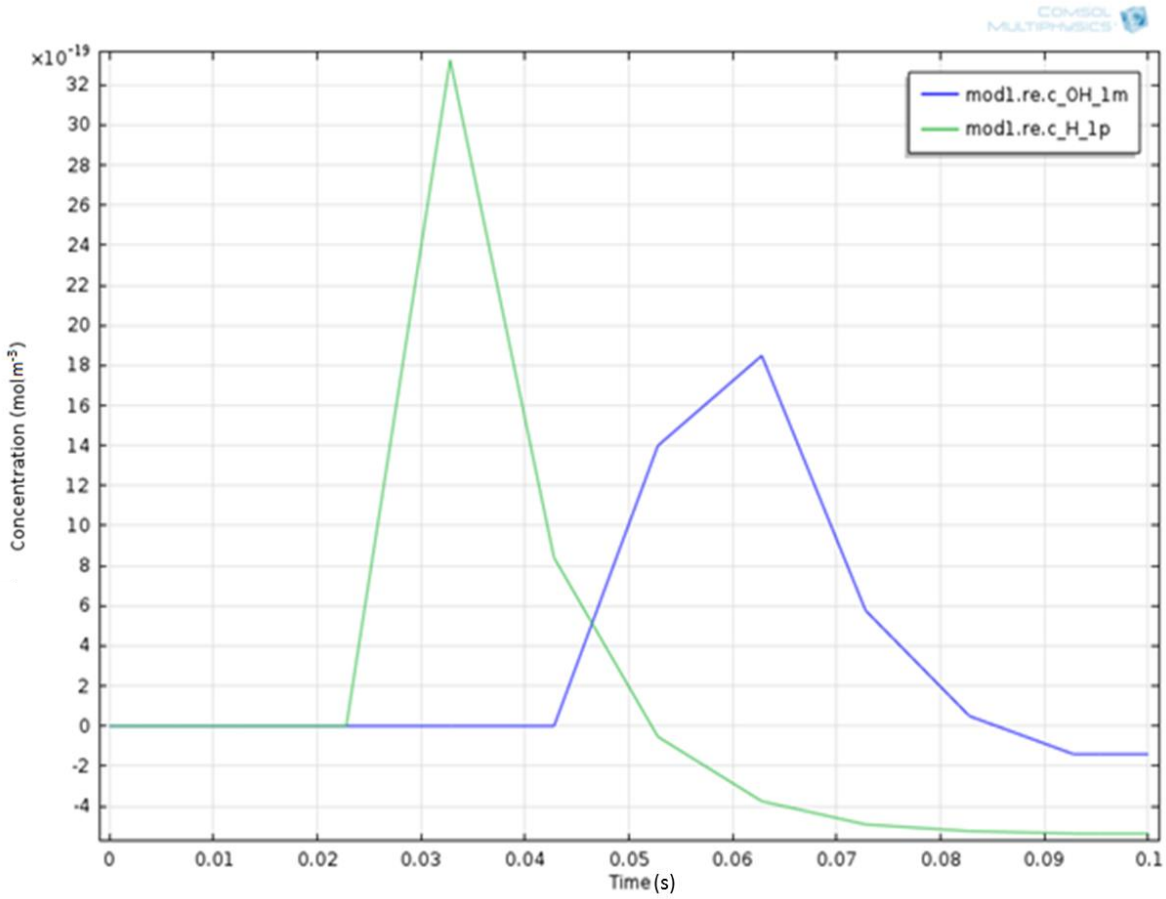

Figure 49: A plot of concentration of species against time for a constant diffusion rate through the air/water interface described by Vacha et al. (2012).

The results of a simple simulation using the above functions to generate OH^- and H^+ are shown in Figure 49, the two peaks can be seen to resemble the distribution of charge suggested by Vacha et al. (2012), in equivalent concentrations of charged species. These reactions can be incorporated into the model as a first step towards a chemical kinetic simulation of the air/water interface. This will be referred to as the Nihoyanagi/Vacha model. Despite the efforts of the author it has not been

possible to remove the slight negative concentration from the simulation, however this should remain known about and improved upon in future versions of the model.

3.6.3 Shen and Ostroverkhov model

The dangling OH bonds (section 3.5.1) could be incorporated into a model, but it is not yet known how ozone might react with these OH groups due to their orientation. Literature searches for data on this found some ab-initio calculations on the stability of different static molecular positions involving ozone and other water species (refs), but no experimental data. As it is not known which orientations occur in reality, more experimental research needs to be done in this area before reaction rates can be reliably proposed.

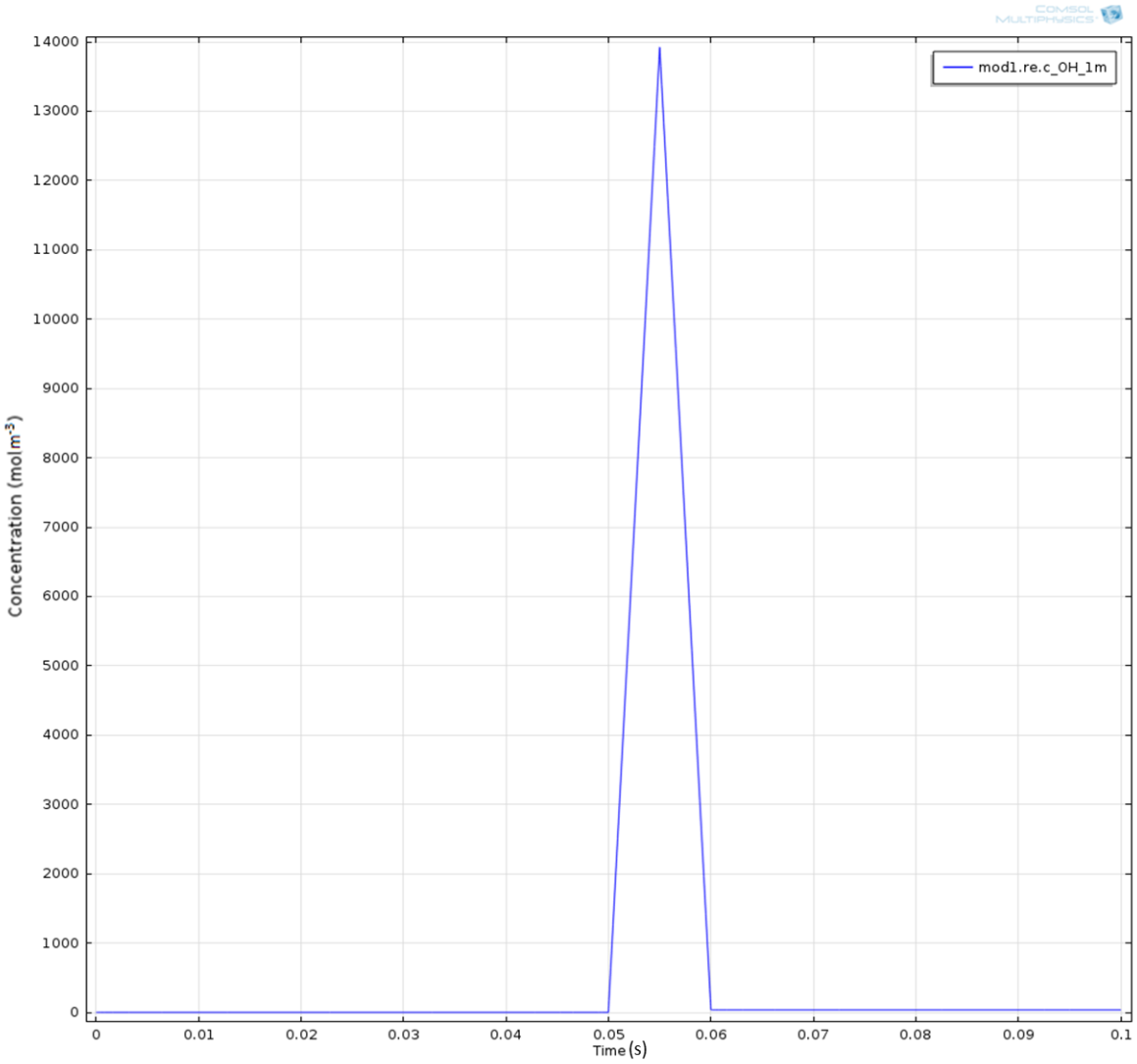

Figure 50: A screenshot of the simulation of the air water interface according to Shen & Ostroverkhov (2006). A single peak of OH^- is present for as long as it would take for an oxygen molecule to diffuse through the depth of the interface.

The interface in this theory could thus be modelled by increasing the concentration of and OH^- ions in one large peak, with the assumption that they will behave as OH^- ions do in solution. The model in the previous section can be adapted by considering the interface to be only one molecule thick, but to give it an extremely high concentration of OH^- ions (25% of the total volume). The concentration would be 13900mol m^{-3}, whilst this seems extremely large it must be pointed out that the concentration only exists in a very small area, and so the other chemical species are only exposed to such extreme interfacial conditions for a very short time. Assuming the same rate of motion as for the Nihonyanagi/Vacha model, this "OH^- pulse" will be assumed to be equal for the time taken for an oxygen molecule to travel the distance of a single water molecule. Since water molecules have an OH bond length of around 1 Å, the interfacial region in this case would be two Å long (0.2 nm). 0.2/20 = 0.01 s.

This concentration should then be multiplied by the predicted volume of interface, to give the additional number of moles of OH- per unit volume in solution. An assumption is made for simplicity that the volume of gas and bulk liquid are equal to simplify the prediction.

3.6.4 Gas species interaction with the surface – droplet skin chemistry – accommodation coefficients

As plasma reactions on the skin of bubbles is a novel concept, kinetics for such processes are extremely hard to find, if not non-existent. One area where such rate coefficients might be found is for reactions on the skin of water droplets in the upper atmosphere, as this is necessary for meterological prediction simulations. There have been some useful kinetic studies of the heterogeneous chemistry of water droplets (Jacobson, 2005) and this chemistry can be extrapolated to the conditions on the air/water interface of a microbubble, as the interfacial processes and importance of surface area are the same.

Rate constants for the formation of liquid species from gaseous species can be found from accommodation coefficients (Ammann et al., 2013).

A basic assumption can be made that due to the fact that the process is a continuous process and therefore non-equilibrium, that there is always a lower concentration of the gases in the liquid phase than in the gas phase (as in Figure 42), and therefore the direction of mass transfer is predominantly into the liquid from the gas, and not the other way round. Therefore it can be assumed that once the gas has been accommodated into the liquid, that its tendency to return from

the liquid into the gas is negligible, and can be ignored for the purposes of simplifying the kinetic scheme.

3.7 Bulk liquid reactions

Efforts were made to find rate constants for aqueous phase reactions of many of the short lived species of the plasma, as there was little data available on these, it was decided to focus on the more long lived oxygen and nitrogen species. Rate constants for reactions of these in water were found from a variety of reliable references (Buhler, Staehelin, & Hoigne, 1984; Buxton et al., 1988; Neta et al., 1988; Staehelin & Hoigne, 1982).

These reactions are invariably affected by the pH and temperature of the solution, and often rate constant data in the tables were only present for one, or two different pH values, and normally at room temperature. Room temperature was assumed for the plasma model gas temperature, and thus most of the temperature dependence of these rate constants would not be an issue. Room temperature was assumed due to the other rate constants used in the model. Some of the rate constants in the model were not functions of any variable such as temperature, and it was likely in this case that room temperature conditions had been used in their measurement. The pH dependence of the k values was such that it did not vary outside of the same order of magnitude, thus compared to the rates and timescales of many of the plasma reactions, these minor variations in the bulk liquid reactions were not as significant as would be the case for a reaction scheme based solely in the liquid phase.

3.8 Full integrated model

The component models of all the previous sections were combined to make a kinetic model of the plasma, interface and bulk liquid reactions (Figure 51).

The model begins with the plasma phase, then the electron energies, electron temperature and reduced electric field are all dropped to close to zero to simulate the afterglow, the interface phase then begins and simultaneously the rates of the gas-liquid processes are increased rapidly to simulate the appearance of the interface. The bulk liquid reactions then follow (Figure 52). The plasma region has a residence time of 10^{-6} s, which based on a reactor of 0.5mm diameter, corresponds to a plasma reactor length of approximately 0.1mm for an air flow rate of 1LPM (Figure 53). The afterglow region has a residence time of 10^{-3} s, equivalent to a distance of approximately 10mm from the plasma to the air/water interface for the same flow rate. The interface region was simulated with a mean bubble diameter of 0.5mm.

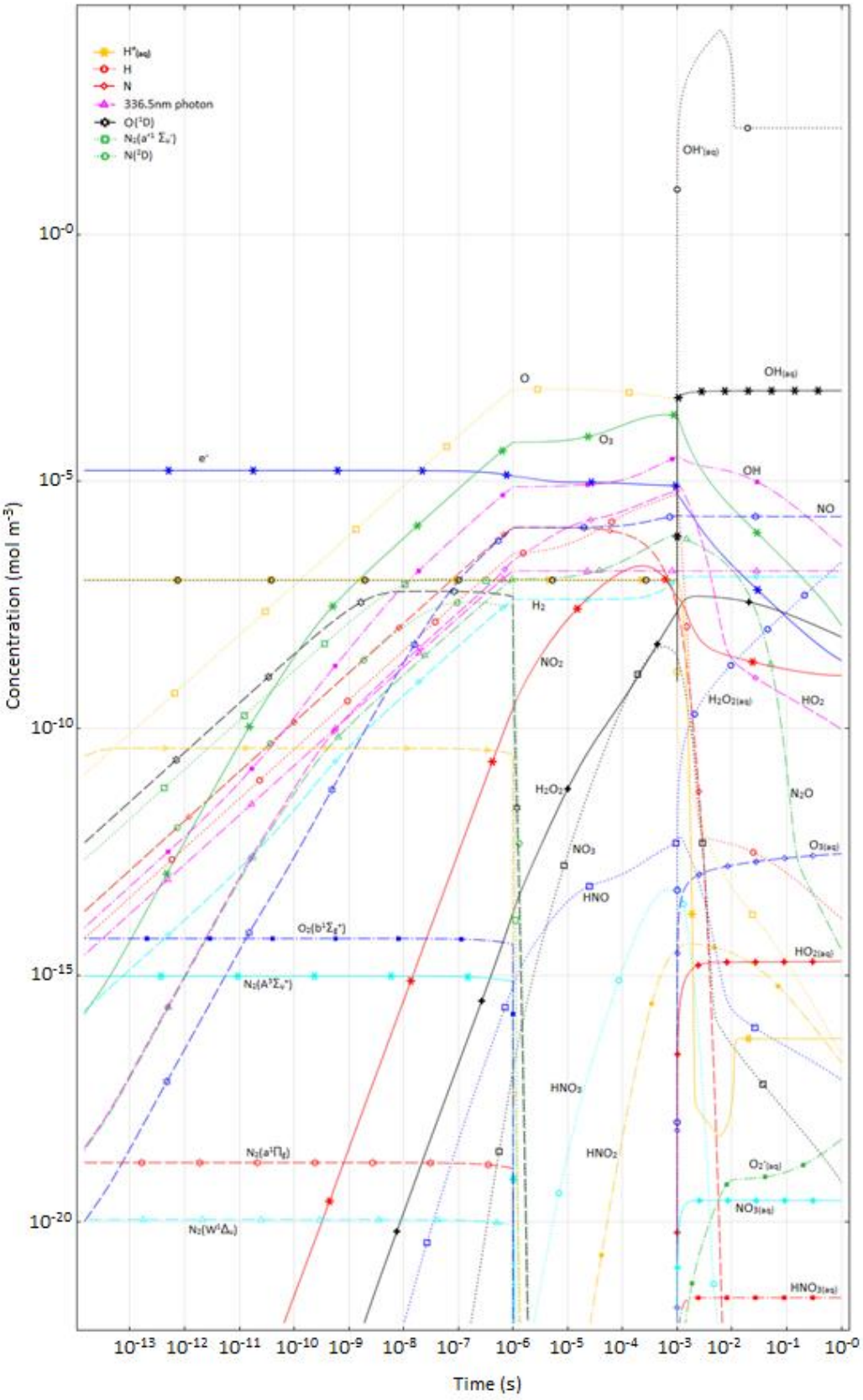

Figure 51: A plot of the time dependent kinetic simulation of the plasma, afterglow, interface and bulk liquid processes. The interface model is based on the Shen & Ostroverkhov interface model.

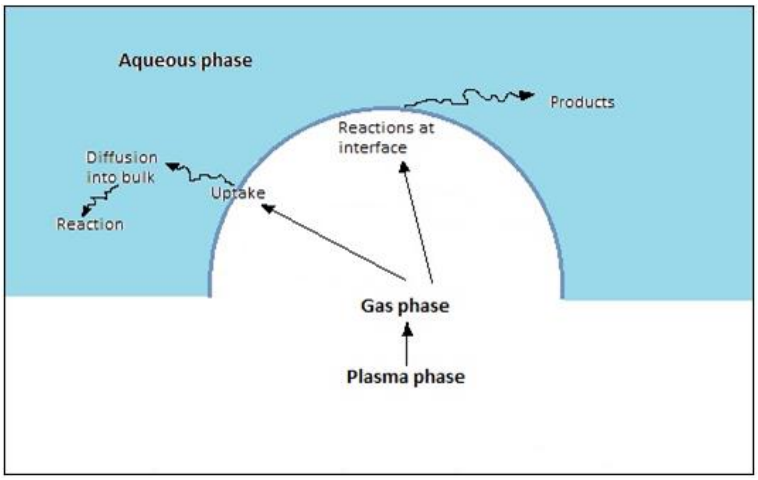

Figure 52: Diagrammatic illustration of the processes considered in the kinetic simulation.

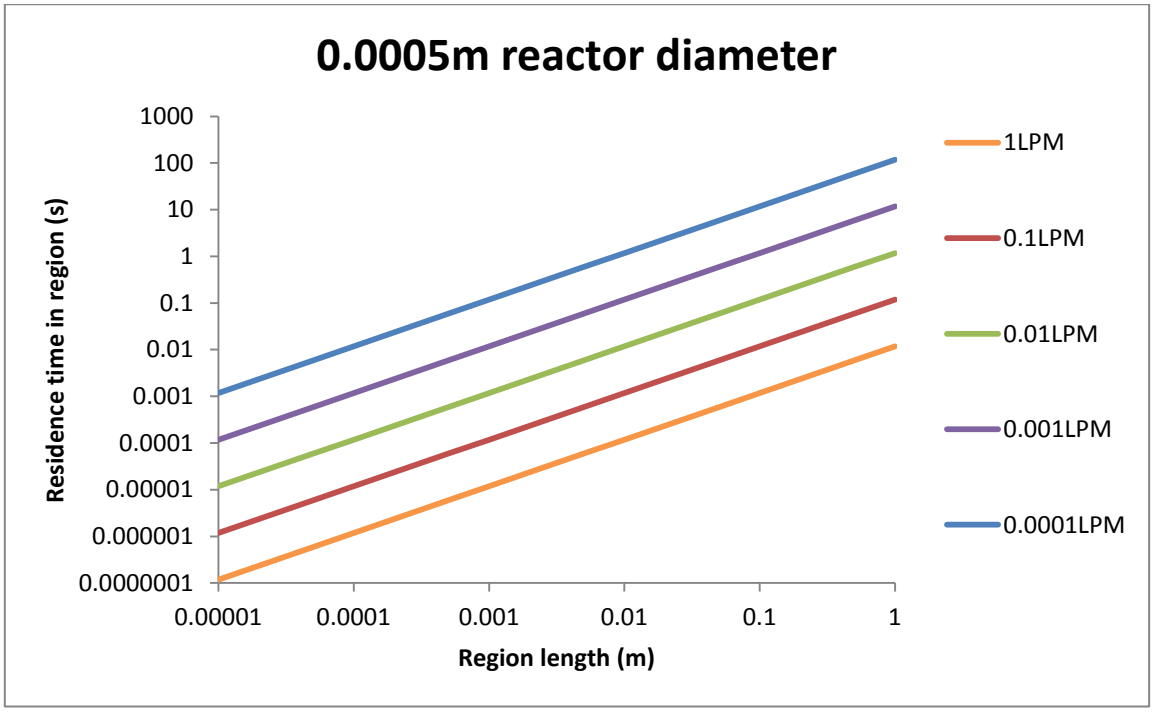

Figure 53: Residence times the regions relative to their lengths for a cylindrical plasma reactor of 0.5mm diameter.

Whilst it is clear that the motion of all the particles will not be linear, the model can be used to predict the general behaviour of the plasma products and the interface. The temperature, electron energy, duration of plasma discharge, time gap between species leaving the plasma and entering the bubble, bubble diameter, and hydroxyl radical concentration of the interface, can all be varied. The model will predict the concentration of many observable species in the bulk liquid phase, the chemical species that are present in the plasma, and also to some extent the intensity of light that

should be emitted from the plasma. All these parameters are extremely valuable in the design of plasma microbubble reactors.

The interface model used was the Shen & Ostroverkhov (2006) model, and interfacial conditions were varied by varying the adsorption and surface reaction coefficients (the rate constants of which were functions of the surface area to volume ratio of the droplets). A plot of the concentrations of some key species over time using the model is shown in Figure 51. The evolution of the excited species and of 336.5nm photons can be clearly seen up to 10^{-6} s where the electron energies are then dropped to background values, the following rapid decrease in the concentration of the excited species marks the afterglow region of the plasma, where the O atom concentration, which is approximately one order of magnitude higher than ozone, begins to decrease. The appearance of the air/water interface can be seen at 10^{-3} s by the extremely rapid appearance of aqueous species, of which the OH radical, due to the instantaneous reaction of O at the interface, appears to be the most prevalent. There is a need for refinement of the model as the concentration of the OH^- ion in solution would have been expected to decrease further after the interface phase.

There were some important points to make for the benefit of the reader. The first is that for the sake of simplicity not all of the results were displayed in Figure 51, therefore some of the chemical species that were playing a part will not be seen on the graph. The electron concentration would seem to decrease, with no positive ion increasing to replace it, but this will have been due to recombination reactions with nitrogen and oxygen ions, neither of which were displayed in Figure 51. Secondly, the hydroxyl radical appears to be constant, implying that it has a much longer lifetime, but the steady value is due to a temporary equilibrium between the destruction of the OH radical and its continued production from decomposing ozone and other reactions. It should also be noted that there was no absolute volume modelled for the bulk liquid, the reaction rates are based on a surface area to volume ratio included in the equations for the rate constants.

3.9 Discussion

The results of the model clearly show that the O atom is formed in higher concentrations than ozone in the plasma. Once the electrons lose their energy, the O then reacts with O_2 to form ozone. Although the interfacial OH^- concentration will accelerate ozone breakdown to form the OH radical, the O atom clearly reacts directly with the air/water interface to form OH radical. Minor amounts of NO_x and N_2O species are also absorbed into the liquid phase, although there may be many unknown reactions on the interface surface which may occur with these species.

The model also does not take into account the fact that there may be higher residence times at the interface, but to include all of this in the model would be outside of the scope of this work. There is data on this from *ab initio* studies. Much of the data presented in *ab initio* studies allows the activation energy of certain processes to be predicted. Another way of looking at it is that the *ab initio* studies, if done correctly, predict with absolute certainty what the energetic behaviour of a process will be. What cannot be known from these studies is whether or not the predicted processes actually occur. This can either be predicted from whichever function is deemed most reliable, or derived empirically.

This model takes into account only the kinetic scheme. There are many other factors to take into account, such as the fluid pattern of the bubble, the geometry of the bubble in the liquid, and temperature and pressure factors relating to oscillations in the bubble size. Suggestions of how the model could form a more complete view of the interactions with plasma at the air water interface are illustrated in Figure 54.

It must also be noted that the model does not take into account any effects that the electric field may have on the orientation of molecules on the interface. Increasing the proximity of the plasma to the bubble inevitable increases the proximity of the electric field to the interface. As the interfacial properties are dependent on the orientation of molecules, the electric field may alter the properties by changing the bond angles. Whether this would have a positive or a negative effect on the process cannot be speculated on at present, more research in this area is needed.

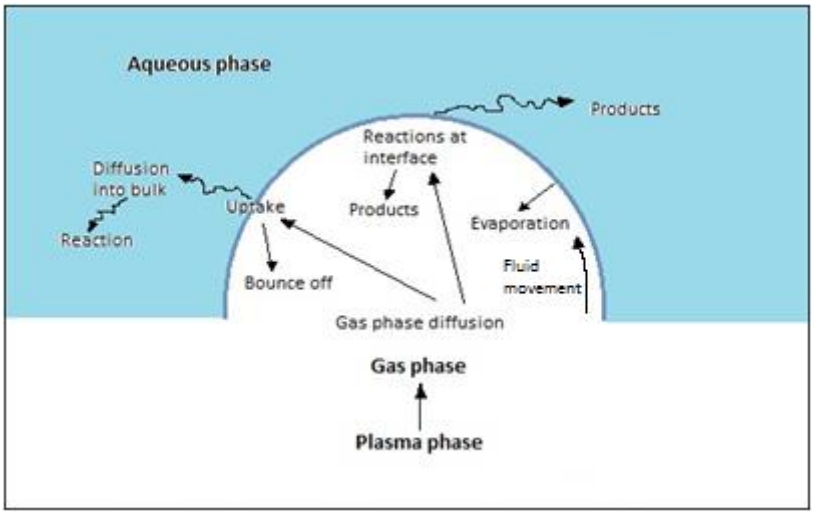

Figure 54: Diagrammatic representation of a more rigorous simulation of the interaction of plasma with the bubble interface.

The model simulation in Figure 51 predicts that there will be free electrons present to react with the interface. Possible reactions of electrons with the interface are not known, but interactions of

hydrated electrons in the bulk liquid have been studied in depth and should be included in future versions of this model.

Future work regarding this model, aside from that mentioned above, should include techniques to observe and verify the interactions at the interface. Spectroscopic observations of interfacial reactions using SFG, for example. Experiments observing any differences in the zeta potential with reactive gases in the bubbles (such as ozone) that might change the hydroxide ion concentration, could also be conducted and would be much more simple than the SFG arrangements. Other spectral measurements that could be employed include those in Buhler et al. (1984).

3.10 Conclusions

- A new kinetic model encompassing the plasma, air/water interface and bulk liquid, comprising over 700 reactions, has been assembled by the author. The sections of this model agree with other simulations in the literature and this suggests that the combined sections can be used with similar reliability to simulate the conditions of a reactor with the combined conditions.

- Sufficient decrease in bubble diameter for the same volume effectively increases the concentration of hydroxide ions in solution for species crossing the air/water interface (Figure 47).

- O is present in the plasma in concentrations one order of magnitude greater than ozone, and a high OH radical concentration is observed with a short time between the plasma and the air/water interface.

4 On the design aspects of a microplasma/microbubble reactor

4.1 Summary

The aim of this chapter is to assemble a compilation of the key principles relevant to the design of a microbubble-microplasma reactor. Whilst there are many texts available on plasmas, there are few which deal explicitly with the construction of plasma reactors. The texts that do exist focus mainly on low pressure thermal plasmas of the type used in nuclear fusion applications. The remainder that deal with the subject of atmospheric pressure plasmas generally do not cover microplasmas to any great extent. As the utilisation of reactive oxygen and nitrogen species has the potential of increasing the effectiveness of plasma reactors, and the combination of microplasmas with microbubbles is means of achieving this, a single reference containing all the important design principles for an integrated microbubble-microplasma reactor would be most desirable. As no such reference existed, the author has attempted it in this chapter.

The chapter begins with examining the electrical principles by treating the reactor as an equivalent circuit. It then addresses the important considerations in the selection of appropriate materials. The following section deals with the bubble formation through a diffuser, and finally the chapter is brought together with a discussion.

The author hopes it will be a useful addition to the body of knowledge on plasma chemical reactor design.

4.2 Electrical aspects

As air is broken down to form plasma by an electric field, plasma reactors are primarily electrical devices. The electrical aspects of a plasma micro-reactor can be considered as independent components in an equivalent circuit (Figure 55).

The most important part of the setup is the power supply, the plasma cannot exist without it, the electrical connections to and from the electrodes and the electrical behaviour of the dielectrics protecting the electrodes are also important to consider. These electrical aspects of the plasma micro-reactor will be addressed in the next few sections.

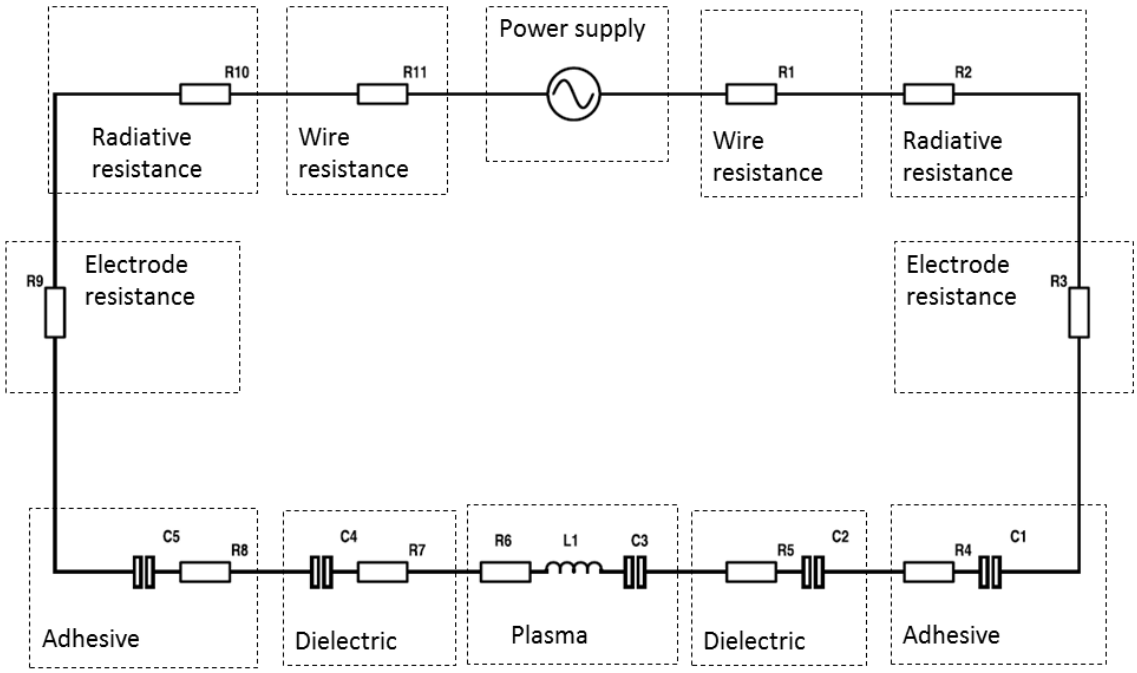

Figure 55: A circuit diagram of the equivalent circuit of a plasma microreactor, taking into account the materials used in its construction. The radiative resistance is an important property for predicting the quantity of electromagnetic interference that will be caused due to the length of the wires and the frequency of the power supply, and the power that this is likely to consume.

The equivalent circuit of the plasma itself is of prime importance. The behaviour of its equivalent circuit is to some extent dependent on its geometry, and in the case of a dielectric barrier discharge, the plasma's equivalent circuit is predominantly capacitative and resistive (Bhosle, Zissis, Damelincourt, & Dawson, 2004; Z. Chen, 2002, 2003; Seunghun, Ho-Cheol, & Gon-Ho, 2009; Singh & Roy, 2007). As the DBD configuration is two parallel plate electrodes, the inductance would be small due to the absence of inductive loops.

It is inevitable where charged particles are in motion that they will create magnetic fields around them, however small, and inevitable that these fields should affect the movement of particles around them. However, the result of this that more kinetic energy is transferred to the particles, and thus the effects are not strictly "parasitic". At the very least they are unavoidable, and also most likely unmeasurable as well.

Other arrangements of plasma reactors (aside from DBD) may experience greater inductive impedance, and could still be classified as microreactors. Therefore the inductive component is included on the diagram in Figure 55.

4.2.1 Power supply signal requirements

The first criteria of a power supply must satisfy is to provide the right voltage. The voltage required to form a plasma is proportional to the inter-electrode distance, and gas pressure, the product of these two parameters makes the similarity parameter "pd". It is desirable for the pressure to be atmospheric pressure, thus the pressure can be set as constant at 760 Torr, and dependence of the breakdown voltage on the gap size only can be plotted (Figure 56).

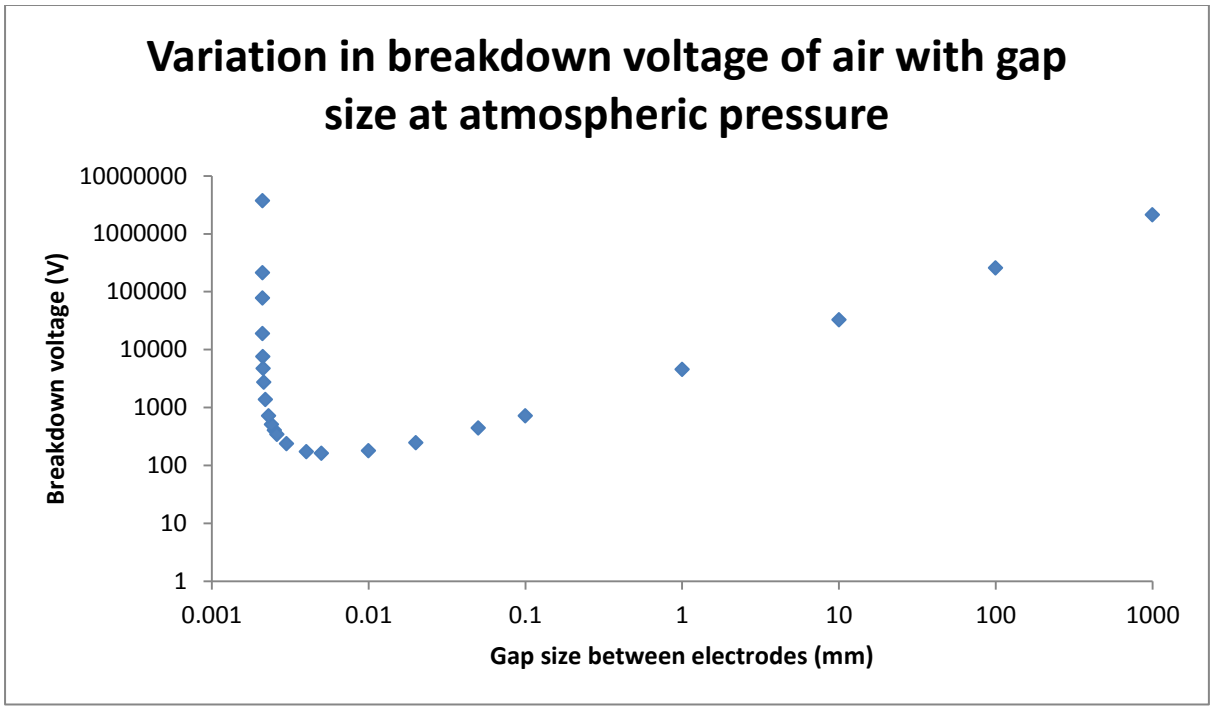

Figure 56: A plot of the Paschen curve for predicting the breakdown voltage from the inter-electrode distance. This function assumes the pressure is atmospheric pressure. The equations for the curve can be found in Fridman (2008).

To prevent "sparkover" (the formation of direct current channels between the electrodes) a dielectric layer covers the electrodes to prevent the flow of direct current and therefore alternating current must be used. The frequency must be high enough that the cycle time is shorter than the time required for the dielectric material to fully charge, otherwise the current available to the plasma will be substantially reduced.

The current draw (once breakdown has occurred) is in the form of many small individual peaks, each one typically lasting only a few nanoseconds. These are due to the formation of individual microdischarge streamers, and in contrast to the gas composition, the pressure, and the electrode configuration the characteristics of the external circuit do not really affect the microdischarge properties. Each microdischarge is more or less identical. The number of microdischarges can be increased, however, with an increase in the power (Fridman, 2008). It should also be mentioned that

at the points at and around the time when the alternating current is changing polarity, the electric field strength will be low and there will be no new microdischarge formation (Baldur Eliasson & Kogelschatz, 1991)(Figure 57). With this in mind, a square wave or sawtooth wave may be the most suitable power supply signal for the plasma with respect to maximising microdischarge formation.

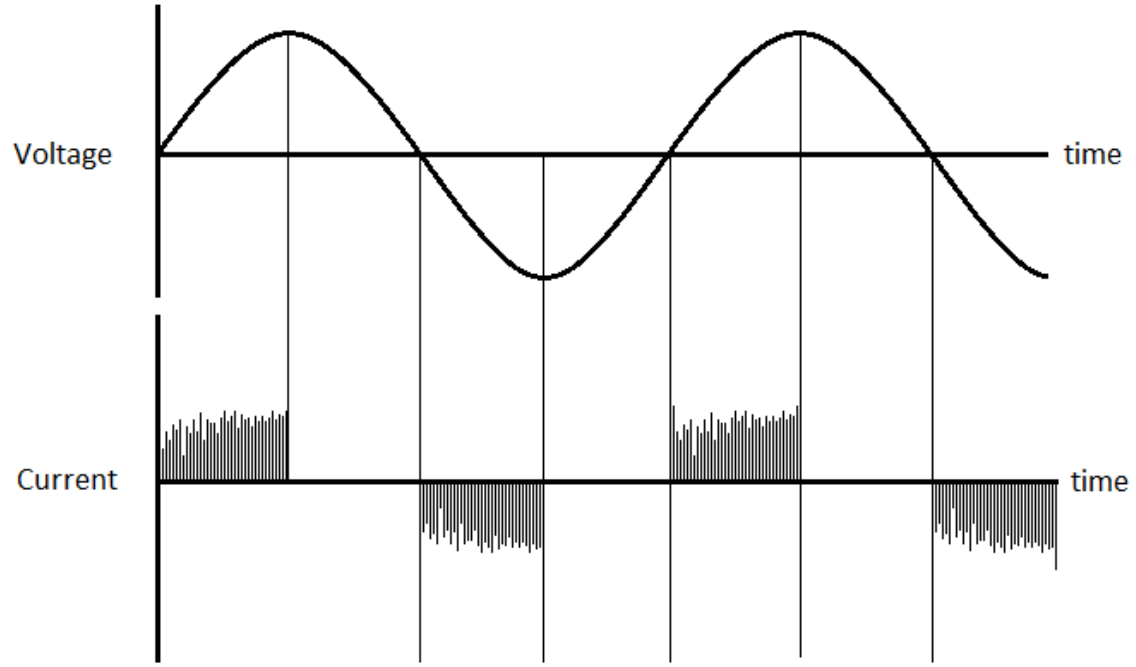

Figure 57: Voltage and current characteristics of a dielectric barrier discharge. Each of the tiny peaks in the current plot corresponds to an individual microdischarge streamer (Baldur Eliasson & Kogelschatz, 1991)**.**

4.2.2 Gap size and tolerances

Higher tolerances produce more suitable sites for streamer formation, and can theoretically increase the number of streamers per unit time for a given power (Fridman, 2008). As the gap size is decreased the tolerances become more significant, as irregularities in the flatness of the electrode surface become greater in proportion to the gap size.

The optimal gap size can be found from the pd ratio and a paschen curve (Figure 56). As the plasmas here are effectively operating at atmospheric pressure, the pressure is kept constant at 760 Torr, and only gap size was varied to draw this paschen curve. It should be noted that the breakdown voltage for a gap size of 1mm was approximately 4.5 kV. The absolute minimum voltage for breakdown at atmospheric pressure occurred at a gap size of 0.005mm (5µm) with a breakdown voltage of approximately 160 V.

Decreasing the gap size reduces the breakdown voltage, but inevitably increases electron collisions with the dielectric materials per unit volume of plasma. The effect of this is to heat up the reactor walls (bear in mind the electrode temperature is extremely high in these plasmas relative to the gas temperature).

An experiment was conducted to test the effects of varying the gap size over the scales relevant to the study. Two parallel plate electrodes with dielectric barriers were positioned facing each other in a plastic adjustable gap size apparatus. The electrodes were connected to the power supply and high voltage probes were connected across the electrode setup. A fibre optic probe connected to a USB spectrometer (Ocean Optics USB 2000 UV/Vis Spectrophotometer) was secured directly above the electrode setup, and aimed between the electrodes in the centre (Figure 58).

A constant 25kHz AC power signal with a peak voltage of around 4-5kV was applied to the electrodes, the signal was analysed using a USB oscilloscope (Pico Technology PicoScope 4424 High Resolution Oscilloscope) and the associated software (Picoscope 6)(Figure 59). Visual observations of the plasma between the electrodes were also made using a digital camera (Figure 60). It was noted that decreasing the gap size increased the number of streamers formed to the point where the plasma appeared to be homogeneous. Decreasing the gap size had the opposite effect and beyond a gap size of around 1mm plasma was not observed.

Differences were observed in the peak voltage signal that was detected by the high voltage probes, rms voltage values were found from the voltage waveforms for each of the gap sizes. The voltage output from the power supply did not change much in response to the gap size change, but there was a slight decrease in the measured rms voltage from the power supply as the gap size was decreased (Figure 61).

The emission spectrum intensity increased significantly with reduced gap size (Figure 61). This increased emission intensity could only have been as a result of increased concentrations of excited nitrogen species, which corresponds to an increase in the mean electron energy $\langle \varepsilon \rangle$.

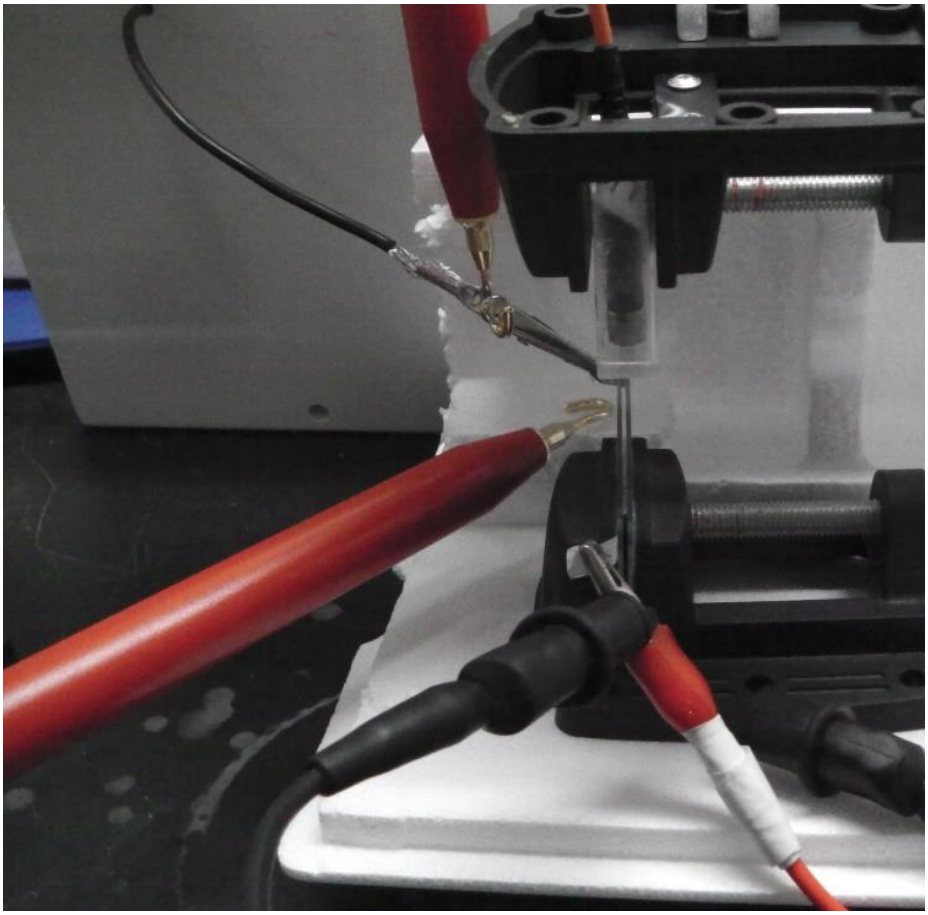

Figure 58: A photograph of the experimental setup for the gap size experiments.

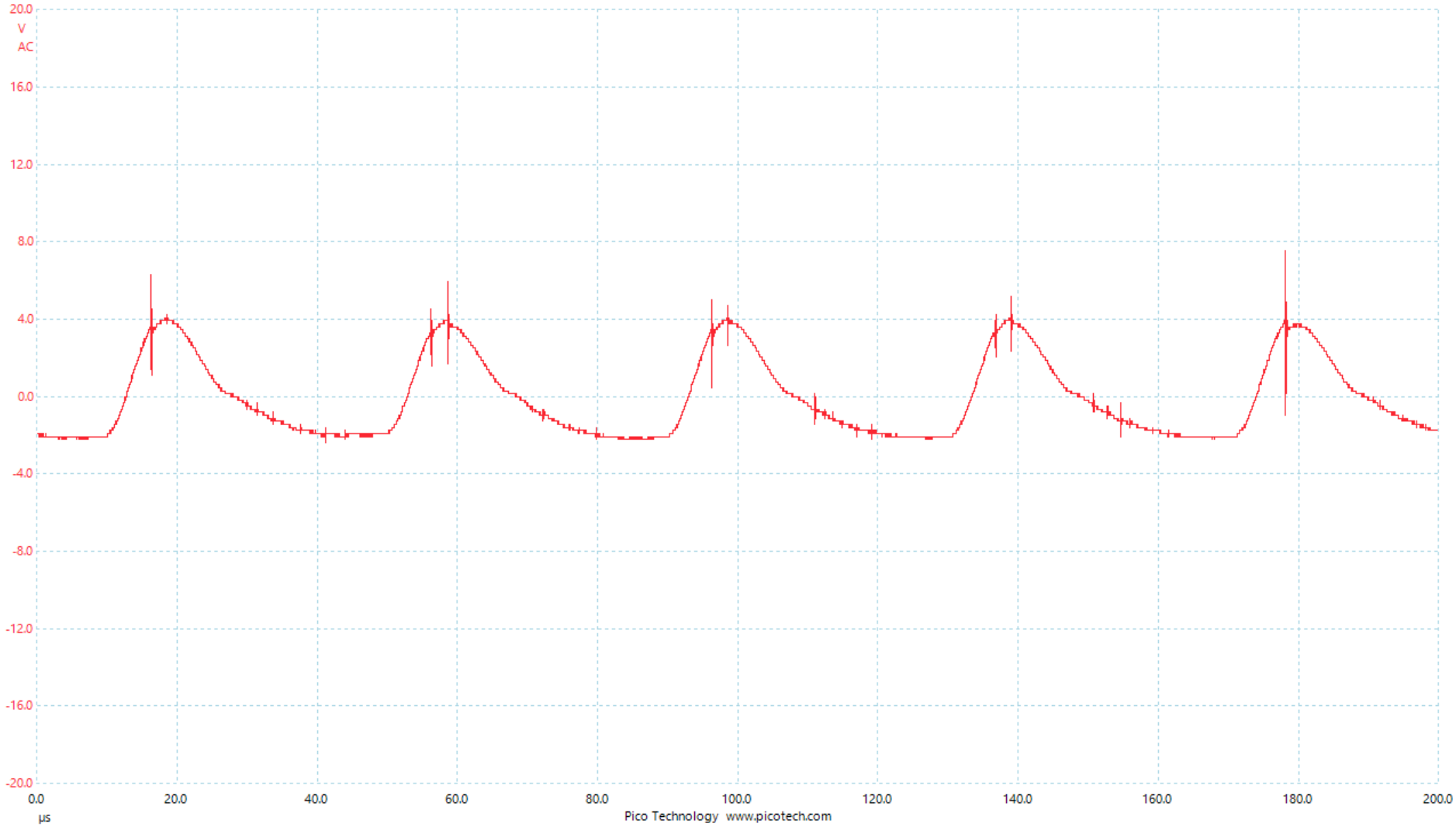

Figure 59: An oscilloscope reading of the voltage waveform of the plasma power supply.

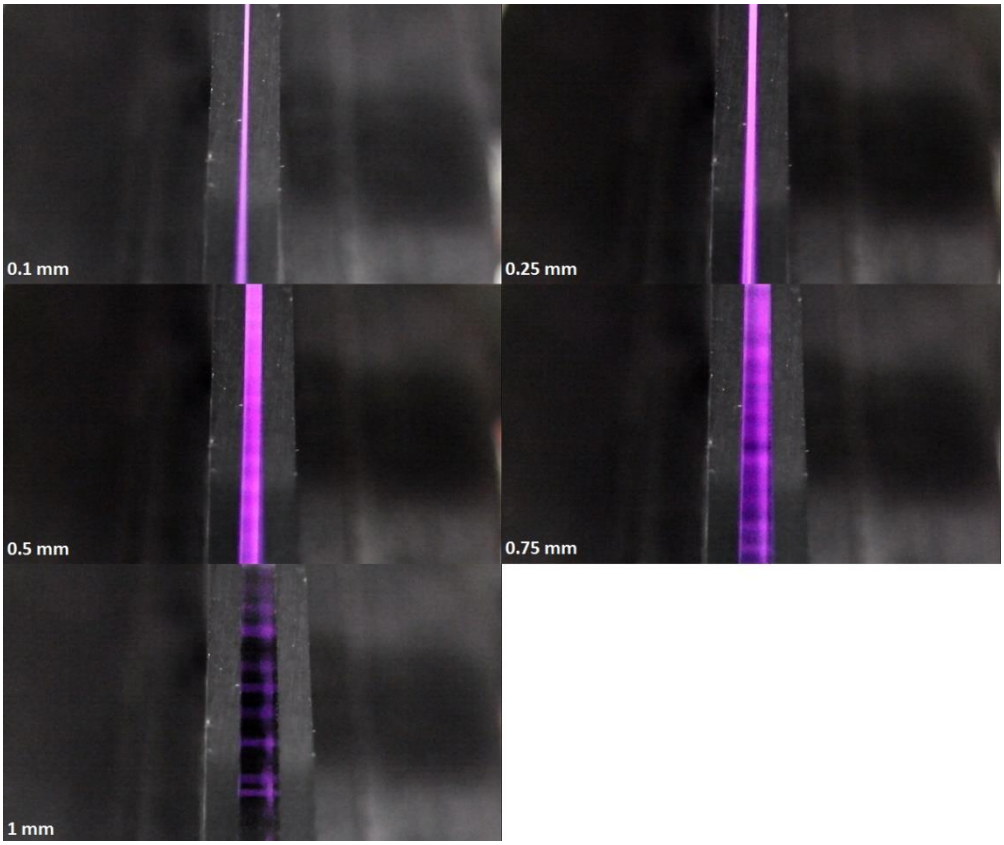

Figure 60: Photographs of the plasma discharges for different gap sizes using the power supply signal in (Figure 59). The values in the bottom left hand corners of each image refer to the distance between the two parallel dielectric plates.

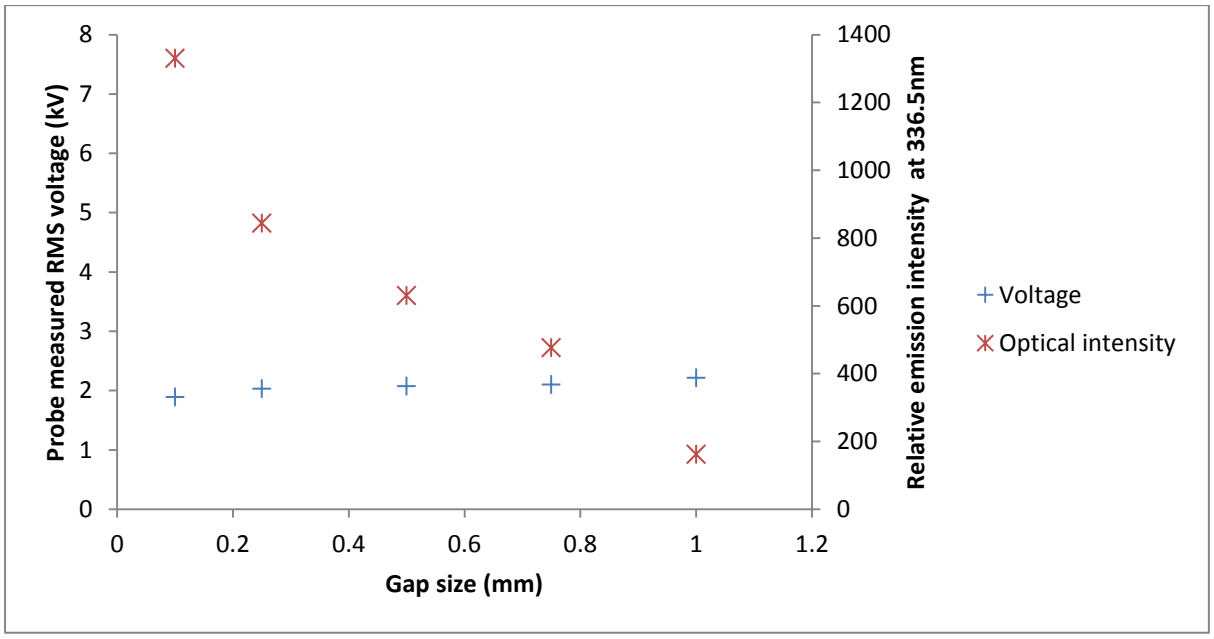

Figure 61: A plot of the effect of the gap size on the emission intensity of 336.5 nm light (obtained from USB spectrometer), and on the rms voltage values from the power supply (obtained from USB oscilloscope).

4.2.3 Conductivity of the cables and electrodes

Due to the high voltages involved in the plasma, it is important to know the properties of the electrical conductors used. Losses will inevitably occur due to resistive heating, even in materials of high conductivity, and the extent of these losses and the amount of heating that will occur must be considered. Resistive loss can be estimated by the simple resistance equation

$$R = \frac{\rho L}{A},$$

where R is the resistance, ρ is the resistivity, L is the length of the wire and A is the cross sectional area of the wire. Note that resistivity is the inverse of conductivity

$$\sigma = {}^{1}/_{\rho}\,.$$

4.2.4 Radiative resistance of the cables

Due to the necessary high frequency of the alternating current, the wires from the power supply to the plasma effectively behave as a radio antenna, and emit electromagnetic waves. This constitutes a power loss through the wires, but also causes electromagnetic interference of other electrical devices, which can lead to problems. The energy lost, and thus the relative strength of the EM interference, can be estimated from the following frequency dependent relationship:

$$R_{rad} = 80\pi^2 \left[\frac{dl}{\lambda}\right]^2,$$

where R_{rad} is the radiative resistance of the wires, d is the wire diameter, l is the wire length, and λ is the wavelength of the AC signal. This relationship assumes the cables to be a Hertzian Dipole (reasonable for a simple estimate of radiative loss due to the wires).

4.2.5 Dielectric barrier electrical behaviour

The dielectric layers covering the electrodes can be treated as capacitors in series with the plasma (Figure 55). Capacitors prevent the flow of direct current, but also effectively store charge under the influence of an electric field. This charge can then be released if the polarity of the electric field is reversed. The charge stored by a capacitor is given by its capacitance, which can be calculated from the following relationship:

$$C = \frac{k\varepsilon_0 A}{d},$$

where k is the dielectric constant, A is the area of the plates, d is the distance between the two electrodes (equal to the thickness of the dielectric in a capacitor, as the two electrodes are directly in contact with it), and ε_0 is the permittivity of empty space (8.854 * 10^{-12} F/m).

When capacitors are placed in series, the total capacitance is different from the sum of the individual capacitors. In the equivalent circuit of the plasma reactor, the dielectric plates are in series with the plasma, thus the following relationship applies:

$$\frac{1}{C_{total}} = \frac{1}{C_1} + \frac{1}{C_2} \ldots + \frac{1}{C_n}.$$

In storing a quantity of charge per cycle, the dielectric effectively impedes the flow of alternating current to some extent. The extent to which it does this is dependent on the frequency and on its capacitance as follows:

$$X_c = \frac{1}{2\pi f C},$$

where f is the frequency of the alternating current signal, and X_c is the capacitative reactance. The capacitative reactance of the dielectric layer makes up one component of the impedance of the plasma reactor. As this is a changing quantity, the power supply must be designed to adjust its own impedance in accordance with the plasma reactor, if the reactor is to be energy efficient. The impedance, Z, is given by

$$Z = \sqrt{R^2 + (X_L - X_C)^2},$$

where X_L is the inductive reactance, and R is the resistance of the circuit. When the capacitor charges, a certain proportion of the energy that is stored is lost as heat. In calculating the efficiency of the plasma reactor it is useful to be able to estimate the quantity sequestered by the dielectric material for a given electric field state. The energy lost in the capacitor is given by the effective series resistance (ESR):

$$ESR = \frac{DF}{2\pi f C}$$

where DF is the dissipation factor, which can be estimated from the ratio of the permittivity to the resistivity, however experimentally determined values from the suppliers of dielectrics will be more reliable. It must be borne in mind that the dielectric constant is also temperature dependent, but the effect of temperature on the dielectric constant is different for each material, and must be considered separately.

In identifying appropriate dielectric materials, it is worth bearing in mind about exactly how the dielectric materials "store" charge under the influence of an electric field. The electric field polarizes the material of a dielectric by orienting its molecules' dipole moments. Electrons in conductive material have a great freedom of movement. Whereas electrons in insulative materials can also move but have very limited movement. Small movements of charge in an insulator in response to an electric field is known as polarization, which can take the form of either stretching or rotation.

It is worth bearing in mind that, generally speaking, polar molecules (such as water) can be more strongly polarized than non-polar ones (such as nitrogen), as the former tend to both stretch and rotate, whilst the latter can only stretch. Once in their polarized states, the insulators can remain so for varying lengths of time (hours to centuries, depending on the material).

4.2.6 Plasma conductivity

Some sets of parameters are useful to know for plasmas, and can be estimated from knowledge of the discharge. Important for the calculations of the equivalent circuit is the plasma conductivity which is given as

$$\sigma = \frac{n_e e^2}{m v_{en}},$$

$$\sigma = 2.82 \times 10^{-4} \frac{n_e(cm^{-3})}{v_{en}(s^{-1})}, ohm^{-1} cm^{-1},$$

where v_{en} is the frequency of electron-neutral collisions, e is the charge on an electron, m is the mass of an electron and n_e is the electron number density (Fridman, 2008).The power transferred to the plasma from the external electric field is referred to as Joule heating and can be calculated from

$$P = \sigma E^2 = \frac{n_e e^2 E^2}{m v_{en}},$$

where E is the electric field strength. These parameters can be estimated from literature values, or from kinetic modelling but it must be stressed that the conditions in the plasma are always changing and that such predictions may well differ from what is observed in reality.

4.3 Materials aspects

Whilst efficiencies can be improved of the component parts in the plasma microreactors, it is inevitable that heat will be evolved, and the response of the materials to this heat is important to know for the design of future reactors.

To decide which materials to select, one does not really need to know which direction they will expand or contract into, but only to what extent expansion or contraction will occur in response to thermal and mechanical/electrical stimuli. Thus extensive modelling is not necessary for this materials section, as long as the dimensions of the reactors are relatively simple.

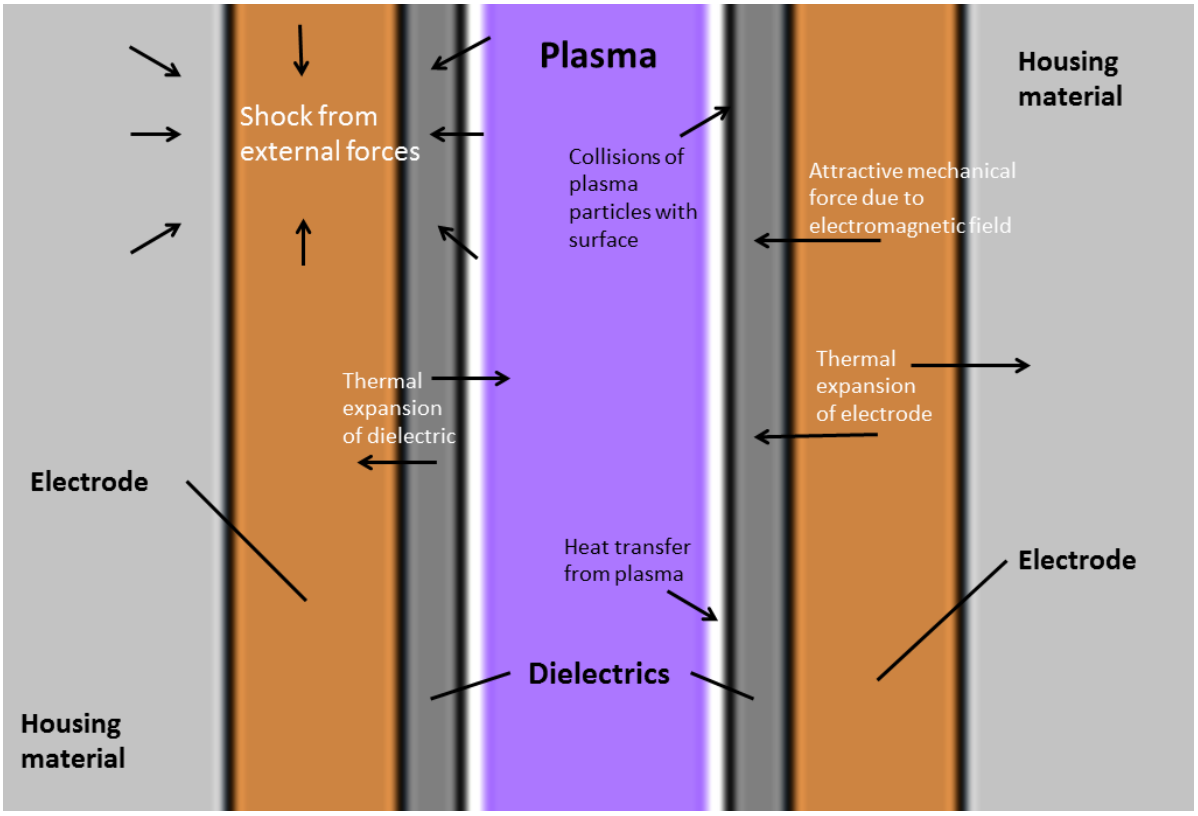

Figure 62: A diagram to show some of the different physical forces at work on the plasma micro-reactors during their operation.

The main source of heat in the system is from collisions of the accelerated electrons with the dielectric walls. Estimation of the heat transfer from the plasma is difficult due to constantly changing conditions which are specific to the plasma and reactor. As can be seen in Figure 60 and Figure 61, reducing the gap size for the same power signal increases the number of streamers formed per unit time, each streamer terminating with electron collisions onto the dielectric surface. Smaller gap sizes also mean more wall area per unit volume of plasma, which will inevitably mean that more heat will be transferred from the plasma to the dielectric surfaces for the same power signal than for larger gap sizes.

The consequence of this are that a lot of unwanted heat is inevitably generated in microplasmas, thus the response of materials to heat must be taken into account in any design.

4.3.1 Mechanical properties of materials

Different materials will undergo changes in volume to varying degrees upon receiving and releasing heat. The extent that they do this is quantified using their thermal expansion coefficients.

The electric field also acts as a source of stress on the electrode and the electrode in turn puts stress on the dielectric layer, and on any bonding material between them. To avoid material fracture or deformation, it is important that the electrode and the dielectric material have similar Young's Moduli.

Any material failure in the dielectric layers will result in sparkover between electrodes. Arcing occurred at the weakest points of the dielectric materials due to material failure whenever the power was turned too high in the industrial field trials, and has been observed in the laboratory many times (Figure 63) and at least for the first stage of the field trials, the power had to be kept below a certain point.

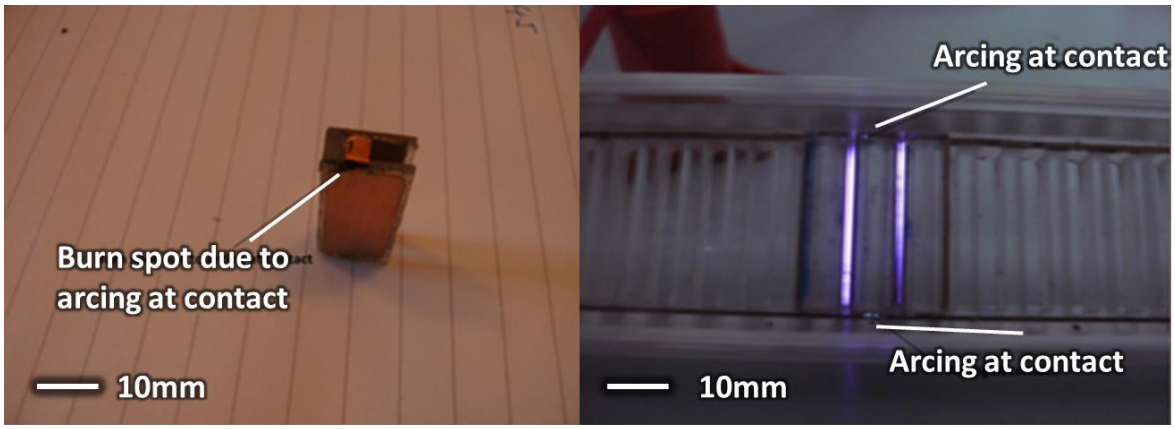

Figure 63: (left) Image of two of the individual plasma reactor glow discharges with evidence of some arcing at the points where they contact the rail, (right) Image of the effects of arcing on the device (courtesey of Muhammad Bashir).

4.3.2 Maintenance of temperature

As well as material issues, the temperatures involved can also affect the chemistry in the plasma. For example, if ozone generation is the aim, then the temperature must be controlled due to the strong temperature dependence of the ozone destruction rate. Figure 64 shows a variation in the rate of ozone thermal decomposition over a range of temperatures and initial ozone concentrations as per

$$\tau_{O_3} = \frac{5 \cdot 10^{-18}}{\alpha O_3} \cdot exp\left(\frac{14050K}{T_0}\right),$$

(Fridman, 2008)

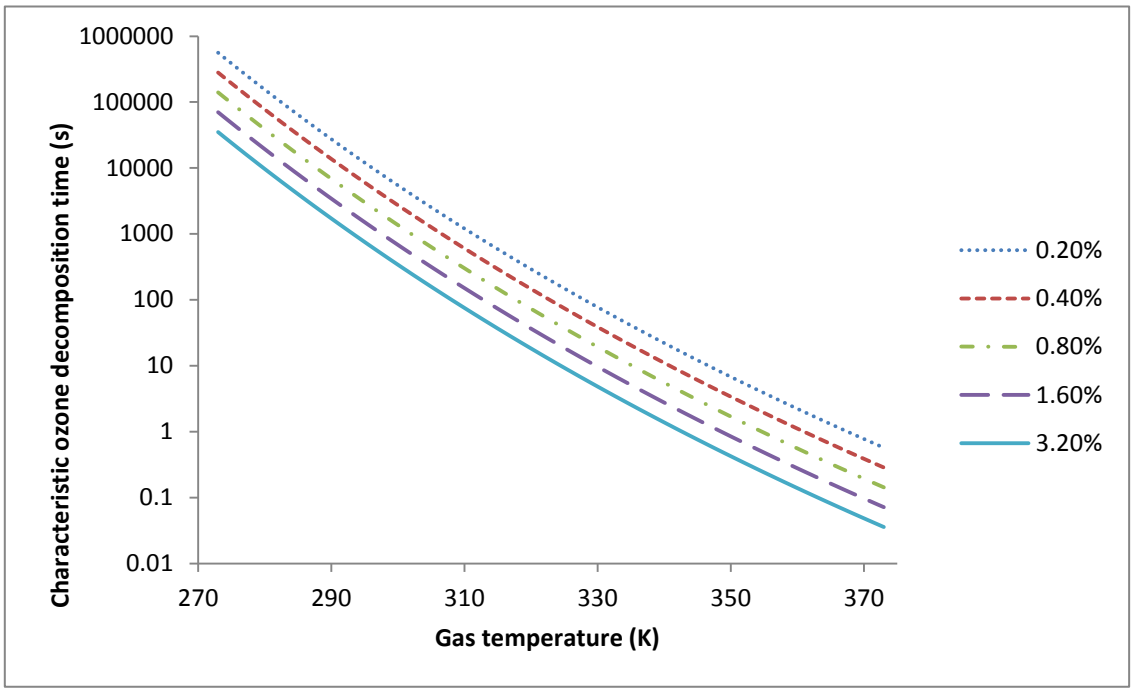

Figure 64: A plot of ozone decomposition with temperature for different concentrations of ozone in air.

Cooling systems can be employed to remove the unwanted heat from the plasma to prevent this build-up, which is given as a function of the dimensions of the reactor (in this case as an equivalent cylinder) and the thermal conductivity of the material

$$\frac{Q}{t} = \frac{kA(T_{hot} - T_{cold})}{d}$$

where k is the thermal conductivity of the material, Q/t is the heat conduction per unit time, A is the area over which heat is conducted, and d is the thickness through which the heat will flow (Bird, Stewart, & Lightfoot, 2002). One of the benefits of small reactors here is the increased rate of heat removal.

Maintenance of temperature can be achieved either by external cooling of the electrodes, cooling of the air supply, or natural cooling by alternating off and on of the power supply to allow the dielectric surface time to cool.

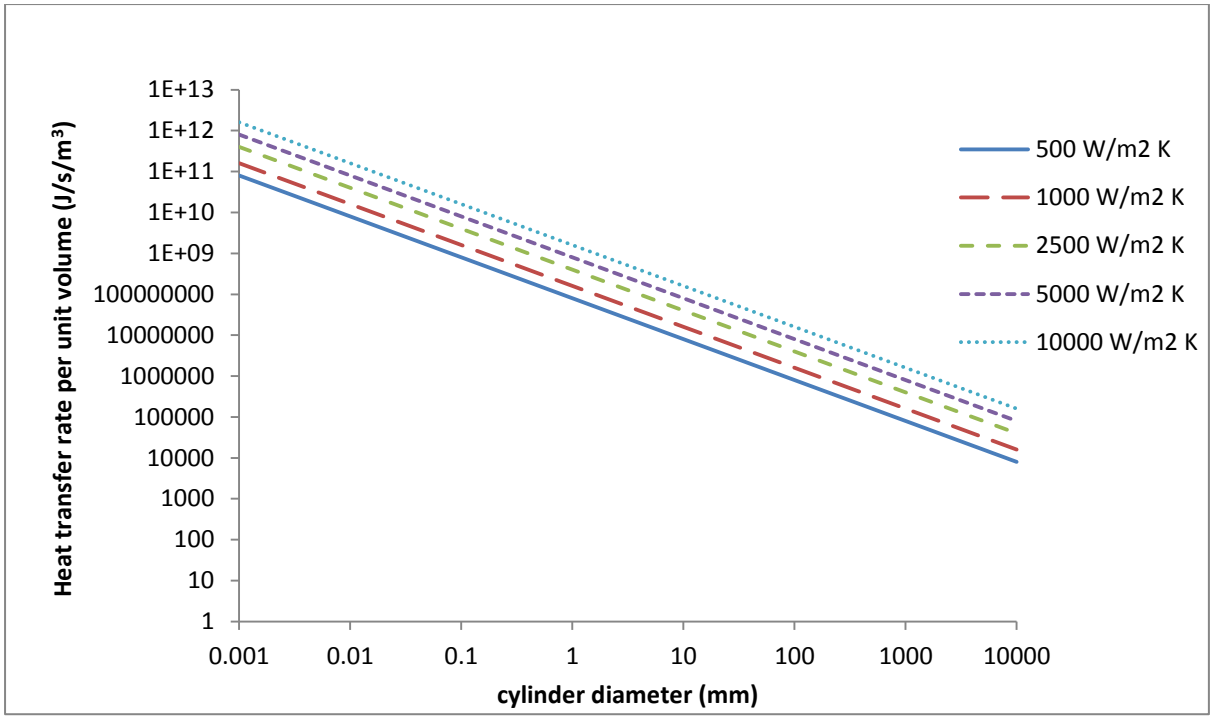

Figure 65: A plot to show the effect of the diameter on the rate of heat transfer by convection from a cylinder for a range of values of heat transfer coefficients.

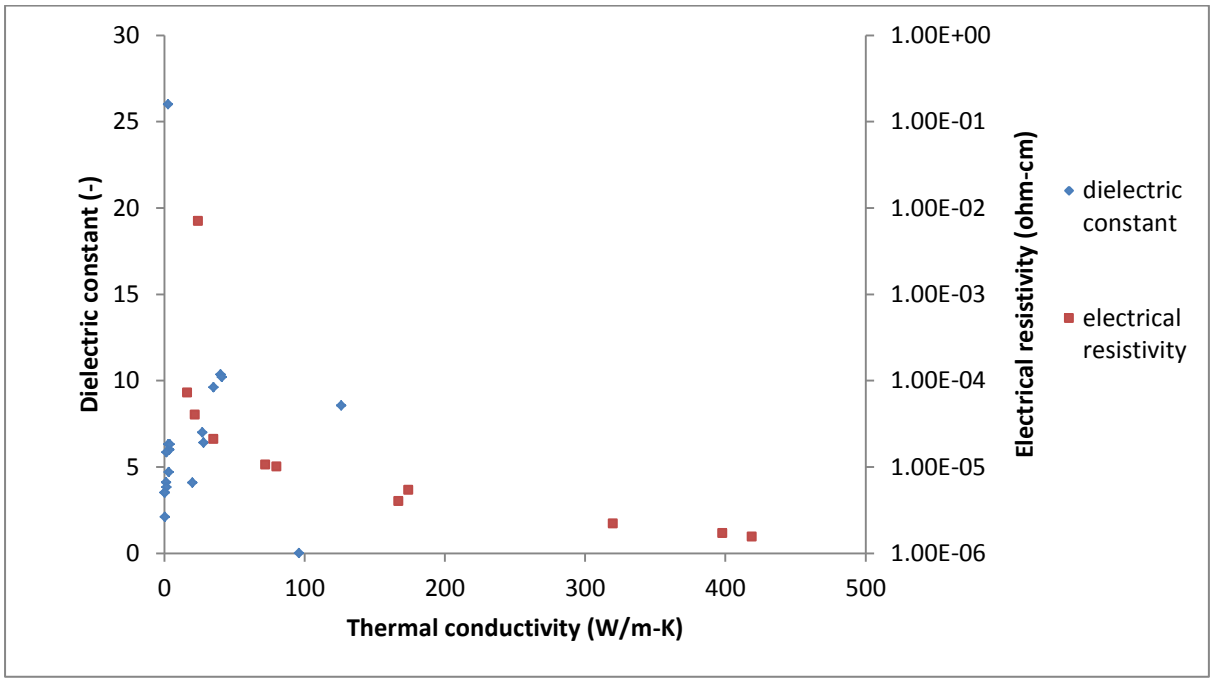

Figure 66: A plot of thermal conductivity against dielectric strength of some common dielectric materials that could be used in the locations shown in Figure 62, and of thermal conductivity against electrical resistivity of come common conductive materials (See Appendix 4).

As reactors are scaled down, the gap sizes scale down accordingly, and on this scales even small expansions can cause irregularities which can lead to inefficiencies, or to arcing. The behaviours of the materials in response to heat should not be ignored.

4.3.3 Adhesive methods of dielectrics to electrodes

The electrodes and the dielectric materials needed to be attached to each other in order to prevent plasma occurring in the small gaps between them. If this was allowed to happen then the plasma in such a confined space would heat up until it reached thermal equilibrium, or arcing point, which would then destroy the electrodes. Selecting the appropriate adhesive involves knowing its thermal properties (thermal conductivity, heat capacity and thermal expansion coefficient), as well as its electrical properties (dielectric strength and conductivity) and of course its adhesive properties. Polymer based adhesives were used for the field trials, but in retrospect, metallization would be the best solution to this, which bonds the electrodes directly to the dielectric, without the need for a chemical adhesive.

4.4 Diffuser aspects

For the Zimmerman method of microbubble formation (see section 1.6.2) a bubble diffuser is required, and this was included in the dosing lance design.

4.4.1 Effect of water vapour re-entrainment into the reactor on ozone formation alone

The air moisture content must be kept to a minimum for ozone formation as water vapour has a negative effect on ozone generation in a plasma for two reasons: the first is that the water increases that the surface conductivity of dielectrics is increased at high humidities, which leads to stronger individual microdischarges causing the negative effects of high temperatures and NO_x poisoning effects. The second reason is that water vapour leads to catalytic ozone destruction due to the formation of both the OH and HO_2 radicals:

$$OH + O_3 \rightarrow HO_2 + O_2$$

$$HO_2 + O_3 \rightarrow OH + O_2 + O_2$$

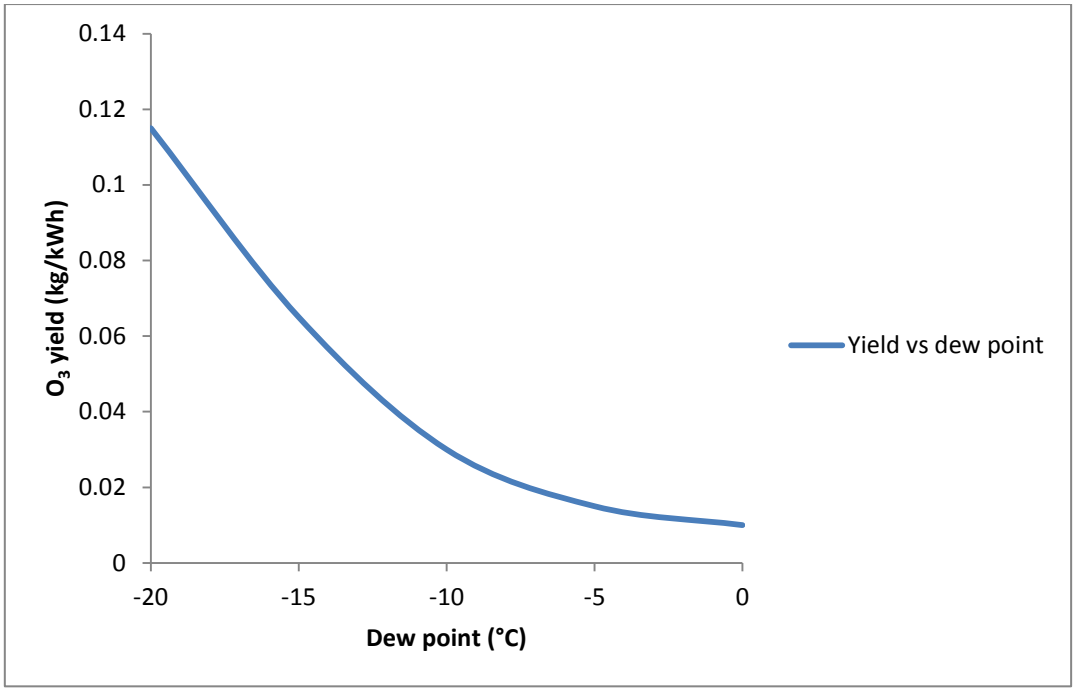

Figure 67: The relationship of ozone yield from reactors with the dryness of the feed air (Razumovsky & Zaikov, 1974).

Air supplied to conventional ozone generators is generally preferred to have a dew point of -60°C or less (Razumovsky & Zaikov, 1974).

The moisture content of air is related to its temperature. The higher the temperature of air, the more moisture it can hold. Thus, when air has a low moisture content its dew point temperature is low, since if there is a very small amount of moisture in the air, the air can hold on to this moisture at very low temperatures. As the air is cooled, the air moisture holding capacity decreases so that when the temperature drops below the point at which the air capacity is equal to the actual air moisture content, some of the moisture will precipitate out (condense) into droplets of liquid water. The point at which this occurs is called the dew point. Measurements of the dew point can be converted into measurements of actual air moisture content by the use of hygrometric tables.

4.4.2 Effect of water re-entrainment into the reactor

Dielectric breakdown of water generally requires much higher voltages than breakdown of air due to the high particle densities. The presence of liquid water in the gap space will therefore inhibit plasma formation at the voltage ranges required for air plasma formation.

Even if water re-entrainment does not completely block the gap, a film of water covering the electrodes can reduce streamer formation by causing the gap size to become irregular along its

length. If the film of water connects with the bulk water above this can also provide an alternative current path if the conductivity of the water is high enough, bypassing the reactor gap space and preventing plasma formation in the gas.

The breakdown voltage for water over length L is given as (Fridman, Gutsol, & Cho, 2007):

$$V \geq \sqrt{\frac{D\rho C_p T_0^2}{\sigma_0 E_a}} \cdot \frac{L}{R_0}$$

Where D is the thermal diffusivity of water, ρC_p is the specific heat per unit volume, T_0 is the temperature, σ_0 is the water conductivity, E_a is the Arrhenius activation energy for the water conductivity, L is the channel length and R_0 is the radius of the breakdown channel (Fridman et al., 2007).

The density of water will vary only between 1000 and 960kg m^{-3} over the range of 377-463K, the specific heat of water also does not vary much over this range, and a value of 4187Jkg^{-1}K^{-1}was used. Data for the Arrhenius activation energy and thermal diffusivities were found in Horne & Courant (1964) and James (1968) respectively.

From Figure 68 it can be seen that the effect of water re-entrainment into the reactor is very much dependent on the amount of dissolved material present in the water. Highly pure water would neither break down to form plasma, nor act as a conductor, but would constitute a strong extra dielectric layer within the reactor. Such highly pure water is not common, and lab bench solutions are more likely to resemble drinking water or sea water, with industrial and waste waters having much higher salinities.

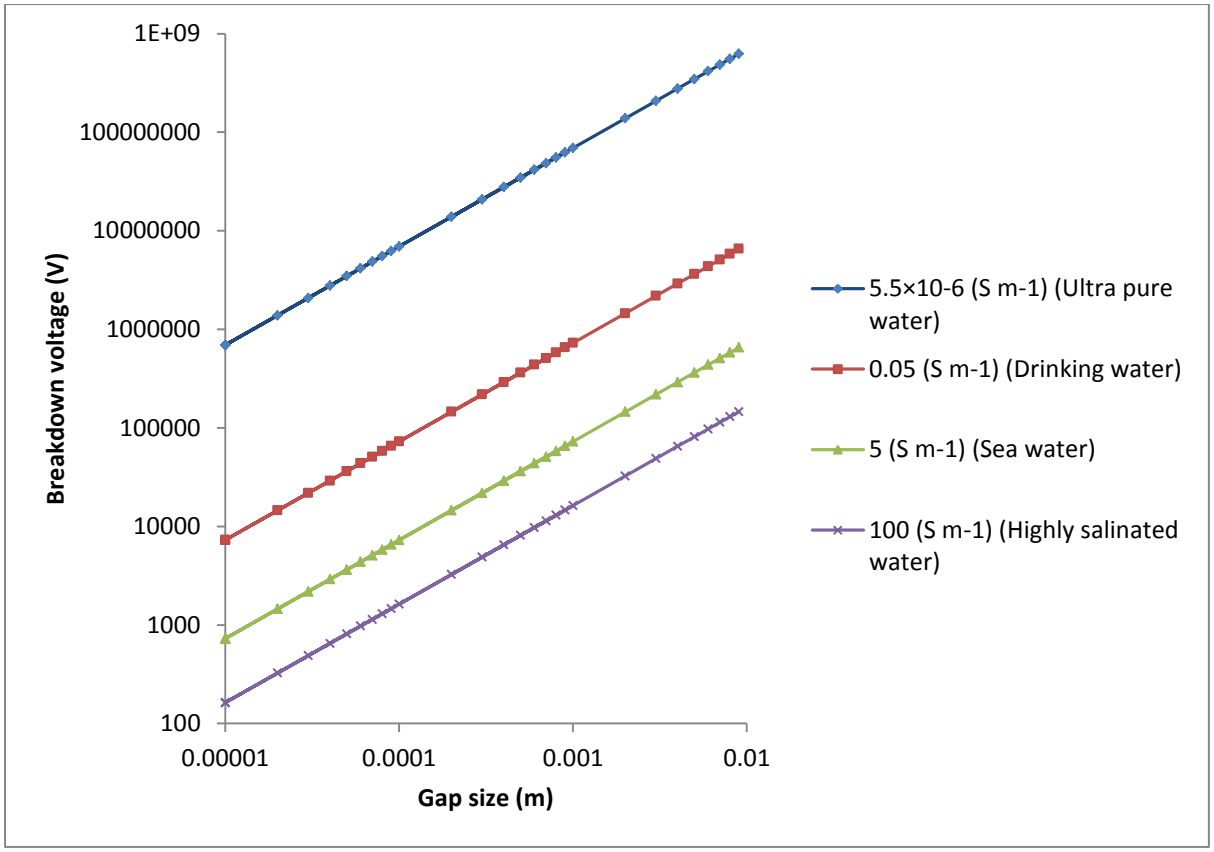

Figure 68: A plot to show the breakdown voltage of water with gap size for a range of water types of different electrical conductivities. The plot can be used as reference of the effect that water re-entrainment will have on the reactor regarding both the likelihood of formation of plasma in the water or water acting as a dielectric, or of the current by-passing the discharge gap and taking an alternative path through the water due to the conductivity.

4.4.3 Diffuser materials

The first diffuser material that was tried for the dosing lance was a diffuser material supplied by HP Technical Ceramics. This diffuser material is a mixture of porous alumina and silica. The ratio of alumina to silica is 8:2 by weight (Figure 69 and Figure 70).

Figure 69: Magnified view of diffuser surface for idea of pore size. (left) magnification at 100x, (right) magnification at 400x, black line of roughly 120µm thickness included for scale.

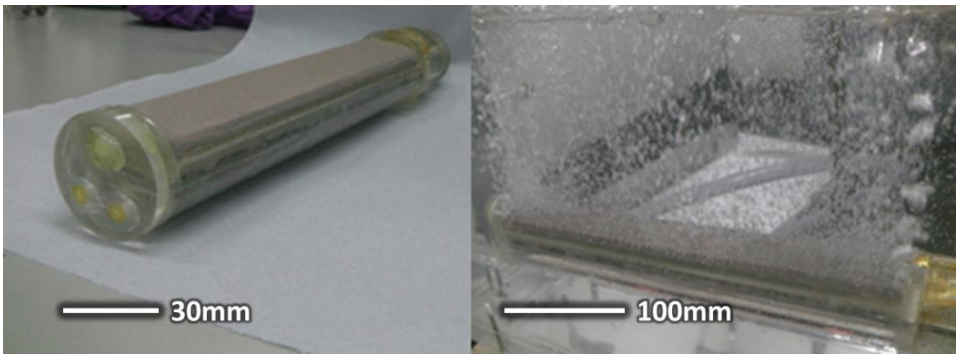

Figure 70: (left) Image of modified flattened top design of the dosing lance diffuser, (right) a photograph of the bubble formation from this new diffuser geometry.

Figure 71: Magnified views of the surface of the point four diffuser, (left) 100x magnification, (right) 400x magnification, the black line of approximately 120µm thickness is included for scale.

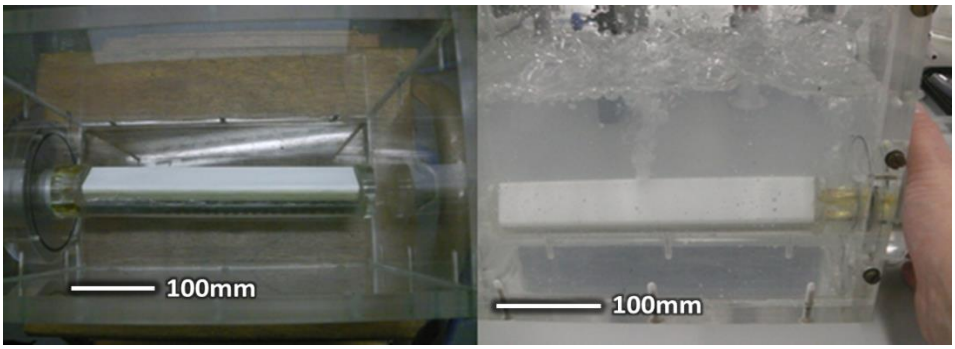

Figure 72: (left) image of the dosing lance with a Point Four diffuser fitted in the place of the original aluminosilicate diffuser, (right) the result of an attempt at blowing bubbles through this diffuser in the lance.

A material from the Point Four company with an extremely small pore size was also tried (Figure 71 and Figure 72). The main problem with the Point Four material was a sealing problem. The sealant would have to be extremely strong, otherwise it would burst. A gauge pressure of 5 bar was observed before the sealing on the lance broke. Due to the effect of pressure on the plasma conditions it was decided that other diffusers should be considered. Other diffuser materials were tried, all with bubble sizes ranging between the point four and aluminosilicate diffuser performances, and with pressures ranging between 0.2-5 gauge pressure.

4.4.4 A note on the effect of the diffuser geometry

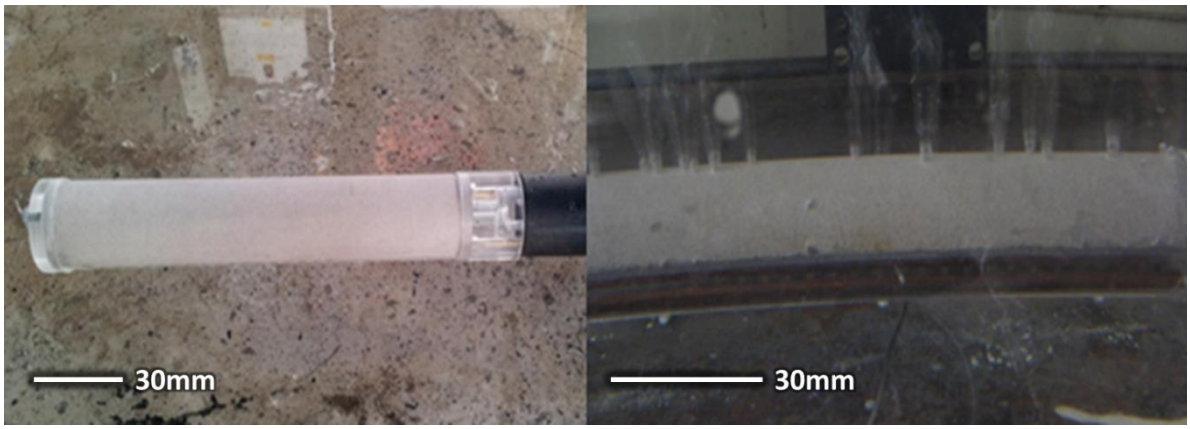

Figure 73: (left) A photograph of the dosing lance diffuser (right) a photograph of the bubble formation regime at low flow rates in the dosing lance curved top diffuser.

The problem with bubble formation in the semi-cylindrical diffuser setup is that the bubbles always preferentially form where the pressure head is lowest. Thus one of the problems encountered with dosing lance was that the bubbles preferentially formed at the top of the diffuser, where due to a slight difference in head, the pressure above the diffuser was slightly lower at this point. Bubble formation may have been enhanced by some of the naturally occurring surfactants in the wastewater, but this could not be observed due to the low visibility of the water. Flat diffusers were found to give a much more even bubble formation.

4.4.5 Microbubble Formation pressure

If bubble formation is done using a diffuser then the pressure required to blow air through the diffuser must be considered, as this will have an effect on the breakdown voltage. The pressure required to blow air through the diffuser is in part dependent on the height of water above the diffuser, but the range of pressures used in the lab to blow air through diffusers was between 0-5bar

gauge pressure (1-6 bar). The effect of pressure on the plasma breakdown voltage over this range can be seen in Figure 74.

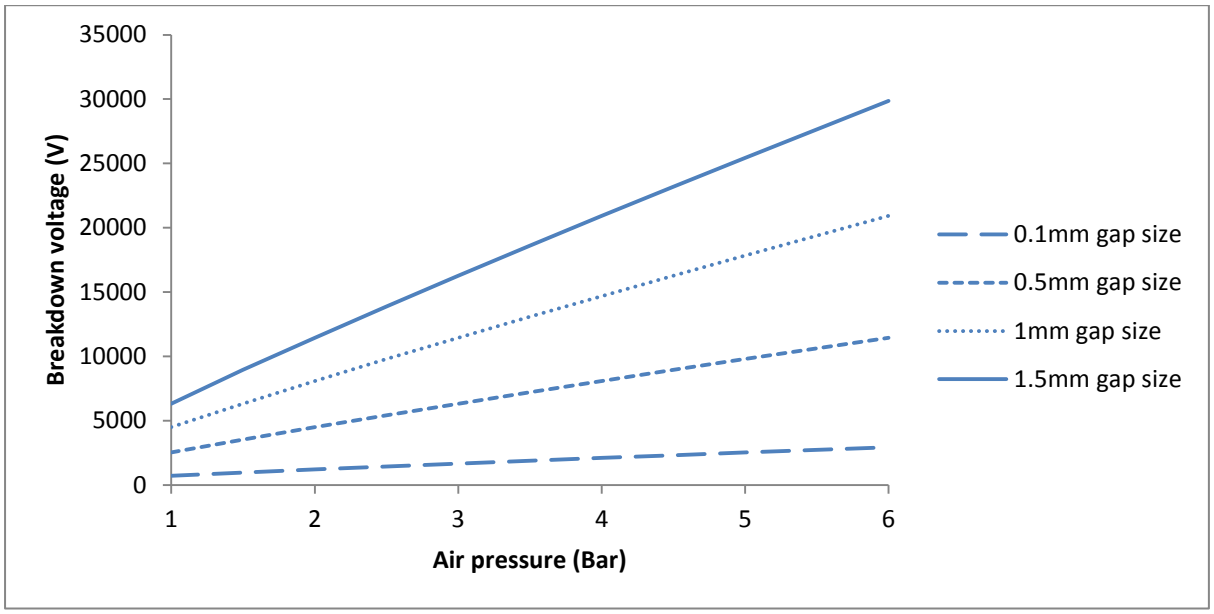

Figure 74: Effect of increasing pressure on the voltage required to make plasma.

4.4.6 Reactions of plasma with diffuser material surfaces

Reactions of plasma with surfaces is a science all of itself. The interaction of the plasma with the surface is very much dependent on the chemistry in the plasma (which is in turn dependent on the electron and gas temperatures) and the chemistry if the material in question, as well as its topography. As each material is different, the rates of reactions of plasma species on surfaces will be specific to the chemical composition and the topography of that surface. Data on reactions of plasma on the surfaces of materials is best determined experimentally, and the collection of such data is beyond the scope of this work. However, the high reactivities of the plasma constituents, as well as the increased surface areas per volume involved in the plasma micro-reactors due to their smaller widths or diameters mean that, wherever possible, any surfaces between the plasma reactors and the point of use (in this case the bubble) should be minimised unless they are required to play a part in the plasma chemical reactions, as they will inevitably reduce the efficiency.

The significance of interactions of gas particles with surfaces in a porous media can be considered using the Knudsen number

$$Kn = \frac{\lambda}{d_e},$$

where *Kn* is the Knudsen number, λ is the mean free path of a gas molecule between successive collisions and d_e is the equivalent pore diameter. If the Knudsen number is less than 1 then collisions

with the walls of the medium are of greater importance than collisions with other gas molecules. The mean free paths of air molecules at atmospheric pressure are between 60 and 70nm (Wijngaarden, Westerterp, & Kronberg, 2008), thus if the diffusers are nanoporous then collisions of the molecules with the surface will be quite significant.

As well as providing high surface areas for particle collisions, diffusers can also affect the flow rate of the air between the plasma and the point of use. The flow rate through a porous medium is given by the Darcy equation

$$Q = \frac{\kappa A}{\mu} \frac{P_1 - P_2}{L}$$

where κ is the permeability of the porous media, μ is the fluid viscosity, L is the length of the media, and A is the area of the media (Bird et al., 2002).
From this it can be seen that both increasing the thickness of the diffuser, and decreasing the permeability will decrease the gas flow rate through the diffuser. Decreasing the flow velocity will increase the time elapsed from the products of the plasma leaving the reactor and reaching the water, and will also increase the probability of particle collisions occurring on the walls of the diffuser pores. Diffusers with smaller pore sizes, especially in ceramic diffusers, will most likely have lower permeabilities in order to retain structural stability, and as can be seen from the kinetic studies in section 3, the products of the plasma decrease rapidly even over timescales of milliseconds, thus any obstacle which decreases the flow velocity would result in an efficiency loss of the plasma products.

4.4.7 Effect of fluidic oscillator on plasma conditions

The fluidic oscillator essentially alternates regular periods of flow and non-flow through its outlets (see Figure 75). The most immediately obvious effect of this is to increase the residence time of particles in the plasma during periods of non-flow, and decrease the residence time of them during periods of flow to a residence time shorter than would be experienced in steady flow conditions. Increasing the residence time increases the amount of energy transferred to the plasma per unit time (as this energy from the power supply is more or less constant per unit time, at least in the time scales of the oscillation frequency) and this has an effect on the plasma chemistry as described in Eliasson & Kogelschatz (1991). Even though, as the mean volumetric flow rate is the same, one would also expect the mean energy supplied per unit volume to be the same, the effect of fluidic oscillation on the plasma should be tested.

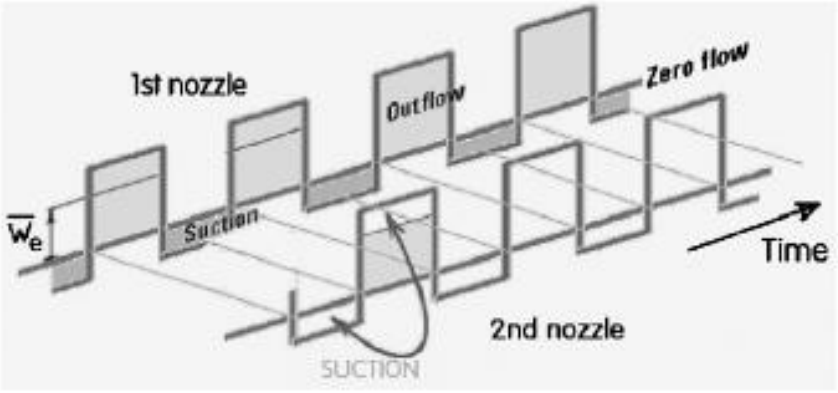

Figure 75: Depiction of oscillatory flow through the twin nozzles of a fluidic oscillator. (Tesař, 2009)

4.5 Discussion

It is clear that the formation of plasma in the dielectric barrier discharge configuration results in the formation of microdischarge streamers and that decreasing the gap size for the same power signal increases the number of streamers formed and the intensity of the emission spectrum. Whist reducing the gap distance between electrodes allows increase in plasma intensity or reduction in breakdown voltage, it will also inevitably increase the probability of collisions of plasmas with the walls of the reactor unless the length of the reactor is also scaled down accordingly. Thus, if the reactor were to be used as a pore through which a microbubble would be formed, the electrode components of such a reactor would need to be extremely short.

As wall collisions will increase with a decrease in plasma reactor size, especially with the higher pressures involved with the microbubble diffusers, the generation of heat is more of an issue in these reactors, and the selection of suitable materials all the more important. It can be seen from Figure 66 that most of the commonly used dielectric materials have low thermal conductivities, meaning that heat build-up in DBD microplasmas would be a problem. There is a clear relationship between increasing temperatures and decreasing ozone yields due to the increase in ozone decomposition (Figure 64), but this is not to say that higher temperatures are undesirable for the formation of other RONS. The other effects of increasing temperatures within the reactors are that a decrease in the thickness of the dielectric layers results in a decrease of their mechanical strength, which makes them more susceptible to fracture due to thermal expansion of the other materials. Regarding the electrode materials, the most electrically conductive materials are fortunately also the most thermally conductive (Figure 66) and the electrodes can thus be used to facilitate heat transfer from the reactors, the rate of heat transfer increasing exponentially per unit volume as the reactors are scaled down (Figure 65).

The increasing intensity of the emission spectrum observed with decrease in gap size (Figure 60 & Figure 61), is clear indication of increased concentrations of excited species, which are known to reduce ozone generation (by increasing the formation of ozone destructing species) if they are present in sufficiently high concentrations (B Eliasson & Kogelschatz, 1991; Kogelschatz et al., 1999). But the excited species could themselves be used if the proximity to the water is high enough, as indicated from the preliminary results of the kinetic simulation.

As the proximity to water is the goal, possible effects of water on the plasma must not be neglected. It is clear that water re-entrainment into the reactor would interfere with the plasma behaviour.

The breakdown voltage of pure water is much higher than air, thus at the voltages relevant to the air plasma operation, pure water would act as a dielectric material, increasing the impedance of the reactor and making less power available to the air plasma, resulting in an efficiency loss. This loss aside, the presence of water in the reactor would create irregularities in the gap distances, allowing the current to find a single shortest distance where microdischarge formation would predominate at the expense of all other locations. The high power densities resulting in this area could even damage the reactors by forming runaway thermal discharges. Complete re-entrainment of water into the reactor would prevent the formation of plasma at all. At high electrical conductivities of water the current from the circuit would find an alternative pathway through the water if it came into contact with the dielectric materials and bridged the gap between them, even if it did not occupy the whole space of the reactor. The conclusion of this is that water re-entrainment should be avoided.

A sufficiently thick diffuser should prevent water re-entrainment, but this also has its drawbacks. Bubble formation via the medium of a diffuser has implications as it increases the pressure required to blow air through as the porosity decreases, decreasing porosity is essential to retain structural solidity as the pore size decreases, and the decreased pore size is essential for the formation of smaller bubbles. As the pore size decreases there is also an increased likelihood of destruction of reactive species generated in the plasma by collisions with the diffuser walls, especially below micro-scales. Any extra steps between the plasma and the bubble should ideally be avoided if the extremely short lived species in the plasma are to be made use of.

4.5.1 Possible explanations of the dosing lance performance

As the dosing lance gap sizes were so small, and the plasmas were operated continuously, the heat build-up is the most likely explanation for the low ozone output of the lance, and also for the material failures.

The diffuser may also have had some destructive effect on the ozone generated, although the concentration of ozone may have been too low for the probability of destructive collisions with the diffuser walls to be significant. As assembling and disassembling the lance was costly and time consuming during the field trials, and risked damaging the expensive and delicate ceramic diffuser, the effect that the diffuser had on the plasma was not observed.

4.5.2 Conclusions

- Bubble formation is much more uniform and with smaller mean bubble size if the diffuser is flat instead of semi-cylindrical.

- The minimum breakdown voltage for plasma formation occurs for gap sizes between 1-10 µm at atmospheric pressure. There is a positive correlation between the thermal conductivities and the electrical conductivities of most of the common conductive materials that could be used for the electrodes (Figure 66), and for a cylindrical reactor, the rate of heat transfer increases by an order of magnitude as the diameter of the cylinder decreases by an order of magnitude (Figure 65) which is beneficial for ozone formation as there is a potential for the electrodes to be used directly as the cooling mechanism. The effects of shortening the electrodes in a micro-tube plasma reactor need to be investigated further.

- A reduction in the pore size of the diffuser will increase the back pressure in the reactors, which for relatively large electrode gap distances (such as 1 mm) and relatively high back pressures (such as 5 bar) will prevent the plasma being formed (Figure 74).

- A combination of microbubble formation from pores and plasma micro-reactors can look beyond ozone as the principal means of oxidation, but as decreasing the diffuser pore size increases the rate of particle collisions with the walls the diffuser must be carefully chosen.

- Water re-entrainment is beneficial for bubble formation, but will prevent the formation of plasma if it comes between the electrodes unless the water is highly saline, with a conductivity >100 S m^{-1} for an electrode gap distance of 500 µm. Increasing the waters conductivity increases the likelihood of streamer formation between the electrodes when they are submerged by decreasing the breakdown voltage.

5 Development and characterisation of a single bubble pore plasma capillary reactor

5.1 Summary

The aim of this chapter was to investigate the fabrication and performance of a single bubble-pore plasma reactor in order to gain useful knowledge for design purposes. The principle was to investigate the effects of moving the plasma as close to the interface as possible. First a reactor of the appropriate geometry was selected, then the reactor was characterised. The bubble formation characteristics of the reactor were then investigated and it was found that water re-entrainment into the reactor occurring to an extent too great to allow effective operation of the plasma. An alternative reactor configuration was devised, which allowed the plasma to make contact with the air/water interface and it was found that this increased the oxidation effectiveness (as measured by the decolouration of indigo solution) of the plasma by a factor of 10.

5.2 Introduction

Drawing from what has been learned in the previous chapters, an experimental investigation into the effects of a single pore reactor is now required. Practical observation of the plasma conditions and the behaviour of water in proximity to the reactor will give useful knowledge for application to design. The effect of the plasma proximity to the air/water interface is an important observation that can be gained from the operation of such a reactor, and the effect of the fluidic oscillator on a single pore reactor can also be observed.

Elements of the previous chapters are first discussed.

5.2.1 Implications from the kinetic simulation chapter

From Figure 40 and Figure 41 it can be seen that during the time that the electric field is activated, there is around a ten times higher concentration of O atoms than there is ozone. Once the electric field energy drops to near zero, the O atoms react with O_2 molecules forming O_3. It can be seen from the simulation plot in Figure 51 that the O atoms have a higher propensity to react with surface H_2O molecules and form hydroxyl radicals than does ozone, thus since the O is present in higher concentrations within the plasma then moving the plasma closer to the bubble surface would increase the amount of O that is able to react with directly with the surface instead of forming ozone.

Minimising the bubble diameter increases the surface area or the air/water interface that is available for reactions and for mass transfer (W. Zimmerman, Tesar, Butler, & Bandulasena, 2008), and Figure 47 suggests that decreasing the bubble diameter could have an effect on catalysed ozone decomposition. Thus it is desirable to make the bubble size as small as possible.

There are many different possible dielectric materials and diffuser materials that could be employed. Surface reactions between the plasma and surfaces of these materials were not taken into account, as the reactions would be different depending on the material. It was assumed that due to the high surface area of the materials, and high reactivity of O_3, O and other reactive species in the plasma interaction with any surfaces would lead to increased destruction of these species. Therefore, the ideal design would have nothing in between the plasma and the air water interface.

5.2.2 Implications from the field trials

During the field trials there was nearly always excess ozone produced. This excess ozone needed to be destroyed, as ozone is harmful at ground level and is also a greenhouse gas. Destruction of the ozone required extra resources, which would also have taken energy to manufacture and transport, decreasing the energy efficiency of the overall process. Producing OH radicals directly from the O formed in the plasma could potentially eliminate the need for extra destruction processes.

The multiple plasma reactors in the dosing lance also presented a problem. There was unequal distribution of power, flow and gap size due to various factors.

Changing the flow into a reactor would change the resistance of the plasma, which would change the power flowing into it, and since the reactors were connected in a simple parallel arrangement, the power going through the whole reactor remained the same, thus decreasing the resistance of one reactor would increase the power into that reactor at the expense of the others. Flow distribution was a problem due, in part, to the entry of air from the side of the lance, and possibly to the reactor geometry as well. An improvement on this design would be one which allows the air to enter all reactors in a uniform manner.

The lance also did not have a cooling system, and heating of the electrodes led to warping of the lance material, which altered the gap size which altered the power distribution into the reactors. It also led to cracks in the dielectric barriers, which led to arcing. As well as this, the heating up of the reactors was most likely the main reason why the ozone concentration was so low.

5.2.3 Implications from the design principles

A number of things can be learned from the consideration of the design principles, the first being that the smaller the reactor, the closer the electrodes can be to each other and the lower the voltage is required to form plasma (Figure 56). Decreasing the size of the plasma reactors also increases the rate of heat removal from them (Figure 65), which could be useful in heat removal in maintaining process conditions, but higher wall collision rates mean that the length of the reactor should also be reduced. The dielectric material will also need to be strong on a small scale, as decreasing the reactor diameter will necessitate the dielectric material to be thinner in order to move the electrodes correspondingly closer together. A weak or brittle dielectric material could snap or fracture, which would cause arcing between the plasma electrodes, damaging the reactor and causing electrical problems which would also inevitably affect the process as well as the safety of the device. This was also observed first hand at the field trials. Smaller bubbles clearly require smaller pore sizes, and smaller pore size diffusers require higher pressures to push the air through and form bubbles. The smaller pore size diffusers also inevitably have a higher internal surface area, which would provide surfaces for destruction of the plasma products. The most wettable surfaces are the most desirable to form smaller bubbles, as the water forms a film over the pore surface. This property encourages water re-entrainment into the diffuser, which is good for bubble formation, but undesirable for plasma formation.

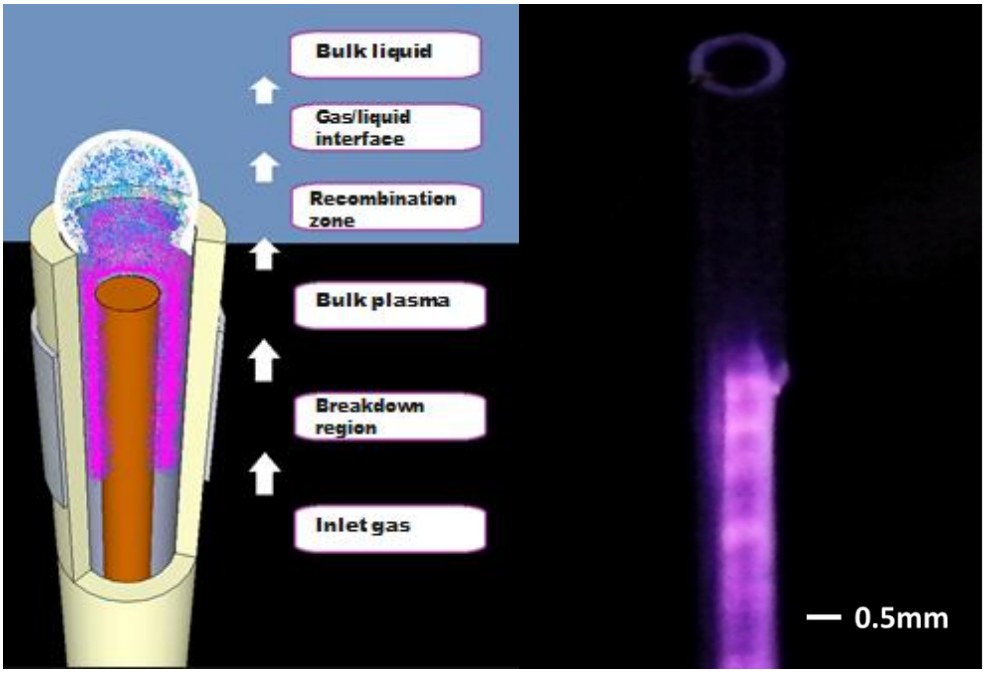

Figure 76: (left) Conceptualised diagram of plasma formation within the bubble pore (right) a photograph of a plasma formed in a glass capillary tube, close to the idea of the conceptual design. The intention was that this tube could be used as a pore from which a bubble of the same diameter as the pore could be formed.

5.3 Aims

As the formation of bubbles requires small pores, and smaller gap sizes require less energy to break down for plasma, and moving the plasma as close as possible to the water would maximise the use of reactive species formed in it, integrating the plasma and the bubble formation pore so that they are essentially the same thing seems like the most logical step.

Forming the plasma in a single tube with a diameter on the micro-level (<1mm) means that individual microbubbles could be blown directly out of the tube, as illustrated in Figure 76. This unit could then be repeated to give arrays of tubes that could give a desired bubble density and oxidant output. The cylindrical geometry of the reactor should allow multiple reactors to have uniform flow by arranging them in a regular symmetrical array.

The aim of this chapter is to investigate the potential of a single bubble formation pore/plasma microreactor. This reactor design aims to also create plasma directly below the point where the bubbles are formed in the water in order to retain as much of the intermediate plasma species as possible up to the air water interface. The findings of this investigation can be applied, along with the rest of the thesis, to the design of reactors integrating the generation of reactive oxidant species, with microbubble formation.

5.4 Development of design

The use of glass dielectric materials in the dosing lance proved to be problematic. The small gap size in the lance required the dielectric materials to be very thin. The glass used was weak on this scale, and a more reliable material was required.

Alumina was found to be a useful material as it is strong, thermally stable, and alumina bore tubes with small diameters are readily available. As aluminium oxide is also extremely common in nature, there should be little if any worry about the environmental consequences of any degradation of the dielectric materials in the water supply.

One consideration was to use an inductively coupled plasma for the pores, as this would allow complete protection of electrodes (i.e. no direct current in contact with water), and a uniform electric field. However, at atmospheric pressure, an inductively coupled plasma would form a thermal plasma (Baldur Eliasson & Kogelschatz, 1991) as it does in arc welding applications, and this is not suitable for cold plasma generation. Eventually, alumina twin bore tubes were used for experimental purposes, as a thin copper wire could be used as an internal electrode.

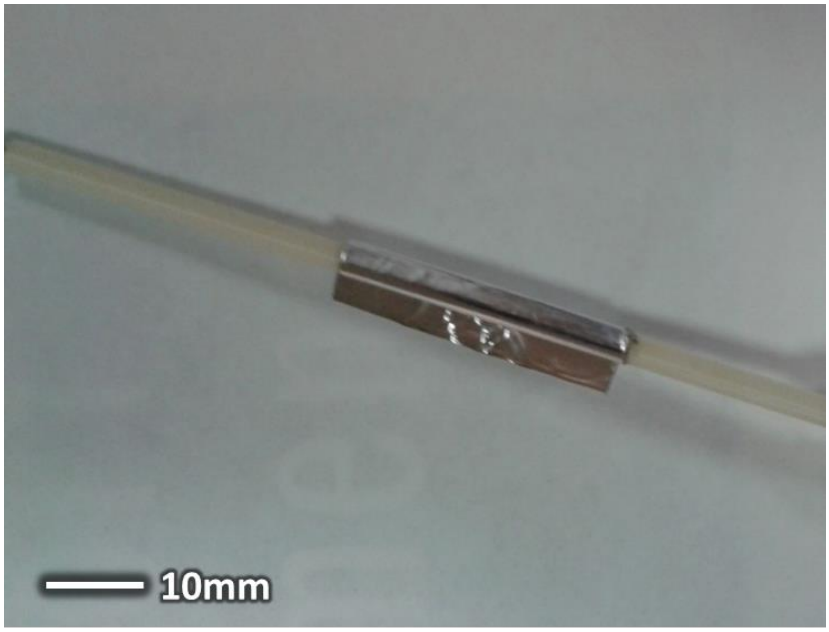

Figure 77: An image of one of the alumina tube reactors with the outer electrode visible in the centre.

This reactor arrangement was then tested, plasma was formed inside the tube. The glow from the plasma inside the tube can be seen on either side of the outer electrode. This effect of the plasma continuing beyond one of the electrodes means it should be possible for the plasma to be continued into the gas/liquid interface.

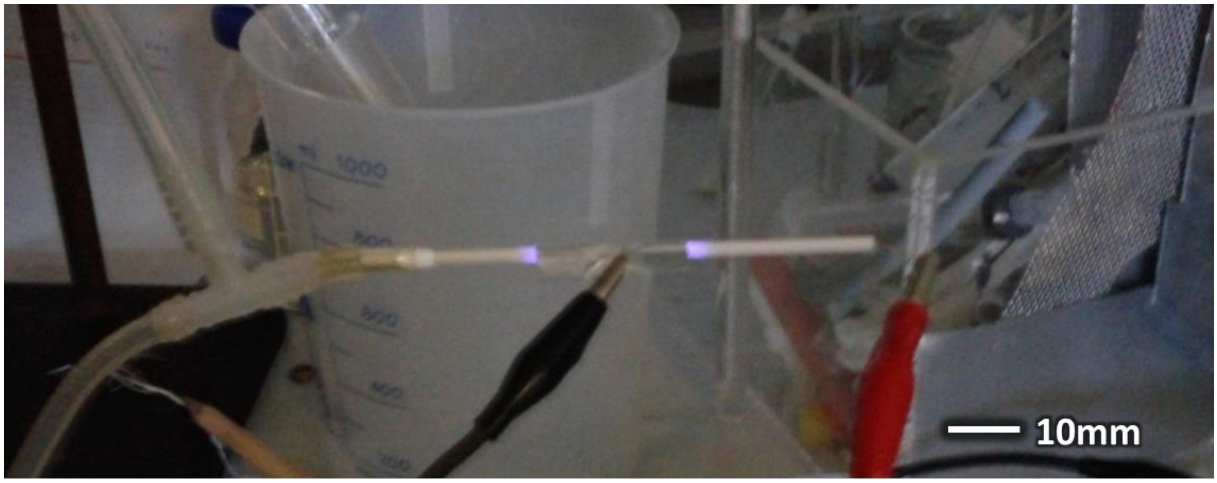

Figure 78: The initial testing of the alumina twin bore reactor.

The twin bore tubes were fitted into the base of a small tank to allow for the observation of bubble formation.

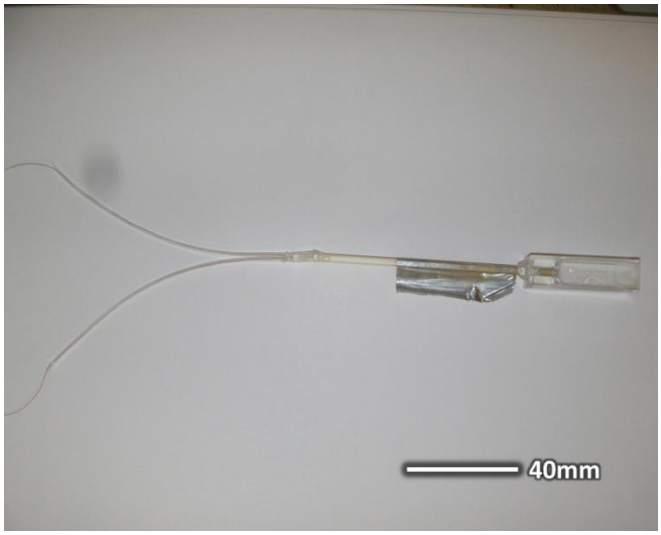

Figure 79: An alumina tube reactor with a separate inlet for each oscillator outlet.

Visual experiments were first conducted to get the smallest possible bubble size using these twin pores. It was found that if oscillated air was blown through both the pores, that the bubbles coagulated to form a single larger bubble (Figure 80 (a)).This design was altered to attempt to prevent this. As the fluidic oscillator worked by alternating pulses out of its two outlets, it was decided that the two bore tubes should be fed out of different oscillator outlets. The effect of this was to form the bubbles at separate times, increasing the space between them and decreasing their tendency to coagulate. Using this technique, and slowing down the flow rate, eventually it was possible to get bubbles with diameters of the pores to form (Figure 80 (b)).

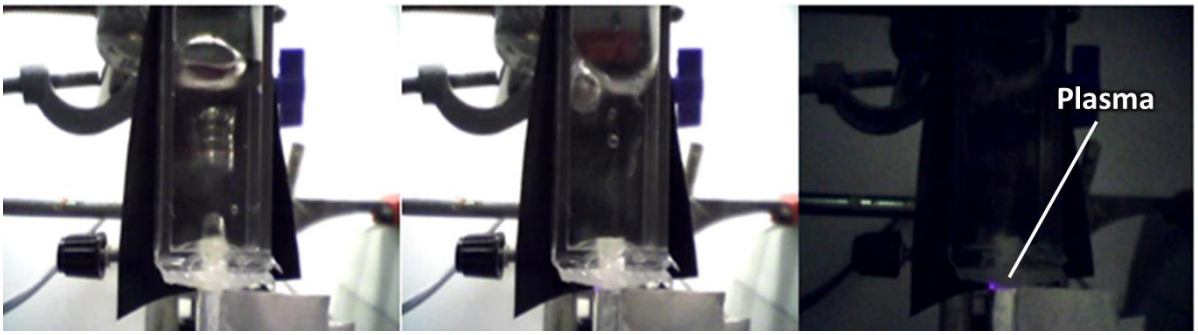

Figure 80: From left to right: (a) Coalescence of the two bubbles into a single bubble. (b) Bubbles forming on the order of the pore size. (c) Plasma briefly formed beneath the bubble formation point.

Once it was clear that the desired bubble size was forming, the reactor was run with the plasma activated. It was found that the plasma formed initially, but then subsequently did not appear. The bubble size remained the same. This was thought to be due to water re-entraining into the reactor, as the dry plasma could run continuously, and increasing the flow rate (and thus increasing the bubble size) eventually led to the plasma re-appearing in the tube, as the tube would have been

dried out by the increased air flow. For this design to work, it was decided that more information was needed about how the plasma behaved inside the tube, and how the water re-entrained.

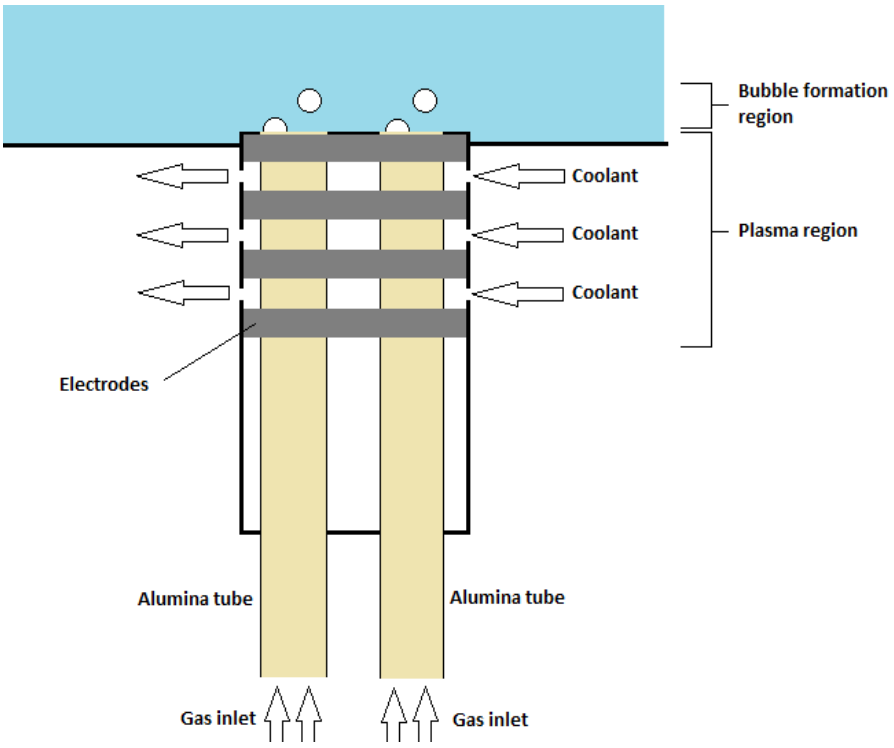

Figure 81: Hypothetical design of plasma/microbubble reactor using alumina tubes.

5.5 Characterisation of a single glass capillary tube reactor

It is not clear from the images of the alumina tube how the plasma is behaving inside the tube, or how far water is re-entraining, as the alumina tube is opaque. Images taken above the tube have shown that the plasma is much fainter when the smaller bubbles are forming, suggesting that the plasma may not be present throughout the tube, and that water may be present all along the tube either partially or fully. The dynamics of the bubbles forming could be investigated with a capillary tube made of glass with the same diameter. It might be the case that the bubbles form with only a small distance of water re-entrainment in which case the reactor would be able to be moved close to the orifice/water zone/point of bubble formation. Or it might be that the water has to re-entrain all the way into the reactor, in which case the formation of plasma would be difficult. Glass has a much higher wettability than alumina, so the extent of the re-entrainment will be greater, but there will still be useful information to found from the observation of the behaviour of water in the glass capillary tube that can be applied to the alumina with this in mind.

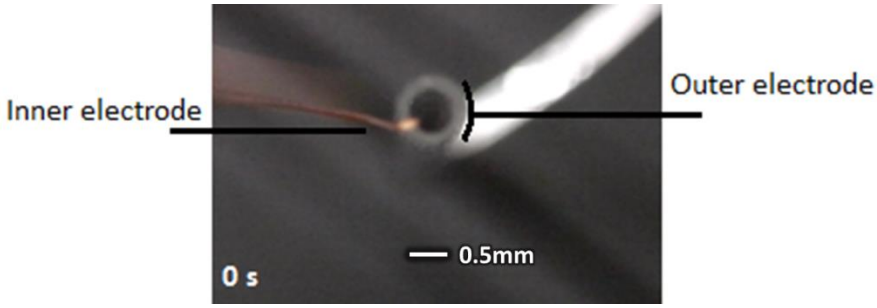

Figure 82: An image taken above the plasma reactor in the light to show the locations of the electrodes and the tube, so that the location of the plama in Figure 83 can be put into context.

In order to imitate the alumina twin bore tube reactors, the internal electrode wire had to be pulled tight to the side of the glass tube so that there was a uniform distance from the outer electrode along the length of the tube. This meant that a concentric electrode configuration was not possible, and if the outer electrode covered the whole outer circumference of the tube then the gap size would be shortest where the inner wire electrode was pulled tight against the tube, and arcing would occur at this point. Due to this the outer electrode could only be wrapped round half of the diameter of the tube.

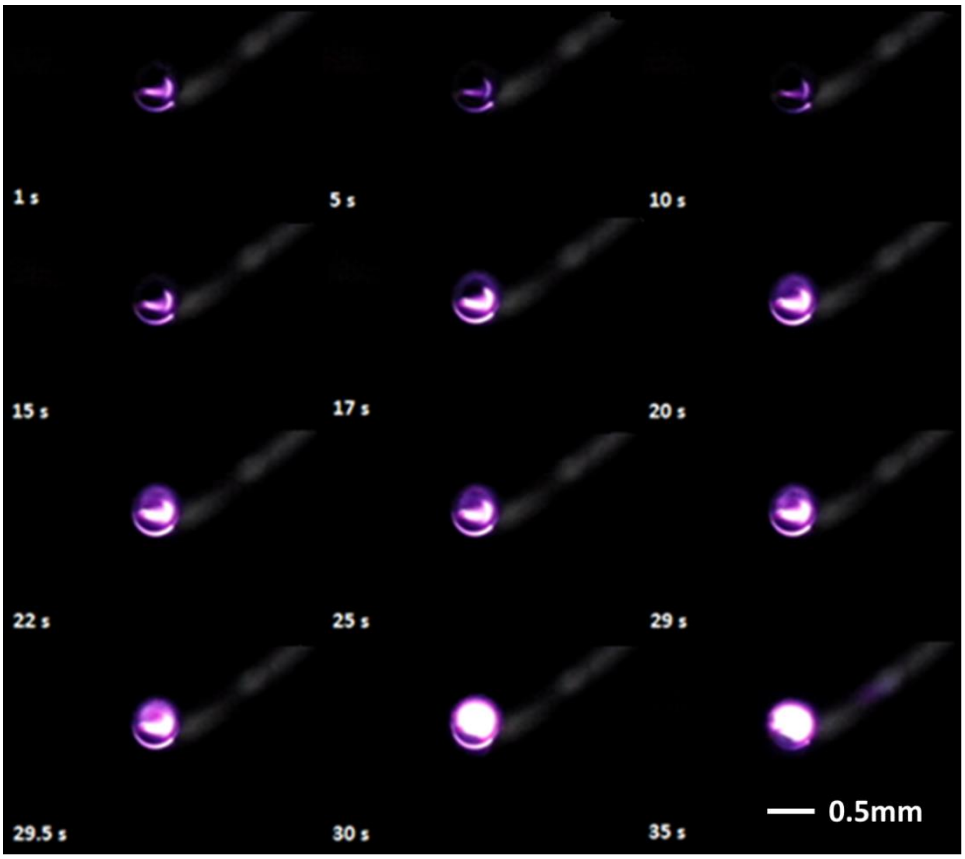

Figure 83: A sequence of frames of the evolution of plasma within a capillary tube with static air flow conditions.

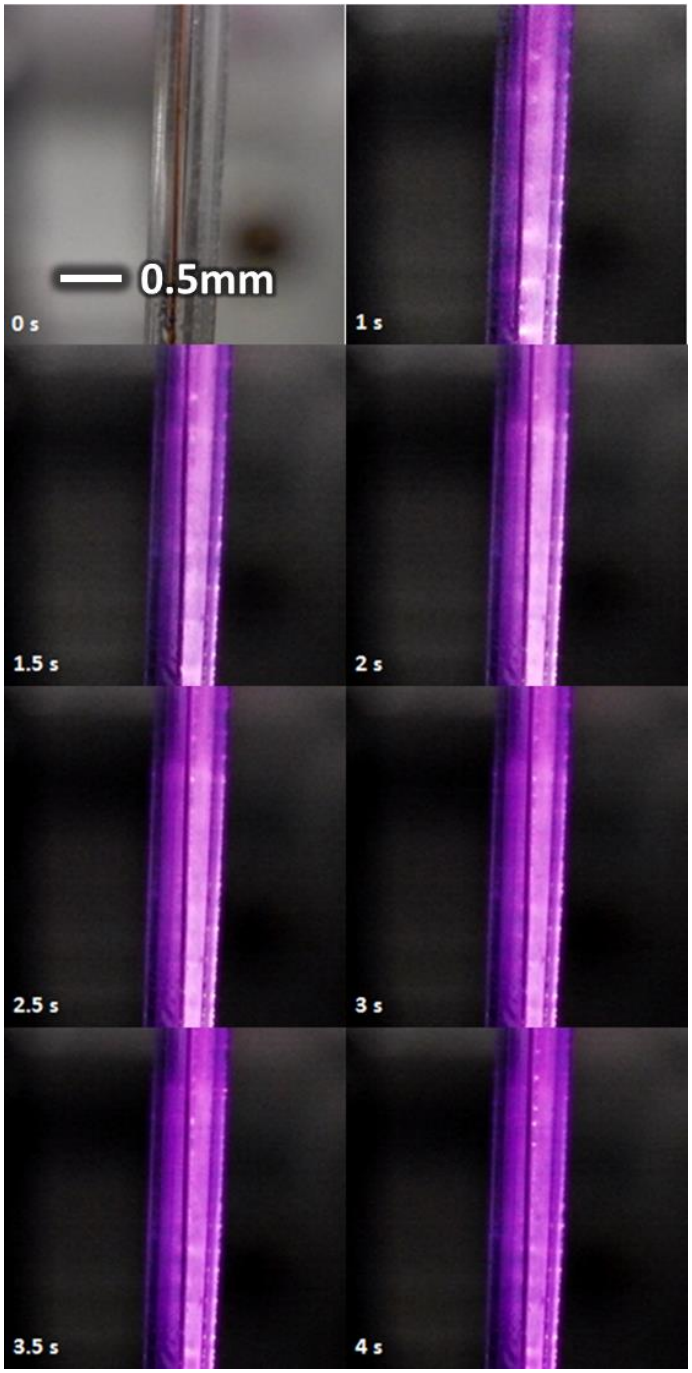

Figure 84: Frame sequence of a single capillary reactor in static air flow conditions. Note the gradual movement of the copper wire to the right.

This electrode configuration was tested without air flowing through the reactor, to observe the behaviour of the plasma in this electrode configuration. A good, stable glow discharge was observed in the tube, more interestingly after 20 seconds the discharge spread into the parts of the tube where there was no contact with the electrodes (Figure 83). This was an interesting phenomenon to

observe and may be useful in future designs, so is worth mentioning here. Observations from the side of the reactor were also made (Figure 84).

It can be noted that the inner electrode moved toward the outer one apparently due to the electrophoretic motion under the applied electric field. This would eventually cause arcing if allowed to continue and the inner electrodes of all subsequent reactor designs were pulled as tightly as possible to prevent this.

Observation of the plasma was possible using this glass reactor. To observe the behaviour of bubble formation, and to potentially make liquid chemical analysis of the reaction products, the capillary reactor needed to be fitted into some kind of liquid receptacle. The low flow rate of the reactor meant the receptacle should be small, and visual observation would be most reliable if the sides of the receptacle were flat, as there would be no distortion of the image due to curvature as was observed in previous experiments. Standard spectrophotometry cuvettes were used as these were relatively inexpensive and had a standard internal width of 1cm, which could simplify calculations made for any absorption techniques. Thus the individual reactor design consisted of a polymer cuvette with capillary tube reactor fitted into its base, allowing bubble formation to occur at the base (Figure 85).

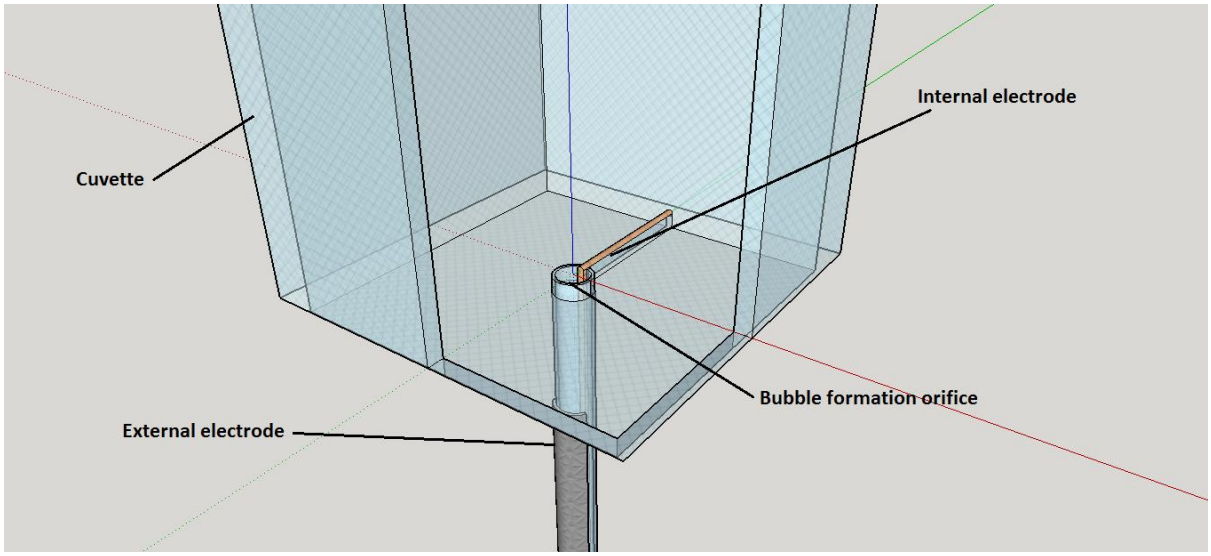

Figure 85: A diagram of the capillary tube test reactors.

As the characteristics of a new reactor could change over a very short time of use due to material strains from the heat generated and the electric fields, or oxidation of the electrodes could occur, reliable repeats of experiments required a new reactor to be built each time. Thus a large number of the test reactors were made to allow for repeats to be done.

The reactors were made by using open ended glass capillary tubes (Mettler Toledo ME-18552), the closed ends were cut off with a silicon carbide blade to allow air to be blown through. Each capillary tube was inserted into a plastic t-piece, then a length of copper wire was threaded through. PTFE tape was used to hold the capillary tube in place, and to prevent air from leaking out from where it was joined to the t-piece. Each capillary tube was fitted into a plastic cuvette with a small hole drilled in the centre of the base, the cuvettes were then sealed in using flowable silicone. The copper wire was threaded through a smaller hole in the edge of the base, and also sealed in. Once the sealant had cured the copper wire could be pulled tight to the side of the capillary tube, and an outer electrode made from accurately cut aluminium tape was carefully fixed on to the tube opposite the copper wire (Figure 86).

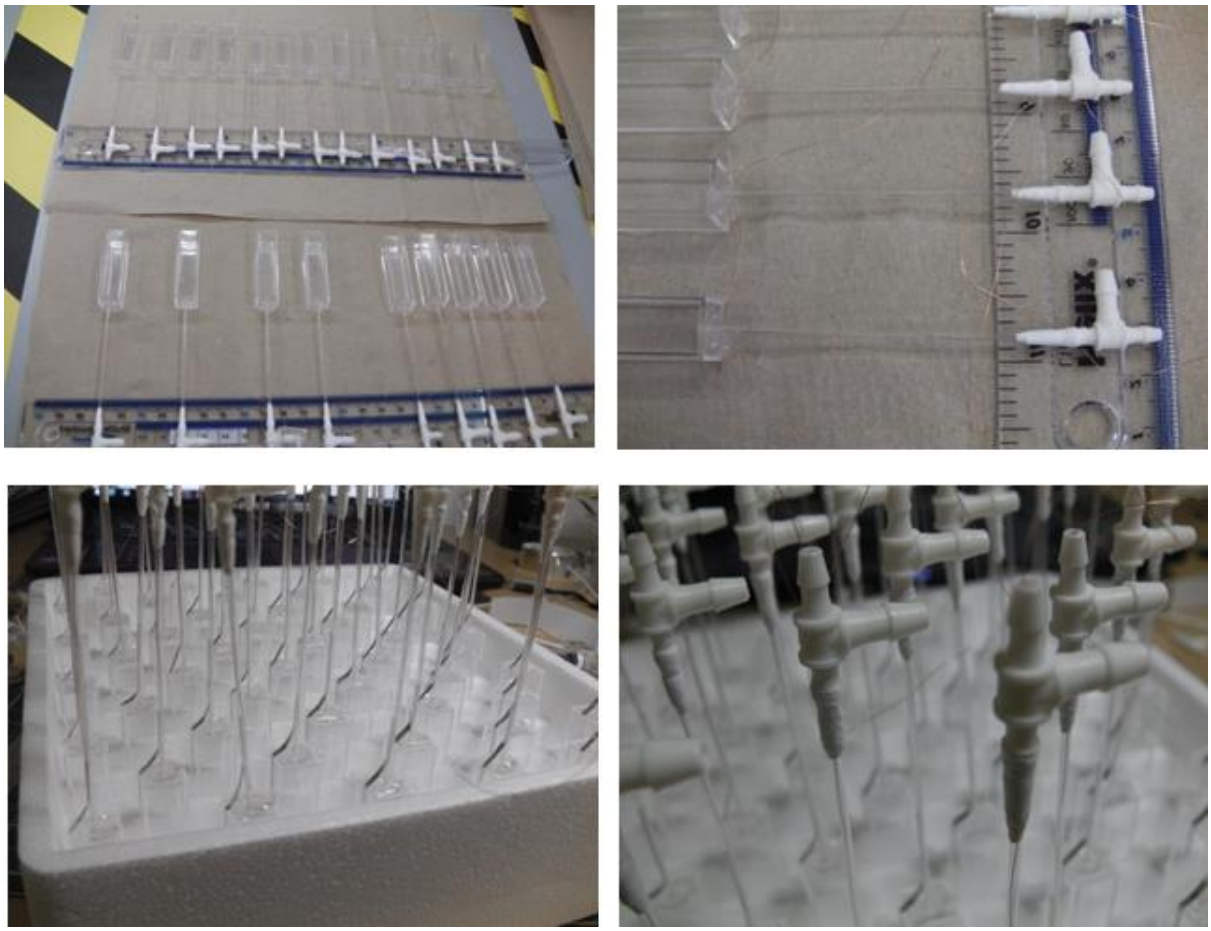

Figure 86: Photographs of the construction individual capillary tube reactors. (Top left) sealant to attach the capillary tubes to the cuvettes is setting, internal copper wire electrodes were threaded through the capillary tubes and fixed to them using silicone adhesive, the reactors were positioned so as to keep the capillary tubes as straight as possible with reference to the cuvettes, (top right) a close up of this. (Bottom left) Once attached to the cuvettes, the capillary tubes were then fitted with external electrodes with the appropriate lengths, (bottom right) a close up of the t-piece attachments that were used to fit the gas flow hose to the capillary reactors.

5.5.1 Emission spectrum measurements analysis and relation with kinetic model predictions

To observe the emission spectrum, a t-piece was used to prevent interference from surrounding light, the fibre optic probe was inserted into the perpendicular hose of the t-piece. The lower-most point of the t-piece was carefully set in line with the lower-most point of the outer electrode.

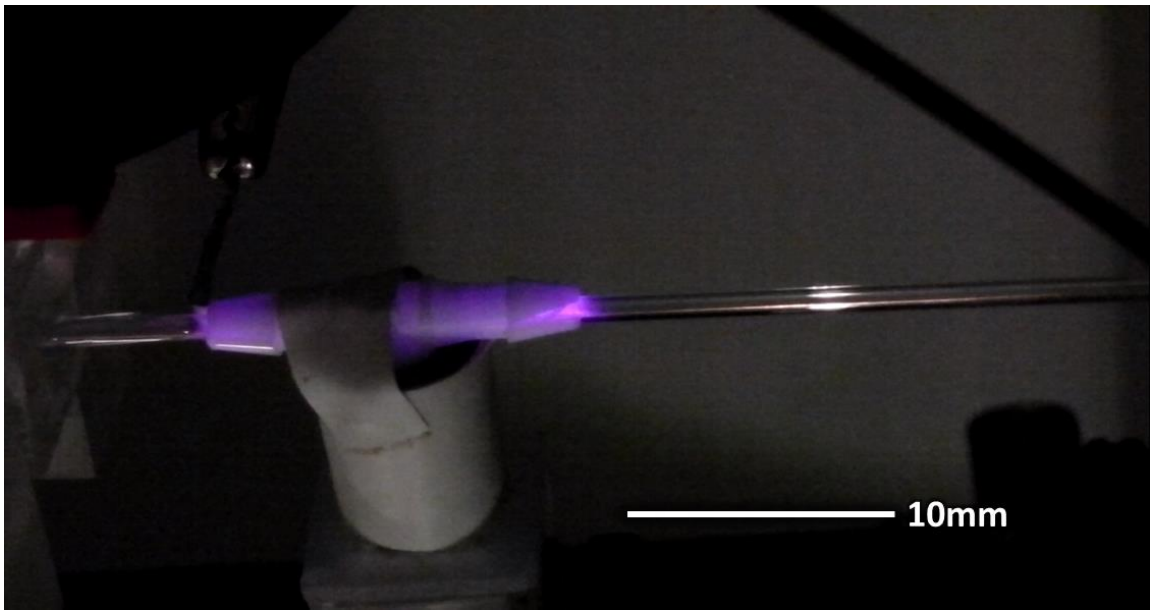

Figure 87: Photograph of the setup for the analysis of the emission spectrum of the capillary reactors. The violet glow of the discharge is visible from inside the tube.

A full spectrum over the range of 178nm – 880nm at approximate 0.3nm intervals was displayed from the spectrometer (Ocean Optics USB 2000 UV/Vis Spectrophotometer) and the Spectrasuite program. It was noted that for all of the emission spectra for the stable non thermal glow discharges, the relative heights of the peaks were always the same. This was convenient for analysis as it meant the plasma could be characterised by a single wavelength. The peak with the highest intensity was identified as the $C^3\Pi_u \rightarrow B^3\Pi_g$ (v 0,0) transition of electronically excited nitrogen molecules with a peak at 336.5nm (Figure 88), and fortunately this is one of the outputs of the kinetic model in section 3. The other peaks were identified and have been indexed in Figure 88 according to the data in (Camacho, Poyato, Díaz, & Santos, 2007) and the height of the peaks always remained the same relative to each other even with variations in the power levels of the plasma, with the 356.99, 315.65, and 380.05 peaks being 0.85, 0.30 and 0.4 times the height of the 336.5nm peak respectively. The spectrum was dominated by electronic-vibrational $C^3\Pi_u \rightarrow B^3\Pi_g$ transitions. No peaks for NO or OH radicals were detected, and any peaks of other species would have been too small to be easily distinguished from the background noise.

Full spectra readings were taken at set time intervals (from 3ms to 1000s), and a tab separated value (tsv) file was generated for each one. Analysis of these files could be done either by playback through spectrasuite, or via 3D analysis which was generated by compiling the individual tsv files into a single tsv matrix, and then plotting using the program Mathematica. The files generated were very large, but were useful for observing the whole experiment.

In some of the experiments, the discharge reached arc point and transfer from a non-thermal to thermal discharge was observed. The thermal discharge is an unwanted occurrence in this study, both from the point of view of ozone generation (due to the high temperatures accelerating ozone decomposition) and for the reason that the reactors simply cannot tolerate such conditions.

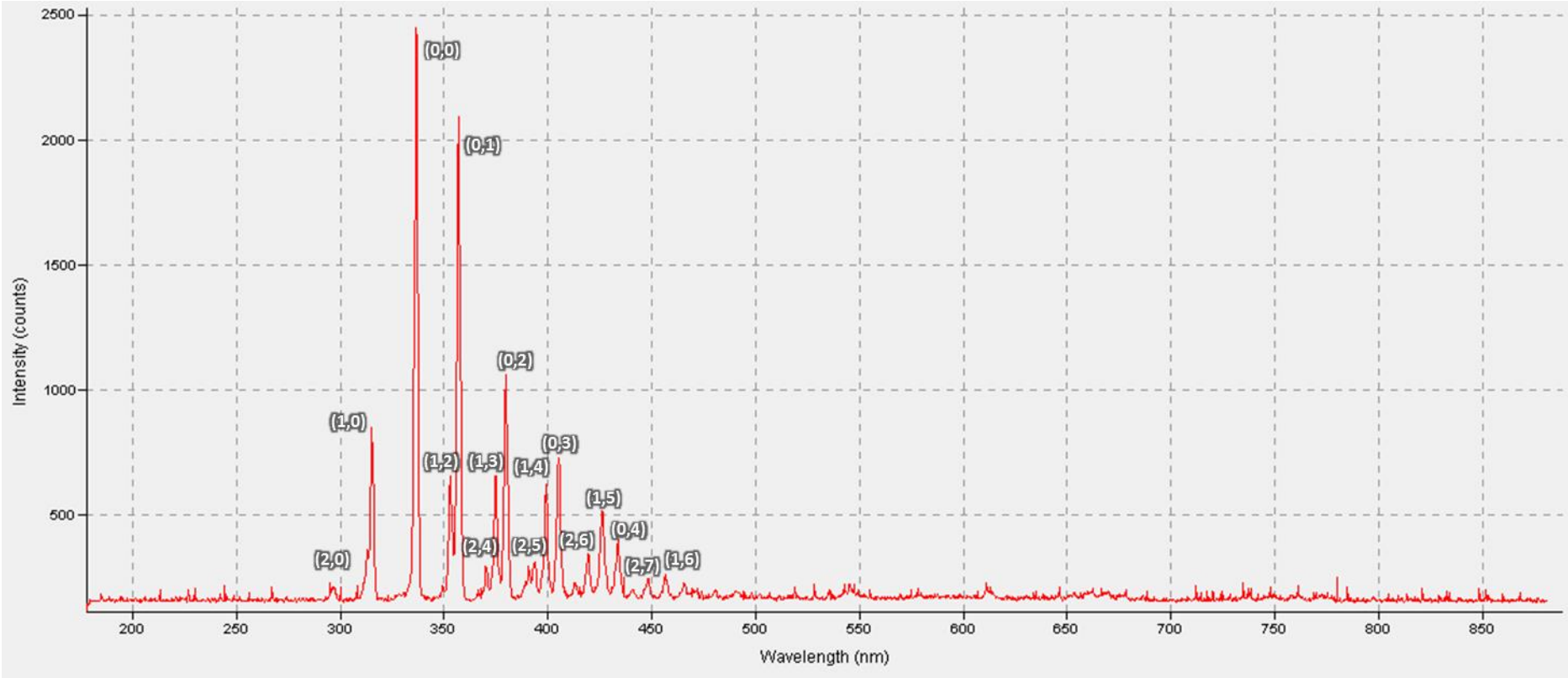

Figure 88: Emission spectrum of a capillary tube reactor plasma. The integration time for this spectrum reading was 1s, which allowed even the small peaks to be visible. The labels refer to the vibrational level changes of the $C^3\Pi_u \rightarrow B^3\Pi_g$ nitrogen transition (v',v'') and it can be seen that all the peaks clearly distinguishable from the background noise can be attributed to activity of electronically and vibrationally excited nitrogen molecules.

5.5.2 Oscillatory flow versus non-oscillatory flow

The fluidic oscillator could theoretically be used in coordination with the power supply, i.e. to activate the plasma only when the flow is static, or when the flow is moving. Activation of the plasma only when the bubble is being formed could have potential benefits of:

1) Reducing the amount of heat generated, as this is primarily the problem when the plasma gas flow is stationary and the heat can build up.
2) Reducing the amount of ozone destruction reactions occurring in the higher specific energy conditions of a stationary gas flow plasma.
3) As there is a slight backflow for each period when using the oscillator, temporary deactivation of the plasma when water may re-entrain into the channel prevents energy wastage lost due to the high impedance of water in the channel.
4) It also ensures that there is no current flowing when the electrode is in contact with the water.

The power supply could be activated in accordance with the oscillation frequency to make use of the kinetics in the plasma. It is first necessary to observe what effects oscillatory flow does have on the plasma.

In trying to observe the effects of the fluidic oscillator on the plasma, several experimental runs were performed at different resolutions with an oscillation frequency of ~80Hz and a flow rate of 5ml/min to test how observable the plasma emission spectrum was at different sampling times. The oscillation frequency of 80Hz was used as the oscillation period at this frequency was long enough for the shortest integration time of the spectrometer (3ms). However, as shorter sampling times mean less photons are available for measurements, the signal intensity inevitably drops for smaller sampling times. Unfortunately, the only sample time that would make any practical sense for observing the actual oscillation pulses was 3ms, and at this low sampling time the signal was unfortunately so low as to be almost indistinguishable from the noise. Since emission spectra of individual oscillation pulses could not be observed, it then made sense to find the best trade-off between signal strength and temporal resolution. Sampling times of either 60ms or 100ms were used in the experiments.

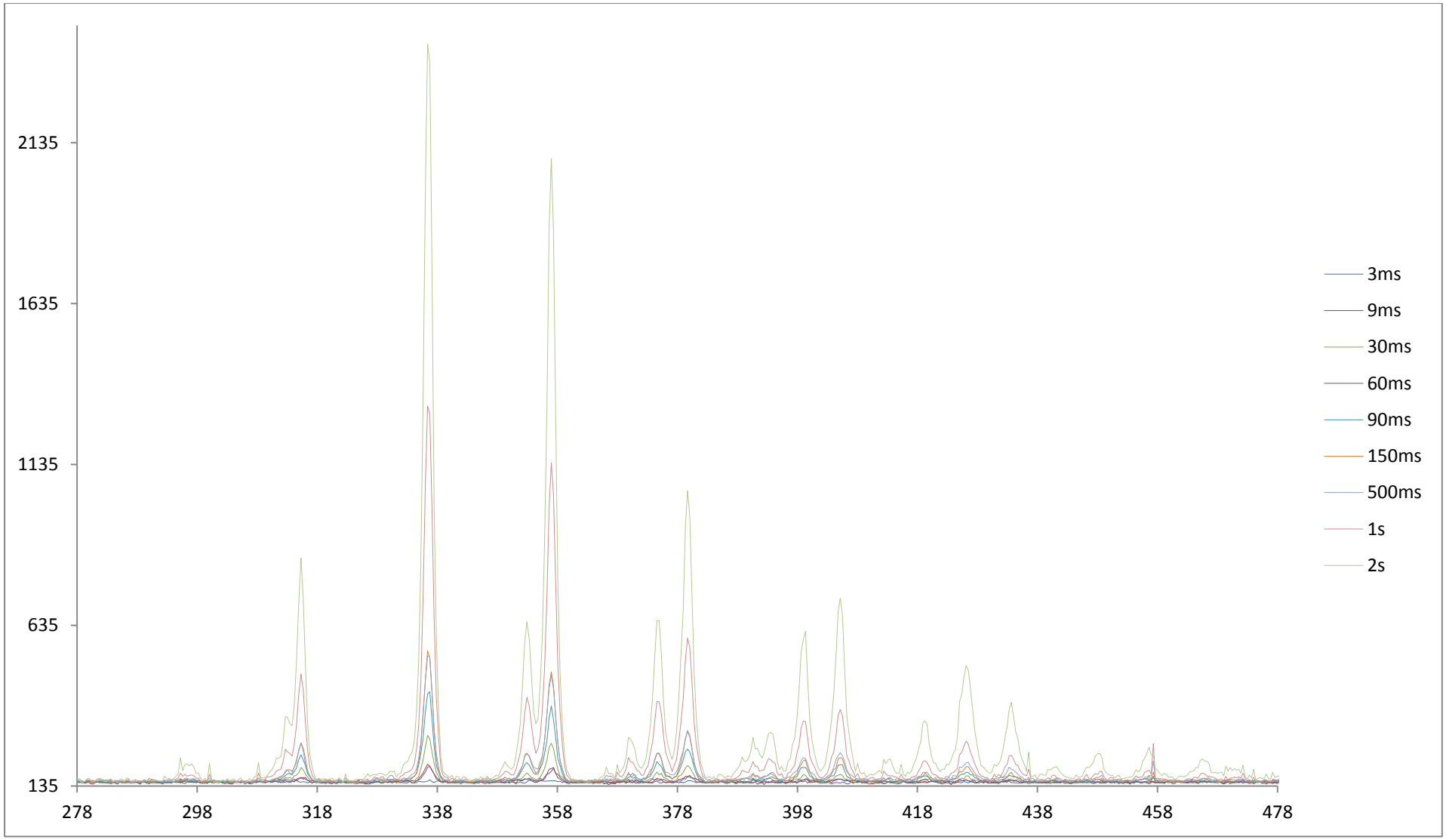

Figure 89: A plot to show the relative intensities of emission spectra with different integration times of the spectrometer. The 3ms integration time would have been extremely useful for observations of spectral behaviour at the flow and non-flow regions of the oscillation cycle, but its signal was so small as to be indistinguishable from the noise.

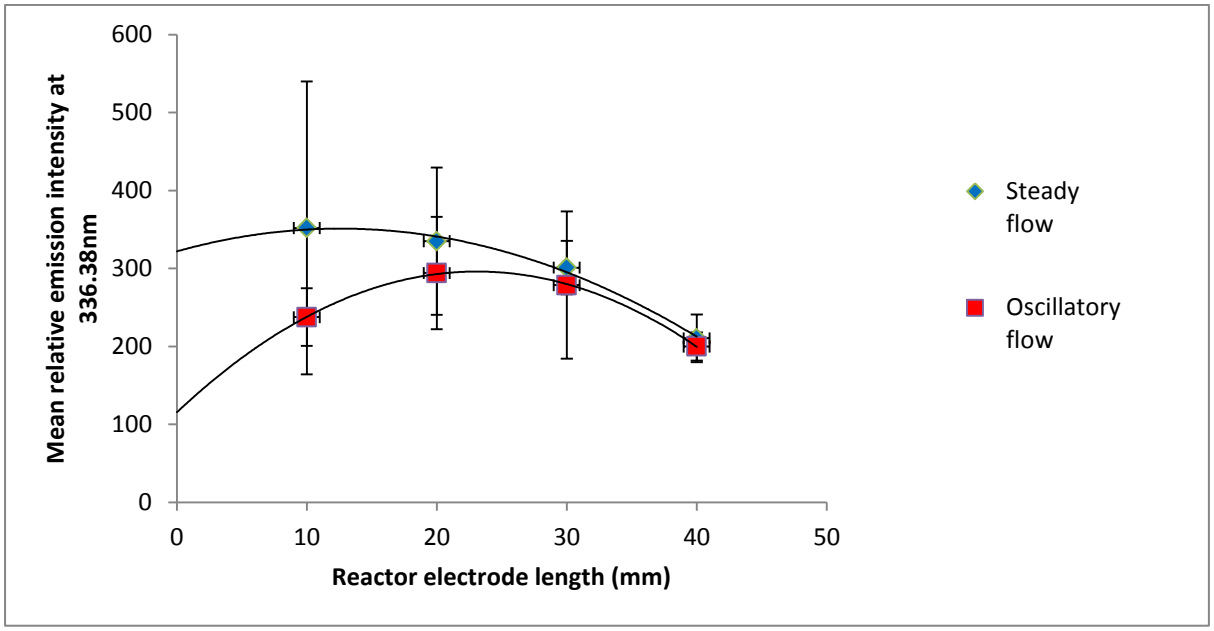

Figure 90: A plot of the mean emission intensity at 336.5nm with electrode length. The two lines are polynomial trend-lines extrapolated to allow speculation of likely reactor behaviour if the electrodes were shortened down to lengths of the order of one millimetre.

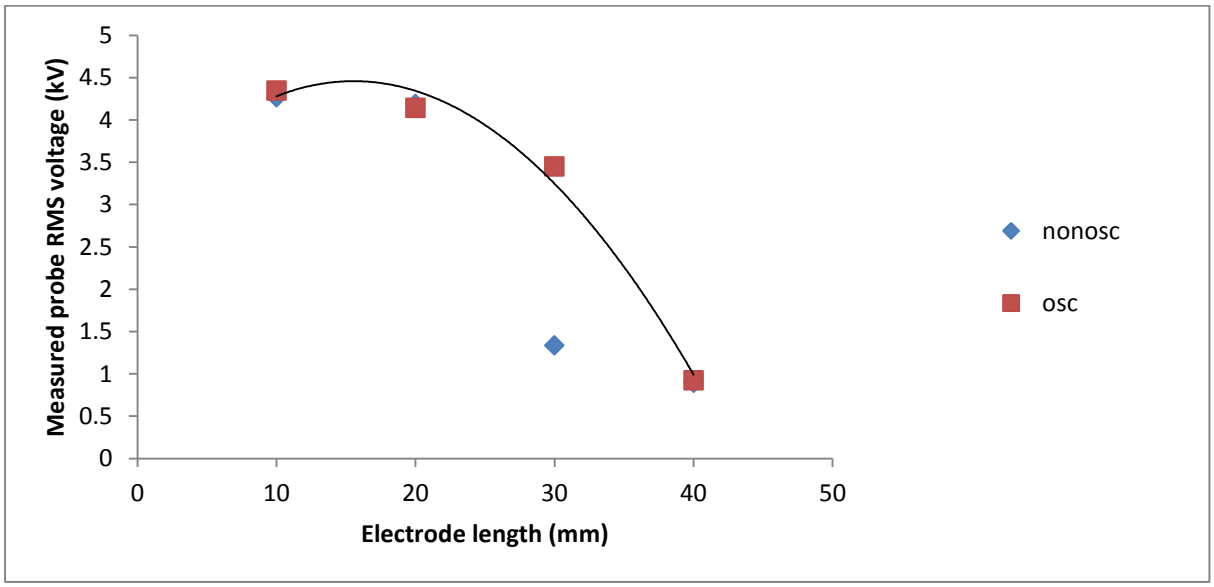

Figure 91: A plot of the mean measured RMS voltages of for each electrode length. The curved line is the polynomial for the pattern of RMS with electrode length for the oscillatory flow. The stray data point for the non-oscillatory flow is likely to be due to an anomaly.

A series of experiments were then conducted to investigate the behaviour of the plasma with and without oscillation, and with varying lengths of external electrode, in order to observe the effects of reducing the electrode length with the same power signal. The results, shown in Figure 90 and

Figure 91, suggested that the plasma emission intensity decreased when oscillatory flow was applied, implying the chemistry could be affected. The full implications of this can be related to the model in future studies. The effects of oscillatory and non-oscillatory flow on the voltage were almost identical, which suggests that the decrease in intensity is not due to variations in power.

5.5.3 Voltage and current characteristics

The plasma voltage waveform is given in Figure 92. The same waveform was observed for each reactor, although the peak voltage tended to change due to matching responses from the power supply. From the voltage waveforms, the RMS voltages could be calculated over a given span of time.

There were problems with electromagnetic interference caused by the plasma, which interfered with the probe readings. As the voltages were high this was not particularly a problem. It made measurement of the current, however, substantially more difficult.

Measurement of the current in a DBD plasma can be done using a series resistor or a monitor capacitor (Ashpis, Laun, & Griebeler, 2012), both methods were tried and it was found that there was no distinguishable signal using the capacitor, and that if the voltages across the series resistor were to be believed (on the order of 1500 V across a 100 ohm resistor) then the fuse in the mains of the whole department ought well to have been blown. The high voltage signal across the resistor was suspected to be due to electromagnetic interference from the plasma itself. In an attempt to remedy this, the cables from the probe to the USB oscilloscope were wrapped in plastic tubing, then in aluminium foil which was then earthed, as a means of shielding them with a Faraday cage. This did nothing to the signal, and it was also found that there was still interference even if one of the probes was stretched as far away from the plasma reactors (around 3m) as possible.

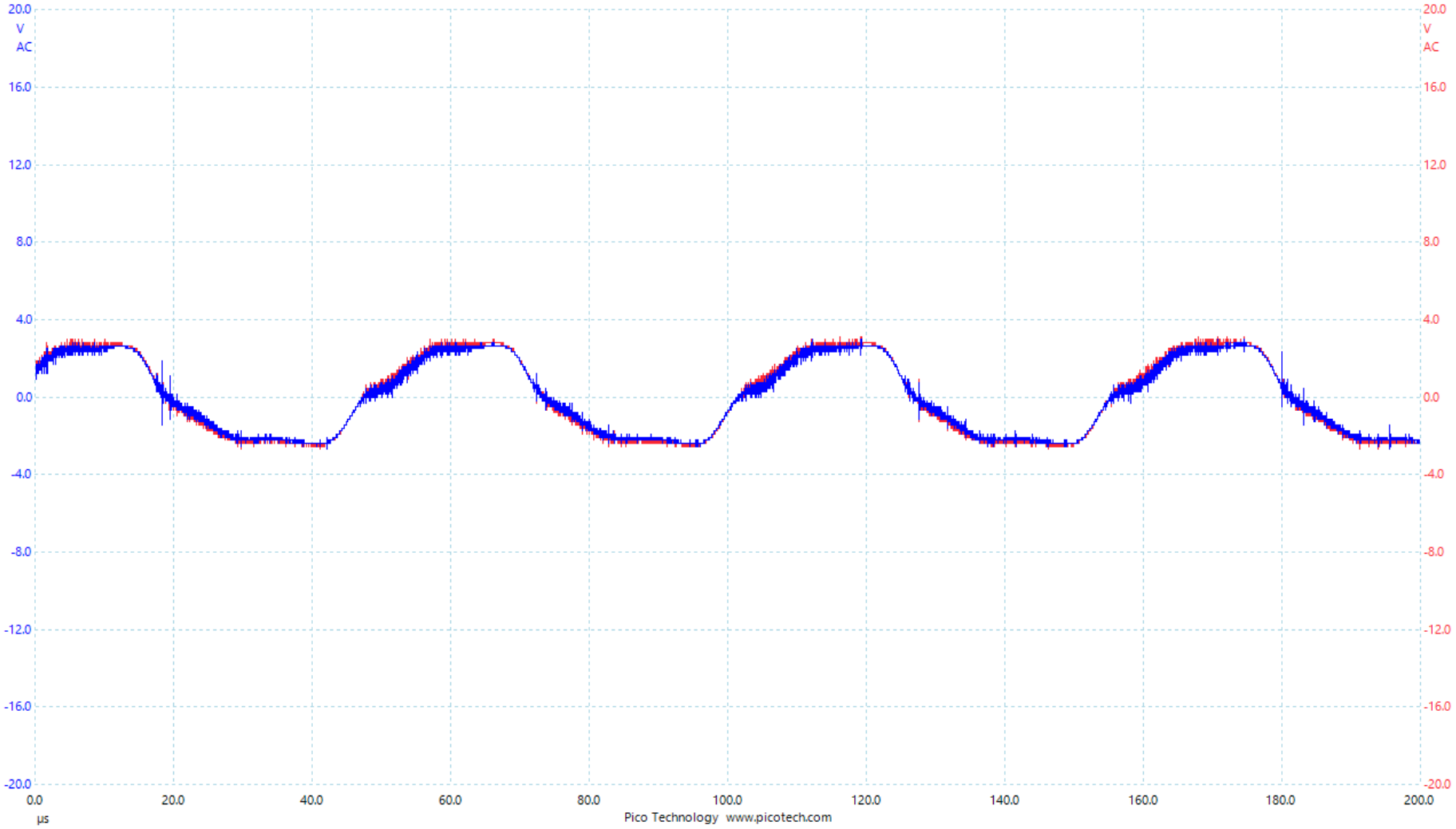

Figure 92: Voltage waveform of the plasma power supply for the capillary tube reactors.

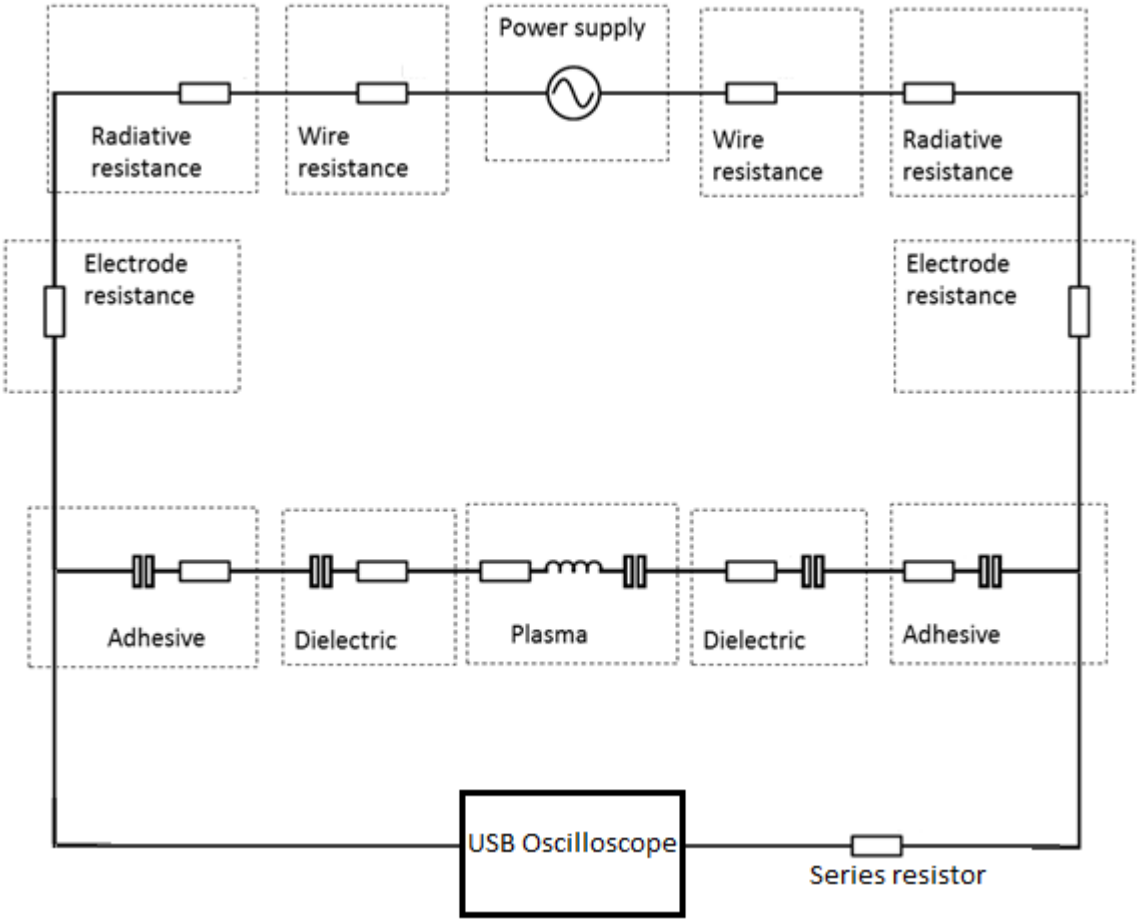

Figure 93: Circuit diagram of the experimental setup. The oscilloscope was connected to the electrodes via a set of high voltage probes. The series resistor was a 100 ohm power resistor.

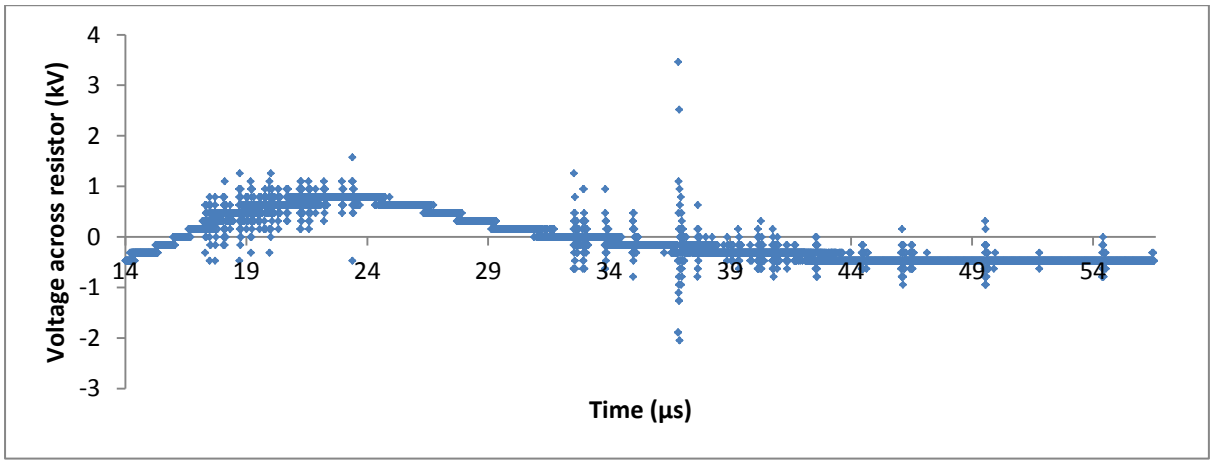

Figure 94: A plot of a typical single waveform cycle for the capillary tube reactors, complete with individual voltage peaks each corresponding to a microdischarge streamer.

A different strategy was then adopted. One high voltage probe was connected across the series resistor, and another probe was placed as close to it as possible without touching the resistor or the other probes. It was assumed that the two probes would experience the same electromagnetic interference with the probe connected across the resistor experiencing the additional voltage across the resistor. The data from a single cycle was recorded, and the two data sets subtracted from one another. This data was then plotted in Figure 95.

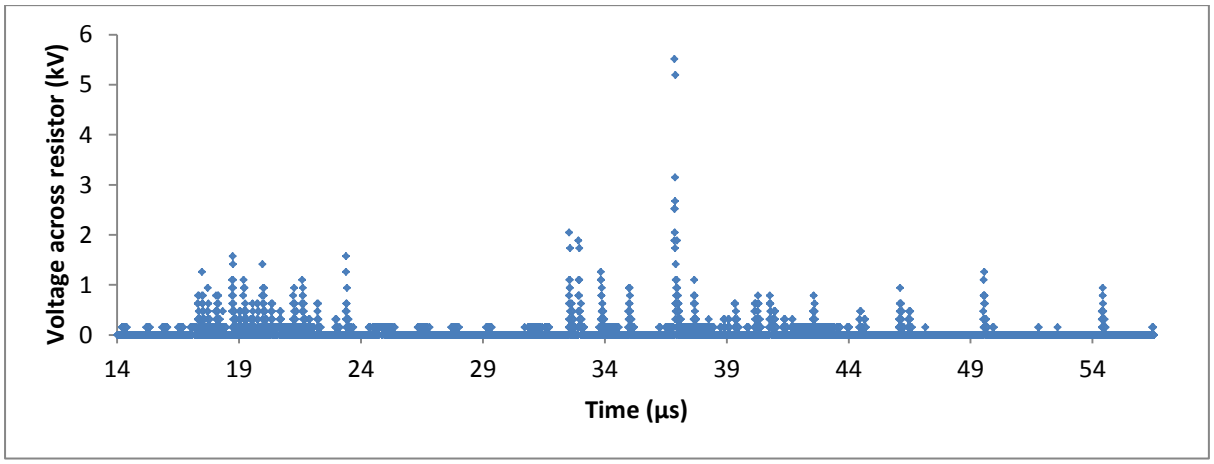

Figure 95: Plots of the absolute values of the voltage peaks across the resistor.

It was observed that the peaks in current appeared as predicted in the rises and peaks of the waveforms, the individual voltage peaks were inspected (as the resolution of the oscilloscope was high enough) and it was found that the duration of the individual voltage peaks were between 2 and 10 ns, which is exactly as predicted by (Baldur Eliasson & Kogelschatz, 1991). It can thus be concluded that the peaks in voltage observed in the waveform are a result of individual microdischarges. Assuming the microdischarges are the only source of the electromagnetic interference, the height of the microdischarge voltage signal must be proportional to the current.

According to Eliasson & Kogelschatz (1991) and Fridman (2008), the typical peak current of a single microdischarge is around 0.1A. Assuming that each of the microdischarges in this plasma are "typical", each voltage peak can be substituted for a current peak of 0.1A for its duration (2-10ns). The mean current can then be calculated from the average current over time. Assuming each microdischarge peak to have an absolute value of 0.1A current draw for its duration, the current for each of these peaks was set to 0.1A using an IF THEN function. The mean current was then calculated as an average over the time of a single cycle, to give an estimate of 4.6mA, which with an RMS voltage of approximately 1.5kV gave an estimate of the power as 6.5watts.

5.5.4 Glass capillary reactor – bubble formation versus plasma formation

Bubble formation was observed with these reactors using a camera (Panasonic HX-DC2). Bubbles were observed to form on the order of the pore size, but in order for this to happen, water needed to be allowed to re-entrain into the reactor (Figure 96).

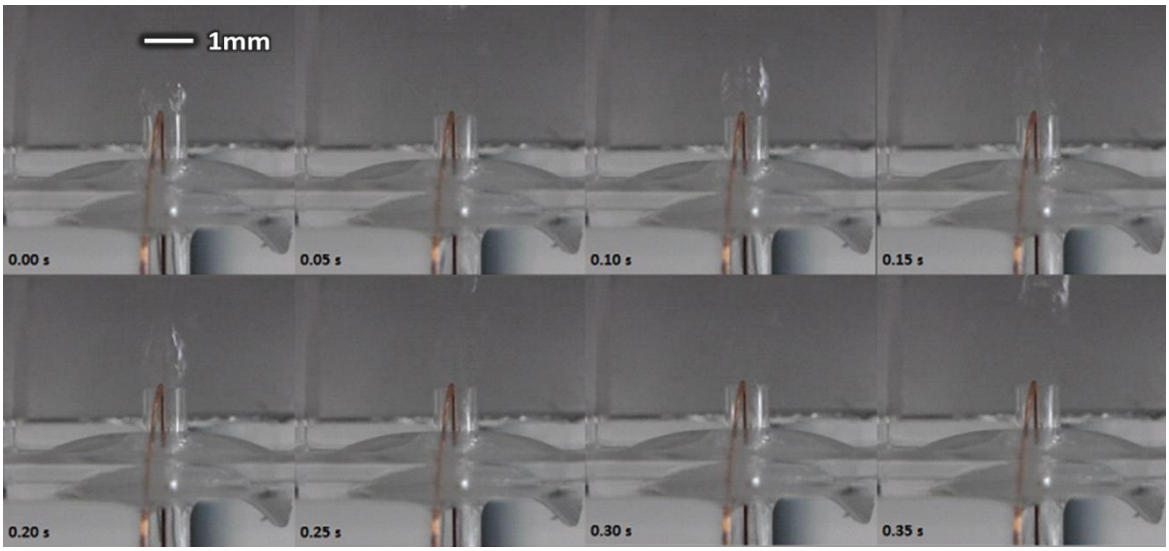

Figure 96: Sequence of frames of bubble formation out of the orifice of the capillary reactors. Bubbles of the diameter of the pore size can be seen forming at 0.00s, 0.10s and 0.20s.

It was observed that the water re-entrainment into the reactor was deeper than expected, and more irregular (Figure 97 and Figure 98). This was in part due to the high wettability of the glass surface. The extent of the re-entrainment meant that it would not be possible to move the plasma so close to the water and still allow the formation of small bubbles. Alterations of the design of the reactor would need to be made. Over the period where bubbles as wide as the pore diameter are forming, occasionally one bubble forms which is significantly wider than the pore diameter. Immediately after this bubble detaches, a relatively large amount of water re-entrains into the whole reactor, and is eventually blown out again after a time as the pressure recovers . The problem with this re-entrainment is that the water will clearly enter the plasma. Water was observed to enter the plasma in the field trials and the result was that the water could not be broken down as the air could, and the reactor essentially stopped producing any products, whilst still consuming power. There was also the additional problem that the cuvette volume was extremely small and large bubbles would cause any liquid in it to splash out, thus liquid chemical measurements could not be made in this container as small bubbles could not be used either due to the re-entrainment of water into the plasma reactor. Also, the flow rate through a single capillary reactor was too small to push gas through the head of a dreschel bottle, and multiple capillary reactors would have been problematic and time consuming to test. It was decided that the emission spectrum, camera frames and power signals of the reactors would be enough to derive useful data from.

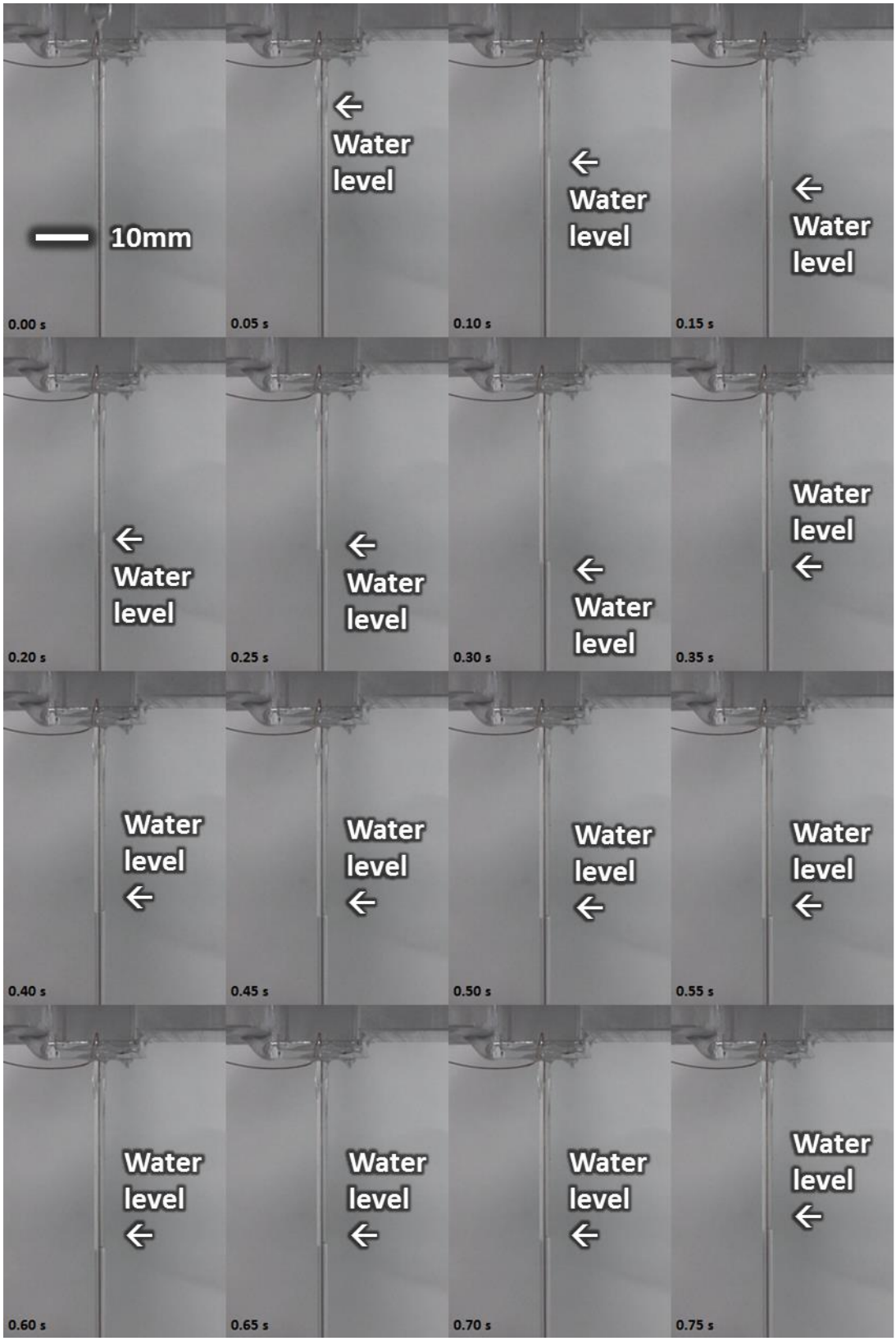

Figure 97: A sequence of frames to show the sequence of water re-entrainment into the capillary reactors with time. Note that at t=0 a large bubble can be observed forming at the orifice, which then gives rise to the following "flooding" of the reactor.

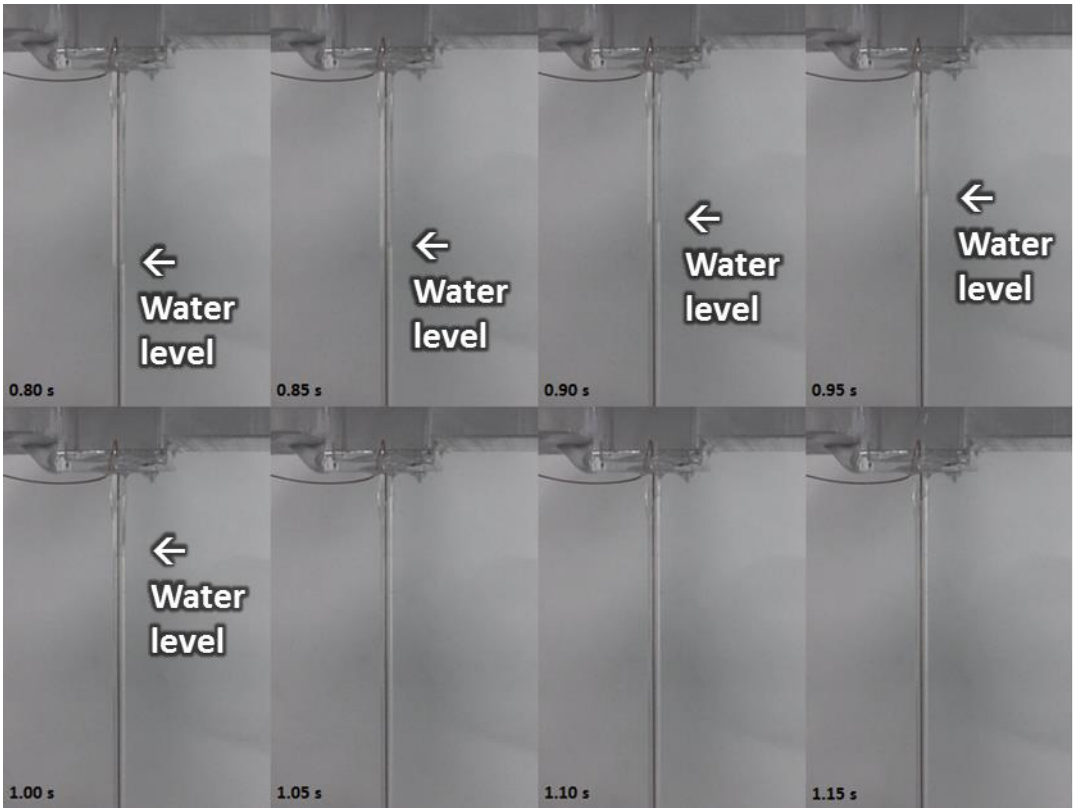

Figure 98: Continuation of Figure 97.

5.6 Solution to water re-entrainment from increasing proximity

A reactor design that allowed for re-entrainment without flooding the plasma reactor was clearly required and a solution to the problem of water re-entrainment into the reactor was pursued. The water re-entrainment was due in part to the high wettability of glass, but a more hydrophobic material would not have the advantage of forming smaller bubbles. Water re-entrainment into the reactor seems to be necessary for the formation of smaller bubbles, so even coating the interior of the pore with hydrophobic material would still adversely affect the bubble formation.

A u-tube arrangement was considered, with the plasma facing downward. This would solve the problem of preventing the plasma from being flooded, but would have meant that the plasma could not be moved close enough to the air/water interface to allow for really short time gaps to maximise the short lived species reaching the interface.

A design was eventually found that allowed bubble formation, and at the same time allowing the interface to get as close to the plasma as possible. The design had the added benefit that the oscillated air from the plasma created a suction that drew water up from the lower tube and out through the upper tube. The result was a continuous flow of interface past the plasma reactor. The

water also formed a film on the inside of the upper tube which gave the advantage of reducing the bubble diameter at the orifice.

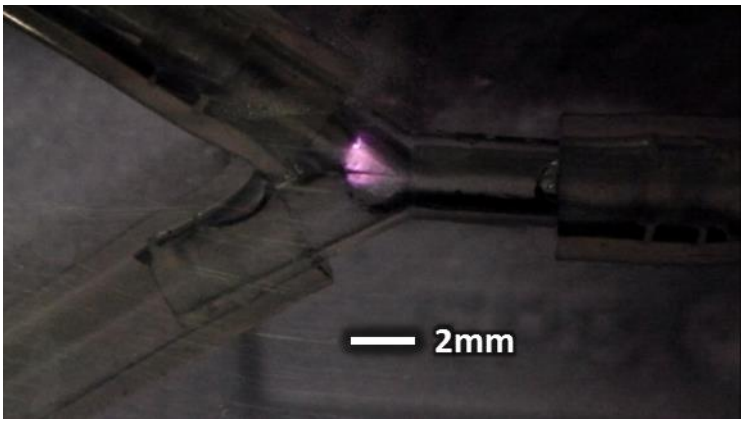

Figure 99: Photograph of the plasma jumping onto the air/water interface.

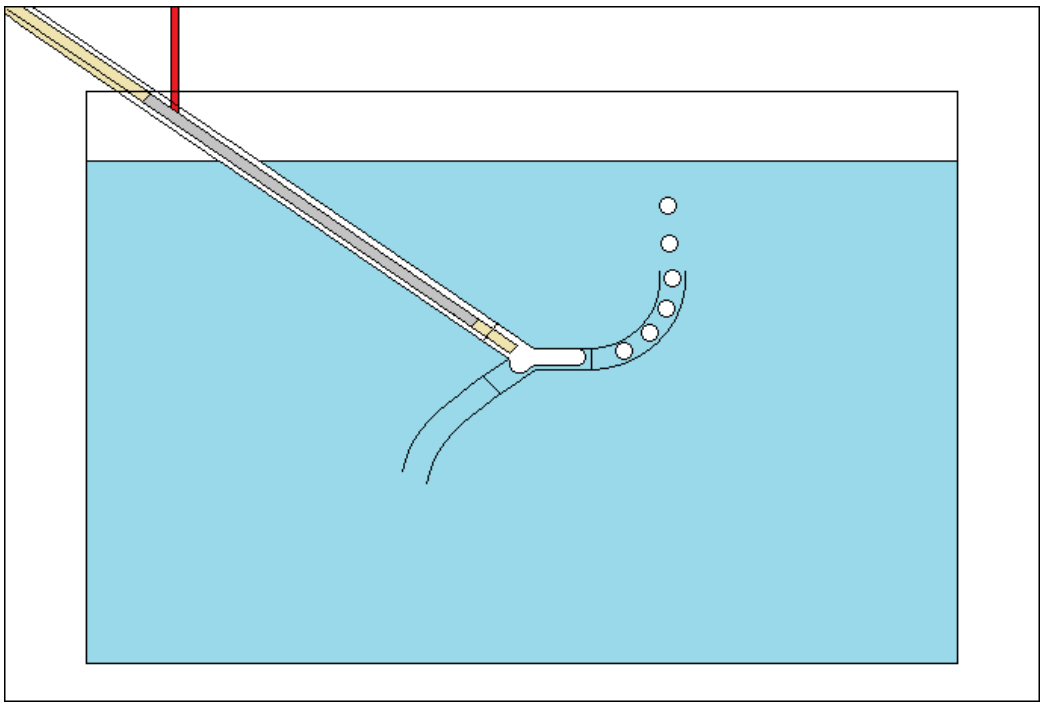

Figure 100: Diagram of the solution to the bubble re-entrainment problem. The tank was filled with water, and chemicals could be dissolved in this for analysis.

For continuous testing of the plasma over longer periods of time (for example, to produce measurable amounts of terephthalic acid results) alumina was used instead of glass, as this is a much more robust material to use as a dielectric. Another reason for using the initial alumina bore tube reactors was that the copper wires for the internal electrodes could not be connected in this reactor configuration as they were for the dry capillary reactor experiments.

The continuous flow of interface was particularly advantageous, as the kinetic model predicted that increasing the plasma proximity to the interface would increase the formation of hydroxyl radicals from the O atom colliding with the surface (Figure 51). Hydroxyl radicals are powerful oxidisers, and react very rapidly, thus would be hard to distribute throughout the liquid as they would likely be quenched by dissolved chemicals close to the source, preventing them from reaching areas deeper in the liquid. This reactor arrangement has the effect of bringing the liquid to the plasma, instead of the other way round.

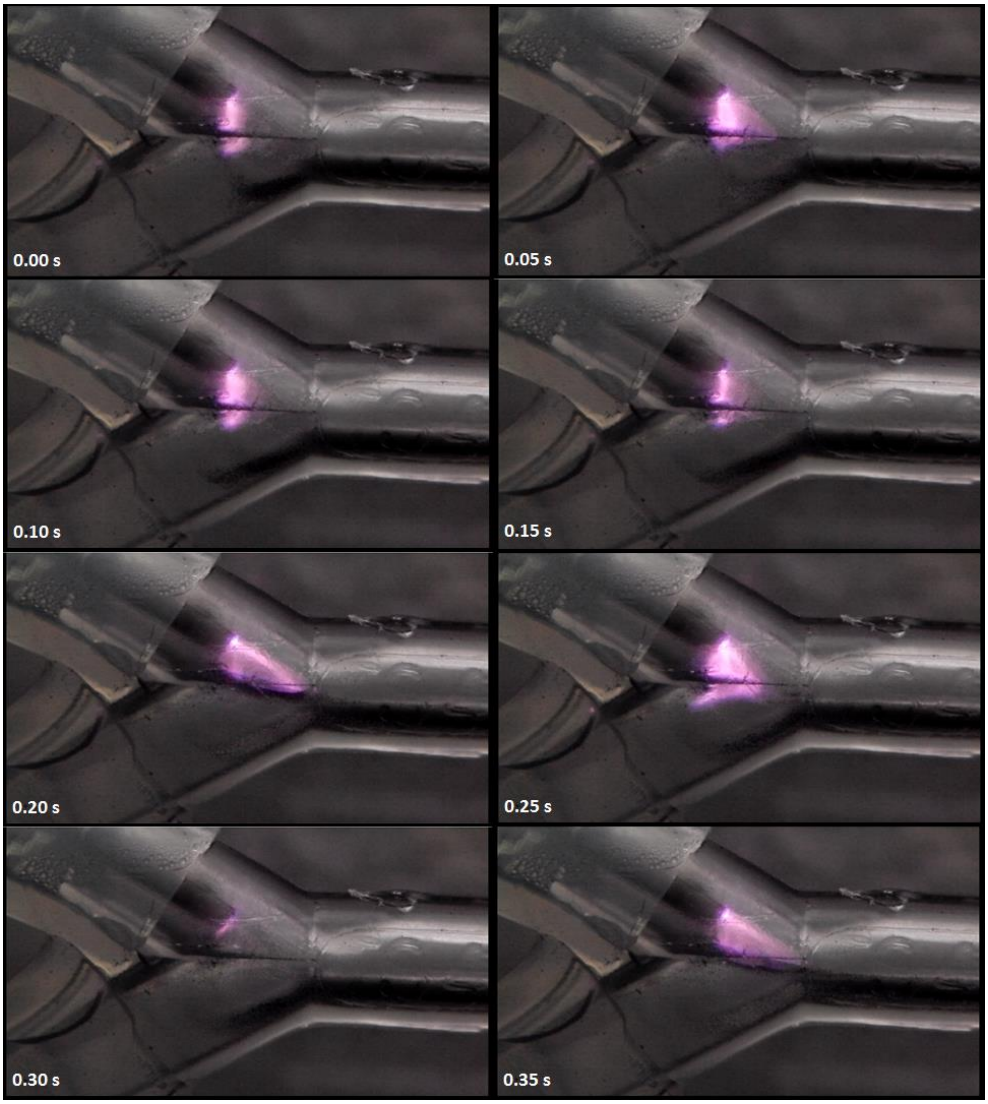

Figure 101: A series of frames of the plasma y-tube reactor, the plasma can be seen jumping on to the air water interface.

A preliminary experiment was conducted with the plasma reactor as close to the interface as possible, which led to some encouraging results. The plasma appeared to jump directly onto the interface (Figure 99), which was an ideal situation for the interfacial chemistry to take place. The plasma would follow the interface as it pulsed back and forth (Figure 101 and Figure 102).

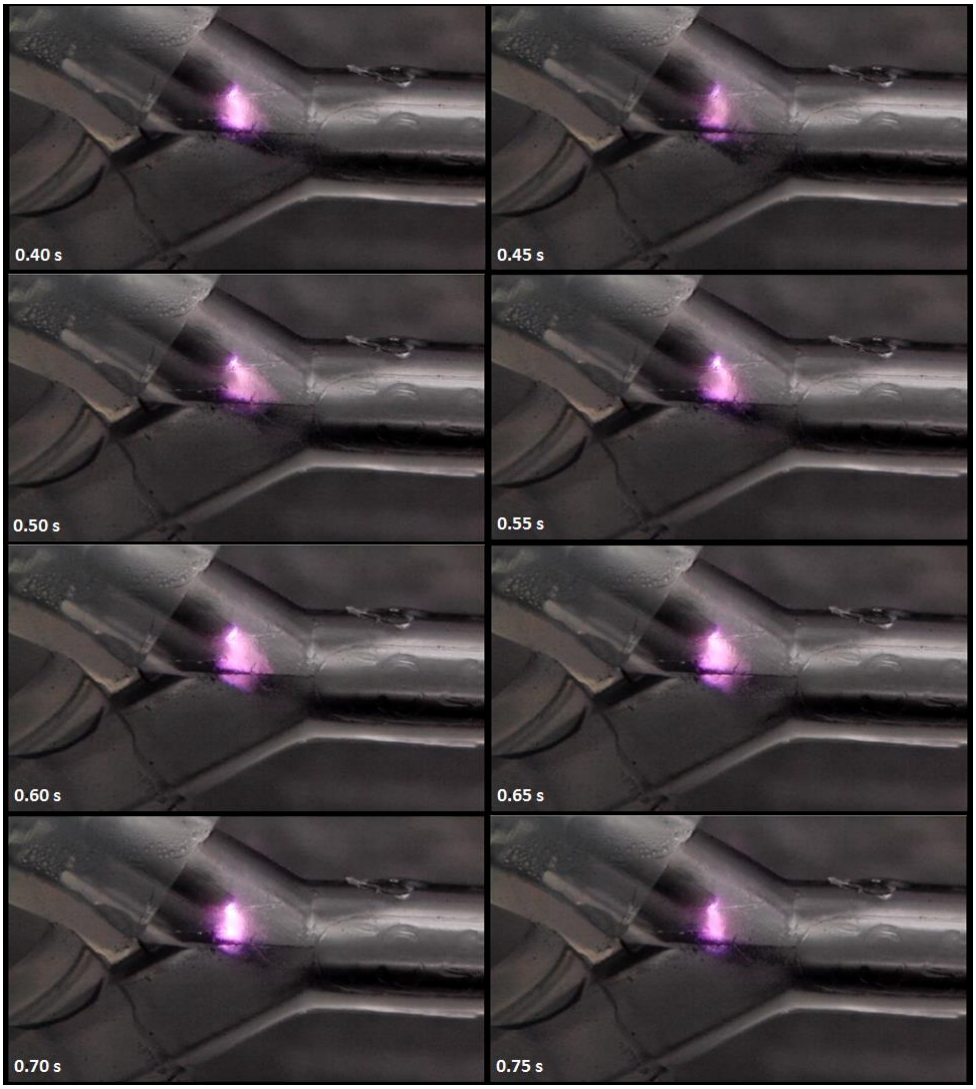

Figure 102: continued from Figure 101.

The emission spectrum and voltage characteristics of this reactor were measured. It was observed that the RMS voltage increased during the times at which the plasma was jumping on to the interface, suggesting that the power draw was proportionally higher at these points (Figure 103 and Figure 104).

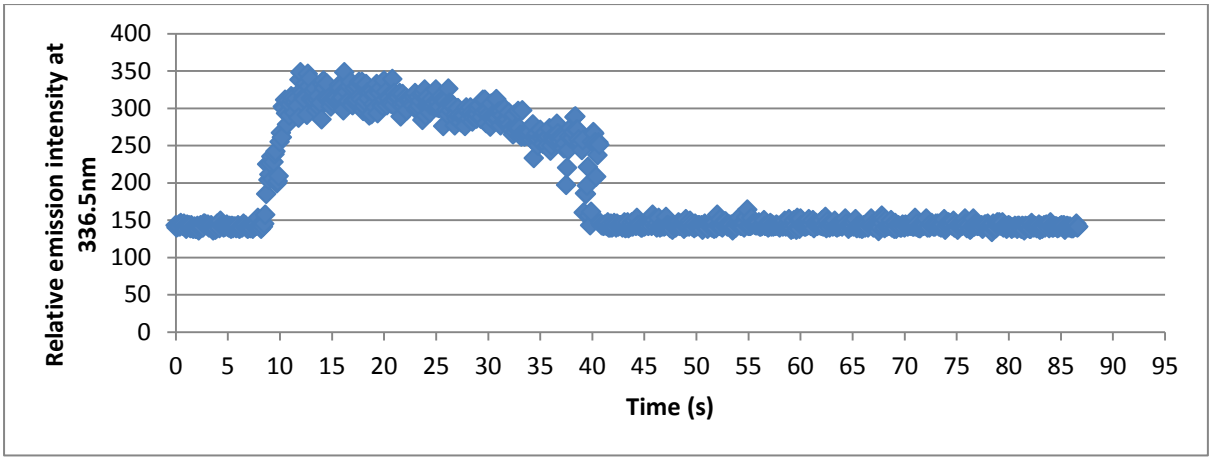

Figure 103: Emission intensity of spectral peak at 336.38nm, taken over a period of operation of the y-tube reactor.

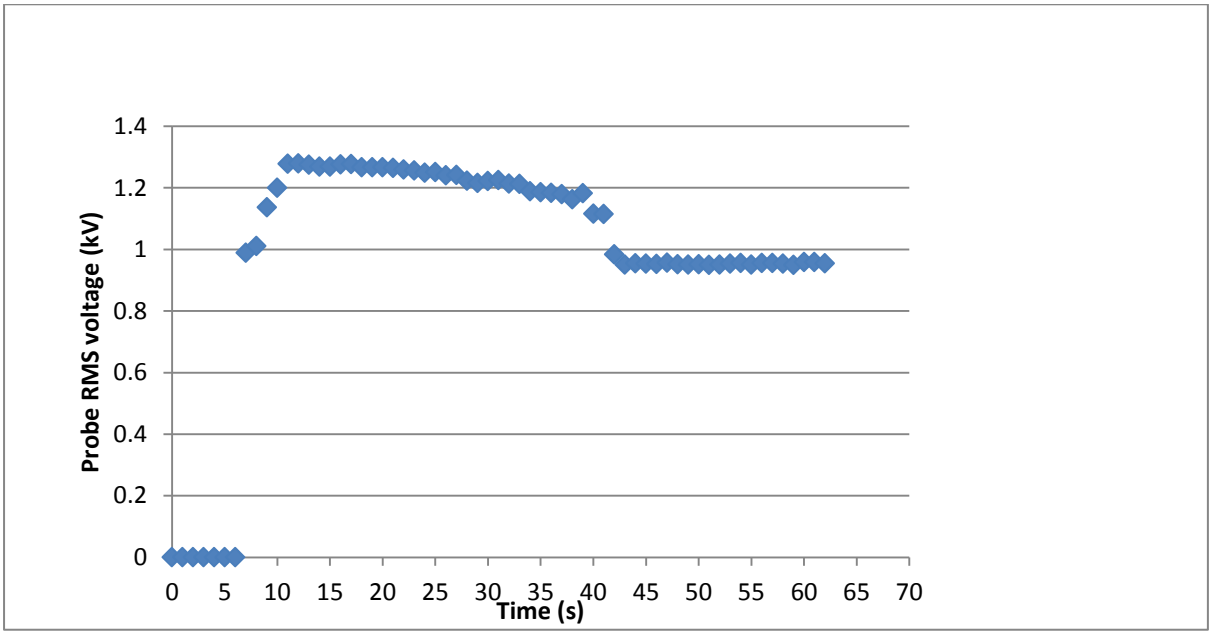

Figure 104: RMS voltage values of measured voltage signals over the period of operation in Figure 103.

Two experiments were conducted varying the proximity of the plasma to the interface. The first was conducted using the indigo method (Bader & Hoigné, 1981) (see Appendix 1). The reactors were identical, the flow rates were identical, the volume of the tank was identical, even the angle was identical. Thus it can be hypothesised that the trends we see here are due to the proximity alone. Indigo is susceptible to interference from many oxidizing species. It is quite possible that the trends seen in indigo oxidation, expressed as ozone equivalents, are due to a combination of reactive oxygen and nitrogen species generated in the plasma streamers. The second experiment was conducted with the terephthalic acid method (Mason et al., 1994) (see Appendix 1) which reacts only with the hydroxyl radical. The slight decrease in hydroxyl radical concentration

after the initial increase for the 1.3mm gap distance can be attributed to fluid circulation within the tank. This does not detract from the qualitative value of the results, namely that plasma acting on the interface was observed to produce hydroxyl radicals, whilst an identical plasma some distance away was not. The results suggest that the increase in OH radical concentration is due to the action of the plasma on the air/water interface. The timescales involved also make the alternative explanation of enhanced ozone decomposition unlikely. The quantitative value, whilst not as accurate as would be ideal, is not dissimilar to the results predicted by the kinetic model in terms of the concentrations of the OH radicals in solution.

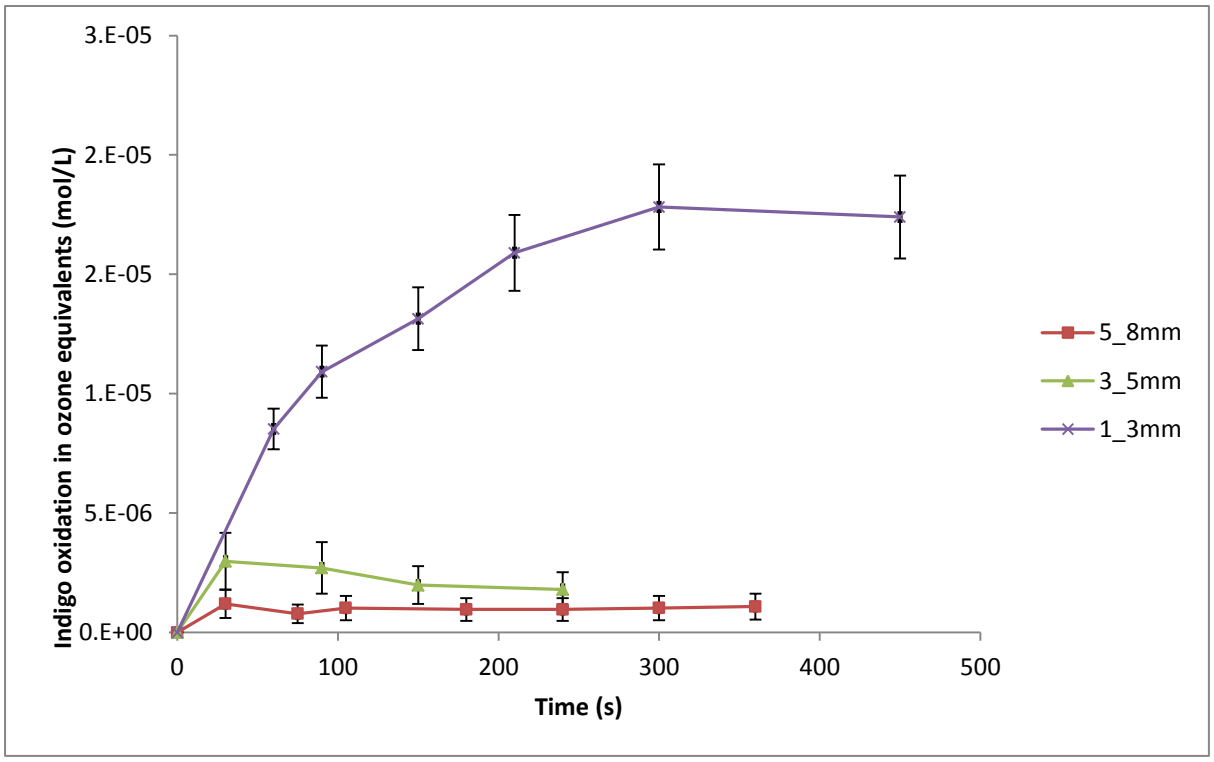

Figure 105: Measured values of indigo decolouration with time with increasing proximity to the reactor. The plasma was observed to be making contact with the interface at the distance of 1.3mm.

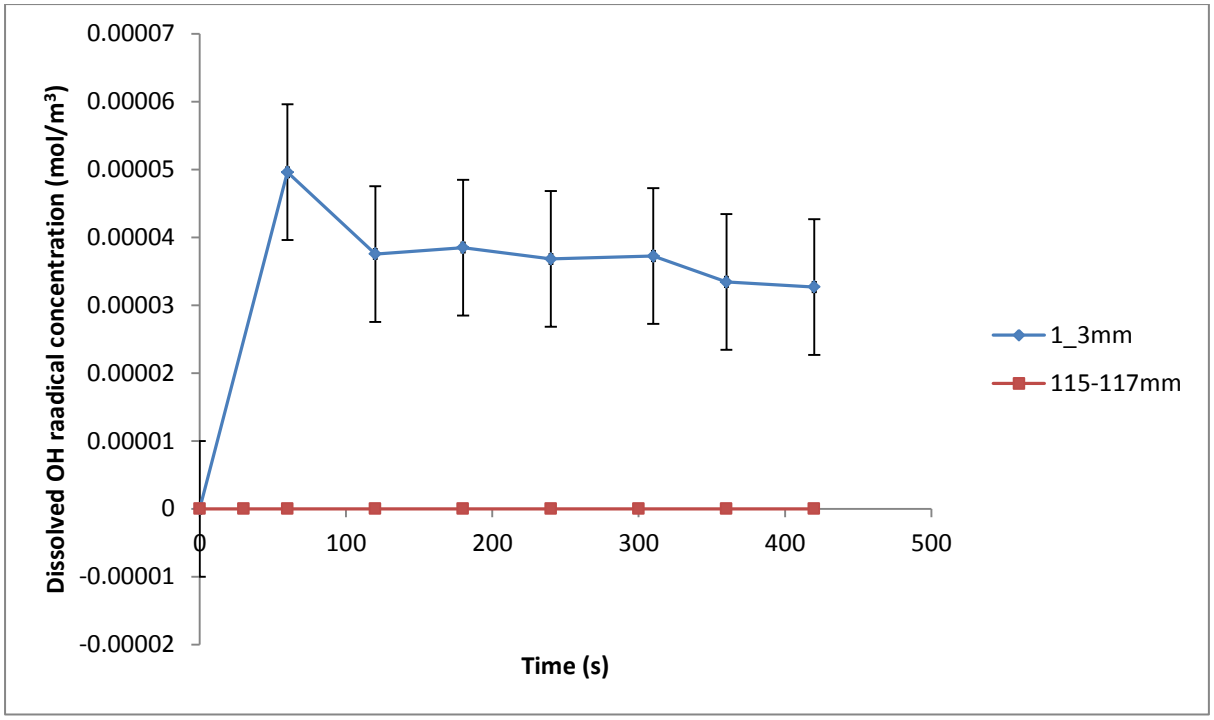

Figure 106: Measurement of hydroxyl radical production by hydroxylation of terephthalic acid for two distances from the air water interface.

5.7 Discussion and conclusions

The emission spectrum intensity became stronger as the electrodes were shortened, and the fluidic oscillator appeared to have the effect of reducing the emission spectrum intensity, suggesting that oscillatory flow reducing the specific energy of the plasma, which may make conditions more preferable for ozone formation.

The flow rate of 5ml/min was used throughout, but accurate measurement was difficult due to the effect of the fluidic oscillator on the use of the rotameter, and the effect of the electromagnetic interference of the plasma on electronic instruments. Very low flow rate rotameters were used, and the flow was at the lowermost reading, even occasionally appearing to stop. Thus, although repeats were made for each electrode length, the error on the data is still large, and a very extensive set of experimental runs would be recommended to be more certain of the trend. However, one does accept the trend then one can conclude that the fluidic oscillator can have an effect on the plasma conditions.

The oscillator alternates rapid stopping and starting of the flow, which might interfere with microdischarge formation. In the stopped flow phase of the fluidic oscillation, the streamer intensity can build up in the same location, reaching higher emission intensities. In the moving flow phase of

the oscillation however, the flow is more rapid than in an equivalent steady flow, which would decrease the time for species excitation in the plasma.

It would be expected that this effect would not be as pronounced when the reactor is long enough for the static and moving flows of the oscillated flow to be averaged along the length of the reactor, but the effect should become more pronounced as the reactor length becomes shorter, as the reactor may alternate between predominantly flowing and predominantly static periods of oscillation.

Shortening the electrodes for the same power clearly increases the emission spectrum, which is an indication of an increase in the power density in the reactor. As seen previously in Chapter 4, the power intensity also increases with a decrease in gap size. Thus an ideal combination of high power intensity and short residence time can be achieved by scaling the plasma reactors down.

Unfortunately, the effect of water re-entrainment was much more pronounced than might have been expected due to irregularities in bubble formation. Irregularities can be reduced, but it is doubtful that they can be eliminated altogether, as even if the flow into the reactor was perfectly controlled there would still be unavoidable variations in the flow of the bulk liquid, especially if the device was applied to industrial conditions.

Water re-entrainment into the pore is desirable for reducing the bubble size and easing bubble break-off, but as can be seen from section 4.4.2, water re-entraining into the reactor would result in problems with the operation of the plasma, increasing the breakdown voltage in the gap to values well above those expected in the design of an air plasma, resulting in reactor down time each time water re-entrains. However, electrolysis or electrical breakdown of water will also result in the formation of oxidative radical species and a reactor would need to be modified to alternate between continuous breakdown of air and intermittent breakdown of water. The power supply of the plasma would need to be sensitive and rapidly responsive to the unpredictable changes in impedance. This would be a project for an electrical and electronic engineering researcher.

The alternative of the y-tube reactor was a way round this. The y-tube can bypass the problem of bubble re-entrainment by altering the angle of the plasma reactor in a u-tube-like fashion. The air blowing through the y tube has the effect of sucking the water up through the upper tube, creating a flow of air water interface past the plasma. This is especially advantageous as the hydroxyl radicals are short lived and their action will be greatest closest to the point of their generation.

The oxidative degradation of the indigo solution may not be due solely to the occurrence of ozone and the OH radical. Electron collisions with the air/water interface will almost certainly play a part as

the streamers of the plasma clearly are forming between the water and the plasma, and the kinetic model would need to be modified to account for this. There are a number of radical species and other reactive species that could also play a part, but accurately measuring each one chemically would have been extremely time consuming, and as many of the species were short lived it would have been even more difficult to take samples and analyse them elsewhere. At present, the oxidation of indigo will have to suffice for a measure of their total oxidative activity, but any future study into this device must include quantification of all the RONS expected to play a part.

Regarding the power consumption, the y-tube reactor is nowhere near optimised, so the effectiveness of treatment might seem low. The temperature in the reactor would be extremely hot, and due to the high insulation produced by the PTFE tube, the plasma is likely to have heated up to the point where NOx formation would take over from ozone and OH radical formation.

5.7.1 Future work

A study of the effects of the fluidic oscillator on the plasma with a more accurate spectrometer would be a useful pursuit, as it may reveal means of increasing the efficiencies of some plasma chemical processes.

The power supply signal could be timed with the oscillation pulse, perhaps with some sensor mechanism to ensure they remain in sync, in order to ensure that the appropriate amount of energy is supplied. Synchronising power supply modulation with the fluidic oscillations would be a future endeavour that could be applied to the effects of cooling the plasma.

As the reactor is scaled down, the diameter of the bubble formation orifice will become smaller and the depth of water re-entrainment into the vertical tube reactor geometry should decrease due to the increased surface adhesion of water resisting the pressure from the water head. However, the y-tube geometry is certainly worth investigating. The contact of the plasma with the water means that a kinetic study of this process would need to have greater emphasis on the activity of the electrons on the interface, and also on the excited species effects on the interface, neither of which was taken into account in the model in chapter 3.

Further tests need to be conducted to verify the formation of other RONS besides ozone and OH radicals from the y-tube reactor.

References

Adewuyi, Y. G. (2005). Critical Review Sonochemistry in Environmental Remediation. 1. Combinative and Hybrid Sonophotochemical Oxidation Processes for the Treatment of Pollutants in Water. *Environmental Science & Technology*, *39*(10), 3409–3420.

Agarwal, A., Ng, W., & Liu, Y. (2011). Principle and applications of microbubble and nanobubble technology for water treatment. *Chemosphere*, *84*, 1175–1180. doi:10.1016/j.chemosphere.2011.05.054

Aleksandrov, N., Bazyelan, E., Kochetov, I., & Dyatko, N. (1997). The ionization kinetics and electric field in the leader channel in long air gaps. *Journal of Physics D: Applied Physics*, *30*, 1616–1624.

Alty, T. (1924). The Cataphoresis of Gas Bubbles in Water. *Proceedings of the Royal Society A: Mathematical, Physical and Engineering Sciences*, *106*(737), 315–340. doi:10.1098/rspa.1924.0072

Alvarez, P., Garciaaraya, J., Beltran, F., Giraldez, I., Jaramillo, J., & Gomezserrano, V. (2006). The influence of various factors on aqueous ozone decomposition by granular activated carbons and the development of a mechanistic approach. *Carbon*, *44*, 3102–3112. doi:10.1016/j.carbon.2006.03.016

Ammann, M., Cox, R. a., Crowley, J. N., Jenkin, M. E., Mellouki, a., Rossi, M. J., … Wallington, T. J. (2013). Evaluated kinetic and photochemical data for atmospheric chemistry: Volume VI – heterogeneous reactions with liquid substrates. *Atmospheric Chemistry and Physics*, *13*(16), 8045–8228. doi:10.5194/acp-13-8045-2013

Andreozzi, R., Caprio, V., Insola, A., & Marotta, R. (1999). Advanced oxidation processes (AOP) for water purification and recovery. *Catalysis Today*, *53*, 51–59.

Andresen, P., Ondrey, G., & Titze, B. (1984). Nuclear and electron dynamics in the photodissociation of water. *The Journal of Chemical Physics*, *80*(6), 2548–2569.

Antonopoulou, M., Evgenidou, E., Lambropoulou, D., & Konstantinou, I. (2014). A review on advanced oxidation processes for the removal of taste and odor compounds from aqueous media. *Water Research*, *53*, 215–34. doi:10.1016/j.watres.2014.01.028

Ashokkumar, M. (2011). The characterization of acoustic cavitation bubbles - an overview. *Ultrasonics Sonochemistry*, *18*(4), 864–872. doi:10.1016/j.ultsonch.2010.11.016

Ashpis, D. E., Laun, M. C., & Griebeler, E. L. (2012). Progress toward Accurate Measurements of Power Consumptions of DBD Plasma Actuators. In *50th AIAA Aerospace Sciences Meeting including the New Horizons Forum and Aerospace Exposition* (pp. 1–24). doi:10.2514/6.2012-823

Babuponnusami, A., & Muthukumar, K. (2014). A review on Fenton and improvements to the Fenton process for wastewater treatment. *Journal of Environmental Chemical Engineering*, *2*(1), 557–572. doi:10.1016/j.jece.2013.10.011

Bader, H., & Hoigné, J. (1981). Determination of ozone in water by the indigo method. *Water Research*, *15*(11100).

Barni, R., Esena, P., & Riccardi, C. (2005). Chemical kinetics simulation for atmospheric pressure air plasmas in a streamer regime. *Journal of Applied Physics*, *97*(7), 073301. doi:10.1063/1.1879081

Barrett, J., & Baxendale, J. H. (1960). The Photolysis of Liquid Water. *Transactions of the Faraday Society*, *56*(1), 37–43.

Beckett, M. a, & Hua, I. (2001). Impact of Ultrasonic Frequency on Aqueous Sonoluminescence and Sonochemistry. *The Journal of Physical Chemistry A*, *105*(15), 3796–3802.

Bellar, T., Lichtenberg, J., & Kroner, R. (1974). The occurrence of organohalides in chlorinated drinking waters. *Journal (American Water Works Association)*, *66*(12), 703–706.

Beltrán, F. (2003, December 29). Ozone Reaction Kinetics for Water and Wastewater Systems. CRC Press. doi:10.1201/9780203509173

Beltran, F., Garcia-Araya, J., & Alvarez, P. (1999). Integration of continuous biological and chemical (ozone) treatment of domestic wastewater: 2. Ozonation followed by biological oxidation. *Journal of Chemical Technology & Biotechnology*, *74*, 884–890.

Bhosle, S., Zissis, G., Damelincourt, J. J., & Dawson, F. P. (2004). Calculation of the impedance of an axisymetric DBD lamp for power supply design purposes. *Conference Record of the 2004 IEEE Industry Applications Conference, 2004. 39th IAS Annual Meeting.*, *3*, 1667–1670. doi:10.1109/IAS.2004.1348694

Bibinov, N., Dudek, D., Awakowicz, P., & Engemann, J. (2007). Characterization of an atmospheric pressure dc plasma jet. *Journal of Physics D: Applied Physics*, *40*(23), 7372–7378. doi:10.1088/0022-3727/40/23/018

Bird, R. B., Stewart, W. E., & Lightfoot, E. N. (2002). *Transport Phenomena*. *Applied Mechanics Reviews* (Vol. 55, p. R1). doi:10.1051/jp4:20020462

Bokare, A. D., & Choi, W. (2014). Review of iron-free Fenton-like systems for activating H2O2 in advanced oxidation processes. *Journal of Hazardous Materials*, *275*, 121–35. doi:10.1016/j.jhazmat.2014.04.054

Bredwell, M., & Worden, R. (1998). Masstransfer properties of microbubbles. 1. Experimental studies. *Biotechnology Progress*, *14*, 31–38.

Buhler, R. E., Staehelin, J., & Hoigne, J. (1984). Ozone Decomposition in Water Studied by Pulse Radiolysis 1. HO2/O2- and HO3/O3- as Intermediates. *Journal of Physical Chemistry*, *88*, 2560–2564.

Buxton, G., Greenstock, C., Helman, W., & Ross, A. (1988). Critical review of rate constants for reactions of hydrated electrons, hydrogen atoms and hydroxyl radicals (· OH/· O−) in aqueous solution. *J.Phys.Chem.Ref.Data*, *17*(2), 513–886.

Camacho, J. J., Poyato, J. M. L., Díaz, L., & Santos, M. (2007). Optical emission studies of nitrogen plasma generated by IR CO 2 laser pulses. *Journal of Physics B: Atomic, Molecular and Optical Physics*, *40*(24), 4573–4590. doi:10.1088/0953-4075/40/24/003

Capitelli, M., Ferreira, C., Gordiets, B., & Osipov, A. (2000). *Plasma Kinetics in Atmospheric Gases*. Springer.

Castillo, M., Herrero, V. J., & Tanarro, I. (2002). Characterization and modelling of the steady state and transients of modulated hollow cathode discharges of nitric oxide. *Plasma Sources Science and Technology*, *11*(4), 368–376. doi:10.1088/0963-0252/11/4/302

Catalkaya, E., & Kargi, F. (2009). Degradation and mineralization of simazine in aqueous solution by ozone/hydrogen peroxide advanced oxidation. *Journal of Environmental Engineering*, *135*, 1357–1364.

Cavalcanti, E. B., Garcia-Segura, S., Centellas, F., & Brillas, E. (2013). Electrochemical incineration of omeprazole in neutral aqueous medium using a platinum or boron-doped diamond anode: degradation kinetics and oxidation products. *Water Research*, *47*(5), 1803–15. doi:10.1016/j.watres.2013.01.002

Chaplin, B. P. (2014). Critical review of electrochemical advanced oxidation processes for water treatment applications. *Environmental Science. Processes & Impacts*, *16*(6), 1182–203. doi:10.1039/c3em00679d

Chen, W. R., Wu, C., Elovitz, M. S., Linden, K. G., & Mel Suffet, I. H. (2008). Reactions of thiocarbamate, triazine and urea herbicides, RDX and benzenes on EPA Contaminant Candidate List with ozone and with hydroxyl radicals. *Water Research*, *42*(1-2), 137–44. doi:10.1016/j.watres.2007.07.037

Chen, Z. (2002). Impedance matching for one atmosphere uniform glow discharge plasma (OAUGDP) reactors. *Plasma Science, IEEE Transactions on*, *30*(5), 1922–1930.

Chen, Z. (2003). PSpice Simulation of One Atmosphere Uniform Glow Discharge Plasma (OAUGDP) Reactor Systems. *IEEE Transactions on Plasma Science*, *31*(4), 511–520.

Chong, M. N., Jin, B., Chow, C. W. K., & Saint, C. (2010). Recent developments in photocatalytic water treatment technology: a review. *Water Research*, *44*(10), 2997–3027. doi:10.1016/j.watres.2010.02.039

Chu, L., Xing, X., Yu, A., Zhou, Y., & Sun, X. (2007). Enhanced ozonation of simulated dyestuff wastewater by microbubbles, *68*, 1854–1860. doi:10.1016/j.chemosphere.2007.03.014

Collins, G. L., Motarjemi, M., & Jameson, G. J. (1978). A method for measuring the charge on small gas bubbles. *Journal of Colloid and Interface Science*, *63*(1), 69–75. doi:10.1016/0021-9797(78)90036-X

Comninellis, C., Kapalka, A., Malato, S., Parsons, S. A., Poulios, I., & Mantzavinos, D. (2008). Advanced oxidation processes for water treatment: advances and trends for R&D. *Journal of Chemical Technology & Biotechnology*, *83*, 769–776. doi:10.1002/jctb

Creux, P., Lachaise, J., Graciaa, A., Beattie, J. K., & Djerdjev, A. M. (2009). Strong specific hydroxide ion binding at the pristine oil/water and air/water interfaces. *The Journal of Physical Chemistry. B*, *113*(43), 14146–50. doi:10.1021/jp906978v

Criegee, R. (1975). Mechanism of ozonolysis. *Angewandte Chemie International Edition in English*, *14*(11), 745–752.

Croue, J., Beltran, F., Legube, B., & Dore, M. (1989). Effect of preozonation on the organic halide formation potential of an aquatic fulvic acid. *Industrial and Engineering Chemistry Res.*, *28*, 1082–1089.

Da Silva, L. M., Franco, D. V., Forti, J. C., Jardim, W. F., & Boodts, J. F. C. (2006). Characterisation of a laboratory electrochemical ozonation system and its application in advanced oxidation processes. *Journal of Applied Electrochemistry*, *36*(5), 523–530. doi:10.1007/s10800-005-9067-x

Dhar, N. R. (1934). Formation of Hydroxyl Radical from the Photolysis of Water and the Generation of Formaldehyde. *Transactions of the Faraday Society*, *30*, 142–147.

Eliasson, B., & Kogelschatz, U. (1991). Modeling and applications of silent discharge plasmas. *IEEE Transactions on Plasma Science*, *19*(2), 309–323.

Eliasson, B., & Kogelschatz, U. (1991). Nonequilibrium volume plasma chemical processing. *IEEE Transactions on Plasma Science*, *19*(6), 1063–1077.

Eliasson, B., & Kogelschatz, U. (1999). Electron impact dissociation in oxygen. *Journal of Physics B: Atomic and Molecular Physics*. doi:10.1088/0022-3700/19/8/018

Fang, G.-D., Dionysiou, D. D., Wang, Y., Al-Abed, S. R., & Zhou, D.-M. (2012). Sulfate radical-based degradation of polychlorinated biphenyls: effects of chloride ion and reaction kinetics. *Journal of Hazardous Materials*, *227-228*, 394–401. doi:10.1016/j.jhazmat.2012.05.074

Farrell, J. R., & McTigue, P. (1982). Precise Compensating Potential Difference Measurements with a Voltaic Cell. The Surface Potential of Water. *Journal of Electronalytical Chemistry*, *139*, 37–56.

Fenton, H. J. H. (1894). Oxidation of tartaric acid in presence of iron. *Journal of the Chemical Society, Transactions*, *65*, 899–910.

Fernández-Castro, P., Vallejo, M., San Román, M. F., & Ortiz, I. (2015). Insight on the fundamentals of advanced oxidation processes. Role and review of the determination methods of reactive oxygen species. *Journal of Chemical Technology & Biotechnology*, *90*(5), 796–820. doi:10.1002/jctb.4634

Ferreira, C. M., Gordiets, B., Tatarova, E., Henriques, J., & Dias, F. M. (2012). Air–water microwave plasma torch as a NO source for biomedical applications. *Chemical Physics*, *398*, 248–254. doi:10.1016/j.chemphys.2011.05.024

Fleagle, R. G., & Businger, J. A. (1980). *An Introduction to Atmospheric Physics* (2nd ed.). Academic press.

Fridman, A. (2008). *Plasma chemistry*. Cambridge University Press.

Fridman, A., Gutsol, A., & Cho, Y. (2007). Plasma Discharges in Water. In A. Fridman & Y. Cho (Eds.), *Advances in Heat Transfer. Transport Phenomena in Plasma* (1st ed., pp. 104–124). Academic press.

Fujishima, a, Zhang, X., & Tryk, D. (2007). Heterogeneous photocatalysis: From water photolysis to applications in environmental cleanup. *International Journal of Hydrogen Energy*, *32*(14), 2664–2672. doi:10.1016/j.ijhydene.2006.09.009

Gatilova, L. V, Allegraud, K., Guillon, J., Ionikh, Y. Z., Cartry, G., Röpcke, J., & Rousseau, a. (2007). NO formation mechanisms studied by infrared laser absorption in a single low-pressure plasma pulse. *Plasma Sources Science and Technology*, *16*(1), S107–S114. doi:10.1088/0963-0252/16/1/S12

Glaze, W. H. (1986). Reaction products of ozone: A review. *Environmental Health Perspectives*, *69*, 151–157. doi:10.1289/ehp.8669151

Gonzalez, M., Oliveros, E., Worner, M., & Braun, a. (2004). Vacuum-ultraviolet photolysis of aqueous reaction systems. *Journal of Photochemistry and Photobiology C: Photochemistry Reviews*, *5*(3), 225–246. doi:10.1016/j.jphotochemrev.2004.10.002

Gordiets, B., Ferreira, C., Guerra, V., Loureiro, J., Nahorny, J., Pagnon, D., … Vialle, M. (1995). Kinetic Model of a Low-Pressure N 2-O 2 Flowing Glow Discharge. *IEEE Transactions on Plasma Science*, *23*(4), 750–768.

Gottschalk, C., Libra, J. A., & Saupe, A. (2000). *Ozonation of Water and Waste Water. A Practical Guide to Understanding Ozone and its Application*. WILEY-VCH.

Graciaa, A., Morel, G., Saulner, P., Lachaise, J., & Schechter, R. S. (1995). THE ZETA-POTENTIAL OF GAS-BUBBLES. *Journal of Colloid and Interface Science*, *172*(1), 131–136.

Graves, D. B. (2012). The emerging role of reactive oxygen and nitrogen species in redox biology and some implications for plasma applications to medicine and biology. *Journal of Physics D: Applied Physics*, *45*(26), 263001. doi:10.1088/0022-3727/45/26/263001

Gray-Weale, A., & Beattie, J. K. (2009). An explanation for the charge on water's surface. *Physical Chemistry Chemical Physics : PCCP*, *11*(46), 10994–1005. doi:10.1039/b901806a

Grčić, I., Mužic, M., Vujević, D., & Koprivanac, N. (2009). Evaluation of atrazine degradation in UV/FeZSM-5/H2O2 system using factorial experimental design. *Chemical Engineering Journal*, *150*, 476–484. doi:10.1016/j.cej.2009.01.037

Guerra, V., & Loureiro, J. (1999). Kinetic model of a low-pressure microwave discharge in O2-N2 including the effects of O- ions on the characteristics for plasma maintenance. *Plasma Sources Science and Technology*, *8*, 110–124.

Guerra, V., Pinheiro, M., Gordiets, B., Loureiro, J., & Ferreira, C. (1997). Calculated data on electron transport and excitation rate coefficients in and discharges. *Plasma Sources Science and Technology*, *6*, 220–230.

Han, P., & Bartels, D. (1996). Temperature Dependence of Oxygen Diffusion in H2O and D2O. *Journal of Physical Chemistry*, *100*, 5597–5602.

Heering, W. (2004). UV sources-basics, properties and applications. *IUVA News*, *6*(4), 7–13.

Hoigné, J., & Bader, H. (1976). The role of hydroxyl radical reactions in ozonation processes in aqueous solutions. *Water Research*, *10*(5), 377–386.

Horne, R. A., & Courant, R. A. (1964). The Temperature Dependence of the Activation Energy of the Electrical Conductivity of Sea Water in the Temperature Range 0°C to 10°C. *Journal of Geophysical Research*, *69*(6), 1152–1154.

Ishiyama, T., & Morita, A. (2009). Analysis of anisotropic local field in sum frequency generation spectroscopy with the charge response kernel water model. *The Journal of Chemical Physics*, *131*(24), 244714. doi:10.1063/1.3279126

Ismail, M., Khan, H. M., Sayed, M., & Cooper, W. J. (2013). Advanced oxidation for the treatment of chlorpyrifos in aqueous solution. *Chemosphere*, *93*(4), 645–51. doi:10.1016/j.chemosphere.2013.06.051

Israelachvili, J. N. (2011). *Intermolecular and Surface Forces* (Third Edit.). Elsevier.

Jacobson, M. . (2005). *Fundamentals of Atmospheric Modelling* (2nd ed.). Cambridge University Press.

James, D. (1968). The thermal diffusivity of ice and water between −40 and +60°C. *Journal of Materials Science*, *3*, 540–543.

Joseph, C. G., Li Puma, G., Bono, A., & Krishnaiah, D. (2009). Sonophotocatalysis in advanced oxidation process: a short review. *Ultrasonics Sonochemistry*, *16*(5), 583–9. doi:10.1016/j.ultsonch.2009.02.002

Jyoti, K. K., & Pandit, a. B. (2004). Ozone and cavitation for water disinfection. *Biochemical Engineering Journal*, *18*(1), 9–19. doi:10.1016/S1369-703X(03)00116-5

Klavarioti, M., Mantzavinos, D., & Kassinos, D. (2009). Removal of residual pharmaceuticals from aqueous systems by advanced oxidation processes. *Environment International*, *35*(2), 402–17. doi:10.1016/j.envint.2008.07.009

Kogelschatz, U., Eliasson, B., & Egli, W. (1997). Dielectric-Barrier Discharges. Principle and Applications. *Journal De Physique Iv*, *7*(4), C4–47–66.

Kogelschatz, U., Eliasson, B., & Egli, W. (1999). From ozone generators to flat television screens: history and future potential of dielectric-barrier discharges. *Pure and Applied Chemistry*, *71*(10), 1819–1828. doi:10.1351/pac199971101819

Kossyi, I., Kostinsky, A., Matveyev, A., & Silakov, V. (1992). Kinetic scheme of the non-equilibrium discharge in nitrogen-oxygen mixtures. *Plasma Sources Science and Technology*, *1*, 207–220.

Kulikovsky, a. a. (1997). Production of chemically active species in the air by a single positive streamer in a nonuniform field. *IEEE Transactions on Plasma Science*, *25*(3), 439–446. doi:10.1109/27.597258

Kulikovsky, a. a. (1998). Analytical model of positive streamer in weak field in air: application to plasma chemical calculations. *IEEE Transactions on Plasma Science*, *26*(4), 1339–1346. doi:10.1109/27.725167

Kusić, H., Koprivanac, N., & Selanec, I. (2006). Fe-exchanged zeolite as the effective heterogeneous Fenton-type catalyst for the organic pollutant minimization: UV irradiation assistance. *Chemosphere*, *65*(1), 65–73. doi:10.1016/j.chemosphere.2006.02.053

Kwon, B. G., Ryu, S., & Yoon, J. (2009). Determination of hydroxyl radical rate constants in a continuous flow system using competition kinetics. *Journal of Industrial and Engineering Chemistry*, *15*(6), 809–812. doi:10.1016/j.jiec.2009.09.004

Langmuir, I. (1928). Oscillations in Ionized Gases. *Proceedings of the National Academy of Sciences of the United States of America*, *14*(8), 627–637.

Lewis, W. K., & Whitman, W. G. (1924). Principles of Gas Absorption. *Industrial and Engineering Chemistry*, *16*(12), 1215– 1220.

Li, P., Takahashi, M., & Chiba, K. (2009). Enhanced free-radical generation by shrinking microbubbles using a copper catalyst. *Chemosphere*, *77*(8), 1157–1160. doi:10.1016/j.chemosphere.2009.07.062

Li, P., Tsuge, H., & Itoh, K. (2009). Oxidation of Dimethyl Sulfoxide in Aqueous Solution Using Microbubbles. *Industrial and Engineering Chemistry Research*, *48*, 8048–8053.

Lieberman, M. A., & Lichtenberg, A. J. (2005). *Principles of Plasma Discharges and Materials Processing: Second Edition*. *Principles of Plasma Discharges and Materials Processing: Second Edition* (pp. 1–757). doi:10.1002/0471724254

Liu, M., Beattie, J. K., & Gray-Weale, A. (2012). The surface relaxation of water. *The Journal of Physical Chemistry. B*, *116*(30), 8981–8. doi:10.1021/jp211810v

Lozano-Parada, J. H. (2007). *Design, Simulation and Fabrication of an Atmospheric Pressure Microchannel Plasma Reactor*. University of Sheffield.

Lozano-Parada, J. H., & Zimmerman, W. B. (2010). The role of kinetics in the design of plasma microreactors. *Chemical Engineering Science*, *65*(17), 4925–4930. doi:10.1016/j.ces.2010.03.056

Mackul'ak, T., Prousek, J., & Švorc, L. (2011). Degradation of atrazine by Fenton and modified Fenton reactions. *Monatshefte Für Chemie - Chemical Monthly*, *142*(6), 561–567. doi:10.1007/s00706-011-0504-8

Mahamuni, N. N., & Adewuyi, Y. G. (2010). Advanced oxidation processes (AOPs) involving ultrasound for waste water treatment: a review with emphasis on cost estimation. *Ultrasonics Sonochemistry*, *17*(6), 990–1003. doi:10.1016/j.ultsonch.2009.09.005

Marx, J. L. (1974). Drinking Source of Water : Another Carcinogens ? *Science*, *186*(4166), 809–811.

Mason, T., Lorimer, J., Bates, D., & Zhao, Y. (1994). Dosimetry in sonochemistry: the use of aqueous terephthalate ion as a fluorescence monitor. *Ultrasonics Sonochemistry*, *1*(2), 2–6.

Matafonova, G., & Batoev, V. (2012). Recent progress on application of UV excilamps for degradation of organic pollutants and microbial inactivation. *Chemosphere*, *89*(6), 637–47. doi:10.1016/j.chemosphere.2012.06.012

McTaggart, H. A. (1914a). Electrification at liquid-gas surfaces. *Philisophical Magazine*, *28*(163-168), 367–378.

McTaggart, H. A. (1914b). The electrification at gas-liquid surfaces. *Philisophical Magazine*, *27*(157-162), 297–314.

Morimoto, Y., Sumitomo, T., Yoshioka, M., & Takemura, T. (2004). Recent progress on UV lamps for industries. *Conference Record of the 2004 IEEE Industry Applications Conference, 2004. 39th IAS Annual Meeting.*, *2*, 1008–1015. doi:10.1109/IAS.2004.1348536

Mrázková, M., Vašina, P., Kudrle, V., Tálský, a, Pintassilgo, C. D., & Guerra, V. (2009). On the oxygen addition into nitrogen post-discharges. *Journal of Physics D: Applied Physics*, *42*(7), 075202. doi:10.1088/0022-3727/42/7/075202

Naidis, G. (1997). Modelling of plasma chemical processes in pulsed corona discharges. *Journal of Physics D: Applied Physics*, *30*, 1214–1218.

Neta, P., Huie, R., & Ross, A. (1988). Rate constants for reactions of inorganic radicals in aqueous solution. *Journal of Physical and Chemical Reference Data*, *17*(3), 1027–1284.

Neyens, E., & Baeyens, J. (2003). A review of classic Fenton's peroxidation as an advanced oxidation technique. *Journal of Hazardous Materials*, *98*(1-3), 33–50. doi:10.1016/S0304-3894(02)00282-0

Ni, C. H., Chen, J. N., & Yang, P. Y. (2003). Catalytic ozonation of 2-dichlorophenol by metallic ions. In *Water Science and Technology* (Vol. 47, pp. 77–82).

Nihonyanagi, S., Ishiyama, T., Lee, T., Yamaguchi, S., Bonn, M., Morita, A., & Tahara, T. (2011). Unified molecular view of the air/water interface based on experimental and theoretical χ(2) spectra of an isotopically diluted water surface. *Journal of the American Chemical Society*, *133*(42), 16875–80. doi:10.1021/ja2053754

Oinuma, G., Inanaga, Y., Noda, S., Tanimura, Y., Kuzumoto, M., Tabata, Y., & Watanabe, K. (2008). Method for real-time measurement of nitrogen atom density in atmospheric pressure post-discharge flows. *Journal of Physics D: Applied Physics*, *41*(15), 155204. doi:10.1088/0022-3727/41/15/155204

Okada, K., & Akagi, Y. (1987). METHOD AND APPARATUS TO MEASURE THE Z-POTENTIAL OF BUBBLES. *Journal of Chemical Engineering of Japan*, *20*(1), 11–15.

Oller, I., Malato, S., & Sánchez-Pérez, J. a. (2011). Combination of Advanced Oxidation Processes and biological treatments for wastewater decontamination--a review. *The Science of the Total Environment*, *409*(20), 4141–66. doi:10.1016/j.scitotenv.2010.08.061

Pekárek, S. (2003). Non-Thermal Plasma Ozone Generation. *Acta Polytechnica*, *43*(6), 47.

Pera-Titus, M., García-Molina, V., Baños, M. a, Giménez, J., & Esplugas, S. (2004). Degradation of chlorophenols by means of advanced oxidation processes: a general review. *Applied Catalysis B: Environmental*, *47*(4), 219–256. doi:10.1016/j.apcatb.2003.09.010

Petrovic, M., Gehringer, P., Eschweiler, H., & Barceló, D. (2007). Radiolytic decomposition of multi-class surfactants and their biotransformation products in sewage treatment plant effluents. *Chemosphere*, *66*(1), 114–22. doi:10.1016/j.chemosphere.2006.05.008

Pintassilgo, C. D., Guerra, V., Guaitella, O., & Rousseau, a. (2010). Modelling of an afterglow plasma in air produced by a pulsed discharge. *Plasma Sources Science and Technology*, *19*(5), 055001. doi:10.1088/0963-0252/19/5/055001

Pintassilgo, C. D., Kutasi, K., & Loureiro, J. (2007). Modelling of a low-pressure N 2 –O 2 discharge and post-discharge reactor for plasma sterilization. *Plasma Sources Science and Technology*, *16*(1), S115–S122. doi:10.1088/0963-0252/16/1/S13

Pintassilgo, C. D., Loureiro, J., & Guerra, V. (2005). Modelling of a N 2 –O 2 flowing afterglow for plasma sterilization. *Journal of Physics D: Applied Physics*, *38*(3), 417–430. doi:10.1088/0022-3727/38/3/011

Pipi, A. R. F., Sirés, I., De Andrade, A. R., & Brillas, E. (2014). Application of electrochemical advanced oxidation processes to the mineralization of the herbicide diuron. *Chemosphere*, *109*, 49–55. doi:10.1016/j.chemosphere.2014.03.006

Pirnie, M., Linden, K. G., & Malley, J. P. J. (2006). Ultraviolet disinfection guidance manual for the final long term 2 enhanced surface water treatment rule. *Environmental Protection*, *2*, 1–436.

Poggie, J., Adamovich, I., Bisek, N., & Nishihara, M. (2013). Numerical simulation of nanosecond-pulse electrical discharges. *Plasma Sources Science and Technology*, *22*(1), 015001. doi:10.1088/0963-0252/22/1/015001

Popov, N. a. (2011). Fast gas heating in a nitrogen–oxygen discharge plasma: I. Kinetic mechanism. *Journal of Physics D: Applied Physics*, *44*(28), 285201. doi:10.1088/0022-3727/44/28/285201

Popov, N. a. (2010). Evolution of the negative ion composition in the afterglow of a streamer discharge in air. *Plasma Physics Reports*, *36*(9), 812–818. doi:10.1134/S1063780X10090084

Qiang, Z., Liu, C., Dong, B., & Zhang, Y. (2010). Degradation mechanism of alachlor during direct ozonation and O(3)/H(2)O(2) advanced oxidation process. *Chemosphere*, *78*(5), 517–26. doi:10.1016/j.chemosphere.2009.11.037

Quincke, G. (1861). Ueber die fortführung materieller theilchen durch strömende elektricität (On the continuation of material particles by the flow of electricity). *Annalen Der Physik*, *189*, 513–598.

Rae, J., Ashokkumar, M., Eulaerts, O., von Sonntag, C., Reisse, J., & Grieser, F. (2005). Estimation of ultrasound induced cavitation bubble temperatures in aqueous solutions. *Ultrasonics Sonochemistry*, *12*(5), 325–9. doi:10.1016/j.ultsonch.2004.06.007

Rastogi, A., Al-Abed, S. R., & Dionysiou, D. D. (2009). Sulfate radical-based ferrous–peroxymonosulfate oxidative system for PCBs degradation in aqueous and sediment systems. *Applied Catalysis B: Environmental*, *85*(3-4), 171–179. doi:10.1016/j.apcatb.2008.07.010

Razumovsky, S. D., & Zaikov, G. E. (1974). Ozone and its reactions with organic compounds. In *Nauka*.

Ribeiro, A. R., Nunes, O. C., Pereira, M. F. R., & Silva, A. M. T. (2015). An overview on the advanced oxidation processes applied for the treatment of water pollutants defined in the recently launched Directive 2013/39/EU. *Environment International*, *75*, 33–51. doi:10.1016/j.envint.2014.10.027

Ricard, A., Oh, S., & Guerra, V. (2013). Line-ratio determination of atomic oxygen and ${\rm N}_2(A\,{}^3\Sigma_{\rm u}^+)$ metastable absolute densities in an RF nitrogen late afterglow. *Plasma Sources Science and Technology*, *22*(3), 035009. doi:10.1088/0963-0252/22/3/035009

Richardson, S. D., Plewa, M. J., Wagner, E. D., Schoeny, R., & Demarini, D. M. (2007). Occurrence, genotoxicity, and carcinogenicity of regulated and emerging disinfection by-products in drinking water: a review and roadmap for research. *Mutation Research*, *636*(1-3), 178–242. doi:10.1016/j.mrrev.2007.09.001

Rizzo, L. (2009). WATER AND WASTEWATER TREATMENT BY HETEROGENEOUS PHOTOCATALYSIS : A REVIEW. In *Handbook of Photocatalysts: Preparation, Structure and Applications.* Nova Science Publishers.

Roeselová, M., Vieceli, J., Dang, L. X., Garrett, B. C., & Tobias, D. J. (2004). Hydroxyl radical at the air-water interface. *Journal of the American Chemical Society*, *126*(50), 16308–9. doi:10.1021/ja045552m

Rook, J. J. (1975). Chlorination reactions of fulvic acids in natural waters. *Environmental Science & Technology*, *2*(4), 478–482.

Rosenfeldt, E. J., Linden, K. G., Canonica, S., & von Gunten, U. (2006). Comparison of the efficiency of *OH radical formation during ozonation and the advanced oxidation processes O3/H2O2 and UV/H2O2. *Water Research*, *40*(20), 3695–704. doi:10.1016/j.watres.2006.09.008

Sahni, M., & Locke, B. (2006). Quantification of hydroxyl radicals produced in aqueous phase pulsed electrical discharge reactors. *Industrial & Engineering Chemistry Research*, *45*, 5819–5825.

Sakiyama, Y., Graves, D. B., Chang, H.-W., Shimizu, T., & Morfill, G. E. (2012). Plasma chemistry model of surface microdischarge in humid air and dynamics of reactive neutral species. *Journal of Physics D: Applied Physics*, *45*(42), 425201. doi:10.1088/0022-3727/45/42/425201

Sato, T., Ito, D., & Nishiyama, H. (2004). Reaction field analysis of a non-thermal plasma flowing in a rectangular reactor. *Thin Solid Films*, *457*(1), 78–83. doi:10.1016/j.tsf.2003.12.034

Sedlak, D., & Andren, A. (1991). Oxidation of chlorobenzene with Fenton's reagent. *Environmental Science & Technology*, *25*(4), 777–782.

Seunghun, L., Ho-Cheol, K., & Gon-Ho, K. (2009). Electron Density Analyzed from V-I Phase Difference of kHz-Atmospheric Pressure Dielectric Barrier Discharge. *Journal of the Korean Physical Society*, *55*(51), 1813. doi:10.3938/jkps.55.1813

Shen, Y. R., & Ostroverkhov, V. (2006). Sum-frequency vibrational spectroscopy on water interfaces: polar orientation of water molecules at interfaces. *Chemical Reviews*, *106*(4), 1140–1154.

Šimek, M., Člupek, M., Babický, V., & Šunka, P. (2006). Production of reactive species by atmospheric pressure streamers in N2-O2 mixtures. *Pure and Applied Chemistry*, *78*(6), 1213–1225. doi:10.1351/pac200678061213

Singh, K. P., & Roy, S. (2007). Impedance matching for an asymmetric dielectric barrier discharge plasma actuator. *Applied Physics Letters*, *91*(8), 081504. doi:10.1063/1.2773932

Smirnov, S. A., Rybkin, V. V, & Kholodkov, I. V. (2002). Simulation of the Processes of Formation and Dissociation of Neutral Particles in Air Plasma : Vibrational Kinetics of Ground States of Molecules, *40*(2), 189–193.

Sotelo, J., Beltran, F., Benitez, F., & Beltran-Heredia, J. (1987). Ozone decomposition in water: kinetic study. *Industrial & Engineering Chemistry Research*, *26*, 39–43.

Staehelin, J., & Hoigne, J. (1982). Decomposition of ozone in water: rate of initiation by hydroxide ions and hydrogen peroxide. *Environmental Science & Technology*, *16*(040), 676–681.

Stevenson, F. J. (1994). *Humus Chemistry: Genesis, Composition, Reactions*. John Wiley & Sons.

Suty, H., Traversay, C. De, & Cost, M. (2004). Applications of advanced oxidation processes: present and future. *Water Science & Technology*, *49*(4), 227–223.

Tachikawa, T., & Majima, T. (2007). Single-molecule detection of reactive oxygen species: application to photocatalytic reactions. *Journal of Fluorescence*, *17*(6), 727–738. doi:10.1007/s10895-007-0181-5

Takahashi, M. (2005a). Zeta potential of microbubbles in aqueous solutions: electrical properties of the gas-water interface. *The Journal of Physical Chemistry. B*, *109*(46), 21858–64. doi:10.1021/jp0445270

Takahashi, M. (2005b). Zeta potential of microbubbles in aqueous solutions: electrical properties of the gas-water interface. *The Journal of Physical Chemistry B*, *109*(46), 21858–21864.

Tauber, A., Mark, G., Schuchmann, H.-P., & von Sonntag, C. (1999). Sonolysis of tert-butyl alcohol in aqueous solution. *J. Chem. Soc. Perkin Trans.*, *2*, 1129–1135.

Tesař, V. (2009). Enhancing impinging jet heat or mass transfer by fluidically generated flow pulsation. *Chemical Engineering Research and Design*, *87*(2), 181–192. doi:10.1016/j.cherd.2008.08.003

Thiruvenkatachari, R., Vigneswaran, S., & Moon, I. S. (2008). JOURNAL REVIEW A review on UV / TiO 2 photocatalytic oxidation process. *Korean Journal of Chemical Engineering*, *25*(1), 64–72.

Toledo, M. (n.d.). 6510i Dissolved Ozone Sensor with ISM. Retrieved June 02, 2015, from http://uk.mt.com/gb/en/home/products/Process-Analytics/DO-CO2-ozone-sensor/dissolved-O3-meter/6510i-ISM.tabs.documents.html

Tomiyasu, H., Fukutomi, H., & Gordon, G. (1985). Kinetics and Mechanism of Ozone Decomposition in Basic Aqueous Solution. *Inorganic Chemistry*, *24*(19), 2962–2966.

Trushkin, a. N., & Kochetov, I. V. (2012). Simulation of toluene decomposition in a pulse-periodic discharge operating in a mixture of molecular nitrogen and oxygen. *Plasma Physics Reports*, *38*(5), 407–431. doi:10.1134/S1063780X12040083

Tsai, I.-H., & Hsu, C. (2010). Numerical Simulation of Downstream Kinetics of an Atmospheric-Pressure Nitrogen Plasma Jet. *IEEE Transactions on Plasma Science*, *38*(12), 3387–3392. doi:10.1109/TPS.2010.2084598

Usui, S., Sasaki, H., & Matsukawa, H. (1981). The Dependence of Zeta Potential on Bubble Size as Determined by the Dorn Effect. *Journal of Colloid and Interface Science*, *81*(1), 80–84.

Vacha, R., Marsalek, O., Willard, A. P., Bonthuis, D. J., Netz, R. R., & Jungwirth, P. (2012). Charge Transfer between Water Molecules As the Possible Origin of the Observed Charging at the Surface of Pure Water Robert Va c. *The Journal of Physical Chemistry Letters*, *3*, 107–111.

Vasina, P., Kudrle, V., Tálský, A., Botos, P., Mrázková, M., & Mesko, M. (2004). Simultaneous measurement of N and O densities in plasma afterglow by means of NO titration. *Plasma Sources Science and Technology*, *13*, 668–674. doi:10.1088/0963-0252/13/4/016

Vezzu, G., Lopez, J. L., Freilich, a, & Becker, K. H. (2009). Optimization of Large-Scale Ozone Generators. *IEEE Transactions on Plasma Science*, *37*(6), 890–896.

Von Sonntag, C. (2008). Advanced oxidation processes: mechanistic aspects. *Water Science and Technology*, *58*(5), 1015–1021. doi:10.2166/wst.2008.467

Wijngaarden, R. I., Westerterp, K., & Kronberg, A. (2008). *Industrial Catalysis: Optimizing Catalysts and Processes*. WILEY-VCH.

Winter, B., Faubel, M., Vácha, R., & Jungwirth, P. (2009). Behavior of hydroxide at the water/vapor interface. *Chemical Physics Letters*, *474*(4-6), 241–247. doi:10.1016/j.cplett.2009.04.053

Wols, B. a, & Hofman-Caris, C. H. M. (2012). Review of photochemical reaction constants of organic micropollutants required for UV advanced oxidation processes in water. *Water Research*, *46*(9), 2815–27. doi:10.1016/j.watres.2012.03.036

Yang, S., Cheng, J., Sun, J., Hu, Y., & Liang, X. (2013). Defluorination of aqueous perfluorooctanesulfonate by activated persulfate oxidation. *PloS One*, *8*(10), e74877. doi:10.1371/journal.pone.0074877

Yao, L., He, R. X., Mebel, a. M., & Lin, S. H. (2009). On the calculation of the dissociation rate constant of the water dimer by the ab initio anharmonic RRKM theory. *Chemical Physics Letters*, *470*(4-6), 210–214. doi:10.1016/j.cplett.2009.01.074

Yoon, J., Lee, Y., & Kim, S. (2001). Investigation of the reaction pathway of OH radicals produced by Fenton oxidation in the conditions of wastewater treatment. *Water Science and Technology*, *44*(5), 15–21.

Zhao, G.-B., Garikipati, S. V. B. J., Hu, X., Argyle, M. D., & Radosz, M. (2005). Effect of oxygen on nonthermal plasma reactions of nitrogen oxides in nitrogen. *AIChE Journal*, *51*(6), 1800–1812. doi:10.1002/aic.10452

Zhihui, A., Peng, Y., & Xiaohua, L. (2005). Degradation of 4-chlorophenol by microwave irradiation enhanced advanced oxidation processes. *Chemosphere*, *60*(6), 824–7. doi:10.1016/j.chemosphere.2005.04.027

Zimmerman, W. B., Hewakandamby, B. N., Tesař, V., Bandulasena, H. C. H., & Omotowa, O. a. (2009). On the design and simulation of an airlift loop bioreactor with microbubble generation by fluidic oscillation. *Food and Bioproducts Processing*, *87*(3), 215–227. doi:10.1016/j.fbp.2009.03.006

Zimmerman, W. B. J., & Lozano-Parada, J. H. (2010). Plasma microreactor apparatus, sterilisation unit and analyser. United Kingdom.

Zimmerman, W. B., Zandi, M., Hemaka Bandulasena, H. C., Tesař, V., James Gilmour, D., & Ying, K. (2011). Design of an airlift loop bioreactor and pilot scales studies with fluidic oscillator induced microbubbles for growth of a microalgae Dunaliella salina. *Applied Energy*, *88*(10), 3357–3369. doi:10.1016/j.apenergy.2011.02.013

Zimmerman, W., Tesar, V., Butler, S., & Bandulasena, H. C. H. (2008). Microbubble generation. *Recent Patents on Engineering*, *2*(1), 1–8.

Zoschke, K., Börnick, H., & Worch, E. (2014). Vacuum-UV radiation at 185 nm in water treatment--a review. *Water Research*, *52*, 131–45. doi:10.1016/j.watres.2013.12.034

Appendix 1

Indigo method (Bader & Hoigné, 1981)

The principle of using indigo as a chemical probe for ozone is based on the reaction of ozone with indigo in the following reaction:

Indigo strongly absorbs light at 600nm, on reaction with a single molecule of ozone a molecule of indigo is broken down, therefore the decrease in absorbance of indigo in solution is directly proportional to the ozone dissolved in the liquid, and can be used to measure this.

Stock solution

The following chemicals are weighed out accurately and made up to the mark with distilled water in a 1000ml volumetric flask to make a stock solution of indigo:

Concentrated phosphoric acid 1ml

Potassium indigo trisulfonate powder 0.770g

The solution must be stored in the dark. A standard solution can then be made from this stock solution for use in experiments using chemicals in the following quantities, made up the mark with distilled water in a 1000ml volumetric flask:

Pre-prepared stock solution (see above) 20ml

NaH_2PO_4 10g

Concentrated phosphoric acid 7ml

This should give a concentration of 2.5×10^{-5}mol dm^{-3}. A single ozone molecule in this solution will react with a single molecule of indigo, decreasing the absorbance of the solution be a proportional amount. Samples of the solution can then be taken in spectrophotometer cuvettes and analysed. The solution should be stored in the dark, and should last for about a week. When the absorbance decreases to 80% of its initial value a new reagent solution should be made.

Dilutions of the indigo standard can be made to give varying concentrations of indigo. Using an absorption spectrophotometer, the absorbance of these solutions at 600nm can be plotted against their indigo concentrations, and the gradient of the resulting curve can be used to analyse the absorbance of the samples.

Terephthalic acid method (Mason et al., 1994)

The principle of using terephthalic acid (TA) as a chemical probe for the hydroxyl radical is based on the formation of hydroxyterephthalic acid (HTA) from terephthalic acid in the following reaction:

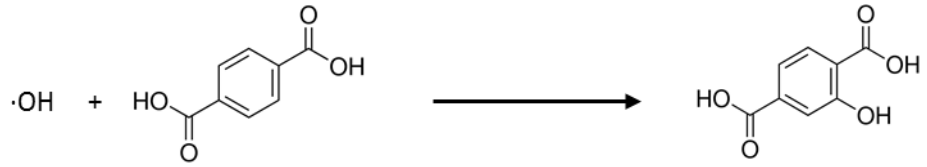

The TA molecule reacts selectively with the hydroxyl radical to form the fluorescent compound HTA, which has a peak excitation wavelength of 315nm and a peak emission wavelength of 425nm.

The following chemicals are weighed out accurately and made up to the mark with distilled water in a 1000ml volumetric flask to make a stock solution of TA

TA 0.332g

NaOH 0.200g

KH_2PO_4 0.589g

Na_2HPO_4 0.981

A single hydroxyl radical in this solution will react with a single molecule of TA to form a single molecule of HTA, samples of the solution can then be taken in fluorimeter cuvettes and analysed. The solution must be stored in the dark.

For the calibration curve, a solution of HTA must be made using the following quantities of chemicals, weighed out accurately and made up to the mark with distilled water in a 500ml volumetric flask

HTA 0.182g

NaOH 0.100g

KH_2PO_4 0.294

Na_2HPO_4 0.491

Dilutions of the TA and HTA stock solutions (1ml stock solution into 100ml of distilled water) can be made and then mixed together to make solutions with different HTA/TA ratios (e.g. 0%/100%, 1%/99%, 10%/90%, 25%/75%, 50%/50%, 75%/25%, 100%/0%). Using a fluorimeter with the excitation wavelength set at 315nm, the emission intensity of these solutions at 425nm can be plotted against their HTA concentrations, and the gradient of the resulting curve can be used to analyse the emission intensity of the samples.

Appendix 2

The complete results of the field trials are presented here. The power drawn by the dosing lance was 150 W for each set of data. The reader will note there are no error bars included in the graphs, as estimating the accuracy of the results, given the unknown nature of wastewater, would be exceedingly difficult especially given constraints regarding time.

The candidate is confident that the results shown are accurately indicative of the samples taken. Whether the samples taken are an accurate representation of the complete water body is difficult to know for sure. However, at least in the case of the batch trials, trends in the data are clearly visible in most cases. This is enough to show that the dosing lance has clearly treated the water to some extent, even with its low ozone production. The graphs presented in this appendix should be enough to give a clear indication of the performance of the lance (in its current state) regarding each individual constituent that was tested for.

Where the graphs show the change in concentration over time of a particular organic compound, the molecular structure of that compound is shown directly to the right of the graph.

Please note that the 0.08 L s^{-1} water flow test results for benzo(g,h,i)perylene and indeno(1,2,3-cd)pyrene have been omitted, as they were on a much larger scale than other trials, and showed no correlation. They were removed so as not to prevent the rest of the data from being visible on the graph.

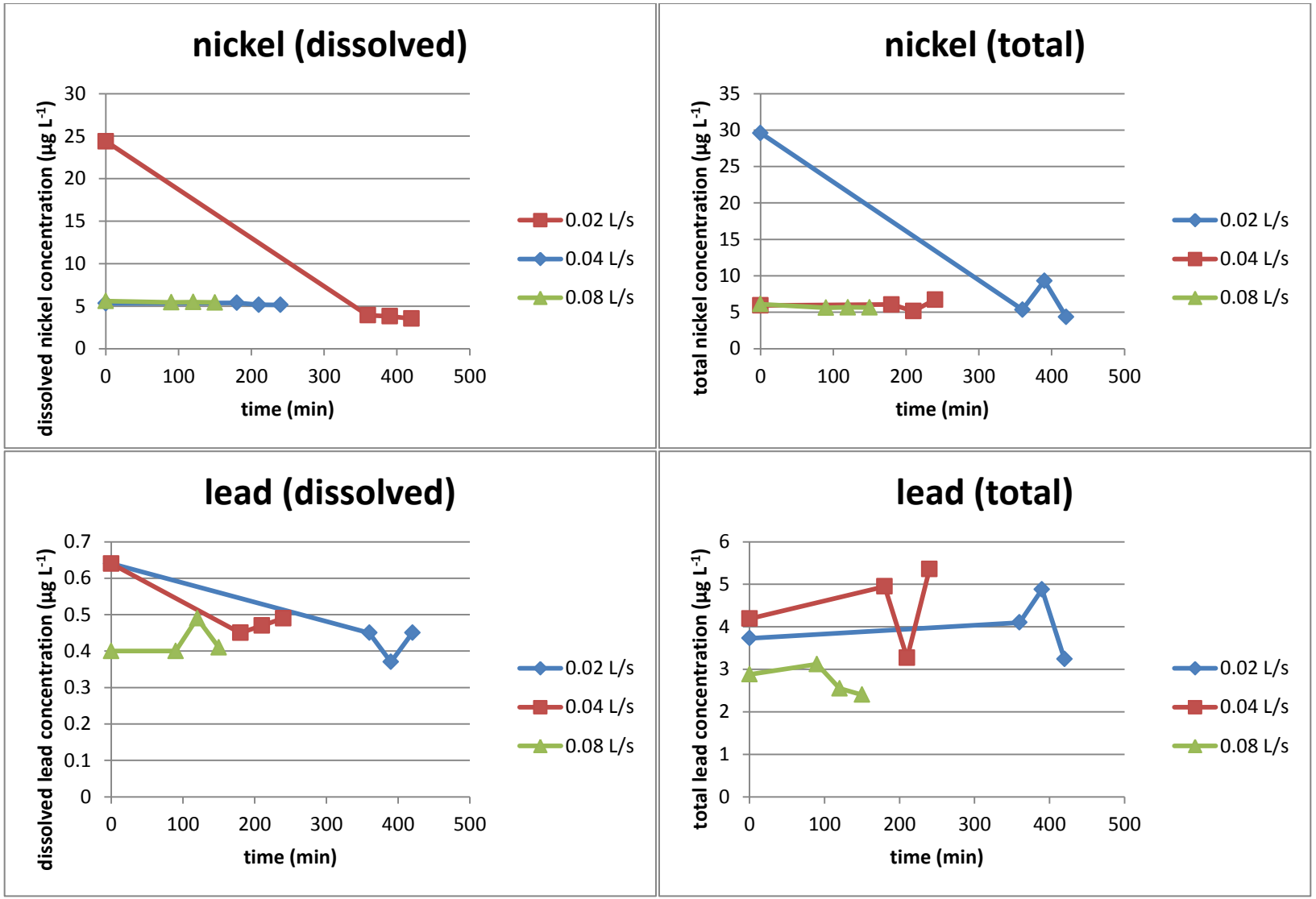
nickel (dissolved)
dissolved nickel concentration (µg L-1)
30
25
20
15
10
5
0
0
100
200
300
400
500
time (min)
0.02 L/s
0.04 L/s
0.08 L/s
nickel (total)
total nickel concentration (µg L-1)
35
30
25
20
15
10
5
0
0
100
200
300
400
500
time (min)
0.02 L/s
0.04 L/s
0.08 L/s
lead (dissolved)
dissolved lead concentration (µg L-1)
0.7
0.6
0.5
0.4
0.3
0.2
0.1
0
0
100
200
300
400
500
time (min)
0.02 L/s
0.04 L/s
0.08 L/s
lead (total)
total lead concentration (µg L-1)
6
5
4
3
2
1
0
0
100
200
300
400
500
time (min)
0.02 L/s
0.04 L/s
0.08 L/s

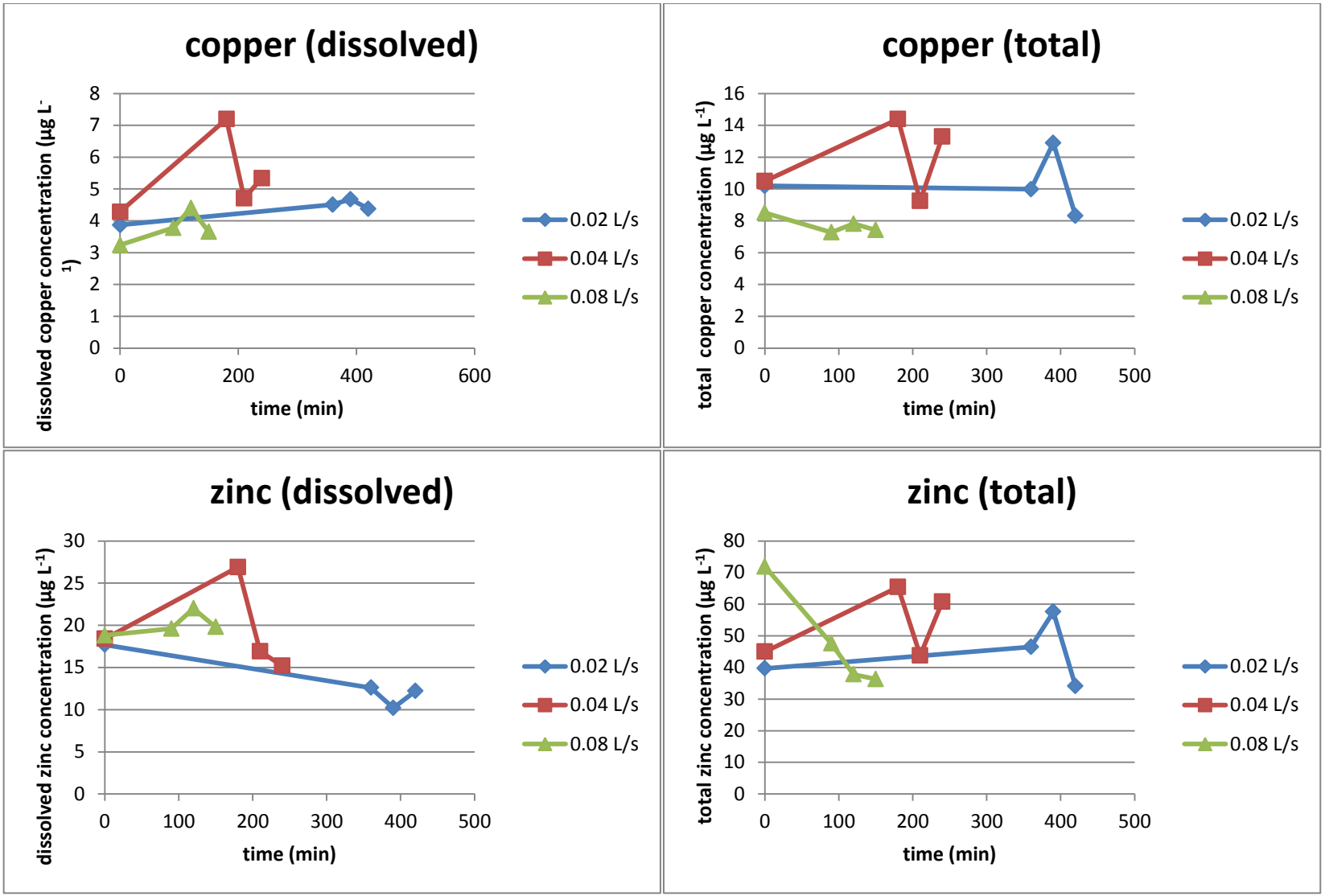
copper (dissolved)
dissolved copper concentration (µg L-1)
time (min)
0.02 L/s
0.04 L/s
0.08 L/s
copper (total)
total copper concentration (µg L-1)
time (min)
0.02 L/s
0.04 L/s
0.08 L/s
zinc (dissolved)
dissolved zinc concentration (µg L-1)
time (min)
0.02 L/s
0.04 L/s
0.08 L/s
zinc (total)
total zinc concentration (µg L-1)
time (min)
0.02 L/s
0.04 L/s
0.08 L/s

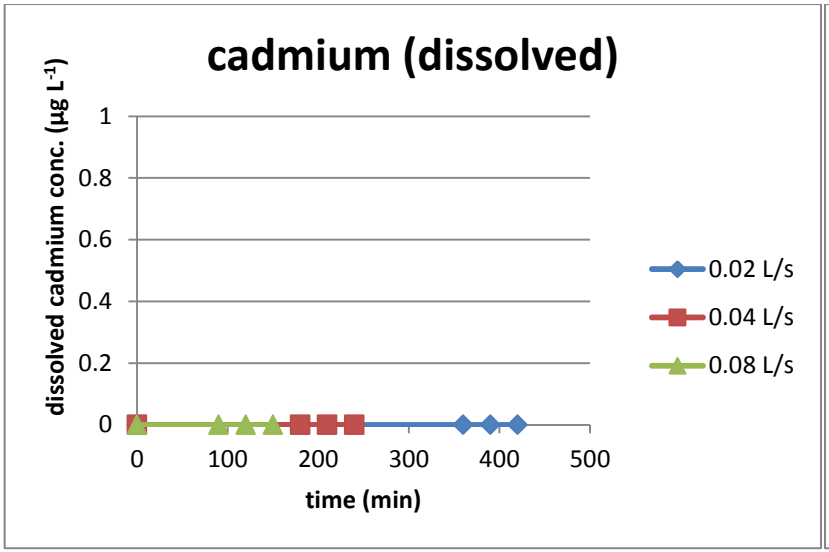
cadmium (dissolved)
dissolved cadmium conc. (µg L-1)
1
0.8
0.6
0.4
0.2
0
0
100
200
300
400
500
time (min)
0.02 L/s
0.04 L/s
0.08 L/s

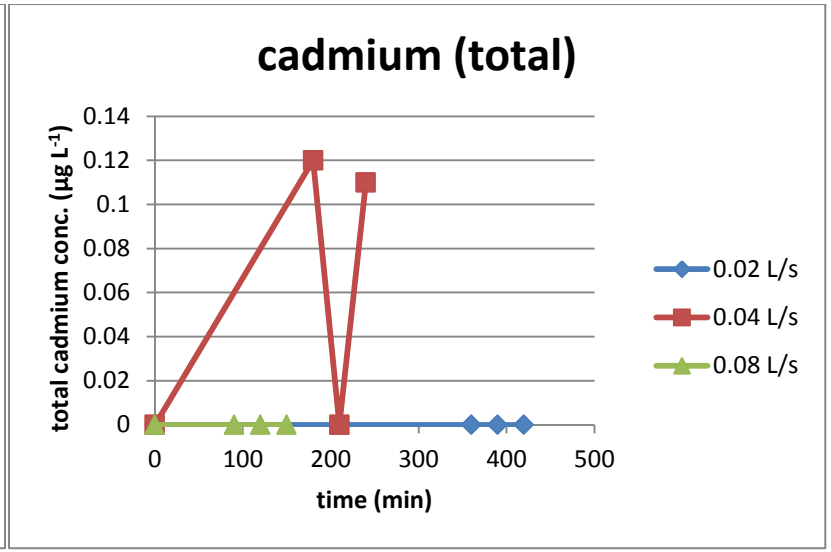
cadmium (total)
total cadmium conc. (µg L-1)
0.14
0.12
0.1
0.08
0.06
0.04
0.02
0
0
100
200
300
400
500
time (min)
0.02 L/s
0.04 L/s
0.08 L/s

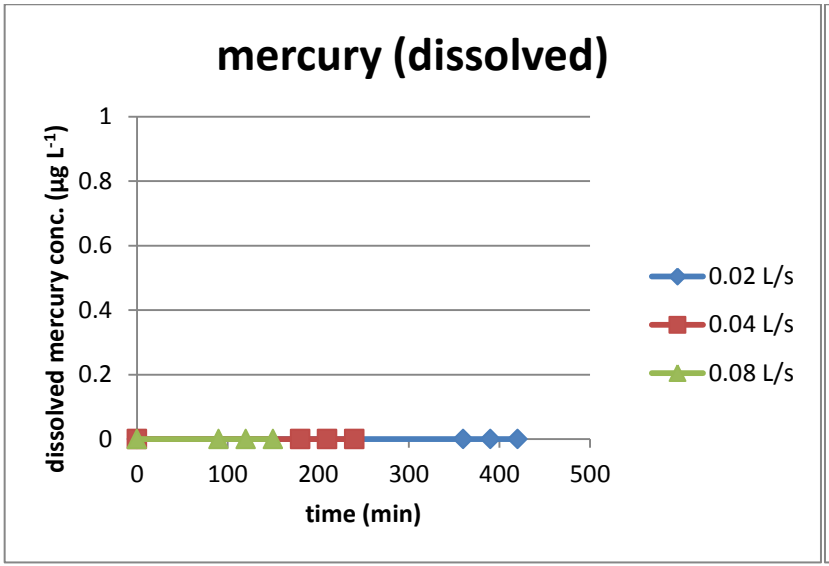
mercury (dissolved)
dissolved mercury conc. (µg L-1)
1
0.8
0.6
0.4
0.2
0
0
100
200
300
400
500
time (min)
0.02 L/s
0.04 L/s
0.08 L/s

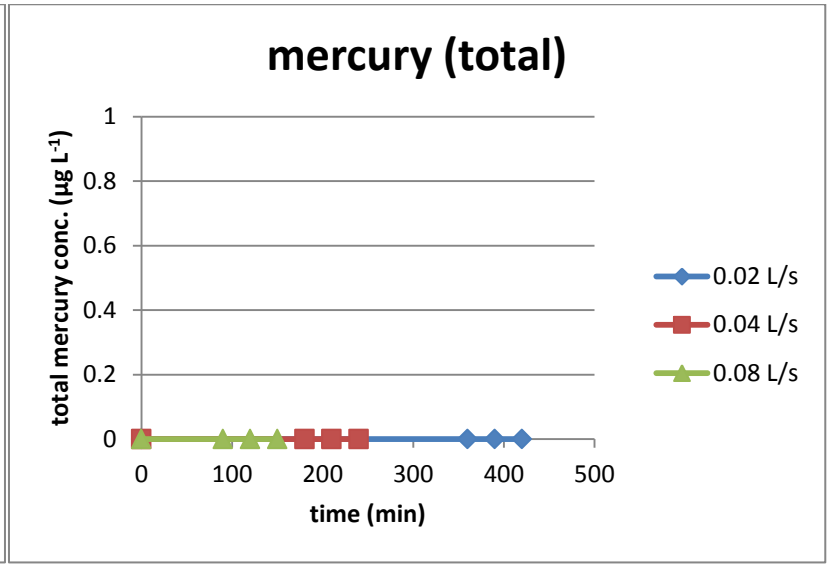
mercury (total)
total mercury conc. (µg L-1)
1
0.8
0.6
0.4
0.2
0
0
100
200
300
400
500
time (min)
0.02 L/s
0.04 L/s
0.08 L/s

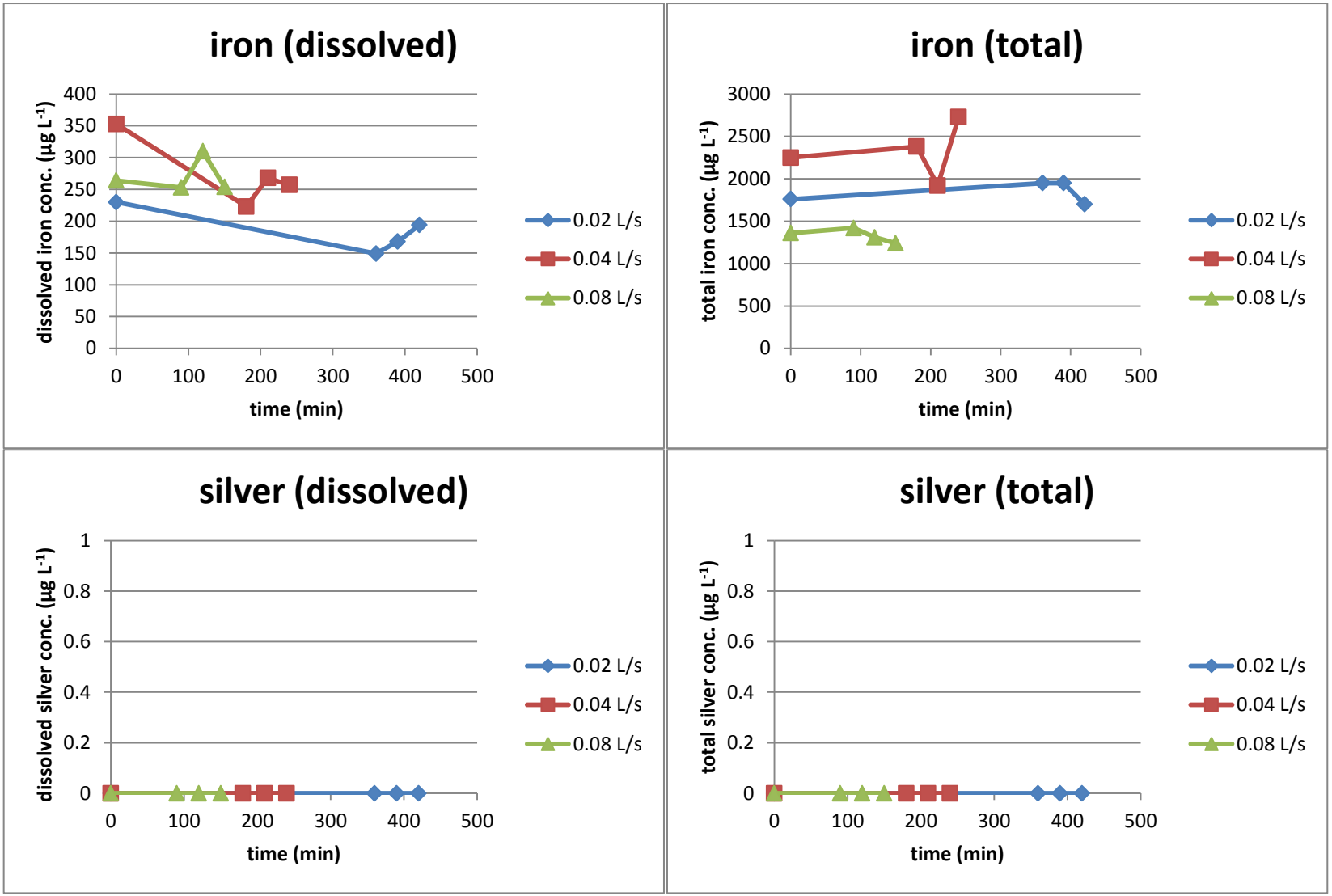
iron (dissolved)
dissolved iron conc. (µg L-1)
400
350
300
250
200
150
100
50
0
0
100
200
300
400
500
time (min)
0.02 L/s
0.04 L/s
0.08 L/s
iron (total)
total iron conc. (µg L-1)
3000
2500
2000
1500
1000
500
0
0
100
200
300
400
500
time (min)
0.02 L/s
0.04 L/s
0.08 L/s
silver (dissolved)
dissolved silver conc. (µg L-1)
1
0.8
0.6
0.4
0.2
0
0
100
200
300
400
500
time (min)
0.02 L/s
0.04 L/s
0.08 L/s
silver (total)
total silver conc. (µg L-1)
1
0.8
0.6
0.4
0.2
0
0
100
200
300
400
500
time (min)
0.02 L/s
0.04 L/s
0.08 L/s

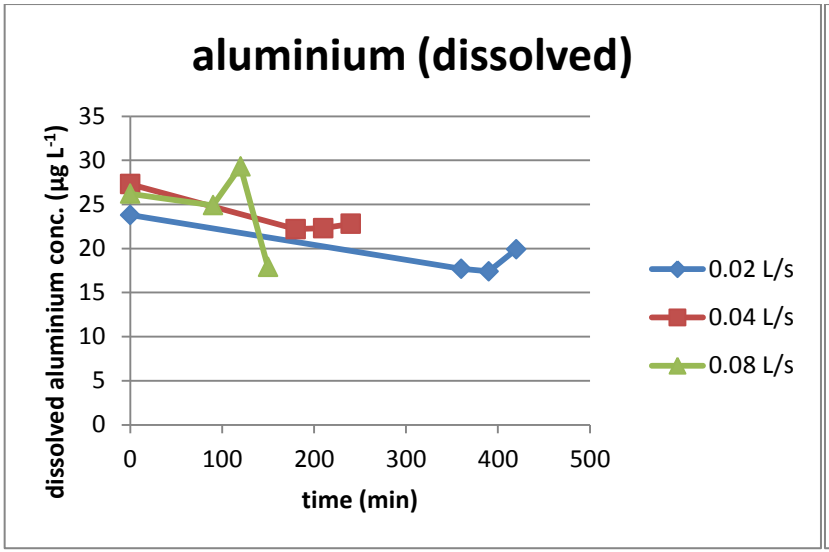
aluminium (dissolved)
dissolved aluminium conc. (µg L-1)
35
30
25
20
15
10
5
0
0
100
200
300
400
500
time (min)
0.02 L/s
0.04 L/s
0.08 L/s

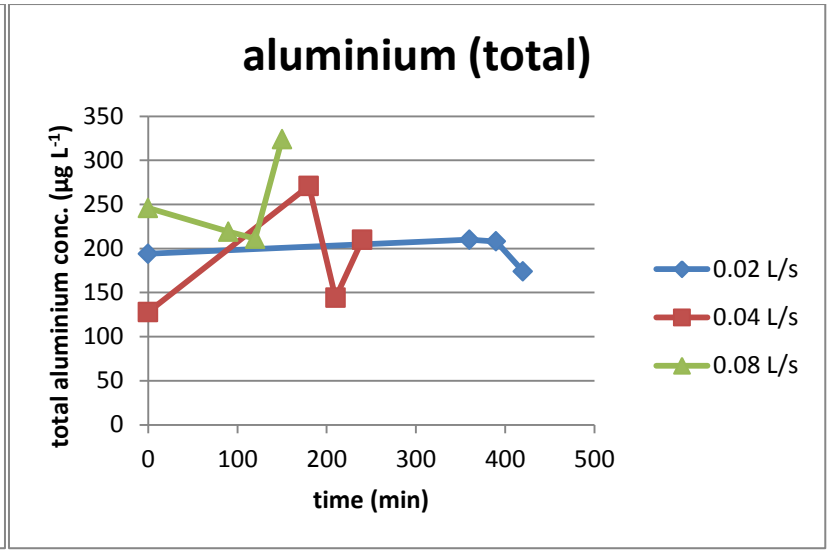
aluminium (total)
total aluminium conc. (µg L-1)
350
300
250
200
150
100
50
0
0
100
200
300
400
500
time (min)
0.02 L/s
0.04 L/s
0.08 L/s

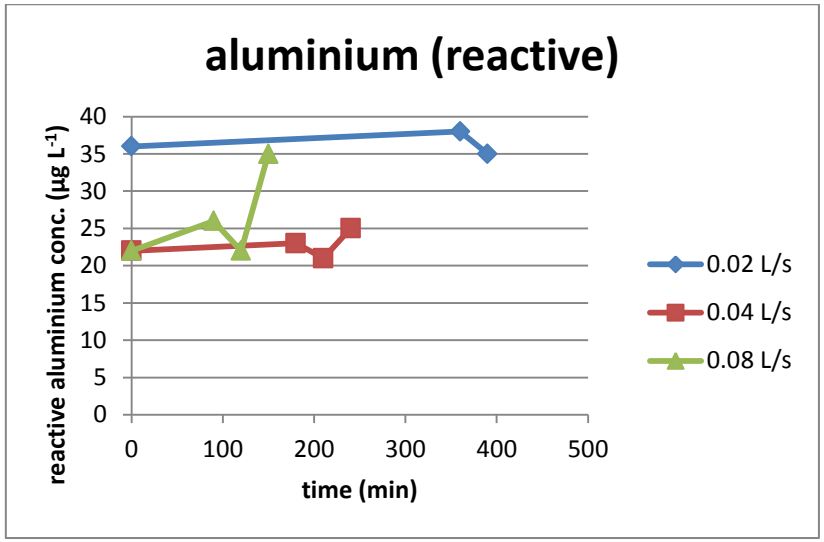
aluminium (reactive)
reactive aluminium conc. (µg L-1)
40
35
30
25
20
15
10
5
0
0
100
200
300
400
500
time (min)
0.02 L/s
0.04 L/s
0.08 L/s

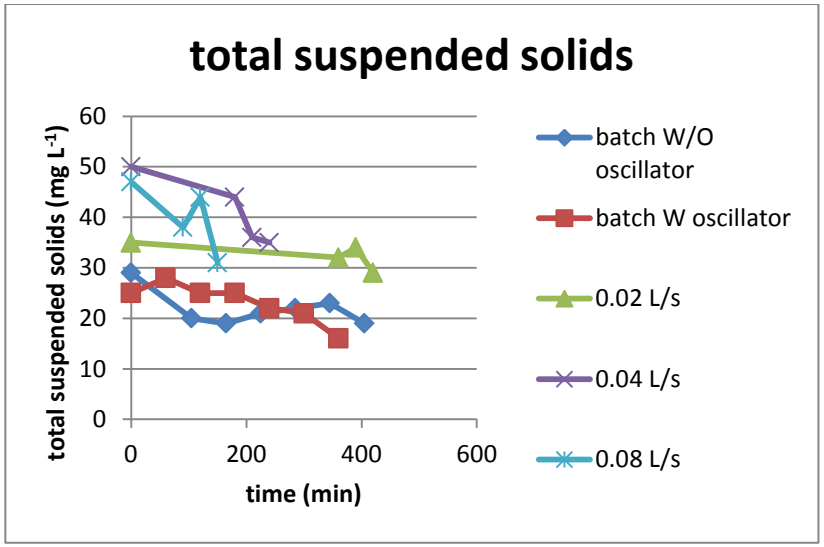
total suspended solids
total suspended solids (mg L-1)
60
50
40
30
20
10
0
0
200
400
600
time (min)
batch W/O oscillator
batch W oscillator
0.02 L/s
0.04 L/s
0.08 L/s

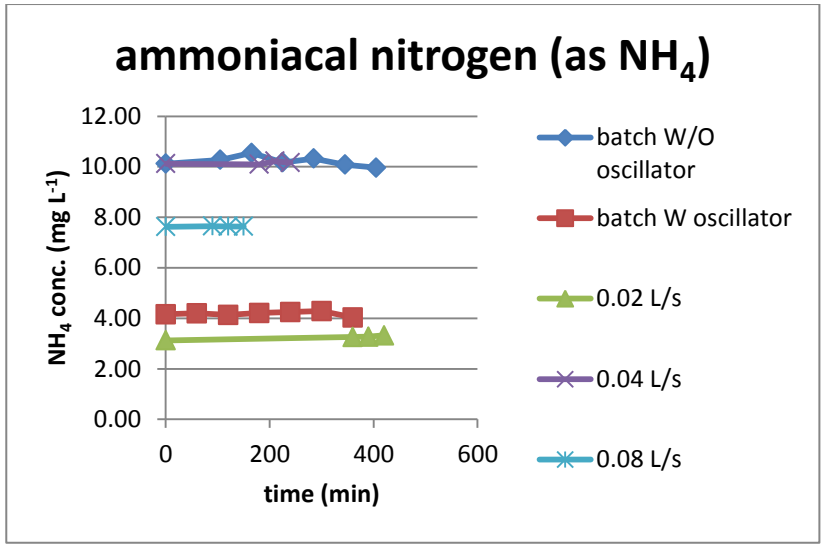
ammoniacal nitrogen (as NH4)
NH4 conc. (mg L-1)
12.00
10.00
8.00
6.00
4.00
2.00
0.00
0
200
400
600
time (min)
batch W/O oscillator
batch W oscillator
0.02 L/s
0.04 L/s
0.08 L/s

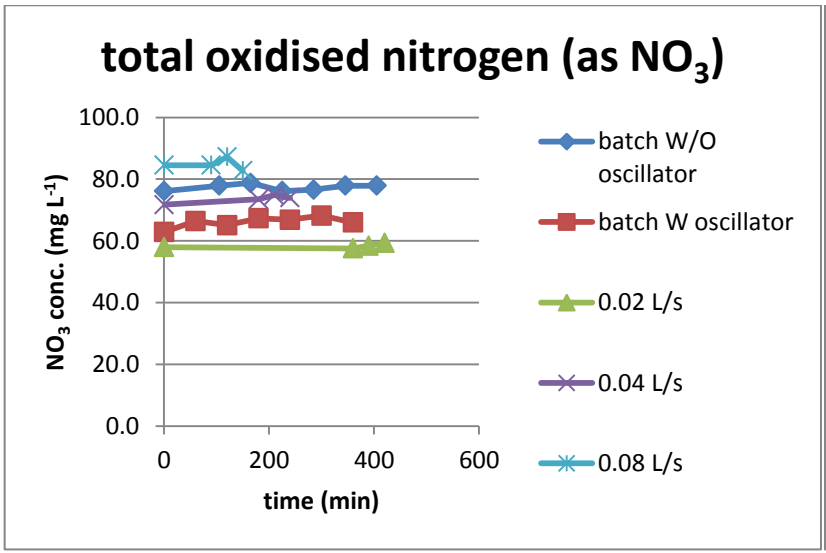
total oxidised nitrogen (as NO3)
NO3 conc. (mg L-1)
100.0
80.0
60.0
40.0
20.0
0.0
0
200
400
600
time (min)
batch W/O oscillator
batch W oscillator
0.02 L/s
0.04 L/s
0.08 L/s

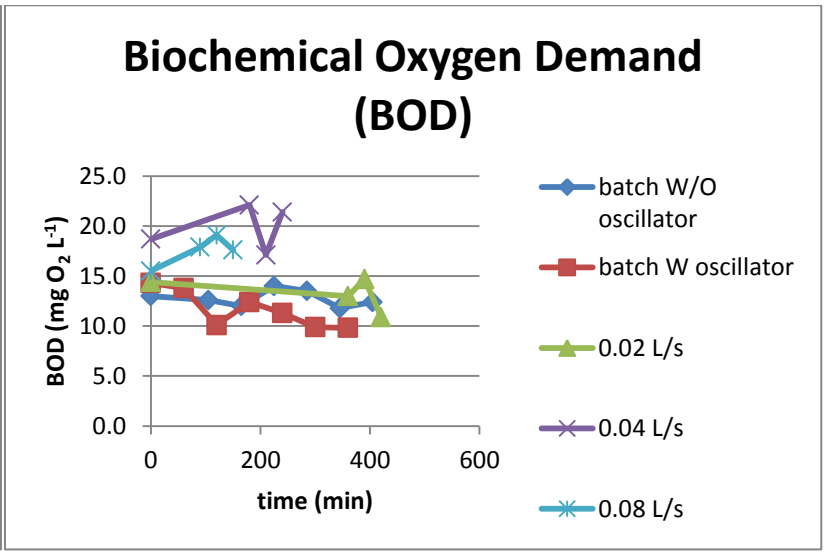
Biochemical Oxygen Demand (BOD)
BOD (mg O2 L-1)
25.0
20.0
15.0
10.0
5.0
0.0
0
200
400
600
time (min)
batch W/O oscillator
batch W oscillator
0.02 L/s
0.04 L/s
0.08 L/s

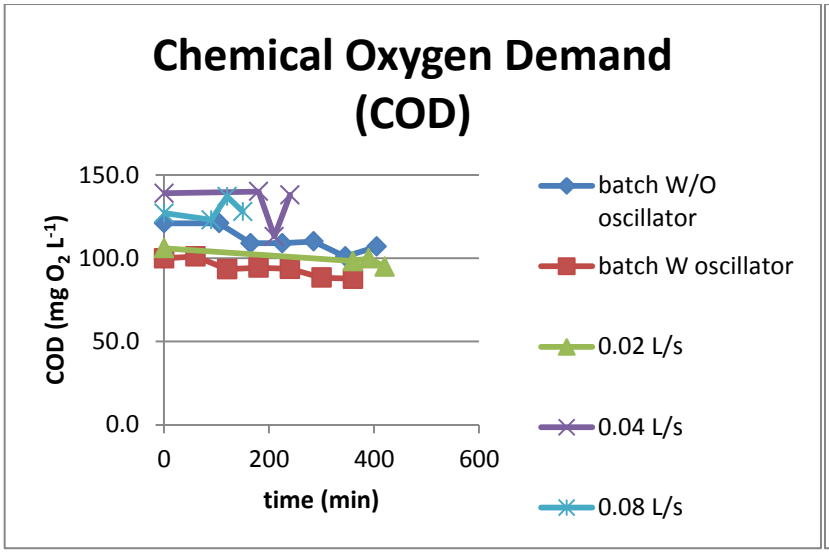
Chemical Oxygen Demand (COD)
COD (mg O_2 L^{-1})
150.0
100.0
50.0
0.0
0
200
400
600
time (min)
batch W/O oscillator
batch W oscillator
0.02 L/s
0.04 L/s
0.08 L/s

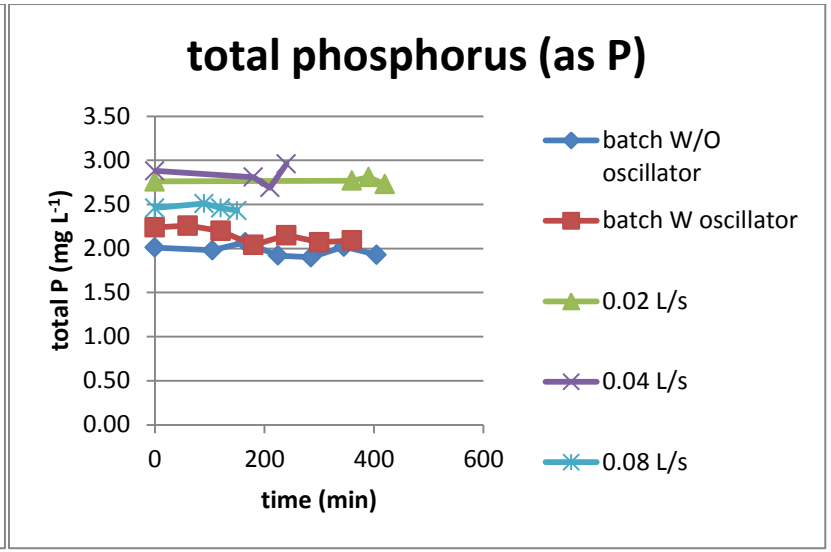
total phosphorus (as P)
total P (mg L^{-1})
3.50
3.00
2.50
2.00
1.50
1.00
0.50
0.00
0
200
400
600
time (min)
batch W/O oscillator
batch W oscillator
0.02 L/s
0.04 L/s
0.08 L/s

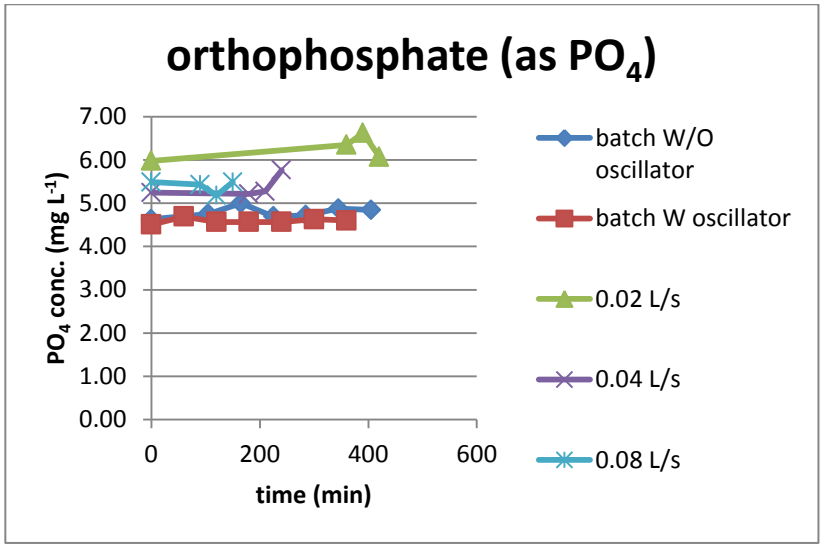
orthophosphate (as PO_4)
PO_4 conc. (mg L^{-1})
7.00
6.00
5.00
4.00
3.00
2.00
1.00
0.00
0
200
400
600
time (min)
batch W/O oscillator
batch W oscillator
0.02 L/s
0.04 L/s
0.08 L/s

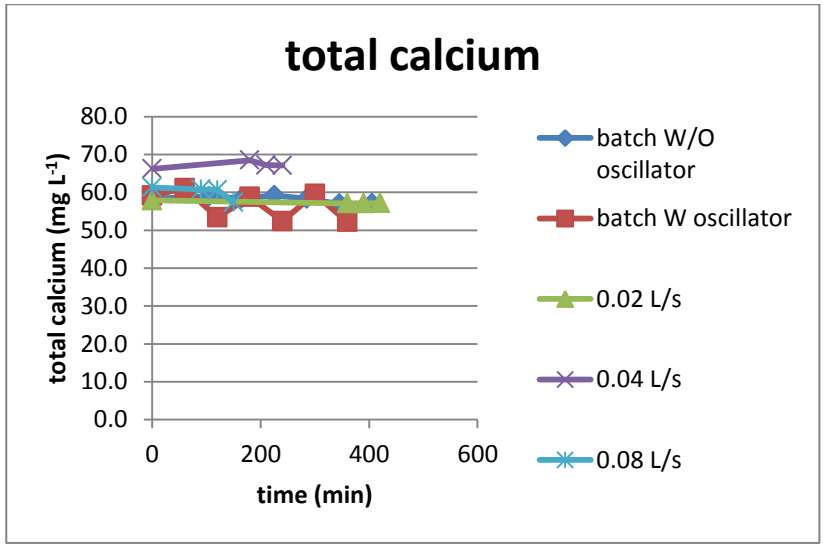
total calcium
total calcium (mg L^{-1})
80.0
70.0
60.0
50.0
40.0
30.0
20.0
10.0
0.0
0
200
400
600
time (min)
batch W/O oscillator
batch W oscillator
0.02 L/s
0.04 L/s
0.08 L/s

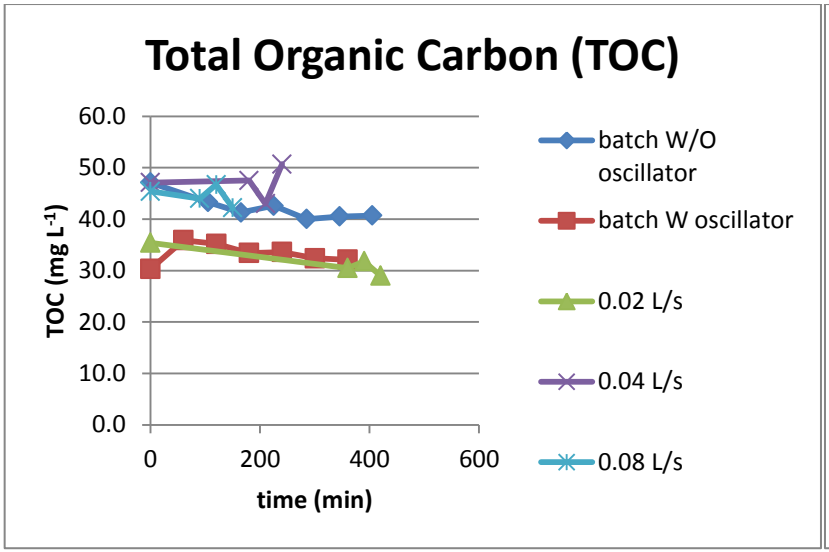
Total Organic Carbon (TOC)
TOC (mg L-1)
60.0
50.0
40.0
30.0
20.0
10.0
0.0
0
200
400
600
time (min)
batch W/O oscillator
batch W oscillator
0.02 L/s
0.04 L/s
0.08 L/s

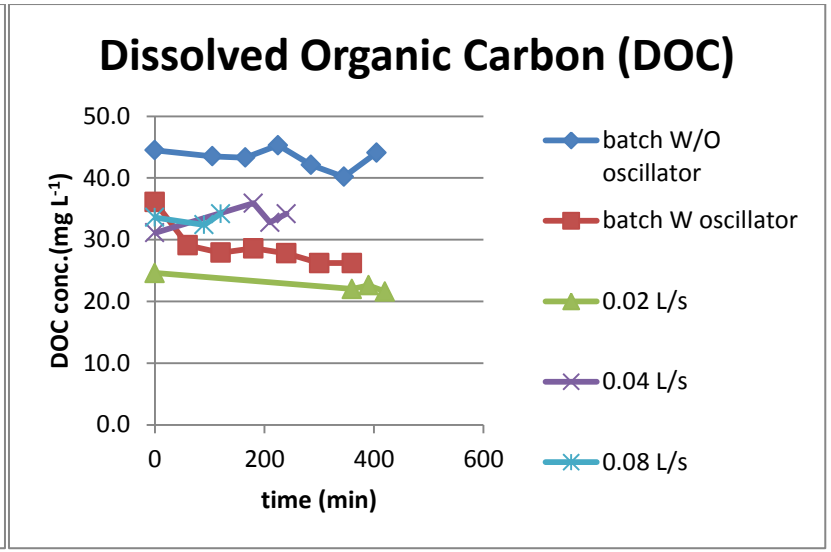
Dissolved Organic Carbon (DOC)
DOC conc.(mg L-1)
50.0
40.0
30.0
20.0
10.0
0.0
0
200
400
600
time (min)
batch W/O oscillator
batch W oscillator
0.02 L/s
0.04 L/s
0.08 L/s

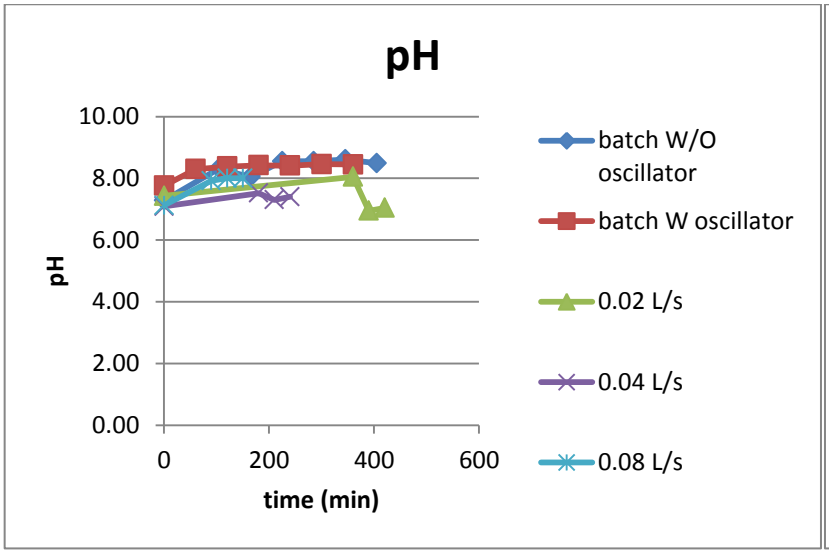
pH
pH
10.00
8.00
6.00
4.00
2.00
0.00
0
200
400
600
time (min)
batch W/O oscillator
batch W oscillator
0.02 L/s
0.04 L/s
0.08 L/s

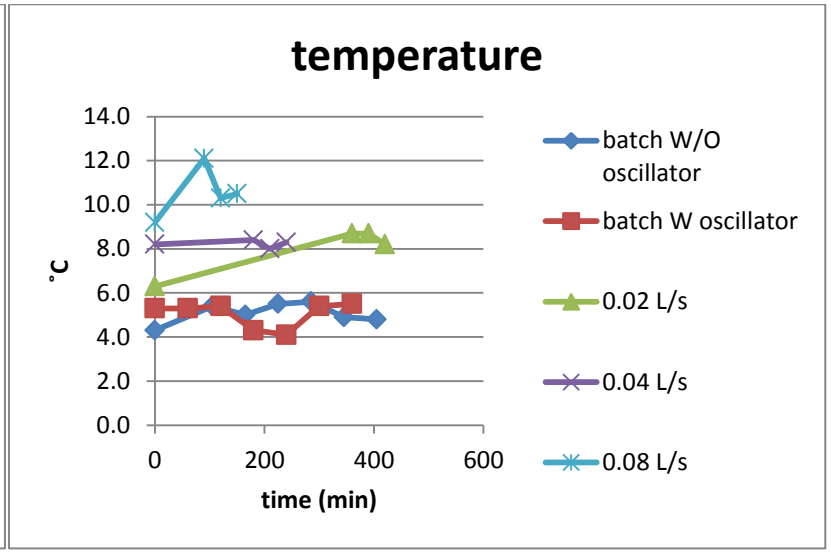
temperature
°C
14.0
12.0
10.0
8.0
6.0
4.0
2.0
0.0
0
200
400
600
time (min)
batch W/O oscillator
batch W oscillator
0.02 L/s
0.04 L/s
0.08 L/s

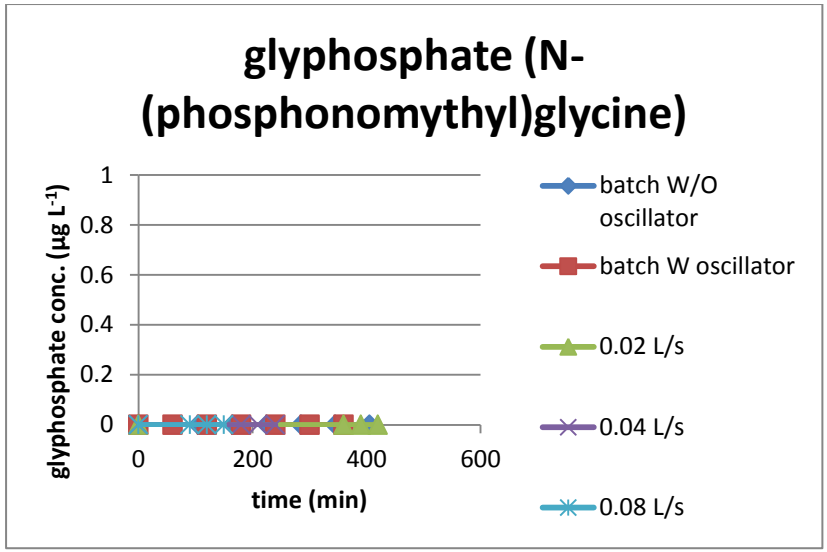
glyphosphate (N-(phosphonomythyl)glycine)
glyphosphate conc. (µg L-1)
1
0.8
0.6
0.4
0.2
0
0
200
400
600
time (min)
batch W/O oscillator
batch W oscillator
0.02 L/s
0.04 L/s
0.08 L/s

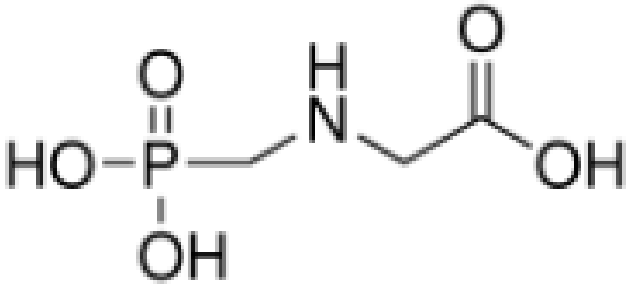
HO
P
O
OH
H
N
O
OH

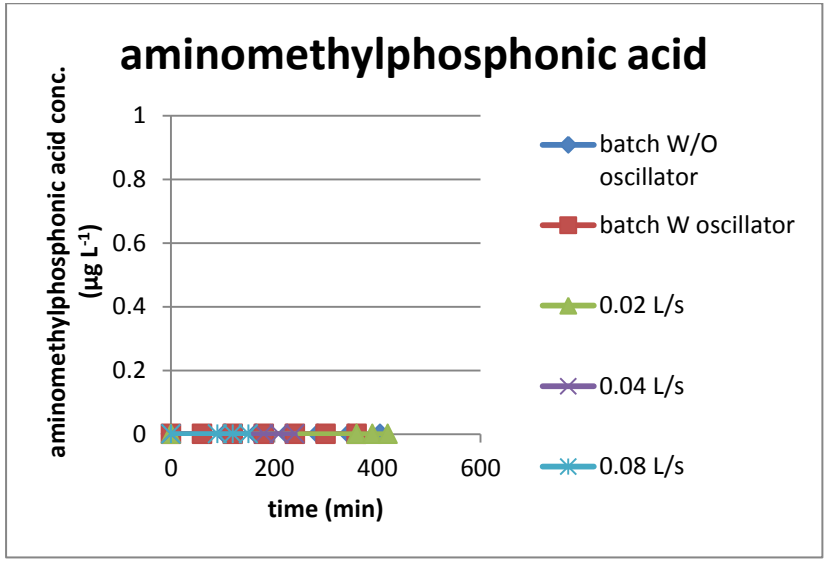
aminomethylphosphonic acid
aminomethylphosphonic acid conc. (µg L-1)
1
0.8
0.6
0.4
0.2
0
0
200
400
600
time (min)
batch W/O oscillator
batch W oscillator
0.02 L/s
0.04 L/s
0.08 L/s

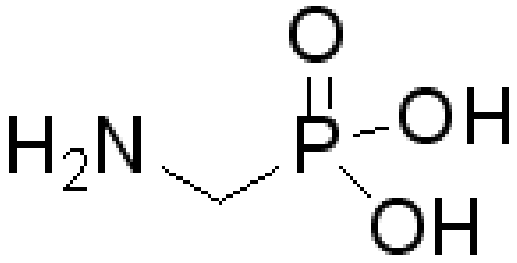
H2N
P
O
OH
OH

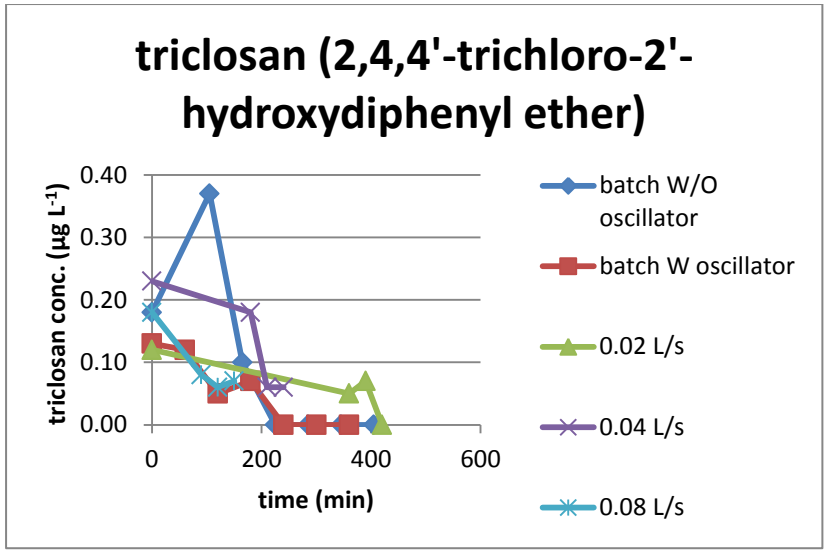
triclosan (2,4,4'-trichloro-2'-hydroxydiphenyl ether)
triclosan conc. (µg L-1)
0.40
0.30
0.20
0.10
0.00
0
200
400
600
time (min)
batch W/O oscillator
batch W oscillator
0.02 L/s
0.04 L/s
0.08 L/s

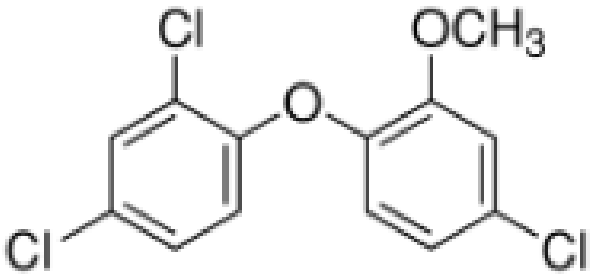
Cl
OCH3
O
Cl
Cl

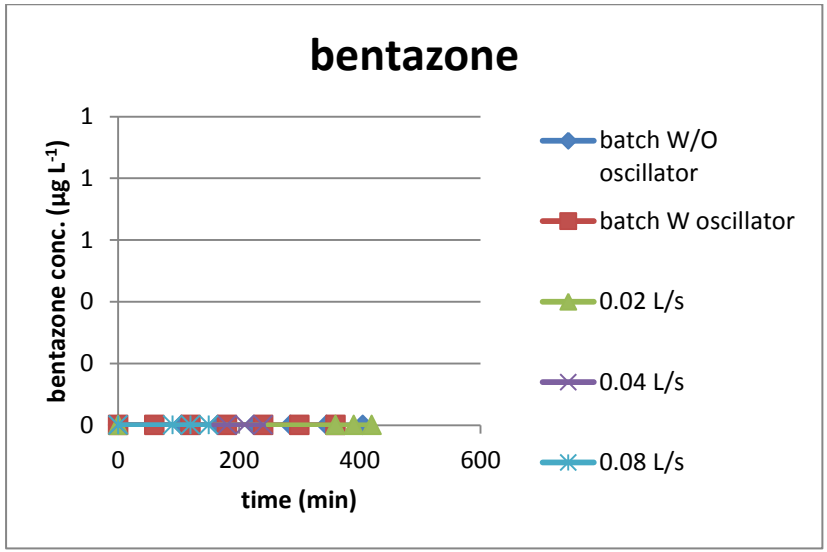
bentazone
bentazone conc. (µg L-1)
1
1
1
0
0
0
0
200
400
600
time (min)
batch W/O oscillator
batch W oscillator
0.02 L/s
0.04 L/s
0.08 L/s

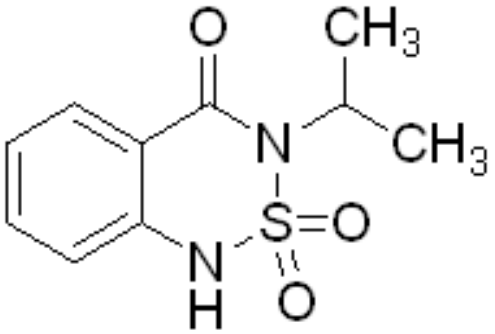
O
CH3
N
CH3
S=O
N
H
O

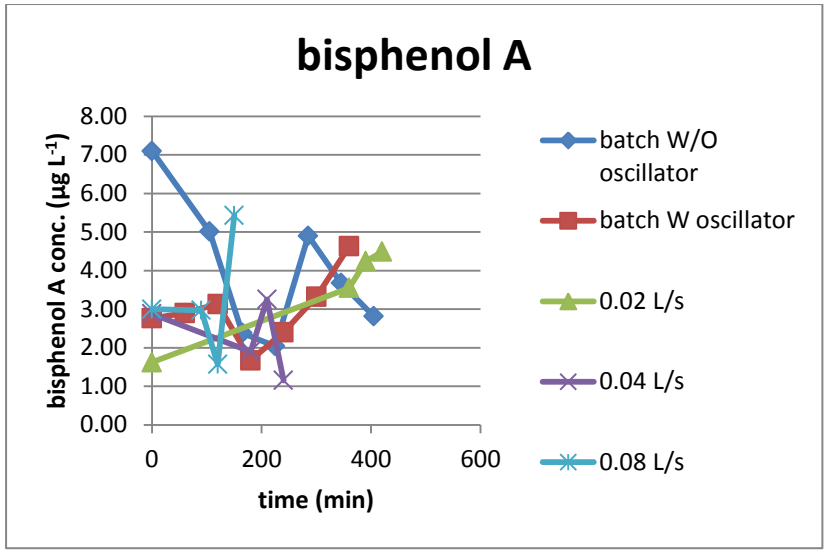
bisphenol A
bisphenol A conc. (µg L-1)
8.00
7.00
6.00
5.00
4.00
3.00
2.00
1.00
0.00
0
200
400
600
time (min)
batch W/O oscillator
batch W oscillator
0.02 L/s
0.04 L/s
0.08 L/s

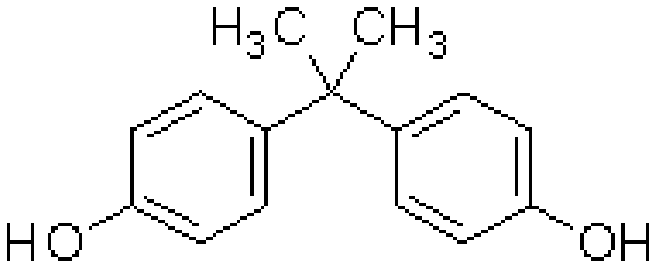
H3C
CH3
HO
OH

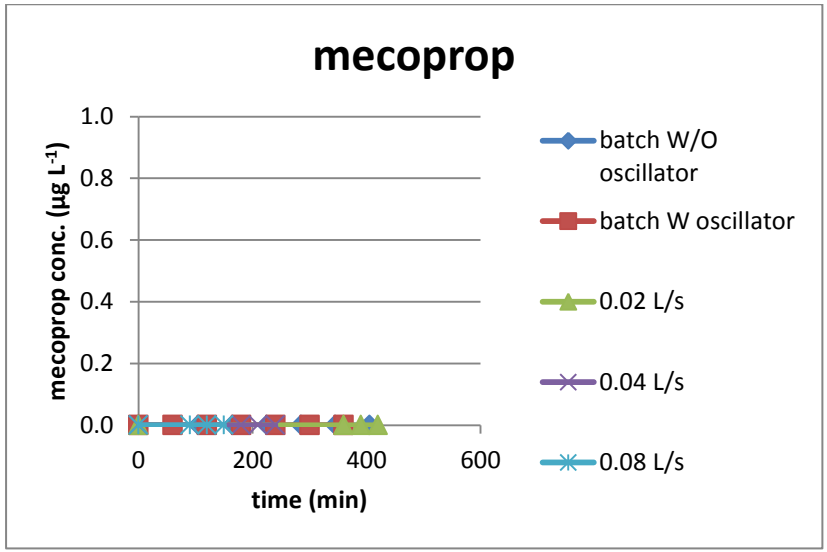
mecoprop
mecoprop conc. (µg L-1)
1.0
0.8
0.6
0.4
0.2
0.0
0
200
400
600
time (min)
batch W/O oscillator
batch W oscillator
0.02 L/s
0.04 L/s
0.08 L/s

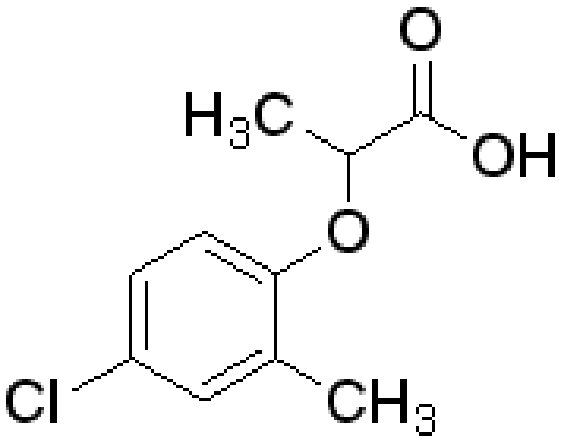
O
H3C
OH
O
Cl
CH3

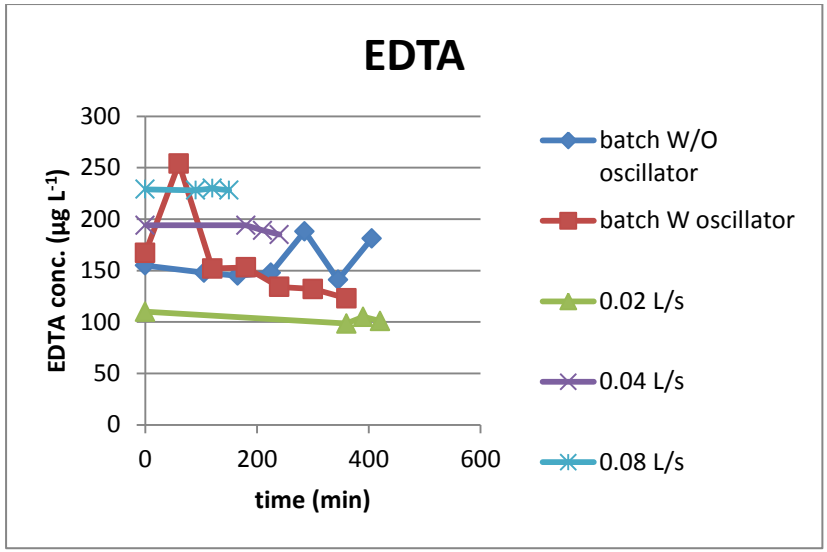
EDTA
EDTA conc. (µg L-1)
300
250
200
150
100
50
0
0
200
400
600
time (min)
batch W/O oscillator
batch W oscillator
0.02 L/s
0.04 L/s
0.08 L/s

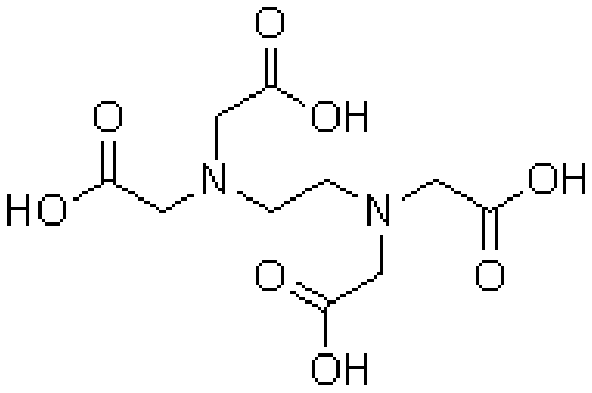
O
OH
O
HO
N
N
OH
O
O
O
OH

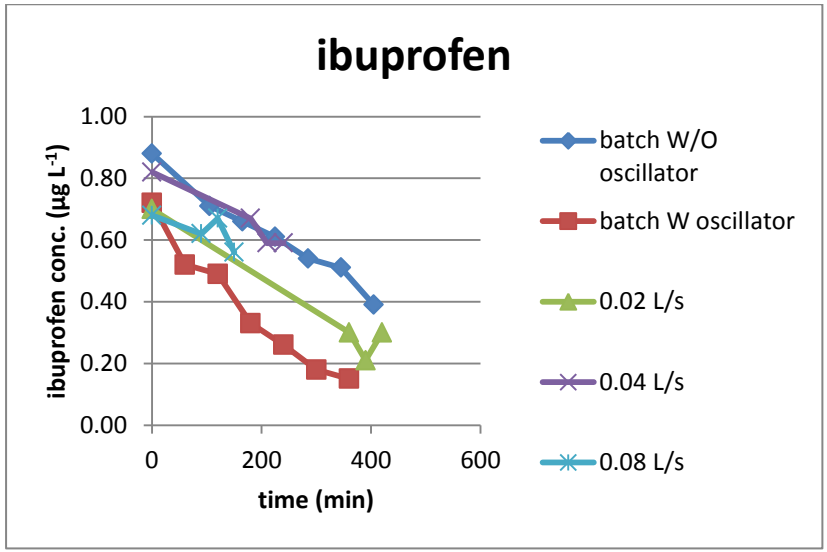
ibuprofen
ibuprofen conc. (µg L-1)
1.00
0.80
0.60
0.40
0.20
0.00
0
200
400
600
time (min)
batch W/O oscillator
batch W oscillator
0.02 L/s
0.04 L/s
0.08 L/s

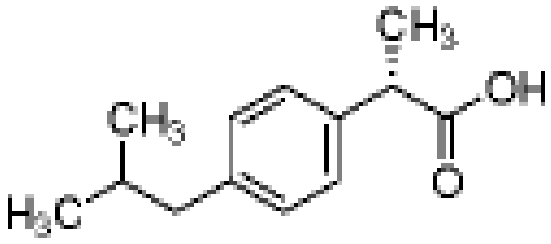
CH3
OH
CH3
H3C
O

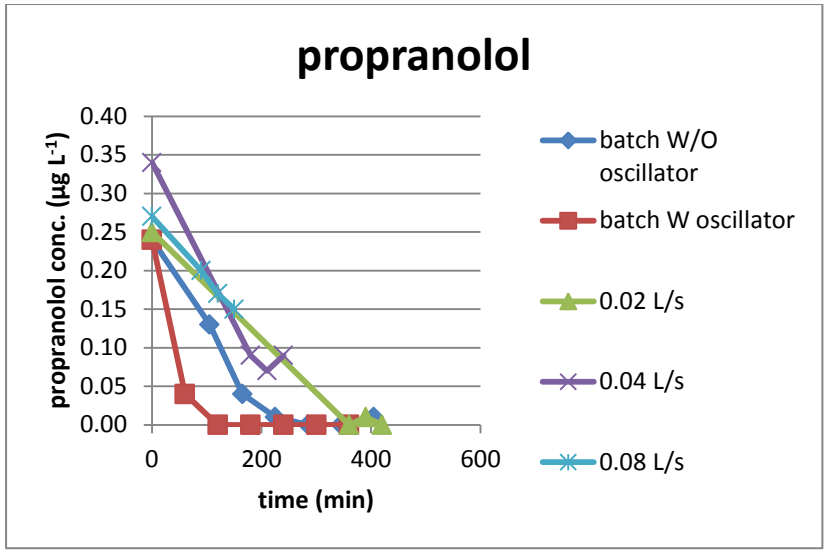
propranolol
propranolol conc. (µg L-1)
0.40
0.35
0.30
0.25
0.20
0.15
0.10
0.05
0.00
0
200
400
600
time (min)
batch W/O oscillator
batch W oscillator
0.02 L/s
0.04 L/s
0.08 L/s

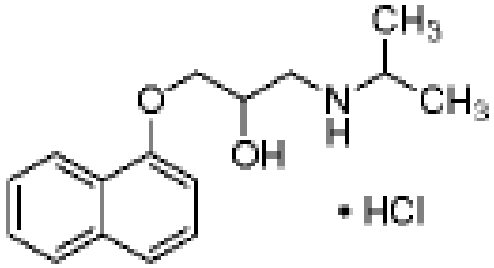
CH3
O
N
H
CH3
OH
• HCl

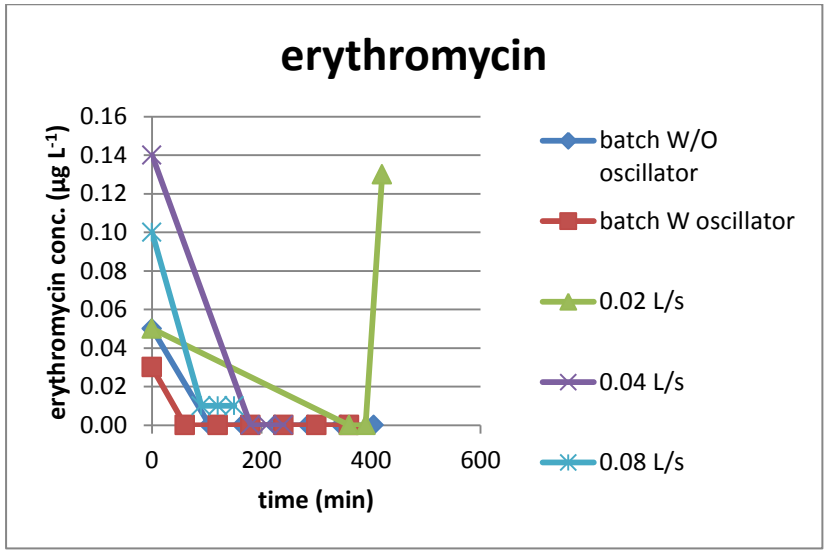
erythromycin
erythromycin conc. (µg L-1)
0.16
0.14
0.12
0.10
0.08
0.06
0.04
0.02
0.00
0
200
400
600
time (min)
batch W/O oscillator
batch W oscillator
0.02 L/s
0.04 L/s
0.08 L/s

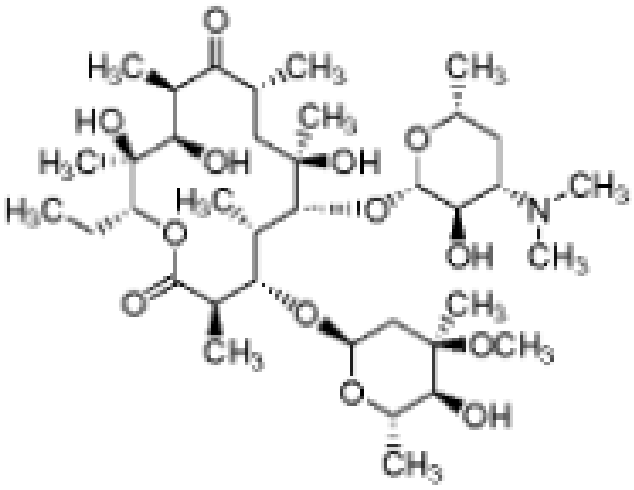
O
H3C
CH3
HO
OH
CH3
OH
H3C
H3C
O
O
O
CH3
N
CH3
OH
CH3
CH3
O
CH3
OCH3
O
OH
CH3

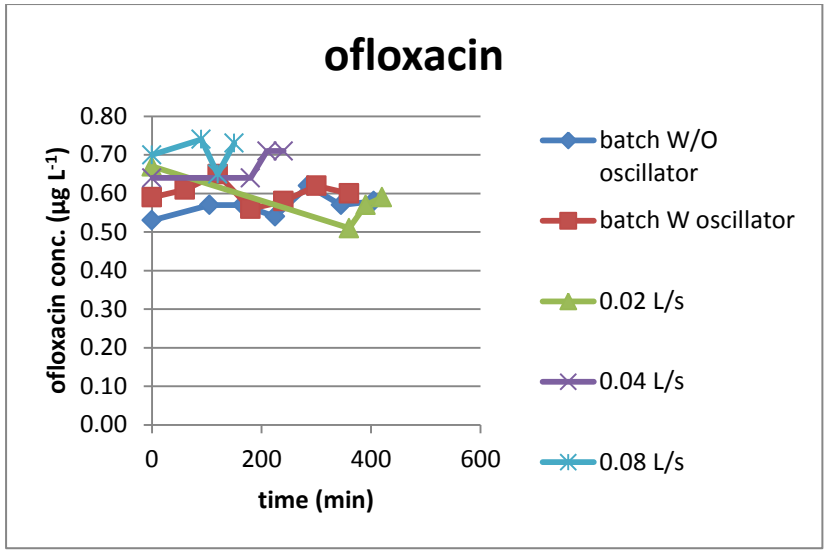
ofloxacin
ofloxacin conc. (µg L-1)
0.80
0.70
0.60
0.50
0.40
0.30
0.20
0.10
0.00
0
200
400
600
time (min)
batch W/O oscillator
batch W oscillator
0.02 L/s
0.04 L/s
0.08 L/s

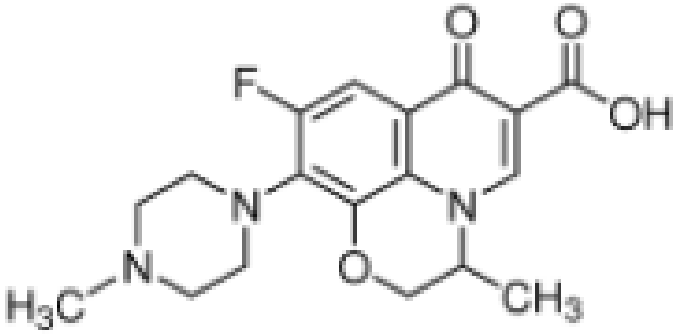
O
O
F
OH
N
N
N
O
H3C
CH3

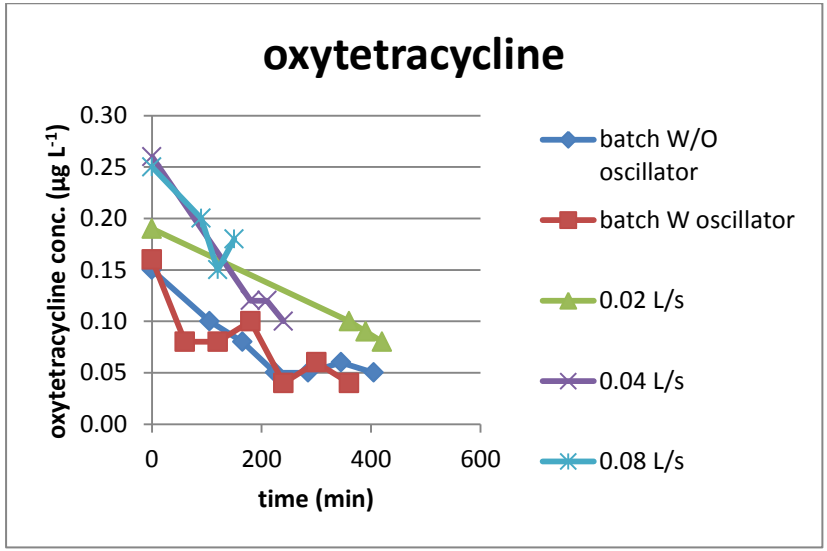
oxytetracycline
oxytetracycline conc. (µg L-1)
0.30
0.25
0.20
0.15
0.10
0.05
0.00
0
200
400
600
time (min)
batch W/O oscillator
batch W oscillator
0.02 L/s
0.04 L/s
0.08 L/s

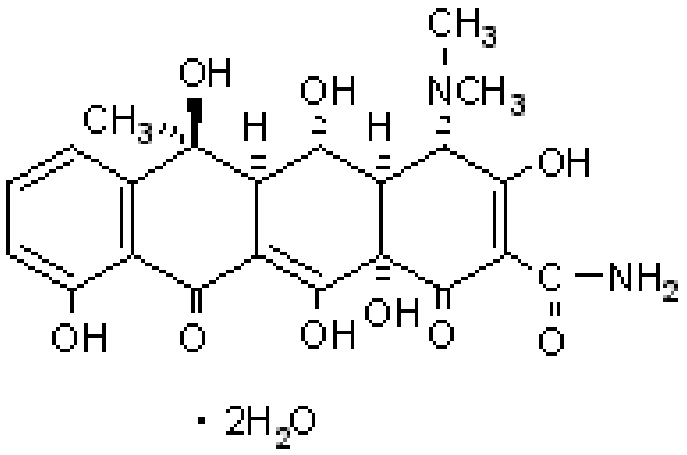
CH3
NCH3
OH
CH3
H
OH
H
OH
C
NH2
OH
O
OH
OH
O
O
· 2H2O

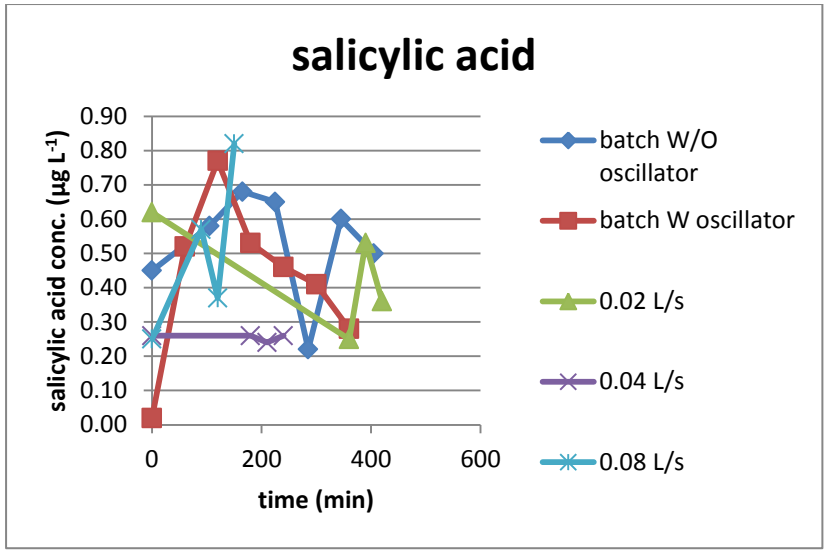
salicylic acid
salicylic acid conc. (µg L-1)
0.90
0.80
0.70
0.60
0.50
0.40
0.30
0.20
0.10
0.00
0
200
400
600
time (min)
batch W/O oscillator
batch W oscillator
0.02 L/s
0.04 L/s
0.08 L/s

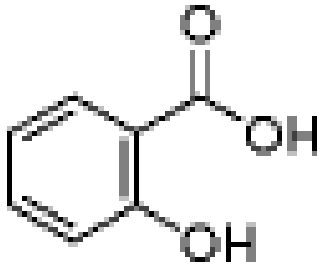
O
OH
OH

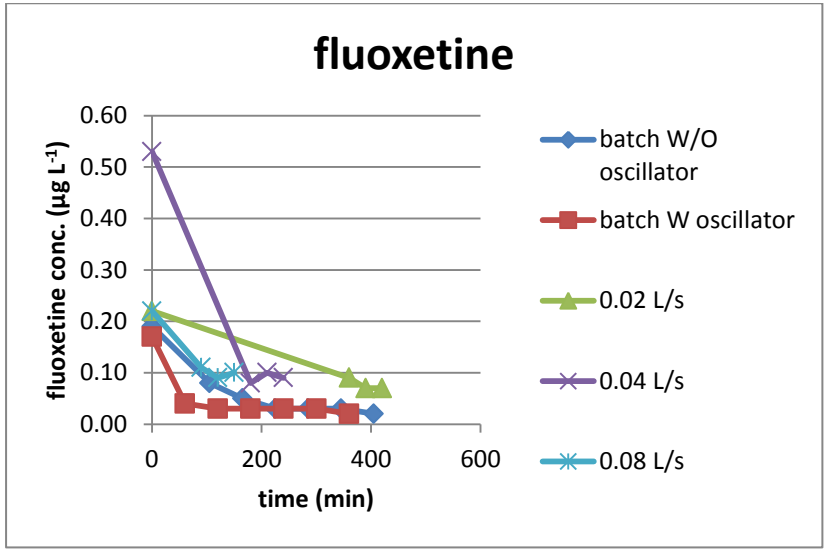
fluoxetine
fluoxetine conc. (µg L-1)
0.60
0.50
0.40
0.30
0.20
0.10
0.00
0
200
400
600
time (min)
batch W/O oscillator
batch W oscillator
0.02 L/s
0.04 L/s
0.08 L/s

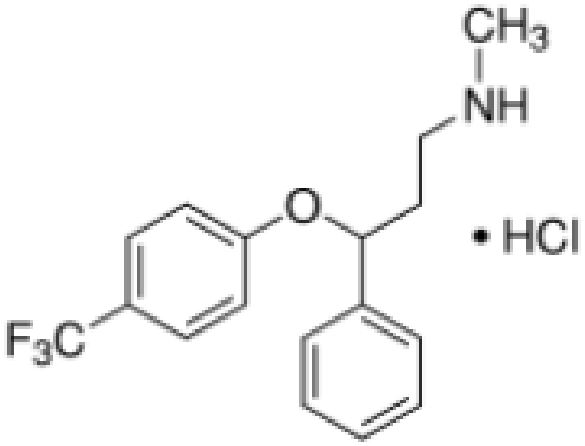
CH3
NH
O
• HCl
F3C

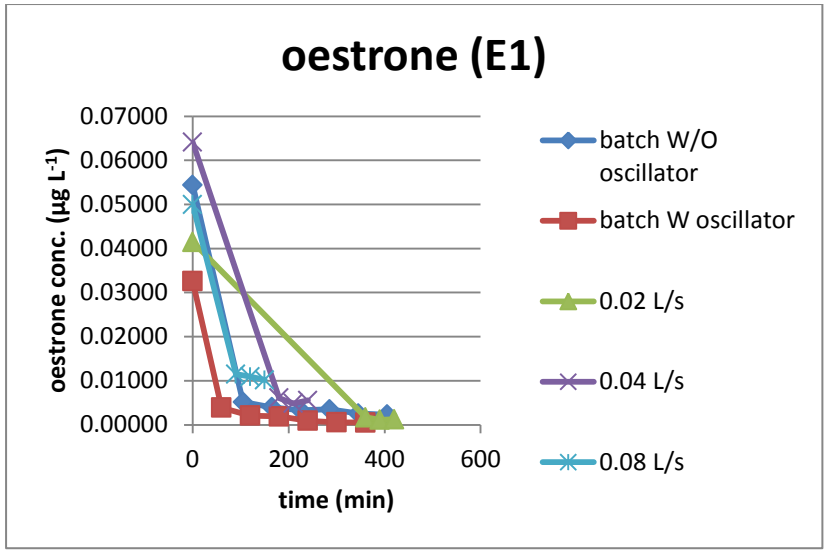
oestrone (E1)
oestrone conc. (µg L-1)
0.07000
0.06000
0.05000
0.04000
0.03000
0.02000
0.01000
0.00000
0
200
400
600
time (min)
batch W/O oscillator
batch W oscillator
0.02 L/s
0.04 L/s
0.08 L/s

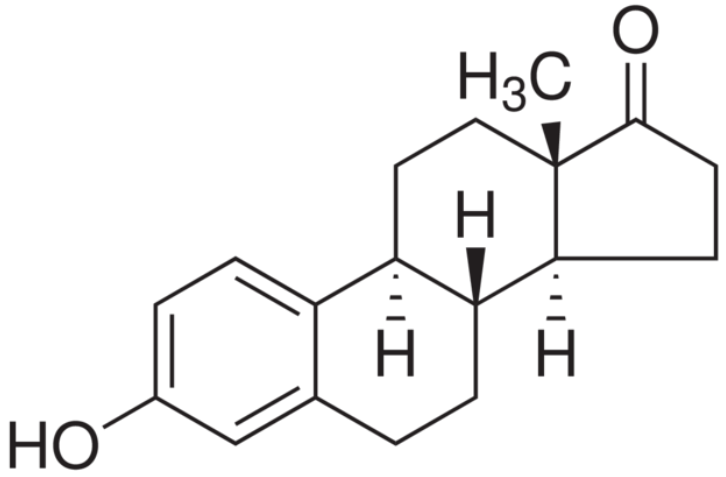
H3C
O
H
H
H
HO

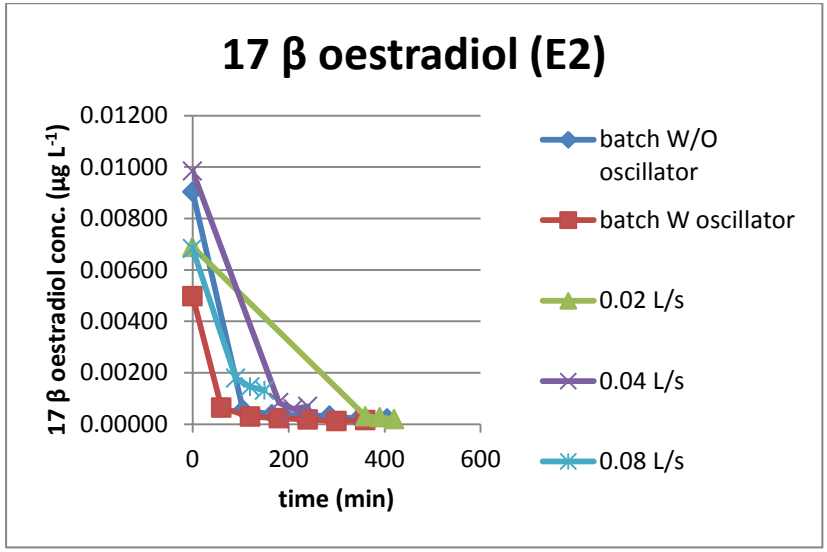
17 β oestradiol (E2)
17 β oestradiol conc. (µg L-1)
0.01200
0.01000
0.00800
0.00600
0.00400
0.00200
0.00000
0
200
400
600
time (min)
batch W/O oscillator
batch W oscillator
0.02 L/s
0.04 L/s
0.08 L/s

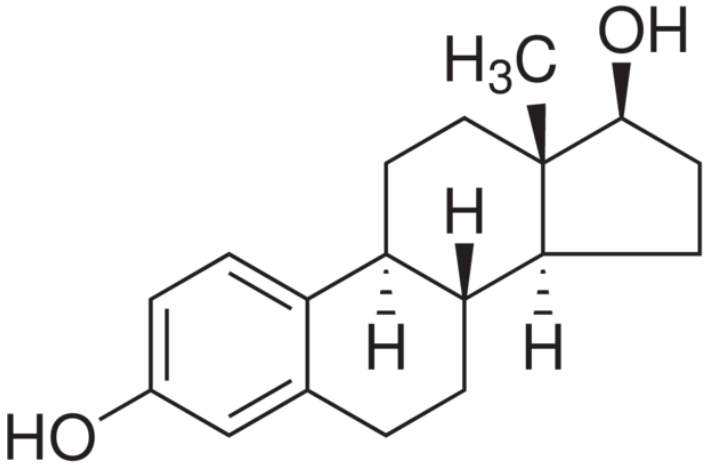
H3C
OH
H
H
H
HO

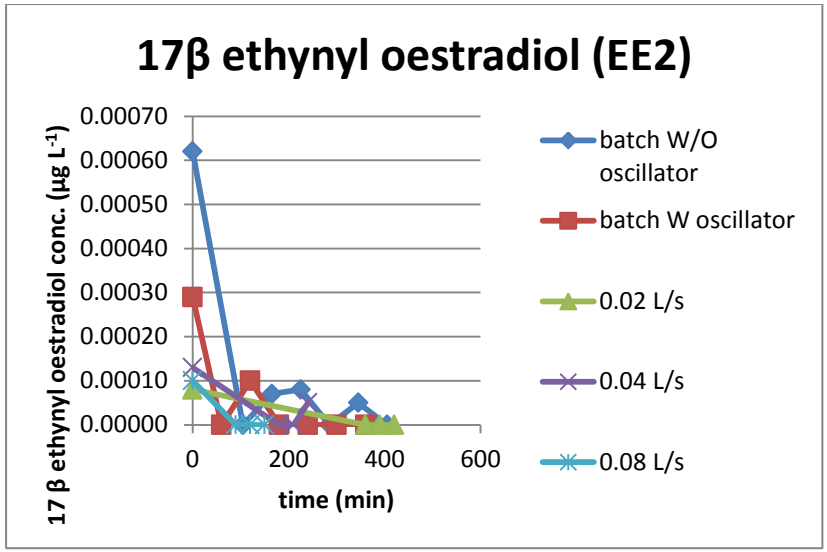

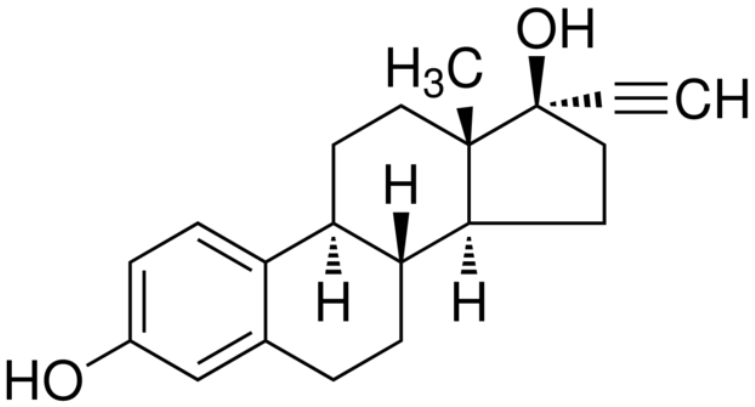

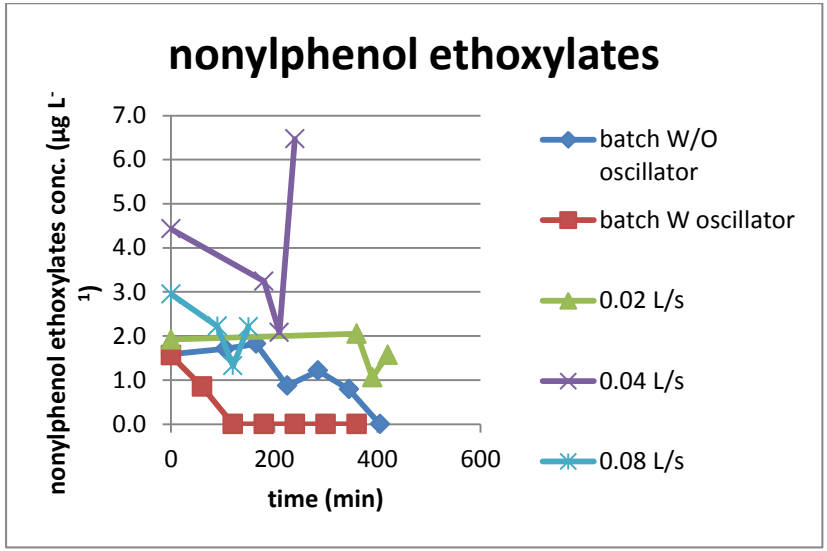

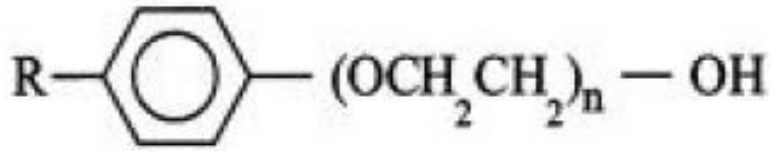

R=C_9H_{19}, nonylphenol ethoxylates (NPE)

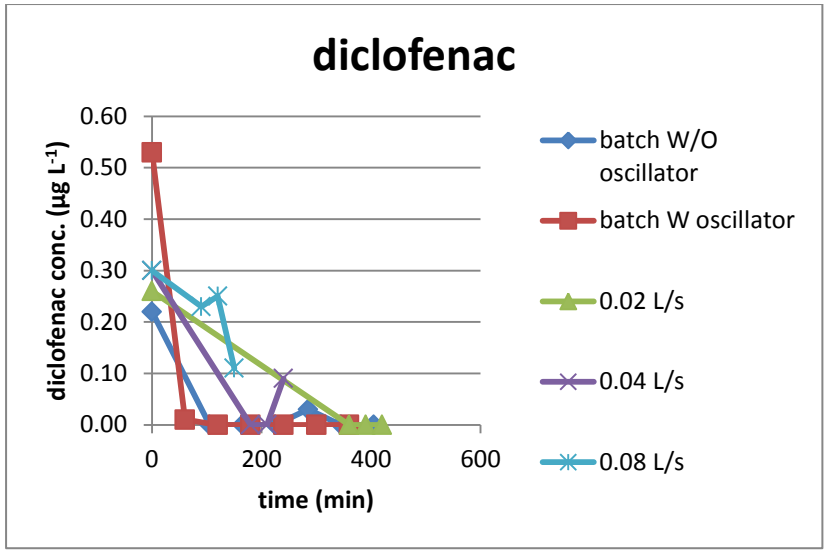
diclofenac
diclofenac conc. (µg L-1)
0.60
0.50
0.40
0.30
0.20
0.10
0.00
0
200
400
600
time (min)
batch W/O oscillator
batch W oscillator
0.02 L/s
0.04 L/s
0.08 L/s

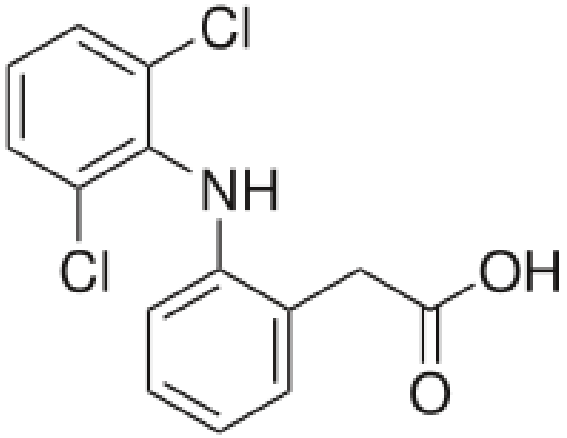
Cl
NH
Cl
OH
O

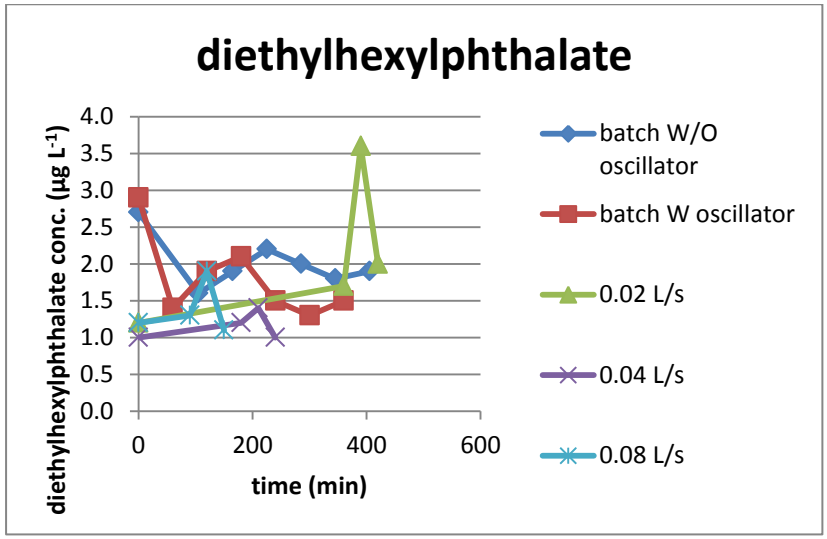
diethylhexylphthalate
diethylhexylphthalate conc. (µg L-1)
4.0
3.5
3.0
2.5
2.0
1.5
1.0
0.5
0.0
0
200
400
600
time (min)
batch W/O oscillator
batch W oscillator
0.02 L/s
0.04 L/s
0.08 L/s

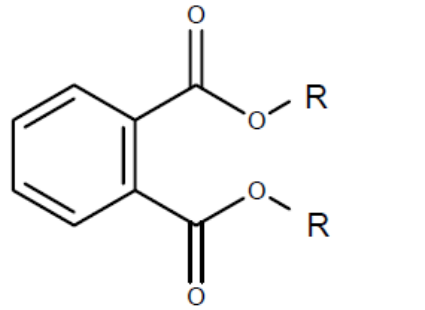
O
O
R
O
R
O

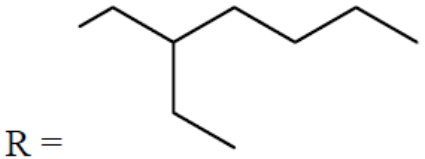
R =

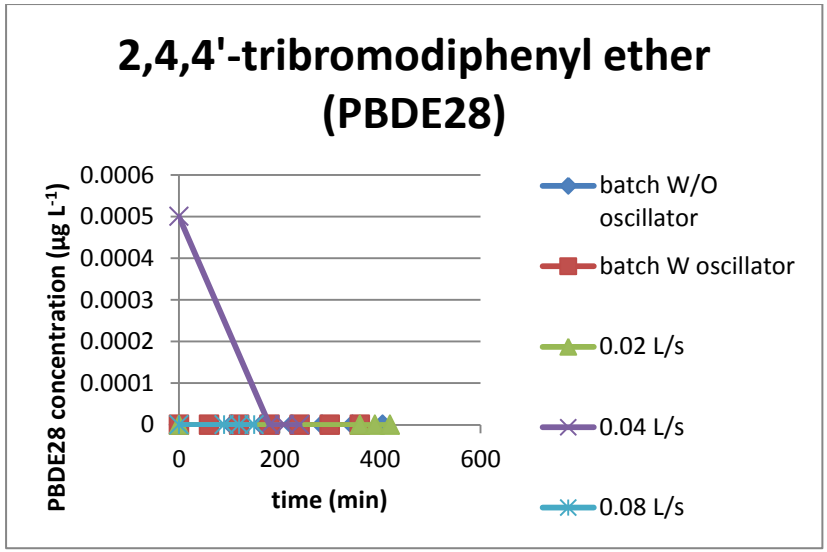
2,4,4'-tribromodiphenyl ether (PBDE28)
PBDE28 concentration (µg L-1)
0.0006
0.0005
0.0004
0.0003
0.0002
0.0001
0
0
200
400
600
time (min)
batch W/O oscillator
batch W oscillator
0.02 L/s
0.04 L/s
0.08 L/s

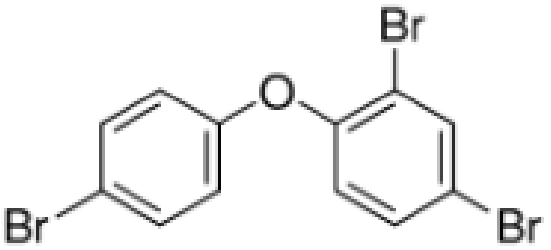
Br
O
Br
Br

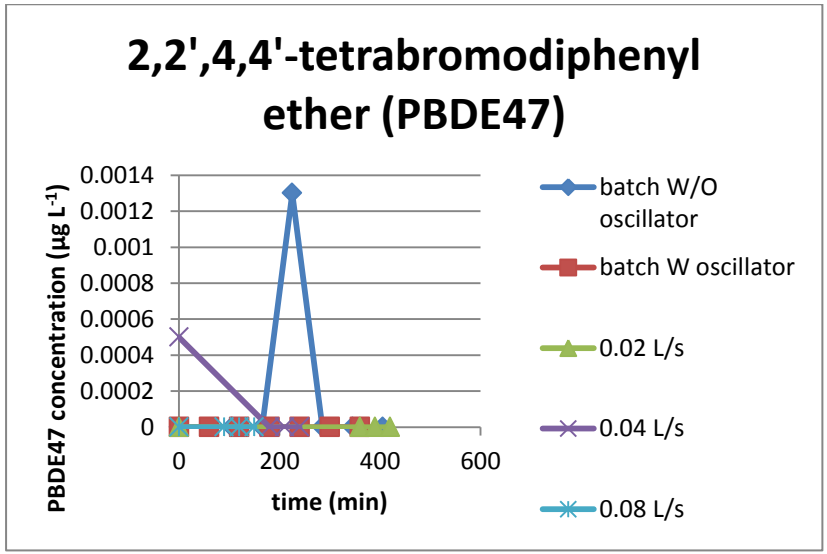
2,2',4,4'-tetrabromodiphenyl ether (PBDE47)
PBDE47 concentration (µg L-1)
0.0014
0.0012
0.001
0.0008
0.0006
0.0004
0.0002
0
0
200
400
600
time (min)
batch W/O oscillator
batch W oscillator
0.02 L/s
0.04 L/s
0.08 L/s

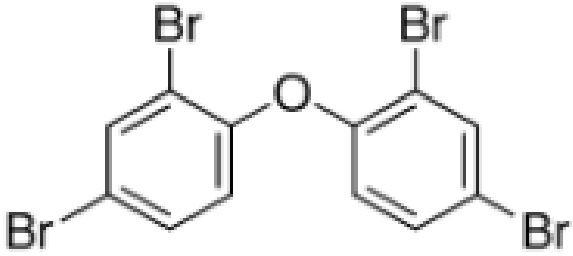
Br
Br
O
Br
Br

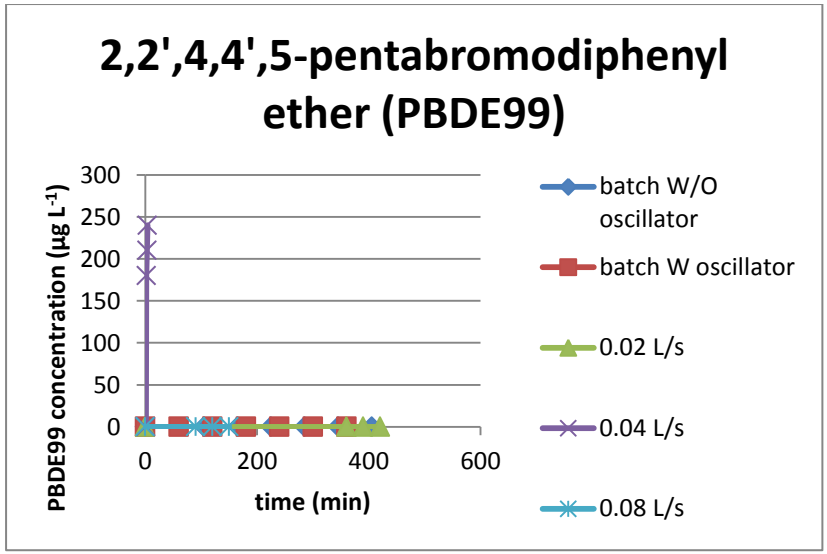
2,2',4,4',5-pentabromodiphenyl ether (PBDE99)
PBDE99 concentration (µg L-1)
300
250
200
150
100
50
0
0
200
400
600
time (min)
batch W/O oscillator
batch W oscillator
0.02 L/s
0.04 L/s
0.08 L/s

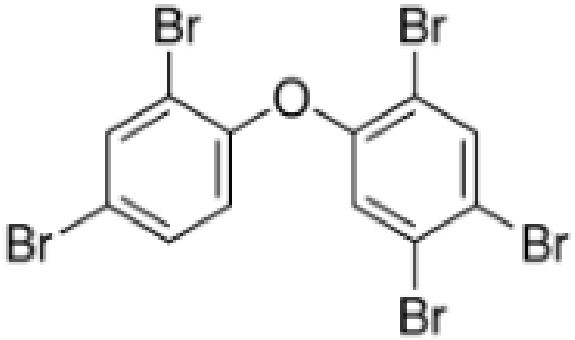
Br
Br
O
Br
Br
Br

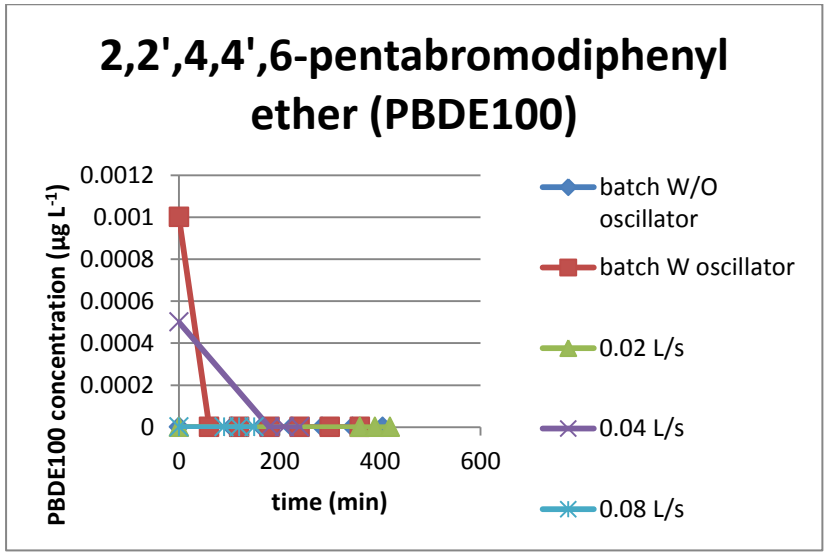
2,2',4,4',6-pentabromodiphenyl ether (PBDE100)
PBDE100 concentration (µg L-1)
0.0012
0.001
0.0008
0.0006
0.0004
0.0002
0
0
200
400
600
time (min)
batch W/O oscillator
batch W oscillator
0.02 L/s
0.04 L/s
0.08 L/s

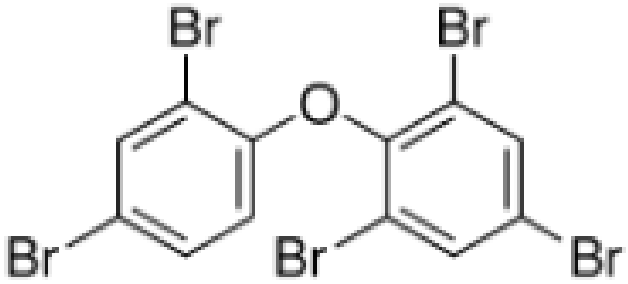
Br
Br
O
Br
Br
Br

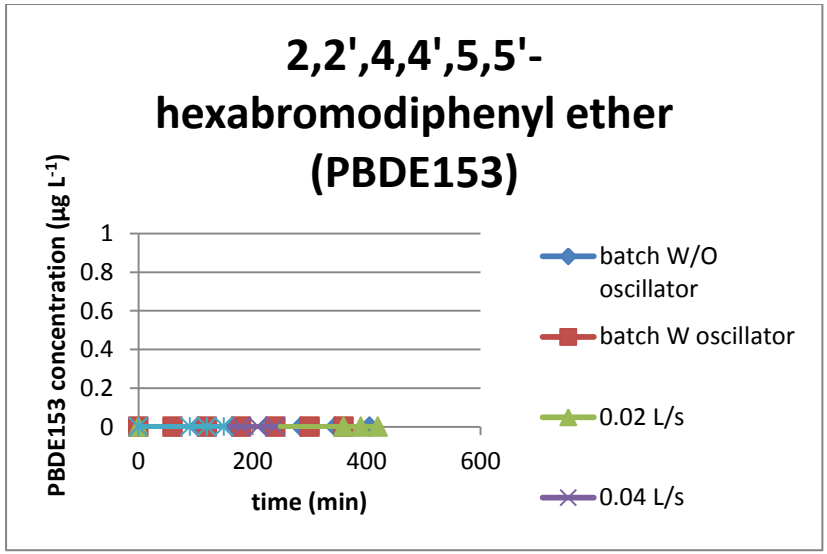
2,2',4,4',5,5'-hexabromodiphenyl ether (PBDE153)
PBDE153 concentration (µg L-1)
1
0.8
0.6
0.4
0.2
0
0
200
400
600
time (min)
batch W/O oscillator
batch W oscillator
0.02 L/s
0.04 L/s

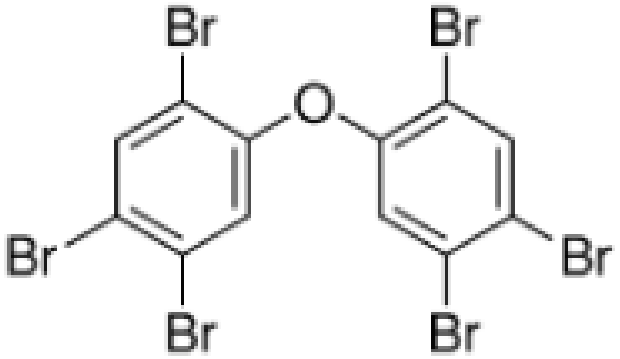
Br
Br
O
Br
Br
Br
Br

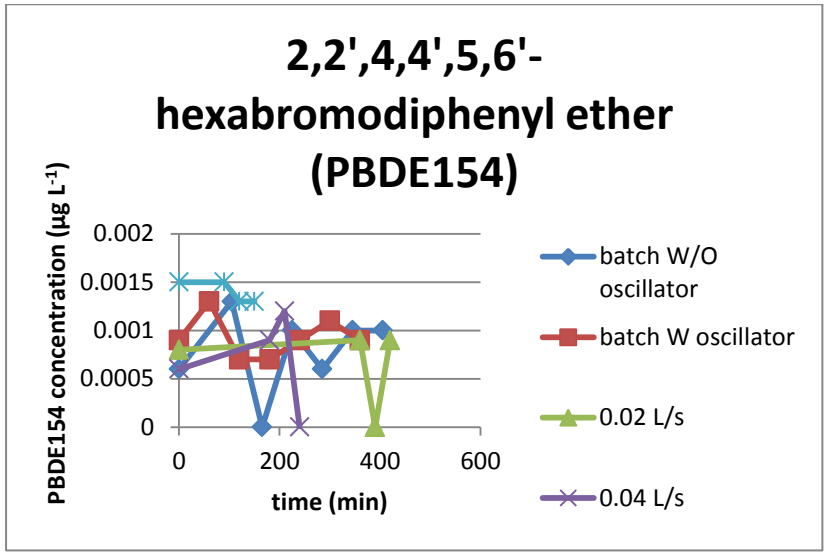
2,2',4,4',5,6'-hexabromodiphenyl ether (PBDE154)
PBDE154 concentration (µg L-1)
0.002
0.0015
0.001
0.0005
0
0
200
400
600
time (min)
batch W/O oscillator
batch W oscillator
0.02 L/s
0.04 L/s

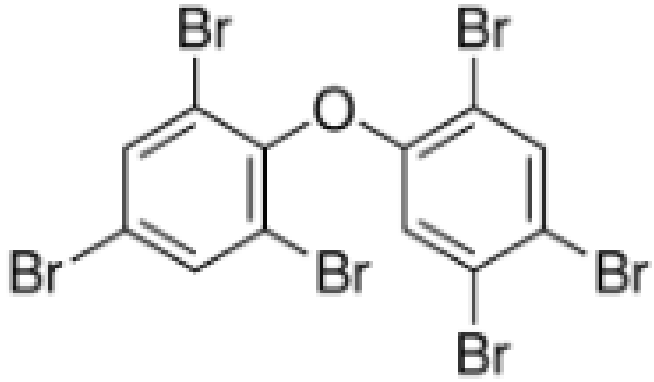
Br
Br
O
Br
Br
Br
Br

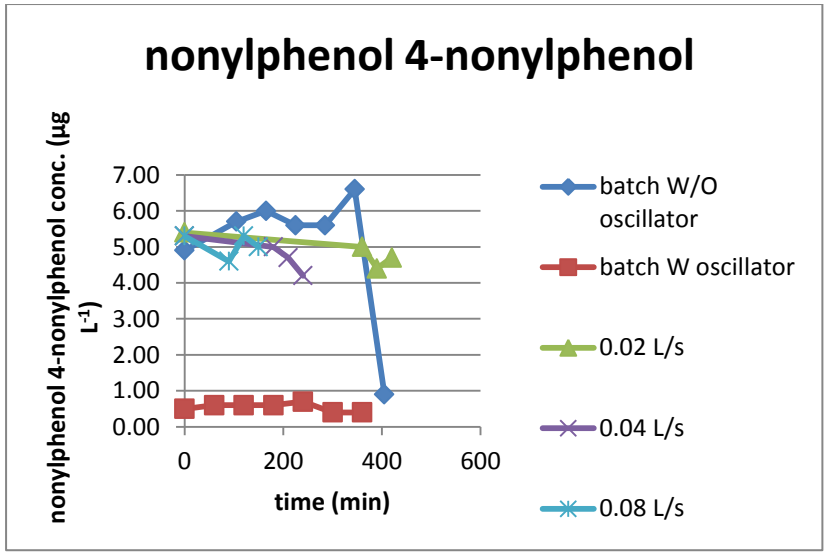
nonylphenol 4-nonylphenol
nonylphenol 4-nonylphenol conc. (µg L-1)
7.00
6.00
5.00
4.00
3.00
2.00
1.00
0.00
0
200
400
600
time (min)
batch W/O oscillator
batch W oscillator
0.02 L/s
0.04 L/s
0.08 L/s

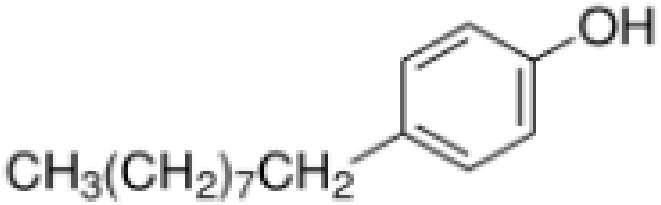
OH
CH3(CH2)7CH2

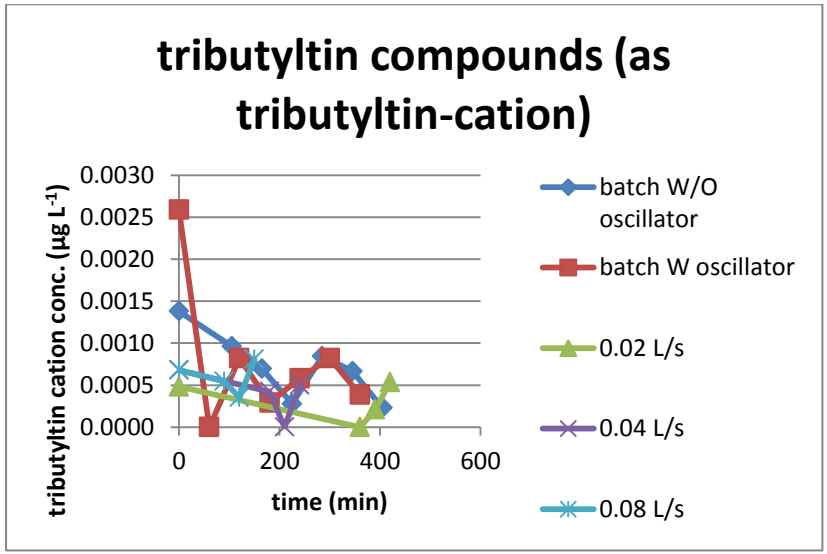
tributyltin compounds (as tributyltin-cation)
tributyltin cation conc. (µg L-1)
0.0030
0.0025
0.0020
0.0015
0.0010
0.0005
0.0000
0
200
400
600
time (min)
batch W/O oscillator
batch W oscillator
0.02 L/s
0.04 L/s
0.08 L/s

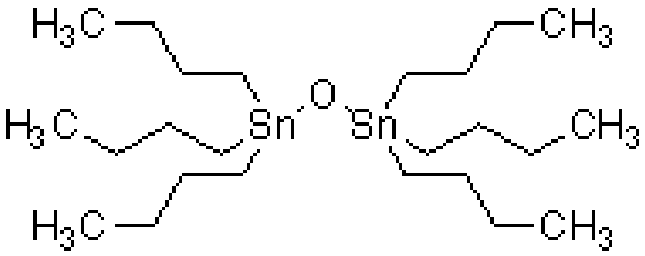
H3C
CH3
H3C
Sn
O
Sn
CH3
H3C
CH3

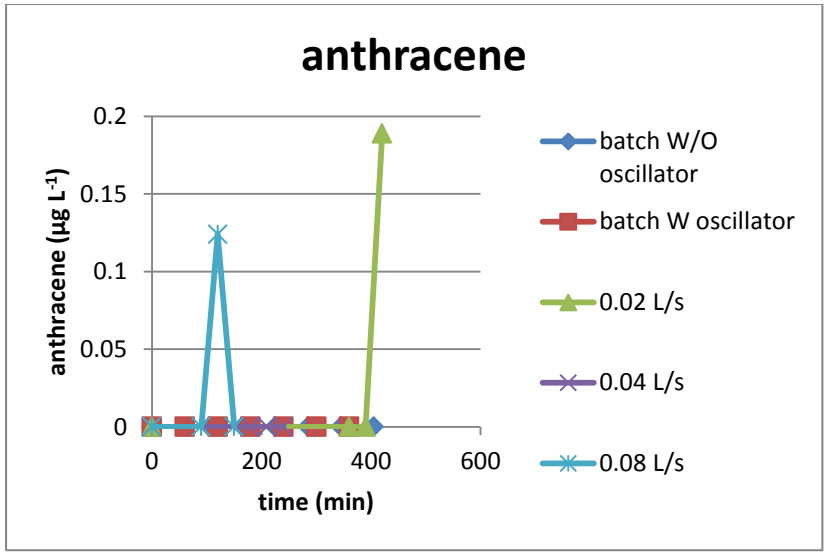
anthracene
anthracene (µg L-1)
0.2
0.15
0.1
0.05
0
0
200
400
600
time (min)
batch W/O oscillator
batch W oscillator
0.02 L/s
0.04 L/s
0.08 L/s

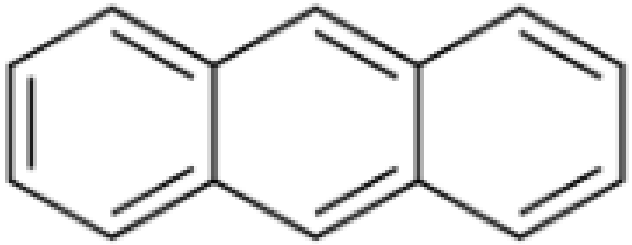

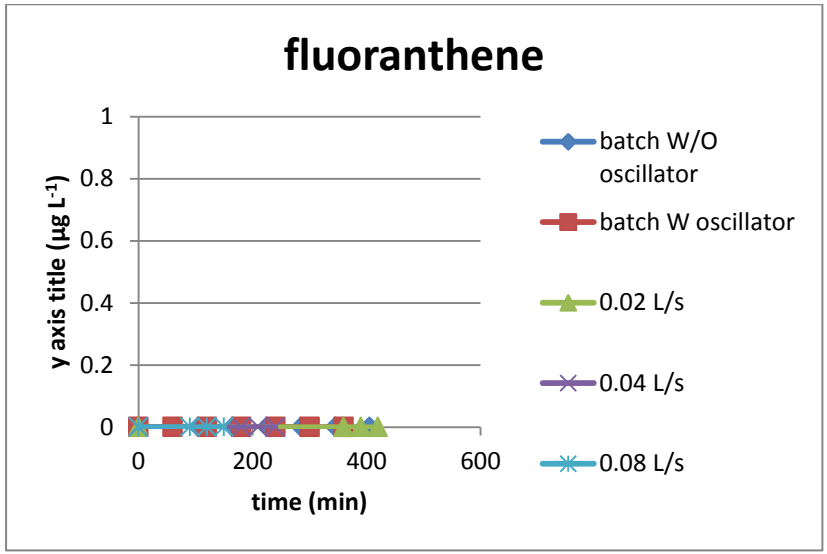
fluoranthene
y axis title (µg L-1)
1
0.8
0.6
0.4
0.2
0
0
200
400
600
time (min)
batch W/O oscillator
batch W oscillator
0.02 L/s
0.04 L/s
0.08 L/s

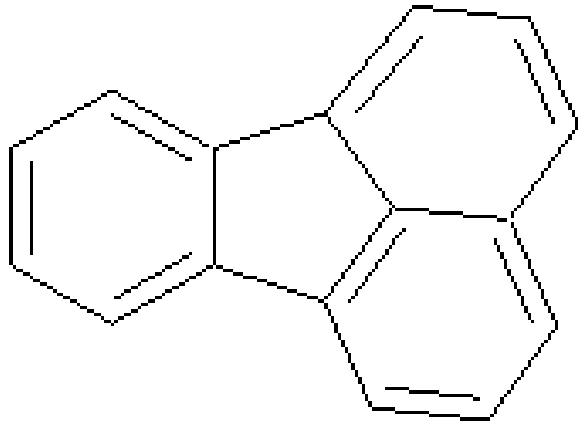

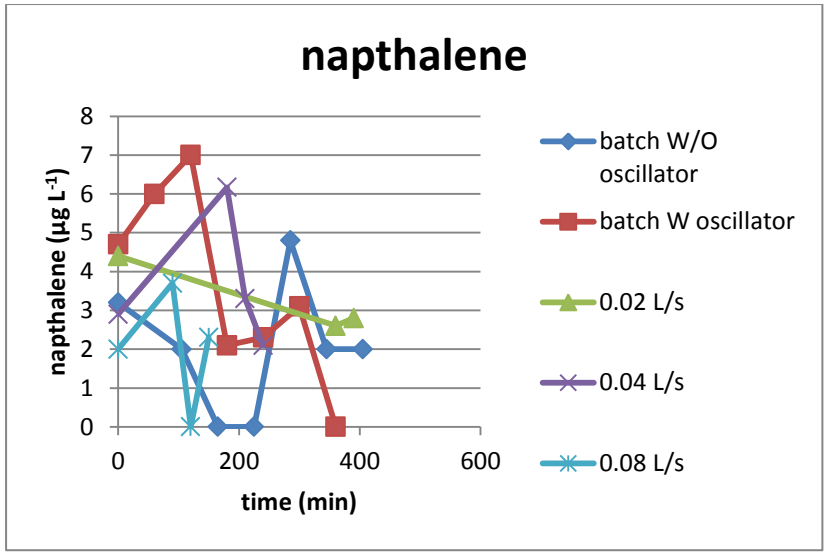
napthalene
napthalene (µg L-1)
8
7
6
5
4
3
2
1
0
0
200
400
600
time (min)
batch W/O oscillator
batch W oscillator
0.02 L/s
0.04 L/s
0.08 L/s

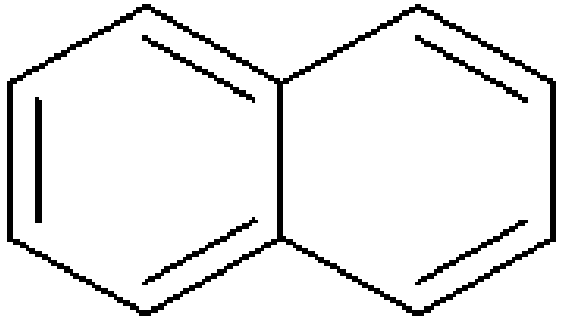

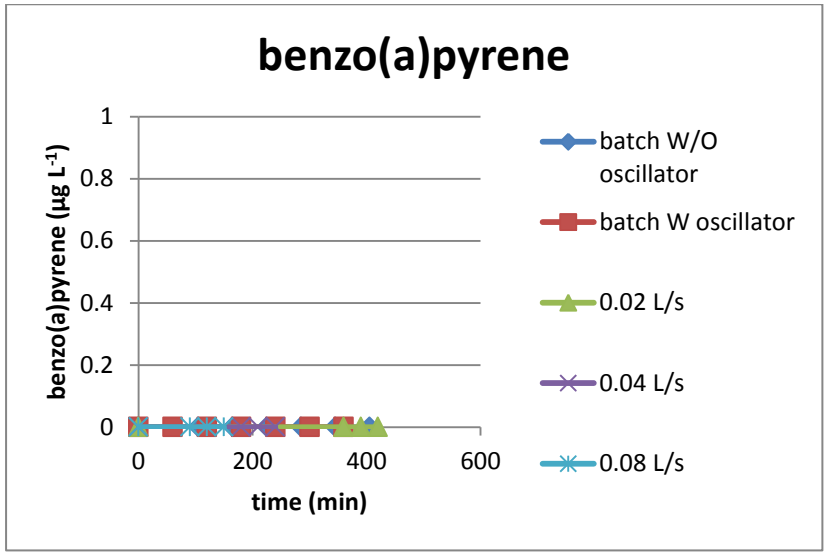
benzo(a)pyrene
benzo(a)pyrene (µg L-1)
1
0.8
0.6
0.4
0.2
0
0
200
400
600
time (min)
batch W/O oscillator
batch W oscillator
0.02 L/s
0.04 L/s
0.08 L/s

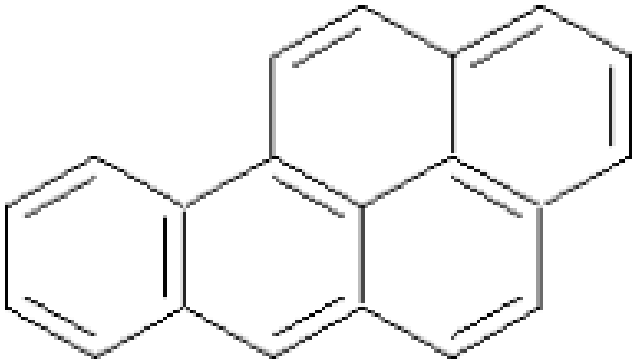

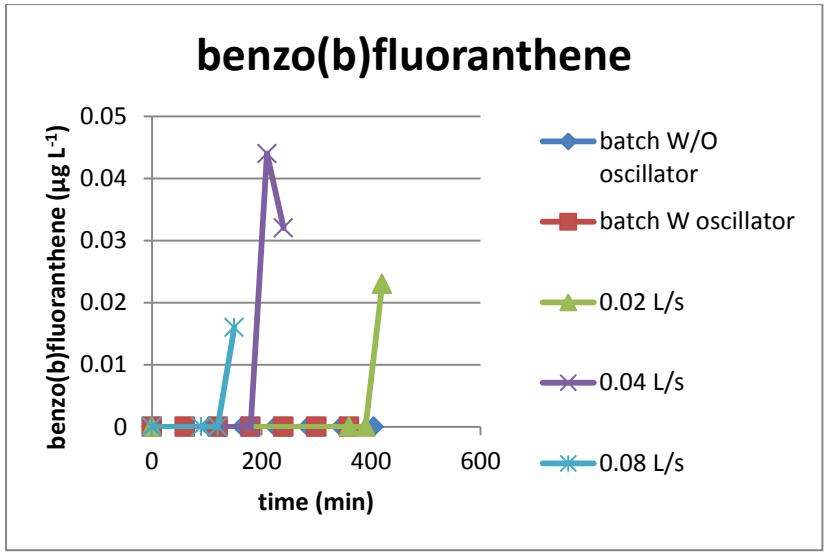
benzo(b)fluoranthene
benzo(b)fluoranthene (µg L-1)
0.05
0.04
0.03
0.02
0.01
0
0
200
400
600
time (min)
batch W/O oscillator
batch W oscillator
0.02 L/s
0.04 L/s
0.08 L/s

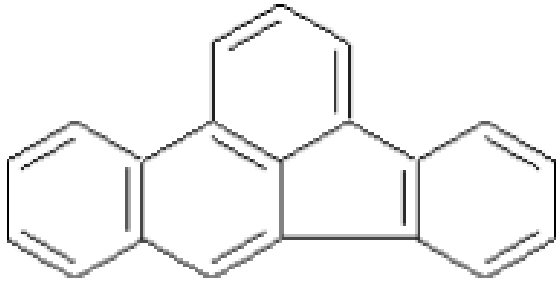

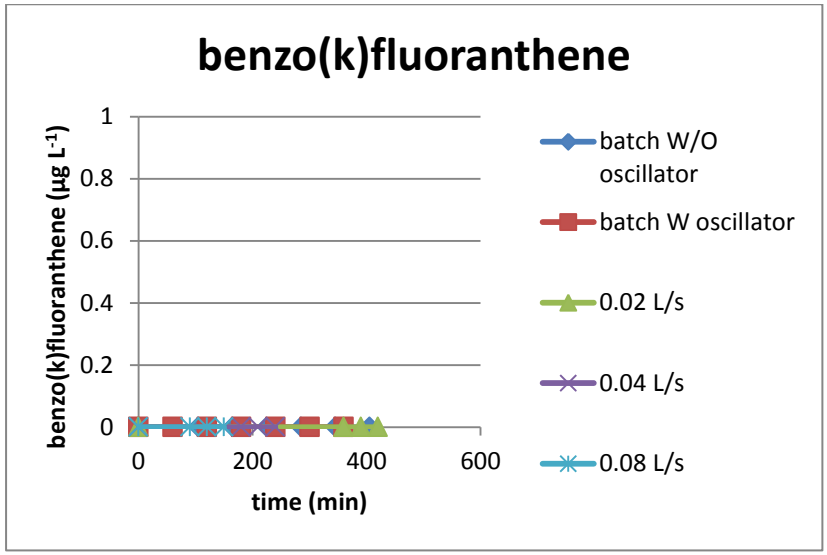
benzo(k)fluoranthene
benzo(k)fluoranthene (µg L-1)
1
0.8
0.6
0.4
0.2
0
0
200
400
600
time (min)
batch W/O oscillator
batch W oscillator
0.02 L/s
0.04 L/s
0.08 L/s

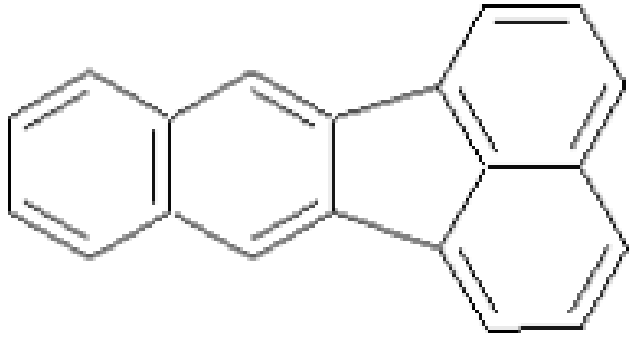

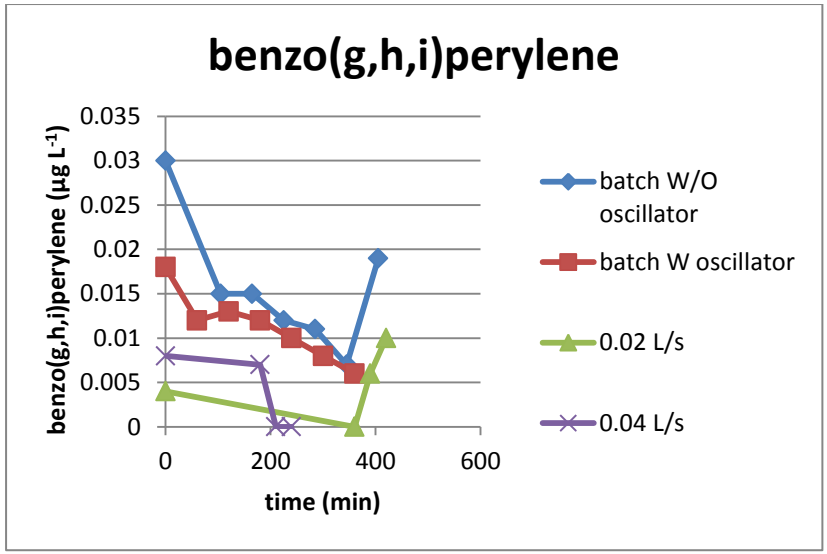
benzo(g,h,i)perylene
benzo(g,h,i)perylene (µg L-1)
0.035
0.03
0.025
0.02
0.015
0.01
0.005
0
0
200
400
600
time (min)
batch W/O oscillator
batch W oscillator
0.02 L/s
0.04 L/s

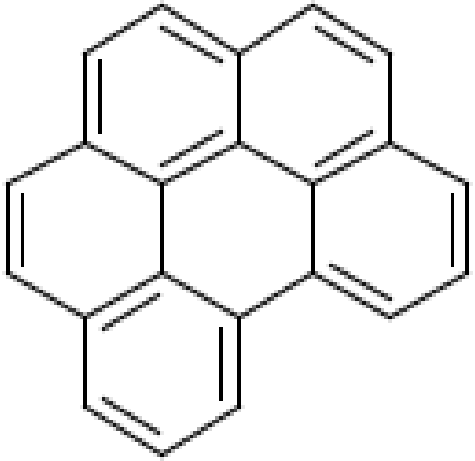

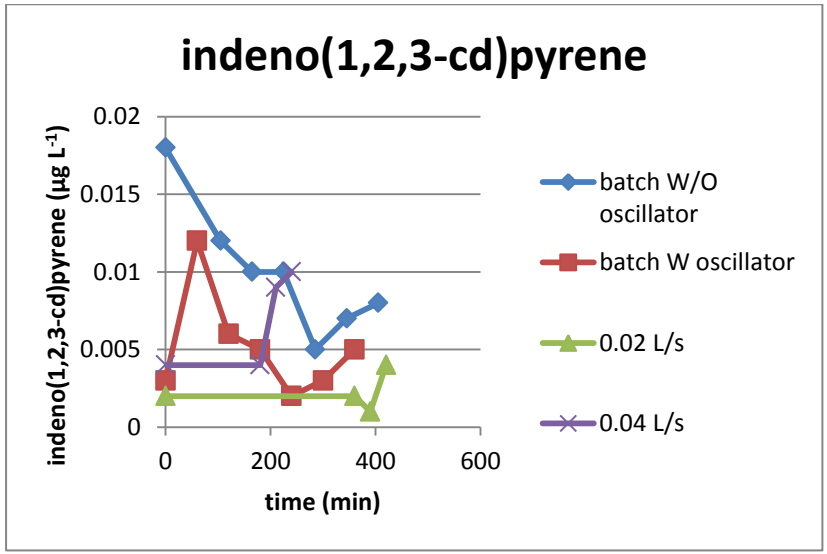
indeno(1,2,3-cd)pyrene
indeno(1,2,3-cd)pyrene (µg L-1)
0.02
0.015
0.01
0.005
0
0
200
400
600
time (min)
batch W/O oscillator
batch W oscillator
0.02 L/s
0.04 L/s

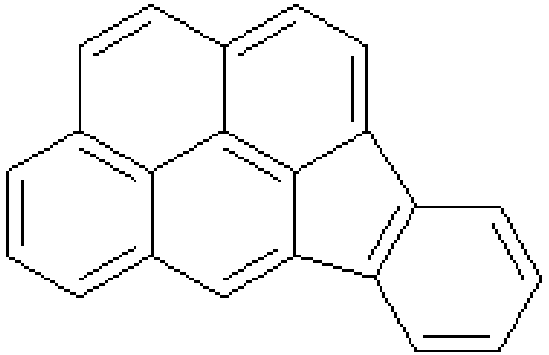

Appendix 3

Number	Reaction	(Sakiyama et al., 2012)	(Kossyi et al., 1992)
R1	N2 + e => N(4S) + N(2D) + e	3.99e-17*abs(ee)^(2.24)*exp(-9.0982/abs(ee))	
R1	N2 + e => N(4S) + N(2P) + e		
R2	N2 + e => N2(A) + e	3.34e-16*abs(ee)^(-0.06)*exp(-8.5/abs(ee))	10^(-8.4-(14/(En)))
R3	N2 + e => N2(B) + e	8.44e-15*abs(ee)^(-0.33)*exp(-9.15/abs(ee))	(10^(-8.2-(14.8/(En))))+(10^(-8.3-(15.4/(En))))+(10^(-8.7-(16.8/(En))))
R4	N2 + e => N2+ + e + e	1.00e-16*abs(ee)^(1.90)*exp(-14.6/abs(ee))	(10^(-8.3-(36.5/(En))))
R5	N(4S) + e => N(2D) + e	5.06e-15*exp(-10.8/abs(ee)^3.95)	
R5	N(4S) + e => N(2P) + e		
R6	e+N=>N++e+e	1.45e-17*abs(ee)^2.58*exp(-8.54/abs(ee))	
R7	O2 + e => O(3P) + O(3P) + e	2.03e-14*abs(ee)^(-0.10)*exp(-8.47/abs(ee))	(10^(-7.9-(13.4/(En))))
R8	O2 + e => O(3P) +	1.82e-14*abs(ee)^(-0.13)*exp(-10.7/abs(ee))	(10^(-8-(16.9/(En))))

	O(1D) + e		
R8	O2 + e => O(3P) + O(1S) + e		(10^(-8.8-(11.9/(En))))
R9	O2 + e => O2(a) + e	1.04e-15*exp(-2.59/abs(ee))	(10^(-10.2-(0.35/(En))))
R10	O2 + e => O2+ + e + e	9.54e-12*abs(ee)^(-1.05)*exp(-55.6/abs(ee))	(10^(-8.8-(28.1/(En))))
R11	O3 + e => O2 + O + e	1.78e-12*abs(ee)^(-0.614)*exp(-11.5/abs(ee))	10*((10^(-7.9-(13.4/(En))))+(10^(-8-(16.9/(En))))+(10^(-8.8-(11.9/(En)))))
R12	O(3P) + e => O(1D) + e	7.46e-15*exp(-5.58/abs(ee)^1.47)	
R12	O(3P) + e => O(1S) + e		
R13	e+O=>O++e+e	4.75e-15*abs(ee)^0.61*exp(-22.1/abs(ee))	
R14	e+H2O=>H2O++e+e	9.65e-18*abs(ee)^2.53*exp(-8.99/abs(ee))	
R15	e+H2O=>OH++H+e+e	9.89e-12*abs(ee)^(-1.64)*exp(-67.6/abs(ee))	
R16	e+H2O=>H++OH+e+e	7.45e-15*abs(ee)^0.34*exp(-54.24/abs(ee))	
R17	e+H2O=>O++H2+e+e	7.40e-16*abs(ee)^0.45*exp(-55.51/abs(ee))	
R18	e+H2O=>H2++O+e+e	8.49e-15*abs(ee)^-1.23*exp(-74.0/abs(ee))	
R19	e+H2O=>OH+H+e	5.15e-15*abs(ee)^(0.62)*exp(-10.87/abs(ee))	

R20	e+H2O=>H2+O(1D)+e	5.19e-18*abs(ee)^(1.2)*exp(-13.75/abs(ee))	
R21	e+H2=>H+H+e	3.29e-15*abs(ee)^0.578*exp(-7.56/abs(ee))	
R22	e+H2=>H2++e+e	4.00e-17*abs(ee)^2.13*exp(-14.88/abs(ee))	
R23	e+N2O5=>NO2++NO3+e+e	2.43e-17*abs(ee)^2.77*exp(-5.62/abs(ee))	
R24	e+N++M=>N+M	3.12e-35/(2*elec/3/kb*abs(ee))^1.5	
R25	N2+ + e => N + N	1.66e-12/(2*elec/3/kb*abs(ee))^0.7	2.8E-7*((300/(En))^0.5)
R26	N2+ + e => N + N(2D)	1.50e-12/(2*elec/3/kb*abs(ee))^0.7	2E-7*((300/(En))^0.5)
R27	e+N2++M=>N2+M	3.12e-35/(2*elec/3/kb*abs(ee))^1.5	
R28	N3+ + e => N2 + N	3.46e-12/(2*elec/3/kb*abs(ee))^0.5	2E-7*((300/(En))^0.5)
R29	N4+ + e => N2 + N2	4.73e-11/(2*elec/3/kb*abs(ee))^0.53	2E-6*((300/(En))^0.5)
R30	e+O++M=>O+M	3.12e-35/(2*elec/3/kb*abs(ee))^1.5	
R31	O2+ + e => O + O	1.68e-11/(2*elec/3/kb*abs(ee))^0.7	2E-7*(300/(En))
R32	e+O2+=>O+O(1D)	1.24e-11/(2*elec/3/kb*abs(ee))^0.7	
R33	e+O2++M=>O2+M	3.12e-35/(2*elec/3/kb*abs(ee))^1.5	1.3E-6*((300/(En))^0.5)
R34	O4+ + e => O2 + O2	2.42e-11/(2*elec/3/kb*abs(ee))^0.5	1.4E-6*((300/(En))^0.5)
R35	N2O+ + e => N2 + O	3.46e-12/(2*elec/3/kb*abs(ee))^0.5	2E-7*((300/(En))^0.5)
R36	NO+ + e => N + O	1.07e-11/(2*elec/3/kb*abs(ee))^0.85	4E-7*((300/(En))^1.5)
R37	NO+ + e => N(2D) +	4.28e-11/(2*elec/3/kb*abs(ee))^0.85	3E-7*(300/(En))

	O		
R38	e+NO++M=>NO+M	3.12e-35/(2*elec/3/kb*abs(ee))^1.5	1.3E-6*((300/(En))^0.5)
			1.3E-6*((300/(En))^0.5)
			1.3E-6*((300/(En))^0.5)
R39	e+NO2+=>NO+O	3.46e-12/(2*elec/3/kb*abs(ee))^0.5	2E-7*((300/(En))^0.5)
R40	e+H2+=>H+H	1.86e-13/(2*elec/3/kb*abs(ee))^0.43	
R41	e+H3+=>H+H2	5.20e-11/(2*elec/3/kb*abs(ee))^0.5	
R42	e+H3+=>H+H+H	1.14e-11/(2*elec/3/kb*abs(ee))^0.97	
R43	e+H2O+=>OH+H	2.73e-12/(2*elec/3/kb*abs(ee))^0.5	
R44	e+H2O+=>O+H2	1.37e-12/(2*elec/3/kb*abs(ee))^0.5	
R45	e+H2O+=>O+H+H	1.37e-12/(2*elec/3/kb*abs(ee))^0.5	
R46	e+H3O+=>OH+H+H	5.46e-12/(2*elec/3/kb*abs(ee))^0.5	
R47	e+e+N+=>N+e	1.0e-31*(tgas/(2*elec/3/kb*abs(ee)))^4.5	
R48	e+e+N2+=>N2+e	1.0e-31*(tgas/(2*elec/3/kb*abs(ee)))^4.5	
R49	e+e+O+=>O+e	1.0e-31*(tgas/(2*elec/3/kb*abs(ee)))^4.5	
R50	e+e+O2+=>O2+e	1.0e-31*(tgas/(2*elec/3/kb*abs(ee)))^4.5	
R51	e+e+NO+=>NO+e	1.0e-31*(tgas/(2*elec/3/kb*abs(ee)))^4.5	
R52	e+e+H+=>H+e	1.0e-31*(tgas/(2*elec/3/kb*abs(ee)))^4.5	
R53	e+e+H2+=>H2+e	1.0e-31*(tgas/(2*elec/3/kb*abs(ee)))^4.5	
R54	e+e+OH+=>OH+e	1.0e-31*(tgas/(2*elec/3/kb*abs(ee)))^4.5	

R55	e+e+H2O+=>H2O+e	1.0e-31*(tgas/(2*elec/3/kb*abs(ee)))^4.5	
R56	e+O+O2=>O-+O2	1.00e-43	1.00E-31
R57	e+O+O2=>O2-+O	1.00e-43	1.00E-31
R58	e+O2+O2=>O2-+O2	1.40e-41*(3*kb*tgas/2/elec/abs(ee))*exp(-600/tgas)*exp(700*(2*elec*abs(ee)/3/kb-tgas)/(2*elec*abs(ee)/3/kb)/tgas)	(1.4E-29)*(300/(En))*(10^(-600/(T)))*(10^((700*((En)-((T)e)))/((En)*((T)e))))
R59	e+O2+N2=>O2-+N2	1.1e-43*(3*kb*tgas/2/elec/abs(ee))^2*exp(-70/tgas)*exp(1500*(2*elec*abs(ee)/3/kb-tgas)/(2*elec*abs(ee)/3/kb)/tgas)	(1.07E-31)*((300/(En))^2)*(10^(-70/(T)))*(10^((1500*((En)-((T)e)))/((En)*((T)e))))
R60	e+O2=>O-+O	2.63e-16*abs(ee)^(-0.495)*exp(-5.65/abs(ee))	
R61	e+O2=>O2-+	((9.72e-15*abs(ee)^(-1.62)*exp(-14.2/abs(ee)))*(abs(ee)>1.13)+2.78e-20*(abs(ee)<1.13))	
R62	e+O3=>O-+O2	1e-17	1.00E-11
R63	e+O3=>O2-+O	1e-15	1.00E-09
R64	e+O3+M=>O3-+M	1e-43	(1.4E-29)*(300/(En))*(10^(-600/(T)))*(10^((700*((En)-((T)e)))/((En)*((T)e))))
R65	e+N2O=>O-+N2	2.00e-16	
R66	e+NO+M=>NO-+M	8.00e-43	1.00E-30
R67	e+NO2=>O-+NO	1.00e-17	1.00E-11

R68	e+NO2+M=>NO2-+M	1.50e-42	3.00E-11
R69	e+NO3+M=>NO3-+M	1.00e-42	
R70	e+H2O=>H-+OH	4.42e-14*abs(ee)^(-2.0)*exp(-13.39/abs(ee))	
R71	e+H2O=>O-+H2	2.97e-15*abs(ee)^(-1.56)*exp(-13.67/abs(ee))	
R72	e+H2O=>OH-+H	9.60e-16*abs(ee)^(-1.70)*exp(-13.31/abs(ee))	
R73	e+HNO3=>NO2-+OH	5e-14	
R74	O-+N=>NO+e	2.60e-16	2.60E-10
R75	O-+N2=>N2O+e	1.00e-18	
R76	O-+N2(A)=>N2+O+e	2.20e-15	
R77	O-+N2(B)=>N2+O+e	1.90e-15	
R78	O-+O=>O2+e	1.4e-16	5.00E-10
R79	O-+O2=>O3+e	1e-18	5.00E-15
R80	O-+O2(a)=>O3+e	3e-16	
R81	O-+O3=>O2+O2+e	3e-16	
R82	O-+NO=>NO2+e	2.60e-16	2.60E-10
R83	O-+H2=>H2O+e	7e-16	
R84	O2-+N=>NO2+e	5.00e-16	5.00E-10
R85	O2-+N2=>N2+O2+e	1.9e-18*(tgas/300)^0.5*exp(-4990/tgas)	(0.0000000000019)*(((T)/300)^0.5)*(10^(-4990/(T)))
R86	O2-	2.10e-15	

	+N2(A)=>N2+O2+e		
R87	O2- +N2(B)=>N2+O2+e	2.50e-15	
R88	O2-+O=>O3+e	1.5e-16	1.50E-10
R89	O2-+O2=>O2+O2+e	2.7e-16*(tgas/300)^0.5*exp(-5590/tgas)	(2.7E-10)*((((T)e)/300)^0.5)*(10^(-5590/((T)e)))
R90	O2-+O3=>O3+O2+e	6.00e-16	
R91	O2- +O2(a)=>O2+O2+e	2e-16	
R92	O2-+H=>HO2+e	1.4e-15	
R93	O3-+O=>O2+O2+e	3e-16	3.00E-10
R94	O3-+O2=>O3+O2+e	2.3e-17	
R95	O3- +O3=>O2+O2+O2+e	3e-16	
R96	NO-+M=>NO+M+e	2.40e-19	
R97	NO-+NO=>NO+NO+e	5.00e-18	
R98	NO- +N2O=>NO+N2O+e	5.10e-18	
R99	NO-+H2=>NO+H2+e	2.3e-19	
R100	NO2-+O=>NO3+e	1.00e-18	1.00E-12

R101	NO2-+N=>N2+O2+e	1.00e-18	
R102	NO3- +O=>NO2+O2+e	1.00e-18	
R103	NO3-+N=>N2+O3+e	1.00e-18	
			1.50E-11
R104	H-+O2=>HO2+e	1.2e-15	
R105	H-+H=>H2+e	1.8e-15	
R106	OH-+O=>HO2+e	2e-16	
R107	OH-+H=>H2O+e	1.8e-15	
R108	N++N+M=>N2++M	1.00e-41	1.00E-29
R109	N++N2+M=>N3++M	4.60e-41	(0.9E-29)*(10^(400/((T)e)))
R110	N++N2O=>NO++N2	5.50e-16	5.50E-10
R111	N++NO=>NO++N	4.72e-16	8.00E-10
R112	N++NO=>N2++O	8.33e-17	3.00E-12
R113	N++NO=>O++N2	1.00e-18	1.00E-12
R114	N++NO2=>NO2++N	3.00e-16	
R115	N++NO2=>NO++NO	5.00e-16	
R116	N++O=>O++N	1.00e-18	1.00E-12
R117	N++O+M=>NO++M	1.00e-41	1.00E-29
R118	N++O2=>NO++O	2.70e-16	2.50E-10

R119	N++O2=>O++NO	2.80e-17	2.80E-11
R120	N++O2=>O2++N	3.00e-16	2.80E-10
R121	N++O3=>NO++O2	5.00e-16	5.00E-10
R122	N++OH=>OH++N	3.4e-16	
R123	N++OH=>NO++H	3.4e-16	
R124	N++H2O=>H2O++N	1.19e-15	
R125	N++H2O=>NO++H2	2.10e-16	
R126	N2++N=>N++N2	1e-18	(2.4E-15)*((T)e)
R127	N2++N+M=>N3++M	1e-41*(300/tgas)	(0.9E-29)*(10^(400/((T)e)))
R128	N2++N2+M=>N4++M	1e-41*(300/tgas)	5.00E-29
R129	N2+ + N2(A) => N3+ + N	3.00e-16	3.00E-10
R130	N2++N2O=>N2O++N2	6.00e-16	5.00E-10
R131	N2++N2O=>NO++N+N2	4.00e-16	4.00E-10
R132	N2++NO=>NO++N2	3.90e-16	3.30E-10
R133	N2++NO2=>NO++N2O	5.00e-17	
R134	N2++NO2=>NO2++N	3.00e-16	

	2		
R135	N2++O=>NO++N	1.40e-16	(1.3E-10)*((300/((T)e))^0.5)
R136	N2++O=>NO++N(2D)	1.8e-16*(300/tgas)	
R137	N2++O=>O++N2	1e-17*(300/tgas)^0.5	(1E-11)*((300/((T)e))^0.2)
R138	N2++O2=>O2++N2	5.00e-17	(6E-11)*((300/((T)e))^0.5)
R139	N2++O3=>O2++O+N2	1.00e-16	1.00E-10
R140	N2++H2O=>H2O++N2	2.3e-15	
R141	N3++N=>N2++N2	6.60e-17	6.60E-11
R142	N3++O2=>O2++N+N2	2.30e-17	2.30E-11
R143	N3++O2=>NO++O+N2	2.00e-17	
R144	N3++O2=>NO2++N2	4.40e-17	4.40E-11
R145	N3++NO=>NO++N2+N	7.00e-17	7.00E-11
R146	N3++NO=>N2O++N2	7.00e-17	7.00E-11
R147	N3++N2O=>NO++N2+N2	5.00e-17	

R148	N3++NO2=>NO++NO+N2	7.00e-17	
R149	N3++NO2=>NO2++N+N2	7.00e-17	
R150	N4++N2=>N2++N2+N2	2.1e-16*exp(tgas/121)	10^((-14.6)+0.0036*((T)-300))
R151	N4++N2O=>N2O++N2+N2	3e-16	
R152	N4++N=>N++N2+N2	1.00e-17	1.00E-11
R153	N4++NO=>NO++N2+N2	3.90e-16	4.00E-10
R154	N4++NO2=>NO2++N2+N2	2.50e-16	
R155	N4++NO2=>NO++N2O+N2	5.00e-17	
R156	N4++O=>O++N2+N2	2.50e-16	2.50E-10
R157	N4++O2=>O2++N2+N2	2.40e-16	2.50E-10
R158	N4++H2=>H2++N2+N2	3e-16*exp(-1800/tgas)	

R159	N4++H2O=>H2O++N2+N2	3e-15	
R160	O++N+M=>NO++M	1.00e-41	1.00E-29
R161	O++N2+M=>NO++N+M	6e-41*(300/tgas)^2	(6E-29)*((300/((T)e))^2)
R162	O++O+M=>O2++M	1e-41	1.00E-29
R163	O++O2=>O2++O	2.1e-17*(300/tgas)^0.5	(3.3E-11)*(10^(-0.00169*((T)e)))
R164	O++O3=>O2++O2	1e-16	1.00E-10
R165	O+ + N(2D) => N+ + O	1.30e-16	1.30E-10
R166	O++NO=>NO++O	1.00e-18	2.40E-11
R167	O++NO=>O2++N	3.00e-18	3.00E-12
R168	O++N2O=>N2O++O	6.30e-16	4.00E-10
R169	O++N2O=>NO++NO	2.30e-16	2.30E-10
R170	O++N2O=>O2++N2	2.00e-17	2.00E-11
R171	O++NO2=>NO++O2	5.00e-16	
R172	O++NO2=>NO2++O	1.60e-15	1.60E-09
R173	O++H=>H++O	6.8e-16	
R174	O++H2=>OH++H	1.7e-15	
R175	O++OH=>OH++O	3.3e-16	

R176	O++OH=>O2++H	3.6e-16	
R177	O++H2O=>H2O++O	3.2e-15	
R178	O2++O2+M=>O4++M	5.5e-43*(300/tgas)^2.7	(2.4E-30)*((400/((T)e))^3.2)
R179	O2++N=>NO++O	1.50e-16	1.20E-10
R180	O2++N2=>NO++NO	1.00e-23	1.00E-17
R181	O2++N2O5=>NO2++NO3+O2	8.80e-16	8.80E-10
R182	O2++NO=>NO++O2	4.60e-16	4.40E-10
R183	O2++NO2=>NO2++O2	6.60e-16	6.60E-10
R184	O2++NO2=>NO++O3	1.00e-17	1.00E-11
R185	O4++O=>O2++O3	3e-16	
R186	O4++O2=>O2++O2+O2	3.3e-12*(300/tgas)^4*exp(-5030/tgas)	
R187	O4++NO=>NO++O2+O2	6.80e-16	
R188	O4++NO2=>NO2++O2+O2	3.00e-16	
R189	O-+O2+M=>O3-+M	1.1e-42*(300/tgas)	(1.1E-30)*(300/((T)e))

R190	O- + O2(a) => O2- + O	1e-16	1.00E-10
R191	O-+O3=>O3-+O	8e-16	5.30E-10
R192	O-+N2O=>NO-+NO	2.00e-16	2.00E-10
R193	O-+N2O=>N2O-+O	2.00e-18	2.00E-12
R194	O-+NO+M=>NO2-+M	1.00e-41	1.00E-29
R195	O-+NO2=>NO2-+O	1.20e-15	1.20E-09
R196	O-+NO3=>NO3-+O	3.00e-16	
R197	O-+H2=>OH-+H	3.3e-17	
R198	O-+H2O=>OH-+OH	1.4e-15	
R199	O2-+O=>O-+O2	3.3e-16	3.30E-10
R200	O2-+O2+M=>O4-+M	3.5e-43*(300/tgas)	(3.5E-31)*(300/((T)e))
R201	O2-+O3=>O3-+O2	3.5e-16	4.00E-10
R202	O2-+N2O=>O3-+N2	1.00e-17	1.00E-12
R203	O2-+NO2=>NO2-+O2	7.00e-16	8.00E-10
R204	O2-+NO3=>NO3-+O2	5.00e-16	5.00E-10
R205	O2-+HNO3=>NO3-+HO2	2.80e-16	
R206	O3-+O=>O2-+O2	1e-17	3.20E-10
R207	O3-+NO=>NO2-+O2	1.00e-17	2.60E-12

R208	O3-+NO=>NO3-+O	1.00e-17	1.00E-11
R209	O3-+NO2=>NO3-+O2	2.00e-17	2.00E-11
R210	O3-+NO2=>NO2-+O3	7.00e-17	7.00E-10
R211	O3-+NO3=>NO3-+O3	5.00e-16	5.00E-10
R212	O3-+H=>OH-+O2	8.4e-16	
R213	O4-+NO=>NO3-+O2	2.5e-16	2.50E-10
R214	O4-+O=>O-+O2+O2	3e-16	3.00E-10
R215	O4-+O=>O3-+O2	4e-16	4.00E-10
R216	O4-+N2=>O2-+O2+N2	1e-16*exp(-1044/tgas)	(1E-10)*(10^(-1044/((T)e)))
R217	N2O++NO=>NO++N2O	2.30e-16	
R218	N2O++N2O=>NO++NO+N2	1.20e-17	
R219	N2O++NO2=>NO++N2+O2	4.29e-16	
R220	N2O++NO2=>NO2++N2O	2.21e-16	
R221	N2O++O2=>NO++NO2	4.59e-17	

R222	N2O++O2=>O2++N2O	2.24e-16	
R223	NO++N2O5=>NO2++NO2+NO2	5.90e-16	5.90E-10
R224	NO++O3=>NO2++O2	1.00e-21	1.00E-15
R225	NO++N+M=>N2O++M	1e-41*(300/tgas)	
R226	NO-+N2O=>NO2-+N2	2.80e-20	2.80E-14
R227	NO-+NO2=>NO2-+NO	3.00e-16	7.40E-16
R228	NO-+NO3=>NO3-+NO	3.00e-16	
R229	NO-+O2=>O2-+NO	5.00e-16	5.00E-10
R230	NO-+O3=>O3-+NO	3.00e-16	
R231	NO-+O=>O-+NO	3.00e-16	
R232	NO2++NO=>NO++NO2	2.75e-16	2.90E-10
			2.90E-10
R233	NO2-+N2O5=>NO3-	7.00e-16	7.00E-10

	+NO3+NO		
R234	NO2-+NO=>NO-+NO2	2.75e-16	
R235	NO2-+NO2=>NO3-+NO	4.00e-18	4.00E-12
R236	NO2-+NO3=>NO3-+NO2	5.00e-16	5.00E-10
R237	NO2-+O3=>NO3-+O2	1.80e-17	1.80E-11
R238	NO2-+H=>OH-+NO	4e-16	
R239	NO2-+N2O=>NO3-+N2	5e-19	
R240	NO2-+HNO3=>NO3-+HNO2	1.6e-15	
R241	NO3-+NO=>NO2-+NO2	3.00e-21	3.00E-15
R242	H++O=>O++H	3.8e-16	
R243	H++O2=>O2++H	1.17e-15	
R244	H++NO=>NO++H	1.9e-15	
R245	H++H2+M=>H3++M	3.1e-41	
R246	H++H2O=>H2O++H	8.2e-15	

R247	H-+N2O=>OH-+N2	1.1e-15	
R248	H-+NO2=>NO2-+H	2.9e-15	
R249	H-+H2O=>OH-+H2	3.8e-15	
R250	H2++O2=>O2++H2	7.83e-16	
R251	H2++H=>H++H2	6.4e-16	
R252	H2++H2=>H3++H	2e-15	
R253	H2++H2O=>H3O++H	3.43e-15	
R254	H2++H2O=>H2O++H2	3.86e-15	
R255	H3++O=>OH++H2	8e-16	
R256	H3++H2O=>H3O++H2	3e-15	
R257	H3++NO2=>NO++OH+H2	7e-16	
R258	OH++O2=>O2++OH	5.9e-16	
R259	OH++NO=>NO++OH	5.2e-16	
R260	OH++NO2=>NO++HO2	1.3e-15	
R261	OH++N2O=>N2O++OH	2.13e-16	

R262	OH++H2=>H2O++H	9.7e-16	
R263	OH++OH=>H2O++O	7e-16	
R264	OH++H2O=>H2O++OH	1.59e-15	
R265	OH++H2O=>H3O++O	1.30e-15	
R266	OH-+O3=>O3-+OH	9e-16	
R267	OH-+NO2=>NO2-+OH	1.9e-15	
R268	H2O++N=>NO++H2	1.9e-16	
R269	H2O++O=>O2++H2	5.5e-17	
R270	H2O++O2=>O2++H2O	4.3e-16	
R271	H2O++NO=>NO++H2O	4.6e-16	
R272	H2O++NO2=>NO2++H2O	1.2e-15	
R273	H2O++H2=>H3O++H	7.6e-16	
R274	H2O++H2O=>H3O++OH	1.7e-15	
R275	H3O++NO=>NO++H+	1.5e-18	

	H2O		
R276	H3O++N2O5=>NO2++HNO3+H2O	5.5e-16	
R277	O++O-=>O+O	2e-13*(300/tgas)^0.5	
R278	O++O2-=>O2+O	2e-13*(300/tgas)^0.5	
R279	O++O3-=>O3+O	2e-13*(300/tgas)^0.5	
R280	O++O4-=>O2+O2+O	1e-13	
R281	O++N2O-=>N2O+O	2e-13*(300/tgas)^0.5	
R282	O++NO-=>NO+O	2e-13*(300/tgas)^0.5	
R283	O++NO2-=>NO2+O	2e-13*(300/tgas)^0.5	
R284	O++NO3-=>NO3+O	2e-13*(300/tgas)^0.5	
R285	O++H-=>O+H	2e-13*(300/tgas)^0.5	
R286	O++OH-=>O+OH	2e-13*(300/tgas)^0.5	
R287	O2++O-=>O+O+O	1e-13	
R288	O2++O-=>O+O2	2e-13*(300/tgas)^0.5	
R289	O2++O2-=>O2+O2	2e-13*(300/tgas)^0.5	
R290	O2++O2-=>O2+O+O	1e-13	
R291	O2++O3-=>O3+O2	2e-13*(300/tgas)^0.5	
R292	O2++O3-=>O3+O+O	1e-13	
R293	O2++O4-	1e-13	

	=>O2+O2+O2		
R294	O2++N2O- =>N2O+O2	2e-13*(300/tgas)^0.5	
R295	O2++N2O- =>N2O+O+O	1.00e-13	
R296	O2++NO-=>NO+O2	2e-13*(300/tgas)^0.5	
R297	O2++NO-=>NO+O+O	1.00e-13	
R298	O2++NO2- =>NO2+O2	2e-13*(300/tgas)^0.5	
R299	O2++NO2- =>NO2+O+O	1.00e-13	
R300	O2++NO3- =>NO3+O2	2e-13*(300/tgas)^0.5	
R301	O2++NO3- =>NO3+O+O	1.00e-13	
R302	O2++H-=>H+O2	2e-13*(300/tgas)^0.5	
R303	O2++H-=>H+O+O	1.00e-13	
R304	O2++OH-=>OH+O2	2e-13*(300/tgas)^0.5	
R305	O2++OH-=>OH+O+O	1.00e-13	
R306	O4++O-=>O+O2+O2	1e-13	

R307	O4++O2- =>O2+O2+O2	1e-13	
R308	O4++O3- =>O3+O2+O2	1e-13	
R309	O4++O4- =>O2+O2+O2+O2	1e-13	
R310	O4++N2O- =>N2O+O2+O2	1e-13	
R311	O4++NO- =>NO+O2+O2	1e-13	
			1.00E-10
R312	O4++NO2- =>NO2+O2+O2	1e-13	
R313	O4++NO3- =>NO3+O2+O2	1e-13	
R314	O4++H-=>H+O2+O2	1e-13	
R315	O4++OH- =>OH+O2+O2	1e-13	
R316	N++N2O-=>N2O+N	2e-13*(300/tgas)^0.5	
R317	N++NO-=>NO+N	2e-13*(300/tgas)^0.5	

R318	N++NO2-=>NO2+N	2e-13*(300/tgas)^0.5	
R319	N++NO3-=>NO3+N	2e-13*(300/tgas)^0.5	
R320	N++O-=>O+N	2e-13*(300/tgas)^0.5	
R321	N++O2-=>O2+N	2e-13*(300/tgas)^0.5	
R322	N++O3-=>O3+N	2e-13*(300/tgas)^0.5	
R323	N++O4-=>O2+O2+N	1.00e-13	
R324	N++H-=>N+H	2e-13*(300/tgas)^0.5	
R325	N++OH-=>N+OH	2e-13*(300/tgas)^0.5	
R326	N2++N2O-=>N2O+N2	2e-13*(300/tgas)^0.5	
R327	N2++N2O-=>N2O+N+N	1.00e-13	
R328	N2++NO-=>NO+N2	2e-13*(300/tgas)^0.5	
R329	N2++NO-=>NO+N+N	1.00e-13	
R330	N2++NO2-=>NO2+N2	2e-13*(300/tgas)^0.5	
R331	N2++NO2-=>NO2+N+N	1.00e-13	
R332	N2++NO3-=>NO3+N2	2e-13*(300/tgas)^0.5	

R333	N2++NO3- =>NO3+N+N	1.00e-13	
R334	N2++O-=>O+N+N	1.00e-13	
R335	N2++O-=>O+N2	2e-13*(300/tgas)^0.5	
R336	N2++O2-=>O2+N+N	1.00e-13	
R337	N2++O2-=>O2+N2	2e-13*(300/tgas)^0.5	
R338	N2++O3-=>O3+N+N	1.00e-13	
R339	N2++O3-=>O3+N2	2e-13*(300/tgas)^0.5	
R340	N2++O4- =>O2+O2+N2	1.00e-13	
R341	N2++H-=>H+N2	2e-13*(300/tgas)^0.5	
R342	N2++H-=>H+N+N	1.00e-13	
R343	N2++OH-=>OH+N2	2e-13*(300/tgas)^0.5	
R344	N2++OH-=>OH+N+N	1.00e-13	
R345	N2O++N2O- =>N2O+N2O	2e-13*(300/tgas)^0.5	
R346	N2O++N2O- =>N2O+N2+O	1.00e-13	
R347	N2O++NO- =>NO+N2O	2e-13*(300/tgas)^0.5	

R348	N2O++NO- =>NO+N2+O	1.00e-13	
R349	N2O++NO2- =>NO2+N2O	2e-13*(300/tgas)^0.5	
R350	N2O++NO2- =>NO2+N2+O	1.00e-13	
R351	N2O++NO3- =>NO3+N2O	2e-13*(300/tgas)^0.5	
R352	N2O++NO3- =>NO3+N2+O	1.00e-13	
R353	N2O++O-=>O+N2O	2e-13*(300/tgas)^0.5	
R354	N2O++O-=>O+N2+O	1.00e-13	
R355	N2O++O2- =>O2+N2O	2e-13*(300/tgas)^0.5	
R356	N2O++O2- =>O2+N2+O	1.00e-13	
R357	N2O++O3- =>O3+N2O	2e-13*(300/tgas)^0.5	
R358	N2O++O3- =>O3+N2+O	1.00e-13	

R359	N2O++O4- =>O2+O2+N2O	1.00e-13	
R360	N2O++H-=>H+N2O	2e-13*(300/tgas)^0.5	
R361	N2O++H-=>H+N2+O	1.00e-13	
R362	N2O++OH- =>OH+N2O	2e-13*(300/tgas)^0.5	
R363	N2O++OH- =>OH+N2+O	1.00e-13	
R364	N3++N2O- =>N2O+N2+N	1.00e-13	
R365	N3++NO- =>NO+N2+N	1.00e-13	
R366	N3++NO2- =>NO2+N2+N	1.00e-13	
R367	N3++NO3- =>NO3+N2+N	1.00e-13	
R368	N3++O-=>O+N2+N	1.00e-13	
R369	N3++O2-=>O2+N2+N	1.00e-13	
R370	N3++O3-=>O3+N2+N	1.00e-13	
R371	N3++O4-	1.00e-13	

	=>O2+O2+N+N2		
R372	N3++H-=>H+N2+N	1.00e-13	
R373	N3++OH- =>OH+N2+N	1.00e-13	
R374	N4++N2O- =>N2O+N2+N2	1.00e-13	
R375	N4++NO- =>NO+N2+N2	1.00e-13	
R376	N4++NO2- =>NO2+N2+N2	1.00e-13	
R377	N4++NO3- =>NO3+N2+N2	1.00e-13	
R378	N4++O-=>O+N2+N2	1.00e-13	
R379	N4++O2- =>O2+N2+N2	1.00e-13	
R380	N4++O3- =>O3+N2+N2	1.00e-13	
R381	N4++O4- =>O2+O2+N2+N2	1.00e-13	
R382	N4++H-=>H+N2+N2	1.00e-13	

R383	N4++OH- =>OH+N2+N2	1.00e-13	
R384	NO++N2O- =>N2O+NO	2e-13*(300/tgas)^0.5	
R385	NO++N2O- =>N2O+N+O	1.00e-13	
R386	NO++NO-=>NO+NO	2e-13*(300/tgas)^0.5	
R387	NO++NO-=>NO+N+O	1.00e-13	
R388	NO++NO2- =>NO2+NO	2e-13*(300/tgas)^0.5	
R389	NO++NO2- =>NO2+N+O	1.00e-13	
R390	NO++NO3- =>NO3+NO	2e-13*(300/tgas)^0.5	
R391	NO++NO3- =>NO3+N+O	1.00e-13	
R392	NO++O-=>O+N+O	1.00e-13	
R393	NO++O-=>O+NO	2e-13*(300/tgas)^0.5	
R394	NO++O2-=>O2+N+O	1.00e-13	
R395	NO++O2-=>O2+NO	2e-13*(300/tgas)^0.5	

R396	NO++O3-=>O3+N+O	1.00e-13	
R397	NO++O3-=>O3+NO	2e-13*(300/tgas)^0.5	
R398	NO++O4-=>O2+O2+NO	1.00e-13	
R399	NO++H-=>H+NO	2e-13*(300/tgas)^0.5	
R400	NO++H-=>H+N+O	1.00e-13	
R401	NO++OH-=>OH+NO	2e-13*(300/tgas)^0.5	
R402	NO++OH-=>OH+N+O	1.00e-13	
R403	NO2++N2O-=>N2O+NO2	2e-13*(300/tgas)^0.5	
R404	NO2++N2O-=>N2O+N+O2	1.00e-13	
R405	NO2++NO-=>NO+NO2	2e-13*(300/tgas)^0.5	
R406	NO2++NO-=>NO+N+O2	1.00e-13	
R407	NO2++NO2-=>NO2+NO2	2e-13*(300/tgas)^0.5	
R408	NO2++NO2-=>NO2+N+O2	1.00e-13	

R409	NO2++NO3- =>NO3+NO2	2e-13*(300/tgas)^0.5	
R410	NO2++NO3- =>NO3+N+O2	1.00e-13	
R411	NO2++O-=>O+NO2	2e-13*(300/tgas)^0.5	
R412	NO2++O-=>O+N+O2	1.00e-13	
R413	NO2++O2- =>O2+NO2	2e-13*(300/tgas)^0.5	
R414	NO2++O2- =>O2+N+O2	1.00e-13	
R415	NO2++O3- =>O3+NO2	2e-13*(300/tgas)^0.5	
R416	NO2++O3- =>O3+N+O2	1.00e-13	
R417	NO2++O4- =>O2+O2+NO2	1.00e-13	
R418	NO2++H-=>H+NO2	2e-13*(300/tgas)^0.5	
R419	NO2++H-=>H+N+O2	1.00e-13	
R420	NO2++OH- =>OH+NO2	2e-13*(300/tgas)^0.5	

R421	NO2++OH-=>OH+N+O2	1.00e-13	
R422	H++N2O-=>N2O+H	2e-13*(300/tgas)^0.5	
R423	H++NO-=>NO+H	2e-13*(300/tgas)^0.5	
R424	H++NO2-=>NO2+H	2e-13*(300/tgas)^0.5	
R425	H++NO3-=>NO3+H	2e-13*(300/tgas)^0.5	
R426	H++O-=>O+H	2e-13*(300/tgas)^0.5	
R427	H++O2-=>O2+H	2e-13*(300/tgas)^0.5	
R428	H++O3-=>O3+H	2e-13*(300/tgas)^0.5	
R429	H++O4-=>O2+O2+H	1.00e-13	
R430	H++H-=>H+H	2e-13*(300/tgas)^0.5	
R431	H++OH-=>OH+H	2e-13*(300/tgas)^0.5	
R432	H2++N2O-=>N2O+H2	2e-13*(300/tgas)^0.5	
R433	H2++N2O-=>N2O+H+H	1.00e-13	
R434	H2++NO-=>NO+H2	2e-13*(300/tgas)^0.5	
R435	H2++NO-=>NO+H+H	1.00e-13	
R436	H2++NO2-=>NO2+H2	2e-13*(300/tgas)^0.5	

R437	H2++NO2- =>NO2+H+H	1.00e-13	
R438	H2++NO3- =>NO3+H2	2e-13*(300/tgas)^0.5	
R439	H2++NO3- =>NO3+H+H	1.00e-13	
R440	H2++O-=>O+H+H	1.00e-13	
R441	H2++O-=>O+H2	2e-13*(300/tgas)^0.5	
R442	H2++O2-=>O2+H+H	1.00e-13	
R443	H2++O2-=>O2+H2	2e-13*(300/tgas)^0.5	
R444	H2++O3-=>O3+H+H	1.00e-13	
R445	H2++O3-=>O3+H2	2e-13*(300/tgas)^0.5	
R446	H2++O4- =>O2+O2+H2	1.00e-13	
R447	H2++H-=>H+H2	2e-13*(300/tgas)^0.5	
R448	H2++H-=>H+H+H	1.00e-13	
R449	H2++OH-=>OH+H2	2e-13*(300/tgas)^0.5	
R450	H2++OH-=>OH+H+H	1.00e-13	
R451	H3++N2O- =>N2O+H+H2	1.00e-13	

R452	H3++NO- =>NO+H+H2	1.00e-13	
R453	H3++NO2- =>NO2+H+H2	1.00e-13	
R454	H3++NO3- =>NO3+H+H2	1.00e-13	
R455	H3++O-=>O+H+H2	1.00e-13	
R456	H3++O2-=>O2+H+H2	1.00e-13	
R457	H3++O3-=>O3+H+H2	1.00e-13	
R458	H3++O4- =>O2+O2+H+H2	1.00e-13	
R459	H3++H-=>H+H+H2	1.00e-13	
R460	H3++OH- =>OH+H+H2	1.00e-13	
R461	OH++N2O- =>N2O+OH	2e-13*(300/tgas)^0.5	
R462	OH++N2O- =>N2O+O+H	1.00e-13	
R463	OH++NO-=>NO+OH	2e-13*(300/tgas)^0.5	
R464	OH++NO-=>NO+O+H	1.00e-13	

R465	OH++NO2- =>NO2+OH	2e-13*(300/tgas)^0.5	
R466	OH++NO2- =>NO2+O+H	1.00e-13	
R467	OH++NO3- =>NO3+OH	2e-13*(300/tgas)^0.5	
R468	OH++NO3- =>NO3+O+H	1.00e-13	
R469	OH++O-=>O+O+H	1.00e-13	
R470	OH++O-=>O+OH	2e-13*(300/tgas)^0.5	
R471	OH++O2-=>O2+O+H	1.00e-13	
R472	OH++O2-=>O2+OH	2e-13*(300/tgas)^0.5	
R473	OH++O3-=>O3+O+H	1.00e-13	
R474	OH++O3-=>O3+OH	2e-13*(300/tgas)^0.5	
R475	OH++O4- =>O2+O2+OH	1.00e-13	
R476	OH++H-=>H+OH	2e-13*(300/tgas)^0.5	
R477	OH++H-=>H+O+H	1.00e-13	
R478	OH++OH-=>OH+OH	2e-13*(300/tgas)^0.5	
R479	OH++OH-=>OH+O+H	1.00e-13	

R480	H2O++N2O-=>N2O+H2O	2e-13*(300/tgas)^0.5	
R481	H2O++N2O-=>N2O+OH+H	1.00e-13	
R482	H2O++NO-=>NO+H2O	2e-13*(300/tgas)^0.5	
R483	H2O++NO-=>NO+OH+H	1.00e-13	
R484	H2O++NO2-=>NO2+H2O	2e-13*(300/tgas)^0.5	
R485	H2O++NO2-=>NO2+OH+H	1.00e-13	
R486	H2O++NO3-=>NO3+H2O	2e-13*(300/tgas)^0.5	
R487	H2O++NO3-=>NO3+OH+H	1.00e-13	
R488	H2O++O-=>O+OH+H	1.00e-13	
R489	H2O++O-=>O+H2O	2e-13*(300/tgas)^0.5	
R490	H2O++O2-=>O2+OH+H	1.00e-13	

R491	H2O++O2- =>O2+H2O	2e-13*(300/tgas)^0.5	
R492	H2O++O3- =>O3+OH+H	1.00e-13	
R493	H2O++O3- =>O3+H2O	2e-13*(300/tgas)^0.5	
R494	H2O++O4- =>O2+O2+H2O	1.00e-13	
R495	H2O++H-=>H+H2O	2e-13*(300/tgas)^0.5	
R496	H2O++H-=>H+OH+H	1.00e-13	
R497	H2O++OH- =>OH+H2O	2e-13*(300/tgas)^0.5	
R498	H2O++OH- =>OH+OH+H	1.00e-13	
R499	H3O++N2O- =>N2O+H2O+H	1.00e-13	
R500	H3O++NO- =>NO+H2O+H	1.00e-13	
R501	H3O++NO2- =>NO2+H2O+H	1.00e-13	

R502	H3O++NO3- =>NO3+H2O+H	1.00e-13	
R503	H3O++O- =>O+H2O+H	1.00e-13	
R504	H3O++O2- =>O2+H2O+H	1.00e-13	
R505	H3O++O3- =>O3+H2O+H	1.00e-13	
R506	H3O++O4- =>O2+O2+H2O+H	1.00e-13	
R507	H3O++H- =>H+H2O+H	1.00e-13	
R508	H3O++OH- =>OH+H2O+H	1.00e-13	
R509	N+N+M=>N2+M	8.3e-46*exp(500/tgas)	
R510	N+NO=>N2+O	2.1e-17*exp(100/tgas)	(1.05E-12)*((T)e)^0.5
R511	N+NO2=>N2O+O	5.8e-18*exp(220/tgas)	3.00E-12
R512	N+NO2=>N2+O+O	9.10e-19	9.10E-13
R513	N+NO2=>NO+NO	6.00e-19	2.30E-12
R514	N+NO2=>N2+O2	7.00e-19	7.00E-13

R515	N+O+M=>NO+M	6.3e-45*exp(140/tgas)	
R516	N+O2=>NO+O	1.5e-17*exp(-3600/tgas)	(1.1E-14)*(((T)e))*(10^(-3150/((T)e)))
R517	N+O3=>NO+O2	5.00e-22	2.00E-16
R518	N+OH=>H+NO	7.5e-17	
R519	N+HO2=>NO+OH	1.7e-17*exp(-1000/tgas)	
R520	N(2D) + N2 => N(4S) + N2	5e-18*exp(-1620/tgas)	6.00E-15
R521	N(2D) + N2O => NO + N2	1.5e-17*exp(-570/tgas)	3.00E-12
R522	N(2D) + NO => N2O	6.00e-17	6.00E-11
R523	N(2D)+NO=>O+N2	4.50e-17	
R524	N(2D)+O=>N+O	7.00e-19	
R525	N(2D) + O2 => NO + O(3P)	1.5e-18*(tgas/300)^0.5	(1.5E-12)*((((T)e)/300)^0.5)
R526	N(2D) + O2 => NO + O(1D)	6e-18*(tgas/300)^0.5	(6E-12)*((((T)e)/300)^0.5)
R527	N2(A) + N2 => N2(X) + N2	2.2e-20	3.00E-18
R528	N2(A)+N2(A)=>N2(B) +N2	4.00e-16	

R529	N2(A)+N2O=>O+N2+N2	8e-17	
R530	N2(A) + N2O => N2 + N + NO	8e-17	1.00E-11
R531	N2(A)+NO2=>N2+NO+O	1.30e-17	
R532	N2(A)+O2=>N2+O+O	5e-18*exp(-210/tgas)	2.54E-12
R533	N2(A)+O2=>O2(a)+N2	1.00e-18	1.29E-12
R534	N2(A)+N=>N+N2	5.00e-17	
R535	N2(A)+O=>NO+N(2D)	7.00e-18	7.00E-12
R536	N2(A)+O=>O(1D)+N2	2.30e-17	
R537	N2(A)+H2O=>H+OH+N2	5.00e-20	
R538	N2(B)+N2=>N2(A)+N2	5.00e-17	5.00E-11
R539	N2(B)=>N2(A)	1.25e+5	1.50E+05
R540	N2(B)+NO=>N2(A)+NO	2.40e-16	2.40E-10

R541	N2(B)+O2=>N2+O+O	3.00e-16	3.00E-10
R542	N2(B)+H2=>N2(A)+H2	2.50e-17	
R543	O+O+M=>O2+M	3.2e-47*exp(900/tgas)	
R544	O+O2+M=>O3+M	3.4e-46*(300/tgas)^1.2	(6.2E-34)*((300/((T)e))^2)
			(6.9E-34)*((300/((T)e))^1.25)
R545	O+O3=>O2+O2	8e-18*exp(-2060/tgas)	(2E-11)*(10^(-2300/((T)e)))
R546	O+NO+M=>NO2+M	1e-43*(300/tgas)^1.6	
R547	O+NO2=>NO+O2	6.5e-18*exp(120/tgas)	(1.13E-11)*((((T)e)/1000)^0.18)
R548	O+NO2+M=>NO3+M	9e-44*(300/tgas)^2	
R549	O+NO3=>O2+NO2	1.70e-17	1.00E-11
R550	O+H+M=>OH+M	1.62e-44	
R551	O+OH=>H+O2	2.2e-17*exp(-350/tgas)	
R552	O+H2O2=>OH+HO2	3.3e-17*exp(-2950/tgas)	
R553	O+HO2=>OH+O2	8.3e-17*exp(-500/tgas)	
R554	O+HNO=>OH+NO	5.99e-17	
R555	O+HNO2=>NO2+OH	2e-17*exp(-3000/tgas)	
R556	O(1D)+O2=>O+O2	6.4e-18*exp(67/tgas)	
R557	O(1D)+O=>O+O	8e-18	
R558	O(1D)+O2(a)=>O+O2	1e-17	

R559	O(1D)+O2=>O+O2(a)	1e-18	
R560	O(1D)+O3=>O+O+O2	1.2e-16	1.20E-10
R561	O(1D)+O3=>O2+O2	1.2e-16	
R562	O(1D)+N2=>O+N2	1.8e-17*exp(107/tgas)	(1.8E-11)*(10^(107/((T)e)))
R563	O(1D)+N2+M=>N2O+M	9.00e-49	
R564	O(1D)+N2O=>N2+O2	4.40e-17	4.40E-11
R565	O(1D)+N2O=>NO+NO	7.20e-17	7.20E-11
R566	O(1D)+NO=>O+NO	4.00e-17	
R567	O(1D)+NO2=>NO+O2	1.40e-16	
R568	O(1D)+H2=>OH+H	1.1e-16	
R569	O(1D)+H2O=>OH+OH	2.2e-16	
R570	O2(a)+O2=>O2+O2	3.8e-24*exp(-205/tgas)	(2.2E-18)*((((T)e)/300)^0.8)
R571	O2(a)+O3=>O+O2+O2	5.2e-17*exp(-2840/tgas)	(9.7E-13)*(10^(-1564/((T)e)))
R572	O2(a)+M=>O2+M	8e-27	
R573	O2(a)+NO=>O2+NO	2.50e-17	2.50E-11

R574	O2(a)+N2=>O2+N2	1.50e-24	3.00E-21
R575	O3+NO=>NO2+O2	1.8e-18*exp(-1370/tgas)	(4.3E-12)*(10^(-1560/((T)e)))
R576	O3+NO2=>NO3+O2	1.4e-19*exp(-2470/tgas)	(1.2E-13)*(10^(-2450/((T)e)))
R577	O3+M=>O+O2+M	3.92e-16*exp(-11400/tgas)	
R578	O3+H=>OH+O2	2.8e-17*(tgas/300)^0.75	
R579	O3+OH=>HO2+O2	1.6e-18*exp(-1000/tgas)	
R580	O3+HO2=>OH+O2+O2	1.4e-20*exp(-600/tgas)	
R581	NO+NO2+M=>N2O3+M	3.09e-46*(300/tgas)^7.7	
R582	NO+NO3=>NO2+NO2	1.8e-17*exp(110/tgas)	1.70E-11
R583	NO+OH+M=>HNO2+M	7.4e-43*(300/tgas)^2.4	
R584	NO+H+M=>HNO+M	1.0e-44*exp(300/tgas)	
R585	NO+HO2=>OH+NO2	3.4e-18*exp(270/tgas)	
R586	NO+HO2=>O2+HNO	3.3e-19*exp(-1000/tgas)	
R587	NO2+NO2+M=>N2O4+M	1.17e-45*(300/tgas)^3.8	
R588	NO2+NO3+M=>N2O	2.8e-42*(300/tgas)^3.5	

	5+M		
R589	NO2+NO3=>NO2+NO+O2	2.3e-19*exp(-1600/tgas)	(2.3E-13)*(10^(-1600/((T)e)))
R590	NO2+H=>OH+NO	1.47e-16	
R591	NO2+OH+M=>HNO3+M	2.2e-42*(300/tgas)^2.9	
R592	NO3+NO3=>NO2+NO2+O2	5e-18*exp(-3000/tgas)	(5E-12)*(10^(-3000/((T)e)))
R593	NO3+H=>OH+NO2	5.8e-16*exp(-750/tgas)	
R594	NO3+OH=>HO2+NO2	2e-17	
R595	NO3+HO2=>NO2+OH+O2	4.8e-18	
R596	NO3+HO2=>HNO3+O2	9.2e-19	
R597	N2O3+M=>NO+NO2+M	1.03e-16*exp(-2628/tgas)	
R598	N2O4+M=>NO2+NO2+M	1.09e-13*exp(-4952/tgas)	
R599	N2O5+M=>NO2+NO	1e-9*(300/tgas)^3.5*exp(-11000/tgas)	

	3+M		
R600	H+O2+M=>HO2+M	5.4e-44*(tgas/300)^(-1.8)	
R601	H+H+M=>H2+M	1.8e-42/tgas	
R602	H+OH+M=>H2O+M	6.1e-38/tgas^2	
R603	H+H2O2=>OH+H2O	1.69e-17*exp(-1800/tgas)	
R604	H+H2O2=>HO2+H2	2.8e-18*exp(-1900/tgas)	
R605	H+HO2=>H2+O2	5.6e-18	
R606	H+HO2=>O+H2O	2.4e-18	
R607	H+HO2=>OH+OH	4.2e-16*exp(-950/tgas)	
R608	H+HNO=>NO+H2	3e-17*exp(-500/tgas)	
R609	H+HNO2=>NO2+H2	2e-17*exp(-3700/tgas)	
R610	H+HNO3=>NO2+H2O	1.39e-20*(tgas/298)^3.29*exp(-3160/tgas)	
R611	H2+OH=>H+H2O	3.2e-17*exp(-2600/tgas)	
R612	OH+OH=>O+H2O	8.8e-18*exp(-503/tgas)	
R613	OH+OH+M=>H2O2+M	6.9e-43*(tgas/300)^(-0.8)	
R614	OH+HO2=>O2+H2O	4.8e-17*exp(250/tgas)	
R615	OH+H2O2=>HO2+H2O	2.9e-18*exp(-160/tgas)	

R616	OH+HNO=>NO+H2O	8e-17*exp(-500/tgas)	
R617	OH+HNO2=>NO2+H2O	1.8e-17*exp(-390/tgas)	
R618	OH+HNO3=>NO3+H2O	1.5e-20*exp(650/tgas)	
R619	HO2+HO2=>H2O2+O2	2.2e-19*exp(600/tgas)	
R620	HNO+O2=>NO+HO2	5.25e-18*exp(-1510/tgas)	
R621	HNO+O2=>NO2+OH	1.66e-21	
R622	HNO+HNO=>N2O+H2O	1.40e-21*exp(-1600/tgas)	
R623	HNO2+HNO2=>NO+NO2+H2O	1e-26	
R624	HNO2+HNO3=>NO2+NO2+H2O	1.6e-23	
R625	N2 + e => N2(W3) + e		(10^(-8.3-(15.4/(En))))
R626	N2 + e => N2(B') + e		(10^(-8.7-(16.8/(En))))
R627	N2(W3) => N2(B)		(Kossyi et al., 1992)
R628	N2(B') => N2(B) + 1524nm	3.40E+04	(Capitelli et al., 2000)

R629	N2 + e => N2(a') + e		(10^(-8.8-(16.7/(En))))
R630	N2 + e => N2(a) + e		(10^(-8.5-(17.4/(En))))
R631	N2 + e => N2(w1) + e		(10^(-8.7-(17.5/(En))))
R632	N2(a) => N2(a') + 8252nm	1.30E+02	(Capitelli et al., 2000)
R633	N2(w1) => N2(a')		(Kossyi et al., 1992)
R634	N2 + e => N2(C) + e		(10^(-8.2-(21.1/(En))))
R635	N2 + e => N2(E) + e		(10^(-10.1-(25.4/(En))))
R636	N2 + e => N2(a'') + e		(10^(-9.2-(26.2/(En))))
R637	N2(E) => N2(C) + 1500nm	1.73E+03	(Capitelli et al., 2000)
R638	N2(a'') => N2(C)		(Kossyi et al., 1992)
R639	O2 + e => O2(b) + e		(10^(-11.2-(0.72/(En))))
R640	N2(A) + N2(a') => N4+ + e		5.00E-11
R641	N2(a') + N2(a') => N4+ + e		2.00E-10
R642	O2- + O2(a) => O2 + O2 + e		2.00E-10
R643	O2- + O2(b) => O2 +		3.60E-10

	O2 + e		
R644	O2- + N2(A) => O2 + N2 + e		2.10E-09
R645	O2- + N2(B) => O2 + N2 + e		2.50E-09
R646	O- + O2(a) => O3 + e		3.00E-10
R647	O- + O2(b) => O + O2 + e		6.90E-10
R648	O- + N2(A) => O + N2 + e		2.20E-09
R649	O- + N2(B) => O + N2 + e		1.90E-09
R650	O4- + O2(a, b) => O2- + O2 + O2		1.00E-10
R651	N2(A) + O2 => N2O + O		7.80E-14
R652	N2(A) + N2(A) => N2(C) + N2(X)		2.00E-11
R653	N2(A) + N(4S) => N2(X) + N(2P)		5.00E-11

R654	N2(A) + O => N2(X) + O(1S)		2.10E-11
R655	N2(A) + NO => N2(X) + NO		7.00E-11
R656	N2(a') + N2 -s(T)-> N2(B) + N2		2.00E-13
R657	N2(a') + O2 => N2(X) + O + O		2.80E-11
R658	N2(a') + NO => N2(X) + N + O		3.60E-10
R659	N2(C) => N2(B) + hv		3.00E+07
R660	N2(C) + N2 -s(T)-> N2(a') + N2		1.00E-11
R661	N2(C) + O2 => N2(X) + O + O(1S)		3.00E-10
R662	O2(a) + O => O2 + O		7.00E-16
R663	O2(b) + O3 => O2 + O2 + O		1.80E-11
R664	O2(b) + N2 => O2(a) + N2		(4.9E-15)*(10^(-253/((T))))

R665	O2(b) + O2 => O2(a) + O2		(4.3E-22)*(((T))^2.4)*(10^(-241/((T))))
R666	O2(b) + O => O2(a) + O		8.00E-14
R667	O2(b) + O => O2(X) + O(1D)		(3.39E-11)*((300/((T)))^0.1)*(10^(-4201/((T))))
R668	O2(b) + NO => O2(a) + NO		4.00E-14
R669	O2(A, c, C) + O2 => O2(b) + O2(b)		2.90E-13
R670	O2(A, c, C) + N2 => O2(b) + N2		3.00E-13
R671	O2(A, c, C) + O => O2(b) + O(1D)		9.00E-12
RATE COEFFICIENTS FROM OTHER REFERENCES			
R672	N2(A) => N2 293nm	5.00E-01	(Capitelli et al., 2000)
R673	N2(C) => N2(B) + 336.5nm	2.45E+07	(Capitelli et al., 2000)

R674	N2(W) => N2(a) + 3578nm	1.51E+09	(Capitelli et al., 2000)
R675	N2(b) => N2(a) + 313.3nm	1.59E+08	(Capitelli et al., 2000)
R676	N2(b') =>N2(a) + 353.1nm	5.56E+05	(Capitelli et al., 2000)
R677	O2(a) =>O2 + 1270nm	2.60E-04	(Capitelli et al., 2000)
R678	O2(b) => O2 (a) + 1900nm	1.50E-03	(Capitelli et al., 2000)
R679	O2(b) => O2 + 762nm	8.50E-02	(Capitelli et al., 2000)
R680	O2(A) + O2(C) + O2(c) => O2 + 243_306nm	1.10E+01	(Capitelli et al., 2000)
R681	O2(B) => O2 + 200nm	2.00E+06	(Capitelli et al., 2000)
R682	H2O(aq) => H+(aq) + OH-(aq)	2*10^-5	(Eigen, 1954)

R683	H+(aq) + OH-(aq) => H2O(aq)	1.5*10^11	(Eigen, 1954)
R684	O3(aq) + OH-(aq) => O2-(aq) + HO2(aq)	70	(Staehelin & Hoigne, 1982)
R685	HO2(aq) => O2-(aq) + H+(aq)	7.5*10^5	(Divisek & Kastening, 1975), (Buhler et al, 1984)
R686	O2-(aq) + H+(aq) => HO2(aq)	4.7*10^10	(Divisek & Kastening, 1975)
R687	O2-(aq) + HO2(aq) => O2(aq) + HO2-(aq)	0.8*10^8	(Divisek & Kastening, 1975)
R688	O3(aq) + O2-(aq) => O3-(aq) + O2(aq)	1.6*10^9	(Buhler et al, 1984)
R689	O3-(aq) + H+(aq) => HO3(aq)	5.2*10^10	(Buhler et al, 1984)
R690	HO3(aq) => O3-(aq) + H+(aq)	3.7*10^4	(Buhler et al, 1984)
R691	HO3(aq) => OH(aq) + O2(aq)	1.1*10^5	(Buhler et al, 1984), (Staehelin et al, 1984)

R692	O2-(aq) + O3(aq) => O3-(aq) + O2(aq)	1.6*10^9	(Staehelin et al, 1984)
R693	OH(aq) + O3(aq) => HO4(aq)	2.0*10^9	(Staehelin et al, 1984)
R694	HO4(aq) => O2(aq) + HO2(aq)	2.8*10^4	(Staehelin et al, 1984)
R695	OH(aq) + OH(aq) => H2O2(aq)	5*10^9	(Staehelin et al, 1984)
R696	OH(aq) + O2-(aq) => OH-(aq) + O2(aq)	1*10^10	(Staehelin et al, 1984)
R697	OH(aq) + HO3(aq) => H2O2(aq) + O2(aq)	5*10^9	(Staehelin et al, 1984)
R698	HO3(aq) + HO3(aq) => H2O2(aq) + O2(aq) + O2(aq)	5*10^9	(Staehelin et al, 1984)
R699	HO3(aq) + O2-(aq) => OH-(aq) + O2(aq) + O2(aq)	1*10^10	(Staehelin et al, 1984)
R700	HO4(aq) + HO4(aq) => H2O2(aq) +	5*10^9	(Staehelin et al, 1984)

	O3(aq) + O3(aq)		
R701	HO4(aq) + OH(aq) => H2O2(aq) + O3(aq)	5*10^9	(Staehelin et al, 1984)
R702	HO4(aq) + O2-(aq) => OH-(aq) + O3(aq) + O2(aq)	1*10^10	(Staehelin et al, 1984)
R703	HO4(aq) + HO3(aq) => H2O2(aq) + O3(aq) + O2(aq)	5*10^9	(Staehelin et al, 1984)
	SurOH => OHaq- + Sur+	0.5*((2.158700594e-8)*(cos((3.14*(1/0.025))*(t-0.05))))	
	Hsur => sur- + Haq+	2*((2.158700594e-8)*(cos((3.14*(1/0.025))*(t-0.025))))	
R706	H2O2 =>H2O2(aq)	417.375366371317*ssa	(Ammann et al., 2013)
R707	NO2 +NO2 =>HNO2(aq) +HNO3(aq)	116.431388724652*ssa	(Ammann et al., 2013)
R708	NO3 =>NO3(aq)	65.1878271375358*ssa	(Ammann et al., 2013)
R709	N2O5 =>N2O5(aq)	41.3845060043205*ssa	(Ammann et al., 2013)
R710	NH3 =>NH3(aq)	957.622930901536*ssa	(Ammann et al., 2013)

R711	HNO2 +HNO2 =>NO+NO2	18.5152341391045*ssa	(Ammann et al., 2013)
R712	NO+NO2 =>HNO2 +HNO2	43976.3375913973*ssa	(Ammann et al., 2013)
R713	HNO3 =>HNO3(aq)	409.13945249584*ssa	(Ammann et al., 2013)
R714	OH =>OH(aq)	957.622930901536*ssa	(Ammann et al., 2013)
R715	H2O =>H2O(aq)	903.673720638238*ssa	(Ammann et al., 2013)
R716	HO2 =>HO2(aq)	3436.62410575337*ssa	(Ammann et al., 2013)
R717	O3 + => O3(aq)	5.6989963521373*ssa	(Ammann et al., 2013)
R718	NO2aq + NO2aq => N2O4aq	4.50E+08	(Neta et al., 1988)
R719	NO2aq + NO2aq => NO3aq- + NO2aq- + Haq+ + Haq+	1.50E+07	(Neta et al., 1988)
R720	NO2aq + NOaq => N2O3aq	1.10E+09	(Neta et al., 1988)
R721	NO2aq + OHaq => HO2NOaq	1.30E+09	(Neta et al., 1988)
R722	NO3aq + NO2aq- => NO3aq- + NO2	1.20E+09	(Neta et al., 1988)

R723	NO2aq-- + H2Oaq => NOaq + OHaq-	1.00E+03	(Neta et al., 1988)
R724	NO3aq-- + H2Oaq => NO2aq + OHaq	1.00E+03	(Neta et al., 1988)
R725	NO3aq-- + O2aq => NO3aq- + O2aq-	2.00E+08	(Neta et al., 1988)
R726	Oaq + OHaq- => HO2aq-	4.20E+08	(Neta et al., 1988)
R727	Oaq + H2O2aq => OHaq + HO2aq	1.60E+09	(Neta et al., 1988)
R728	Oaq + HO2aq- => OHaq + O2aq-	5.30E+09	(Neta et al., 1988)
R729	Oaq + O2aq => O3aq	4.00E+09	(Neta et al., 1988)
R730	O3aq- + OHaq => O2aq- + HO2aq	8.50E+09	(Neta et al., 1988)
R731	O3aq- + Oaq- => O2aq- + O2aq-	7.00E+08	(Neta et al., 1988)
R732	O3aq- + Oaq- => O4aq--	7.00E+08	(Neta et al., 1988)
R733	O3aq- => Oaq- +	6.20E+03	(Neta et al., 1988)

	O2aq		
R734	O3aq- + Haq+ => OHaq + O2aq	9.00E+10	(Neta et al., 1988)
R735	O3aq- + Haq+ => HO3aq	5.20E+10	(Neta et al., 1988)

Appendix 4

Material	Formula	Hardness	Measuring system	Youngs modulus	thermal conductivity	coefficient of linear thermal expansion	specific heat	dielectric constant	electrical resistivity
				GPa	W/m-K	µm/m-K	J/g-K		ohm-cm
Alumina	Al2O3	9.00	Mineral	393.00	35.00	8.40	0.88	9.60	1.00E+14
Aluminium Nitride	AlN	5.00	Mineral	308.00	126.15	5.15	1.05	8.55	1.00E+14
Boron Carbide	B4C	(-)	Knoop	445.00	28.00	5.54	3.96	6.40	10
Boron Nitride	BN	2.00	Mineral	675.00	20.00	1.50	0.80	4.08	1.00E+13
Cordierite	2MgO-2Al2O3-5SiO2	7.00	Mineral	70.00	3.00	1.70	1.47	4.70	1.00E+14
Mullite	3Al2O3-SiO2	8.00	Mineral	150.00	3.50	5.30	0.96	6.00	1.00E+13
Sapphire	a-Al2O3	9.00	Mineral	325.00	40.00	8.35	0.75	10.35	1.00E+17
Silicon Carbide	SiC	9.50	Mineral	476.00	41.00	5.12	0.63	10.20	1.00E+08
Silicon Nitride	Si3N4	9.00	Mineral	317.00	27.00	3.40	0.71	7.00	1.00E+13
Steatite L-5	H2Mg3(SiO3)4	7.50	Mineral	138.00	2.90	7.00	0.92	6.30	1.00E+04
Tungsten Carbide	WC	1706.00	Knoop	562.00	96.00	5.90	0.95	ng	1000
Zirconia	ZrO2	6.50	Mineral	207.00	2.70	11.00	0.42	26.00	1.00E+04
Kapton	(-)				0.12	20.00	1.09	3.50	1.00E+17
Mica	KAl2(Si3Al)O10(OH,F)2	2.50	Mineral		3.75	22.50	0.50	6.30	1.00E+12
PTFE	(C2F4)n	55.00	Durometer	0.48	0.25	100.00	1.40	2.10	1.00E+18
Glass (Borosilicate, Pyrex)	(SiO2)81%(B2O3)13%(Na2O)4%(other)2%	418.00	Knoop	62.75	1.20	3.25	0.80	4.10	1.60E+11

Quartz (silica)	SiO2	600.00	Kg/mm2	72.00	1.40	0.55	0.67	3.82	1.00E+10
Macor	(Al2O3)16%(B2O3)7%(K2O)10%(MgO)17%(SiO2)46%(F)4%	250.00	Knoop	66.90	1.46	9.30	0.79	5.85	1.00E+16
Peek	[OC6H4OC6H4COC6H4]n	97.00	Rockwell M	7.10	0.27	80.70	2.03	3.51	9.18E+15
Aluminium	Al	120.00	Knoop	68.90	167.00	25.20	0.90		3.99E-06
Silver	Ag	25.00	Vickers	76.00	419.00	19.60	0.23		0.00000155
Copper	Cu	50.00	Vickers	110.00	398.00	16.40	0.39		0.0000017
Tungsten	W	3430.00	Vickers	411.00	174.00	4.50	0.13		5.40E-06
Iron	Fe	608.00	Vickers	211.00	80.00	11.80	0.45		1.00E-05
Platinum	Pt	549.00	Vickers	168.00	72.00	8.80	0.13		1.06E-05
Stainless Steel		217.00	Brinell	212.00	16.30	16.60	0.50		7.20E-05
Lead	Pb	1.50	Mineral	16.00	35.00	28.90	0.13		2.10E-05
Titanium	Ti	970.00	Vickers	116.00	21.90	8.60	0.54		4.00E-05
Gold	Au	216.00	Vickers	78.00	320.00	14.20	0.13		2.20E-06
Graphite	C	0.80	Mineral	4.80	24.00	8.39	0.67	-	7.00E-03